

## INFORMATION TO USERS

This manuscript has been reproduced from the microfilm master. UMI films the text directly from the original or copy submitted. Thus, some thesis and dissertation copies are in typewriter face, while others may be from any type of computer printer.

**The quality of this reproduction is dependent upon the quality of the copy submitted.** Broken or indistinct print, colored or poor quality illustrations and photographs, print bleedthrough, substandard margins, and improper alignment can adversely affect reproduction.

In the unlikely event that the author did not send UMI a complete manuscript and there are missing pages, these will be noted. Also, if unauthorized copyright material had to be removed, a note will indicate the deletion.

Oversize materials (e.g., maps, drawings, charts) are reproduced by sectioning the original, beginning at the upper left-hand corner and continuing from left to right in equal sections with small overlaps. Each original is also photographed in one exposure and is included in reduced form at the back of the book.

Photographs included in the original manuscript have been reproduced xerographically in this copy. Higher quality 6" x 9" black and white photographic prints are available for any photographs or illustrations appearing in this copy for an additional charge. Contact UMI directly to order.

# UMI

A Bell & Howell Information Company  
300 North Zeeb Road, Ann Arbor MI 48106-1346 USA  
313/761-4700 800/521-0600



## **NOTE TO USERS**

**The original document received by UMI contains pages with slanted print. Pages were microfilmed as received.**

**This reproduction is the best copy available**

**UMI**

---



UNIVERSITY OF OKLAHOMA

GRADUATE COLLEGE

**Thermoporomechanical Modelling of Inclined  
Boreholes**

A DISSERTATION

SUBMITTED TO THE GRADUATE FACULTY

in partial fulfillment of the requirements for the

degree of

DOCTOR OF PHILOSOPHY

BY

Xu Li  
Norman, Oklahoma  
1998

**UMI Number: 9914403**

---

**UMI Microform 9914403  
Copyright 1999, by UMI Company. All rights reserved.**

**This microform edition is protected against unauthorized  
copying under Title 17, United States Code.**

---

**UMI**  
300 North Zeeb Road  
Ann Arbor, MI 48103

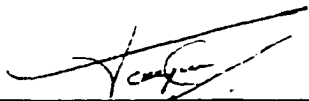
©Copyright by Xu Li 1998  
All Rights Reserved.

---

# Thermoporomechanical Modelling of Inclined Boreholes

A DISSERTATION APPROVED FOR THE  
SCHOOL OF PETROLEUM AND GEOLOGICAL ENGINEERING

BY

  
James M. Ferry  
James M. Ferry  
James M. Ferry  
James M. Ferry  
James M. Ferry

# Dedication

To my family and those who trusted and loved me .....

## Acknowledgments

I would like to express my sincere and deep gratitude to my advisor, Dr. Jean-Claude Roegiers, for his constant guidance and encouragement throughout my Ph.D. work. Dr. Roegiers provided me the opportunity to know, work with, and learn from a group of excellent experts in rock mechanics through OU Rock Mechanics Institute and Rock Mechanics Consortium. The communication with them greatly enriched my knowledge about the current industry concerns as well as the state of the art of the relevant research. Without this precious experience and the generous supports from Dr. Roegiers, the OU Rock Mechanics Institute and Rock Mechanics Consortium, the completion of this dissertation would not be possible. Thanks are also due to my Ph.D. advisory committee members: Dr. Faruk Civan, Dr. James M. Forgotson Jr., Dr. Anuj Gupta, Dr. Roy Knapp, and Dr. Chee P. Tan, for their interest in guiding my work. Especially, I am indebted to Dr. Knapp, for the time, patience, and advise he provided while helping me finalizing my Ph.D. program when Dr. Roegiers was away on sabbatical leave; and to Dr. Tan, who introduced me into the interesting field of wellbore stability studies, and provided me with various supports during my research.

Special thanks also go to Dr. Lizheng Cui, for the many formal and informal technical discussions. His advise in poroelasticity and engineering mechanics definitely speeded me up.

I also wish to thank my former office and classmate, Dr. Helio dos Santos from Petrobras, for the numerous interesting discussions we had during his study here; Dr. Ahmed Abou-Sayed from BP Exploration, for his valuable suggestive comments to this work; Dr. Adel Diek and Dr. Mazen Kanj, for their friendly support and open door policy; Ms. Carla Cates and Ms. Leslie M. Flenniken, for their help in administrative affairs, and Mr. Don Cruickshank, for his support in computer matters.

Finally, I would like to thank my family members, my mother, Ling Yuan, who always loves me, and has always been ready to help in every aspect; my father, Rong Xuan Fang, who gave me a happy and worry-free childhood and loved me until the last minute of his life; my stepfather, Jiu Zhou Li, who built us another happy family after my father passed away; my parents in-law, Depu Zhang and Younan Ma, who treated me as their own daughter; my husband, Lingchao Zhang, who loved me in his own special way, and supported me with his versatile mind and hands; and, last but certainly not the least, one of the most important persons in my life: my daughter, Yuan FeiFei Zhang, who accompanied me through numerous otherwise lonely and boring weekends in my office; her sweet smile, and the regular pat of her small hands on my back when I was tired and down, were one of my most important driving forces.

Without all these love and supports, my life would have been dull and aimless.

# Table of Contents

<b>Acknowledgments</b>	<b>v</b>
<b>List of Tables</b>	<b>xii</b>
<b>List of Figures</b>	<b>xiii</b>
<b>Abstract</b>	<b>xvii</b>
<b>Chapter 1 Introduction</b>	<b>1</b>
1.1 Research Motivations and Objectives . . . . .	1
1.2 Dissertation Outline . . . . .	3
<b>Chapter 2 General Review on Wellbore Stability Studies</b>	<b>5</b>
2.1 Common Wellbore Instability Problems . . . . .	5
2.2 Major Factors Influencing Wellbore Stability . . . . .	7
2.3 Existing Predictive Models . . . . .	7
2.4 Coupled Thermal-hydraulic-mechanical Modelling . . . . .	12
<b>Chapter 3 Theoretical Background</b>	<b>18</b>
3.1 Introduction . . . . .	18
3.2 Governing Equations . . . . .	18
3.2.1 Constitutive relations . . . . .	19
3.2.2 Conservation Laws . . . . .	22
3.2.3 Field Equations . . . . .	24
3.2.3.1 Deformation Field Equation . . . . .	24

3.2.3.2	Fluid Diffusivity Field Equations . . . . .	24
3.2.3.3	Thermal Diffusivity Field Equation . . . . .	25
3.2.4	Kurashige's Model . . . . .	26
3.3	Non-linear and Plastic Rock Behaviors . . . . .	28
3.3.1	Stress- and Temperature-dependent Material Properties . . . . .	28
3.3.1.1	Porosity and Permeability . . . . .	28
3.3.1.2	Poroelastic Parameters . . . . .	31
3.3.1.3	Thermoelastic Parameters . . . . .	32
3.3.1.4	Fluid Properties . . . . .	34
3.3.1.5	Summary . . . . .	35
3.3.2	Thermoporoelastoplastic Constitutive Relations . . . . .	36
3.3.2.1	Plasticity in Geological Materials . . . . .	36
3.3.2.2	General Elastoplastic Constitutive Relations for Non- isothermal Fluid Saturated Porous Media . . . . .	37
3.3.2.3	Mohr-Coulomb and Drucker-Prager Failure Criteria . . . . .	39
3.3.2.4	A Drucker-Prager Model for Strain Hardening and Softening . . . . .	40
3.3.2.5	Thermoporoelastoplastic Constitutive Relations . . . . .	42
<b>Chapter 4</b>	<b>Thermoporoelastic Solutions</b> . . . . .	<b>57</b>
4.1	Introduction . . . . .	57
4.2	General Solutions For Irrotational Displacement Field . . . . .	57
4.2.1	Decoupling of Displacement Field from Temperature and Pore Pressure Fields . . . . .	58
4.2.2	Dimensionless Diffusivity Equations . . . . .	60
4.2.3	Diffusivity Equations in Cylindrical Coordinate System . . . . .	62
4.2.4	Some Simplified Scenarios . . . . .	64
4.2.4.1	Scenario 1 . . . . .	64

4.2.4.2	Scenario 2 . . . . .	64
4.2.4.3	Scenario 3 . . . . .	65
4.3	Solutions for Borehole Problems . . . . .	65
4.3.1	Boreholes Subjected to Non-hydrostatic Stress Field . . . . .	66
4.3.1.1	Problem Definition . . . . .	66
4.3.1.2	Solutions . . . . .	66
4.3.2	Inclined Boreholes . . . . .	75
4.3.2.1	Problem Definition . . . . .	75
4.3.2.2	Loading Decomposition . . . . .	77
4.3.2.3	Solutions . . . . .	78
4.3.3	Thermoelastic Borehole Solutions . . . . .	81
<b>Chapter 5</b>	<b>Finite Element Model For Thermoporoelastoplasticity</b>	<b>87</b>
5.1	Introduction . . . . .	87
5.2	Finite Element Formulae . . . . .	88
5.2.1	Weak Statement of Governing Equations . . . . .	88
5.2.2	Spatial Discretization . . . . .	89
5.2.3	Temporal Discretization . . . . .	93
5.2.4	Partitioned Solution Procedure . . . . .	94
5.2.5	Algorithm for Non-linear and Elastoplastic Analysis . . . . .	95
5.2.6	Program Flow Chart . . . . .	97
5.3	Implementation and Validation of FE Model . . . . .	98
5.3.1	Steady State and Transient Temperature Distribution . . . . .	98
5.3.2	One-dimensional Consolidation . . . . .	106
5.3.3	Temperature-induced Pore Pressure and Stresses . . . . .	107
5.3.4	Elastoplastic Analysis of Thick-walled Tube . . . . .	109

<b>Chapter 6 Applications</b>	<b>131</b>
6.1 Basic Mechanisms of Thermoporoelastic Processes Affecting Borehole Stability . . . . .	131
6.1.1 Case I . . . . .	131
6.1.2 Temperature-induced pore pressure and stresses . . . . .	132
6.1.3 Implications for Wellbore Stability . . . . .	133
6.1.3.1 Shear Failure Potential . . . . .	133
6.1.3.2 Axial Failure Potential . . . . .	134
6.1.3.3 Tensile Failure Potential . . . . .	134
6.1.3.4 Time-delayed Heating-type of Problems . . . . .	135
6.1.3.5 Failure Potential for Different Formations . . . . .	135
6.2 Application Examples . . . . .	136
6.2.1 Case II . . . . .	136
6.2.1.1 Shear Failure . . . . .	136
6.2.1.2 Tensile Failure . . . . .	138
6.2.2 Case III . . . . .	139
6.2.2.1 Shear Failure . . . . .	140
6.2.2.2 Fracturing . . . . .	142
6.2.2.3 Spalling . . . . .	144
6.3 Summary . . . . .	145
<b>Chapter 7 Conclusions, Contributions and Recommendations</b>	<b>172</b>
7.1 Conclusions . . . . .	172
7.2 Contributions . . . . .	174
7.3 Recommendations . . . . .	175
<b>References</b>	<b>177</b>
<b>Appendix A: Stress- and Temperature-dependent Formation Proper-</b>	



## List of Tables

5.1	Comparison of the numerical with the analytical solutions for the steady state temperature distribution in thick-walled tube example	101
5.2	Comparison of the numerical and analytical solutions for the transient temperature distribution for different recurrence schemes ( $dt = 0.187, x = 1.0$ )	103
5.3	Comparison of the numerical and analytical solutions for transient temperature distribution for different recurrence schemes ( $dt = 0.187, x = 1.0$ )(cont.)	104
5.4	Influence of time-step size on the numerical solutions ( $x=1.0$ )	105
5.5	Material properties for one-dimensional consolidation problem	107
5.6	Comparison of numerical and analytical solutions for the radius of plastic zone and the radial displacement at the interface of elastic and plastic zone	110
5.7	Comparison of the numerical and analytical solutions for the stress distribution along the borehole radius	110
6.1	Thermoporoelastic Properties for Case I	132
6.2	Thermoporoelastic properties for Cases II and III	140

## List of Figures

2.1	Commonly observed wellbore problems . . . . .	16
2.2	Schematic diagram of coupling mechanisms for a fully coupled thermal-hydraulic-mechanical system . . . . .	17
3.1	Pore volume contraction of three sand stones as function of temperature at constant stress conditions (after Somerton, 1992 ) . . . . .	45
3.2	Effects of pore pressure on pore volume contraction during temperature change (after Somerton, 1992) . . . . .	46
3.3	Experimentally obtained relationship between void ratio and permeability (after Lewis & Schrefler, 1987) . . . . .	47
3.4	Linear thermal expansion as a function of temperature for some sandstones and quartz (after Somerton, 1992) . . . . .	48
3.5	Thermal conductivity as a function of temperature (after Somerton, 1992) . . . . .	49
3.6	Thermoconductivity as a function of stress (after Somerton, 1992) .	50
3.7	Thermal diffusivity as a function of temperature and stress for dry Berea sandstone (after Somerton, 1992) . . . . .	51
3.8	Typical rock behavior during tri-axial tests . . . . .	52
3.9	Geometric interpretation of hardening/softening models . . . . .	53
3.10	Mohr-Coulomb and Tresca yield functions in principal stress space .	54
3.11	Drücker-Prager and Von Mises yield functions in principal stress space	55
3.12	Upper and lower bound Drücker-Prager yield surfaces . . . . .	56

4.1	Schematic diagram for a borehole subjects to a non-hydrostatic stress fields and wellbore pressure and temperature which are different from initial formation pore pressure and temperature . . . . .	83
4.2	Schematic diagram of an inclined borehole . . . . .	84
4.3	Loading decomposition scheme for inclined borehole problem . . . . .	85
4.4	Relationship between the two local coordinate systems . . . . .	86
5.1	Calculation sequences for non-linear and thermoporoelastoplastic algorithms . . . . .	99
5.2	The schematic diagram of a thick-walled tube subjected to a constant temperture potential at the inner face of the tube . . . . .	111
5.3	The FE mesh for the thick-walled tube example . . . . .	112
5.4	The schematics and FE mesh for a three-side insulated plate with a zero initial temperature and a unit temperature at the left-hand side of the plate ( for $t > 0$ ) . . . . .	113
5.5	Comparison of numerical and analytical solutions for transient temperature distribution for different recurrence schemes ( @ $x = 1.0$ ) . . . . .	113
5.6	Schematic diagram of one-dimensional consolidation problem . . . . .	114
5.7	The FE mesh for one-dimensional consolidation problem . . . . .	114
5.8	Comprison of numerical and analytical solutions for the transient displacement at the top of the soil layer . . . . .	115
5.9	Comprison of numerical and analytical solutions for the pore pressure distribution along the layer depth ( $t = 0.1$ day ) . . . . .	116
5.10	Comprison of numerical and analytical solutions for the pore pressure distribution along the layer depth ( $t = 1$ day ) . . . . .	117
5.11	The FE mesh and the thermal and hydraulic boundary conditions for the Case I in Chapter 6 . . . . .	118
5.12	Comparison of numerical and analytical solutions for temperature distribution along the borehole radius ( $t = 0.01$ day ) . . . . .	119
5.13	Comparison of numerical and analytical solutions for temperature distribution along the borehole radius ( $t = 0.1$ day ) . . . . .	120

5.14	Comparison of numerical and analytical solutions for temperature distribution along the borehole radius ( $t = 1$ day ) . . . . .	121
5.15	Comparison of numerical and analytical solutions for temperature distribution along the borehole radius ( $t = 10$ day ) . . . . .	122
5.16	Comparison of numerical and analytical solutions for temperature induced pore pressure along the borehole radius ( $t = 0.01$ day ) . .	123
5.17	Comparison of numerical and analytical solutions for temperature induced pore pressure along the borehole radius ( $t = 0.1$ day ) . .	124
5.18	Comparison of numerical and analytical solutions for temperature induced pore pressure along the borehole radius ( $t = 1$ day ) . . .	125
5.19	Comparison of numerical and analytical solutions for temperature induced pore pressure along the borehole radius ( $t = 10$ day ) . . .	126
5.20	Comparison of numerical and analytical solutions for the total radial stress distribution along the borehole radius ( $t = 0.01$ day ) . . . .	127
5.21	Comparison of numerical and analytical solutions for the total circumferential stress distribution along the borehole radius ( $t = 0.01$ day ) . . . . .	128
5.22	Comparison of numerical and analytical solutions for total radial stress distribution along the borehole radius ( $t = 0.1$ day ) . . . . .	129
5.23	Comparison of numerical and analytical solutions for total circumferential stress distribution along the borehole radius ( $t = 0.1$ day ) . . . . .	130
6.1	Boundary and initial conditions for Case I . . . . .	146
6.2	Transient temperature distribution . . . . .	147
6.3	Temperature-induced pore pressure . . . . .	148
6.4	Total radial stress profile . . . . .	149
6.5	Total circumferential stress profile . . . . .	150
6.6	Heating induced shear failure potential . . . . .	151
6.7	Cooling induced shear failure potential . . . . .	152
6.8	Comparison of the magnitude of different stresses . . . . .	153

6.9	Comparison of stress magnitudes at 10 days . . . . .	154
6.10	Transient effective radial stress profiles . . . . .	155
6.11	Transient effective circumferential stress profile . . . . .	156
6.12	Schematic diagram of borehole temperature potential at different drilling phase . . . . .	157
6.13	Failure potential at different formations . . . . .	158
6.14	Boundary and initial conditions for Case II . . . . .	159
6.15	Isochrones of stress profile along $\sigma_h$ direction . . . . .	160
6.16	Stress history at some points around the borehole for different tem- perature condition . . . . .	161
6.17	Stress distribution around the borehole for different temperature con- ditions and at different times . . . . .	162
6.18	Different failure modes at different time . . . . .	163
6.19	Effective radial stress profile along $\sigma_h$ direction . . . . .	164
6.20	Effective circumferential stress at different temperature conditions .	165
6.21	Boundary and initiation conditions for Case III . . . . .	166
6.22	Stress clouds for different temperature condition and at different times	167
6.23	Effective collapse stress as a function of borehole deviation angle and temperature ( $\varphi_{z'} = 30^\circ$ ) . . . . .	168
6.24	Effective fracturing stress as a function of borehole deviation angle and temperature ( $\varphi_{z'} = 30^\circ$ ) . . . . .	169
6.25	Effective radial stress as a function of wellbore deviation angle and temperature ( $\varphi_{z'} = 30^\circ$ ) . . . . .	170
6.26	Effective radial stress as a function of borehole deviation angle and mud weight ( $\varphi_{z'} = 30^\circ$ ) . . . . .	171

# Abstract

This dissertation systematically investigated the impact of non-isothermal drilling on borehole stability for boreholes drilled in fluid-saturated porous formations, and subjected to an arbitrarily oriented stress field. Emphasis was put on the analyses of problems occurring in shales, *i.e.*, the thermal diffusivity is generally greater than the fluid diffusivity; and conductive, rather than convective, heat transfer dominates the temperature diffusion process. The thermal-hydraulic-mechanical (THM), or thermoporomechanical processes discussed in this dissertation are fully-coupled. The thermoporoeleastic near-wellbore behavior was thoroughly discussed based on the derived analytical thermoporoeleastic solutions. Theoretical and numerical models for the investigation of non-linear and thermoporoelelastoplastic responses were also developed.

In the theoretical development part, a set of fully-coupled thermoporoeleastic governing equations were proposed and some drawbacks in an existing model discussed. Formulae for stress- and temperature-dependent thermoporoeleastic parameters were derived based on the micromechanical model of volumetric response; non-linear behavior for some thermoelastic and thermodynamics properties were reviewed. Following this, the basic theories for plasticity and failure were revisited, and the fully-coupled thermoporoelelastoplastic constitutive relations for plastic strain and the change of fluid content per unit volume, and for a strain hardening/softening Drucker-Prager material model were deduced.

In the model development part, thermoporoeleastic analytical solutions, including the general solution for axisymmetric loading condition; dimensionless solutions for some extreme boundary conditions; the solution for a borehole subjected to non-hydrostatic far-field loading; and solution for inclined boreholes, were derived. These models furthered the current technologies in this field by taking into account the complete THM coupling mechanism and arbitrary borehole orientations

with respect to the in-situ stress field. A finite element model which is capable of simulating the behaviors of highly non-linear and quasi-static thermoporoelastoplastic systems was also developed. This is an entirely new application attempts in the area of fully-coupled THM modelling. The validation of the finite element model was carried out for several doubly-coupled problems with known solutions. The models developed in this part provide effective tools for both evaluating the potential impacts of thermoporoelastic processes on wellbore stability, and the relative importance of taking into account the non-linear and thermoporoelastoplastic behavior.

In the application part, the basic mechanisms of coupled thermoporoelastic processes influencing borehole stability were thoroughly investigated through a diagnostic example. In addition, the potential impacts of non-isothermal drilling on the stability of boreholes subjected to arbitrary stress field were illustrated through two application examples. The results from these examples have shown that heating the borehole can significantly increase the potential of near-wellbore shear failure at early times. Heating also imposes a high potential of borehole spalling. On the other hand, cooling the borehole tends to stabilize the borehole at the beginning of the drilling; but with time, it could induce time-delayed lost circulation, wellbore spalling, and passive and active shear failures, especially when the cooling effects is combined with the high mud weight. In particular, if an originally cooled borehole is gradually heated up during deepening, time-delayed failure could occur in the upper sections of a borehole. Due to their high porosity and low permeability, thermal effects are especially significant in shales, which could be a new explanation for the high problematic rate in shales. Quantitatively, the impacts of thermal effects on wellbore stability could be significant, it could provide solutions for those wellbore problems that cannot be predicted by isothermal analyses. The findings from these analyses are especially important for offshore high-temperature, high-pressure and deep wells, where high mud weight are usually required to manage the high pressure, a small amount of temperature change on the wellbore wall could

bring in various time-delayed borehole problems. It also implied that cooling the borehole could be an effective way to stabilize the wellbore in these wells, as long as the upper part of the wellbore are cased in time.

# 1 Introduction

## 1.1 Research Motivations and Objectives

With the past decade's maturation in modern drilling technology, the petroleum industry has realized the tremendous value of developing fields utilizing highly deviated, extended-reach and horizontal wells. Such wells promise, for a slightly higher development cost, faster production rates and higher reserve access compared to the conventional vertical wells. However, the wellbore stability problems associated with these wells are also much more difficult to manage. Earlier studies on the stability of inclined boreholes developed the analytical solutions considering formations to be linear elastic media [26][2][120]. Recently, Cui *et al.* [43] derived the analytical poroelastic solution taking into account the coupled pore fluid effects. However, all the afore-mentioned solutions considered only isothermal wellbore conditions.

During the drilling of an oil or gas well, the temperature of the drilling mud is usually quite different from the formation temperature. Due to the geothermal gradient, the drilling fluid is usually cooler than the formation when it first reaches the bottom of the hole. When the borehole deepens, the same section will gradually be heated up by the drilling fluid that is heated up further downhole. For example, for a 3000 m-depth well drilled in an area with a geothermal gradient of  $0.03^{\circ}\text{C}/\text{m}$  and a surface temperature of  $15^{\circ}\text{C}$ , the bottom hole could be cooled up to  $55^{\circ}\text{C}$  and the upper section, at about 1000m depth, could be heated up to  $30^{\circ}\text{C}$  [39]. Such a temperature difference can significantly change the stress and pore pressure distributions around the borehole. Hence, an assumed isothermal wellbore condition may lead to erroneous predictions of wellbore stability condition, especially for the

offshore high-temperature, high-pressure and deep wells.

The fact that drilling is a non-isothermal activity is common knowledge, but the potential impact of the thermal effects on wellbore stability has basically been overlooked by industry, even though some field cases have been reported blaming temperature for time-delayed borehole failures[71], and cooling the mud can effectively reduce wellbore problems[99]. Part of the reason for industry to believe that thermal effects is a trivial problem is due to the fact that the existing analyses are essentially uncoupled, *i.e.*, temperature is taken into account via the thermal expansion coefficient of the rock formation which only results in an additional stress term. The fully-coupled thermoporomechanical analyses conducted in this dissertation reveal that the thermal effects can be crucial to the wellbore stability (mainly due to the high pore pressure induced), much more significant than the results predicted by uncoupled models, especially when fluid diffusivity of the formation is smaller than the thermal diffusivity, such as in shales.

It is well known that 95% of the wellbore instability problems occur in shale, and no uniform recognition has been reached so far as to what are the controlling mechanisms responsible for these problems. Studies conducted in this dissertation revealed the potential causes for the high problematic rate in shales, and suggested a new explanation for the major shale failure mode that has been confirmed by laboratory tests[132].

The major objective of this dissertation is to systematically investigate the impacts of non-isothermal drilling processes on borehole stability for boreholes drilled in fluid-saturated porous formation, and subjected to a stress field that is arbitrarily oriented with respect to the borehole axis. Emphasis is put on the analyses for problems occurring in shales, *i.e.*, the thermal diffusivity is generally greater than the fluid diffusivity; and conductive, instead of convective, heat transfer dominates the temperature diffusion process. The thermal-hydraulic-mechanical (THM), or thermoporomechanical processes discussed in this dissertation are fully-coupled. The non-linear and elastoplastic rock behavior on borehole stability are mean to

be investigated as well.

## 1.2 Dissertation Outline

Chapter 1 stated the research motivations and objectives for this dissertation. A brief overview of the dissertation is also given at the end of this chapter.

Chapter 2 is a general review of the state of the art of wellbore stability studies, including a summary of commonly seen wellbore instability problems, the analysis for the factors influencing the wellbore stability, and an overview of the existing predictive models. In particular, a review of the current technologies on coupled THM modelling, and their applications to wellbore stability study are given in this chapter.

Chapter 3 contains the basic theories applied in the subsequent chapters for the thermoporoelastic/plastic modelling. First, a set of thermoporoelastic governing equations was proposed and some drawbacks in an existing model discussed; then, formulae for some of the stress- and temperature-dependent thermoporoelastic parameters were derived based on the micromechanical model of volumetric response and constitutive relations; non-linear behaviors for other thermoelastic and thermodynamics properties were also reviewed. Following this, the basic theory for plasticity and failure were revisited; and finally, the fully-coupled thermoporoelastoplastic constitutive relations for plastic strain and porosity, and for a strain hardening/softening Drucker-Prager material model were developed.

Chapter 4 presents the thermoporoelastic analytical solutions obtained in this dissertation, including the general solution for axisymmetric loading condition; dimensionless solutions for some extreme boundary conditions; the solution for a borehole subjected to non-hydrostatic far-field loading; and the solution for inclined boreholes. Thermoelastic solutions for inclined boreholes was also derived at the end of this chapter for the purpose of comparison.

Chapter 5 describes the development of a fully-coupled thermoporoelastoplastic

finite element model. The model is capable of simulating the behavior of highly non-linear and quasi-static thermoporoelastoplastic systems. Verifications of the model is carried out for several doubly-coupled problems with known solutions. The model provides a powerful tool for the evaluation of the relative importance of taking into account the non-linear and poroelastoplastic behavior.

Chapter 6 consists of three application examples: Case I, a case that is designed to investigate the basic mechanisms of coupled thermoporoelastic processes influencing borehole stability; and Case II and III which illustrate the potential significant impacts of non-isothermal drilling process on the stability of a vertical borehole subjected to a non-hydrostatic stress field, as well as the more general case of an inclined borehole. Recommendations are made at the end of the chapter on how to avoid borehole problems during drilling under non-isothermal conditions.

Finally, in Chapter 7, a summary of the studies conducted in this dissertation are given, and the major contributions of the work are outlined. Based on the current study, recommendations are proposed on potentially important future developments.

## 2 General Review on Wellbore Stability Studies

### 2.1 Common Wellbore Instability Problems

Problems related to wellbore instability are a well known source of additional costs to the petroleum industry, especially when dealing with hostile environments such as extremely weak, plastic and reactive formations; tectonically very active areas where formation is highly stressed and discontinuous; unfavorable lithology sequences which narrows the mud-weight window, and high formation temperature and pressure. One area where operators experienced immense wellbore problems is the US Gulf Coast[3], where borehole collapse and sanding are plaguing many completions because of the presence of unconsolidated weak sands and reactive shales. There is no doubt that highly geopressed sections and high temperatures in deep wells in this area added to the complexity of the problem. Another typical area is the Cuisiana field in Colombia[5] where approximately 10% of the well costs are spent coping with bad holes, mainly because of the abnormally high tectonic stresses and complicated geological setting at the foot of Andes. In addition to the hostile environments, the increasing use of highly-deviated, extended-reach and horizontal wells, and other innovative technologies such as underbalanced drilling and multilaterals, has definitely escalated the demand for wellbore stability studies.

Wellbore failures can occur during drilling, completion, and production of a well, whenever the stresses around the borehole exceed the local strength of the formation. The commonly observed wellbore failures can be divided into four types:

?

hole closure, hole enlargement, fracturing and sand production (Figure 2.1):

- *Borehole closure* is a ductile-type of compressive shear failure, *i.e.*, the failure due to excessive deformations. Failure of this type occurs in weak and plastic formations such as salt and some shales. When this happens, repeated borehole reaming will be required at the least. In severe cases, it can cause stuck pipe and logging tools, or even casing collapse.
- *Borehole enlargement* means either a breakout or a washout. Breakout here stands for a locally occurring brittle-type compressive shear failure, with their location as well as geometry vary according to the relative magnitude of the three principal stresses acting along the borehole wall. Washout is a total collapse of a section of the wellbore. It could be due to the sloughing of reactive shales, severe shear failure in weak formations such as coal, or borehole spalling due to circumferential tensile failure. The debris from hole enlargement can accumulate in the borehole, leading to stuck pipe, or even inducing further borehole collapse. Besides, the resulted out-of gauge hole can further affect directional control, the quality of logging, and the cementing jobs.
- *Fracturing* means tensile failure in radial or transverse directions with respect to the borehole. It is mainly due to too high a wellbore pressure; but borehole inclination and rock anisotropy also play important roles. When this happens, drilling fluid might will lost into the formation, leading to the lost of drilling time and an increase in cost. In extreme situations, differential pipe sticking can happen.
- *Sanding* is a common problem during the production of relatively weak sandstones, when drawdown is high enough to break and remove formation particles. Fluid velocity and hydrodynamic forces play important roles in the problem. Serious sanding problems limit the production rate which could render the well useless. It also causes damage to equipment.

The classical failure modes mentioned above perceive the formation as a continuum medium. Pre-existing discontinuities in the rock mass can bring additional wellbore problems as well. Shear displacements along an pre-existing discontinuity could occur[98], and "key blocks"[66] in a fractured network can drop into the well.

## 2.2 Major Factors Influencing Wellbore Stability

The factors influencing the stability of a wellbore can be divided into two categories: uncontrollable, and controllable. In trying to strike a balance between the minimum mud weight or the maximum drawdown, and the integrity of a borehole, continuous efforts are being made to accurately evaluate the effects of uncontrollable factors such as the in-situ stresses, formation pore pressure, and rock properties, and optimizing the design of controllable factors such as mud weight, its physical and chemical composition, and borehole orientations (including inclination and azimuth). But not as much attention has been paid to the effects of discontinuity and mud temperature, even though field observations related to them are reported from time to time in the literature. Apart from the reason that the theories related to these topics are more complicated and less matured than the classical elasticity and plasticity, the major reason that hinders the application of the discontinuity theory lies in the difficulty of accurately characterizing the distribution of the discontinuities along the borehole. But the major reason for the less attention to the temperature effects is because of the traditional thoughts that it is not a significant issue.

## 2.3 Existing Predictive Models

Since Hubbert and Willis[80] first applied Kirsch's[22] solution to predict the stability of a vertical borehole subjected to a non-hydrostatic far field stress and constant borehole fluid pressure, considerable efforts and spectacular progresses have been

made in developing mathematical models that predict the wellbore responses as accurately as possible. According to their theoretical background, the mechanical wellbore stability models can generally be divided into three categories: elastic/plastic models, poroelastic/plastic models, and discontinuum mechanics model.

Typically presented by Goodman's joint element[67], Cundall's distinct elements [45] and Shi's key block theory[66], Discontinuum mechanics models were originated in late 70's and popularly used in rock engineering problems such as tunnelling and mining. But such approach are not commonly used in wellbore stability analyses in the petroleum industry. The only published application so far is by Rawling *et al.*[127] who simulated a set of lab polyaxial tests using Cundall's distinct elements model[46]. As it was mentioned before, the major reason hindering the application of discontinuity models could be the difficulty of accurately characterizing the three-dimensional fracture distribution in a deep borehole, which is the basic requirement for using this type of model. Since discontinuity and fracture networks are commonly observed in rock masses, the discontinuum model would be the only possible way of providing accurate predictions of wellbore problems, once the deformations of the discontinuity dominates the rock response around the borehole. Because of this, one would believe that the application of discontinuum models would find its way in the petroleum industry in the future, with the associated developments in geophysics and logging technology.

Elastic/plastic models do not account for the transient pore pressure changes during the stress redistribution around the borehole, even though the effective stress law may be used. After Hubbert and Willis, Fairhurst[57] derived the solution for the stress distribution around an inclined borehole by including the stresses induced by anti-plane shear. Later, Bradley[26] published a series of analyses on the effects of borehole inclination and in-situ stress field on wellbore stability based on Fairhurst's solution. Even though Fairhurst's model and Bradley's work considered only isotropic and linear elastic rock behavior, they provided one of the most reliable tool, and revealed the most significant physical insight into the effects of in-situ

stress field and borehole inclination on wellbore stability. They are recognized as the most valuable fundamental developments, and are still the most popularly referred works in wellbore stability studies.

In the late 80's, Aadnøy[2][1] developed a semi-analytical model taking into account the influence of rock anisotropy on inclined borehole stability, but his model could only solve for the stresses along the borehole wall, and it was limited to an isotropic shear failure criterion. Ong and Roegiers[120][119] modified Aadnøy's model by presenting the stress as a function of borehole radii and adopting an anisotropic shear failure criterion. Based on Ong and Roegiers's model, a wellbore stability analysis tool was developed which is presently extensively used in the petroleum industry[47]. Later, Li *et al.* further improved Ong's wellbore stability analysis tool by including a horizontal stress determination model as its front end[93][94]. Since only 10% of the rock formations exhibit isotropic material properties, and 30% of the rocks has an anisotropy ratio of more than 1.5 for Young's modulus[118], the anisotropic model appears to be more realistic compared to the isotropic models.

Both the field observations and lab tests results have shown that the linear-elastic models give a higher stress concentration rate around the borehole; and thus, require a much higher mud weight to prevent active shear failure[127][151]. This is because the linear elastic models do not take into account the large deformations rock experiences before failure, which will release a certain amount of stresses, or energy, around the borehole. Besides, the peak-strength failure criterion, which is usually used together with the elastic model, assumes that wellbore failure is synonymous to one point at the borehole wall reaching the peak-strength of the rock. But in reality, stress transfer starts as soon as one point in the material reaches its yield limit, and a plastic zone around the borehole, which is characterized by its large deformation and low stresses, will finally form. As long as the borehole deformations are within the tolerance of the drilling tool, the wellbore can generally be considered as being stable during this stage. In other words, deformations,

instead of stresses, is a more suitable criterion for the judgement of borehole failure when plastic deformation comes into play. If, otherwise, the stresses are used as failure criterions, it is proper to believe that a wellbore reached its strength limit only when the stresses in most of the area around the borehole, instead of one point, reached its peak strength. Furthermore, most of the rock-type material exhibits strain-softening at the later stage of the deformation, *i.e.* deformation increases with the decrease of the stresses, and failure may be occurring only when localized softening zones are developed, further extending the bearing capacity of the rock.

Conservative prediction itself is not a serious problem for the industry. However, there are frequent cases where mud weights predicted to prevent active shear failure and fracturing cross each other in mud weight stability profile, *i.e.*, an imaginary negative safe operating mud weight window will be produced, which means either fracturing or differential pipe sticking will occur, or the wellbore will collapse by active shear failure, no matter what mud weight is chosen. The design goal is to use the lowest possible mud weight to prevent active shear failure; and hence, to obtain a widest possible mud weight window. In viewing the differences between the failure mud weight predicted by the linear elastic model and the laboratory and field observations, and the possibility that less conservative mud weight predictions can be obtained from elastoplastic analyses, substantial work has been directed toward the investigation of the elastoplastic rock behavior, and develop the more realistic elastoplastic predictive models.

The pioneer work in elastoplastic stress analysis around a cylindrical cavity dated back to 1938 by Fenner[58]. Over the years, numerous solutions to predict the size of the failure zone and plastic deformation around underground cylindrical cavities induced by the stress redistribution due to the excavation[28][110], drilling[12][70] and production[7][131][109] (to cite a few) have been developed. An extensive review on the models under hydrostatic loading can be found in[28]. Due to the high complexity involved, the similar analysis for non-hydrostatic stress

field started to receive attention only after the finite element method had been applied to this field[11][129]. As a matter of fact, the only semi-analytical model that has been developed so far is by Detournay and Fairhurst[53]. Their model considers a wellbore drilled in an elastoplastic dilatant material, subjected to a non-hydrostatic stress field, but there are several restrictions in their solution such as only a limited range of deviation from hydrostatic loading can be considered. The analysis which reflect more realistic conditions such as inclined boreholes[56][151], and strain-hardening/softening features[151], are all produced using finite element method.

The formation surrounding the borehole is often permeated with fluids, and the pore pressure changes due to drilling or production are a transient diffusion process. This means the stability condition of a borehole could also change with time because of the effective stress law. In viewing the limitation of elastic/plastic model in capturing this feature, poroelastic/plastic models were developed.

Haimson and Fairhurst presented the first poroelastic borehole stability model based on an asymptotic solution[72]. Detournay and Cheng derived a fully-coupled, poroelastic semi-analytical solution for a vertical borehole subjected to a non-hydrostatic stress field[51]. Recently, Cui *et al.* further extended Detournay and Cheng's work and developed a model that is able to evaluate the stability of inclined boreholes[43]. The above poroelastic models consider the rock formation as isotropic material and with isotropic poroelastic properties. On the other hand, semi-analytical and finite element models which take into account the anisotropic poroelastic rock properties were also developed[4][44].

Comparing to poroelasticity, the development and application of poroelastoplastic wellbore stability models are still in their infancy. Attempts have been seen in the literature to conduct poroelastoplastic wellbore stability analyses by incorporating the steady state or transient pore pressure distribution into the existing semi-analytical plastic borehole models[154][25][102]. But these are not fully-coupled poroelastoplastic models, and they never break the limitation of one-dimensional

or hydrostatic loading condition. Besides the mathematical difficulties involved in solving these problems analytically, the limited understanding of fully-coupled poroelastoplastic rock constitutive behavior also hindered the development in this direction. The finite element method has been adopted by several authors to carry out fully-coupled poroelastoplastic analyses in fluid injection during hydrocarbon production[138], and other applications[92]. However, the fully-coupled poroelastoplastic analysis for borehole stability has not been seen yet.

## 2.4 Coupled Thermal-hydraulic-mechanical Modelling

Since Schiffman[134] first extended the Biot theory[14][15][16] for non-isothermal systems, substantial literature on the modelling of coupled THM response of fluid-saturated porous media has been accumulated over the years due to its relevance to many engineering applications including nuclear waste disposal[21][20][90][136][137][140]; geothermal energy production[103][104][13]; seasonal temperature variation on the behavior of structure foundations[105]; fluid injection for hydraulic fracturing or water flooding[123][77][138]; thermal recovery of heavy oil[150][79]; and wellbore instability control during the drilling of gas and oil wells[40][156]. Diverse forms of governing equations taking into account the THM coupling at different levels of generality have been developed [20][13][103][90][88][40]. Due to the complexity of cross-coupling mechanisms involved in this type of problem, the majority of boundary and initial value problems of such type are solved by various numerical techniques [76][90][137][140]. Very few problems of two or three-dimensional geometry, such as a heated borehole[104][156] or a spherical heat source in infinite media[21][20], are solved analytically. As a matter of fact, these existing analytical solutions are limited to axisymmetric boundary conditions, which renders the problems one-dimensional mathematically.

For a phenomenologically coupled problem, the complexity of the analysis de-

depends on the level of coupling which is being simulated. Figure 2.2 is a schematic diagram of coupling mechanisms for a fully-coupled THM system.

Thermomechanical coupling has been studied by many authors[113][114][115][18] in the past. With very few exceptions[18], these now classical studies consider mainly the coupling mechanism I, and are limited in the context of thermoelasticity. Coupling mechanism II is traditionally ignored based on the observation that the temperature variations induced by mechanical deformations is very small compared to the strains/stresses induced by temperature variations[115]. As to the mechanism that mechanical deformation might influence the thermal properties, which in turn could render the thermal behavior non-linear, very few studies have been reported[141], and the subject are not well understood as of today.

Between early 70's to mid 80's, great advances in simulating coupled fluid flow and heat transfer problems have been made in conjunction with the geothermal energy research. Various models, including lumped parameter and distributed parameter models; single and multi-phased (mainly water-steam system) models; and models considering one or two-way coupling mechanism, have been developed[107][157][27][106][64][89]. Solutions to these models mostly rely on numerical procedures such as finite elements and finite differences[106][64]. Non-linearity due to the convective heat transfer or non-linear thermodynamic parameters which usually involves in these types of modelling can lead to serious numerical difficulties such as numerical dispersion and oscillations. Semi-implicit and implicit iteration procedures such as the Newton-Raphson method were generally used to dealing with such problems. Although the scanty input parameters limited the successful applications of these models in field problems[107], the development and implementation of them accumulated a lot of experiences in dealing with numerical difficulties related to non-linear systems.

Subsidence, consolidation and some time-delayed failure phenomena are mainly governed by the hydraulic-mechanical coupling mechanisms. Even though numerous predictive models, including sophisticated non-linear and elastoplastic models,

have been developed and applied to the prediction and diagnosis of field observed problems of these types, most of these models take into account coupling mechanism V only, and ignore the coupling mechanism VI[34][126][74], with very few exceptions[92]. Only in recent years, attention started to turn to the modelling of more realistic two-way coupling mechanisms. As stated in the last section, significant advances have been achieved recently for quasi-static, poroelastic type of time-delayed failure analyses in some applications[52][42]. However, fully-coupled poroelastoplastic modelling are very scanty as of today. In particular, the effects of coupling processes on the constitutive relations and time and environmental variable-dependent material properties, especially at the failure stage, are not well understood and require further investigations.

In spite of the long history of recognizing the importance and broad range of application requirements, the modeling of fully-coupled THM process is still in an early stage of development compared with other topics in rock mechanics. On the one hand, it is limited by the lagged-behind theoretical developments related to these problems, such as the difficulties in computational mathematics and applied mechanics, especially when a real geomechanical system is considered, *i.e.*, when fractures, discontinuities, non-linear and plastic constitutive behavior are involved; on the other hand, the lack of applicable test cases for the verification, validation and evaluation of the mathematical models also hinders the development. Nevertheless, substantial progress has been made in THM modeling through the need of evaluating long-term safety of radioactive waste disposal since the mid 80's. A special issue in *Int. J. Rock Mech. Min. Sci. & Geomech. Abstr.*[144] reported the results of some so-called *bench-mark tests* (initial-boundary value problems designed to compare results from different models and codes applied to solve them) and *test cases* (actual laboratory or field experiments that are to be modeled) from the first phase of an international cooperative research project established under DECOVALEX - a multidisciplinary effort dedicated to the DEvelopment of COupled models and their VALidation against EXperiments. The project has nine fund-

ing organizations from seven countries and over a dozen research teams[85]. Ten finite element models, including two/three-dimensional fully-coupled THM models for elastic[32] or equivalent elastoplastic[19] porous media, two/three-dimensional coupled THM models for non-linear elastic[23] or elastoplastic[112][111] fractured porous media with special joint elements, two-dimensional coupled THM model for porous/fractured media with crack tensor approach[75], two-dimensional TM model without fluid flow[73]; and four Distinct Element models which simulate two-dimensional, quasi-static, coupled THM process for discrete, deformable block assemblages[97], were developed/applied in the project. All the finite element models developed/applied in the project take into account the convective heat transfer except the TM model[73]. Besides, few analytical and semi-analytical solutions to the coupled THM problems were also developed/compiled for further bench marking purposes[128]. Although the models developed in the DECOVALEX project are not yet ready to be applied to the real geological system with full confidence, it significantly furthered the fully-coupled THM modelling technology .

While significant progress in THM modelling are being made in the field of radioactive waste management, little attention has been paid to their effects on wellbore instabilities, as was mentioned in the introduction of this dissertation. As a starting step, analytical solutions for transient temperature and pore pressure diffusion around a borehole subjected to axisymmetric loading have been derived by Coussy[40], Wang[155][156], and Mctigue[104] for conductive heat transfer, and by Hojika *et al.*[79] for convective heat transfer. No work has been reported so far for fully-coupled THM solutions for a borehole subjected to a non-hydrostatic stress field, or inclined boreholes. No attempts have been made for the coupled thermoporoelastoplastic modelling either.

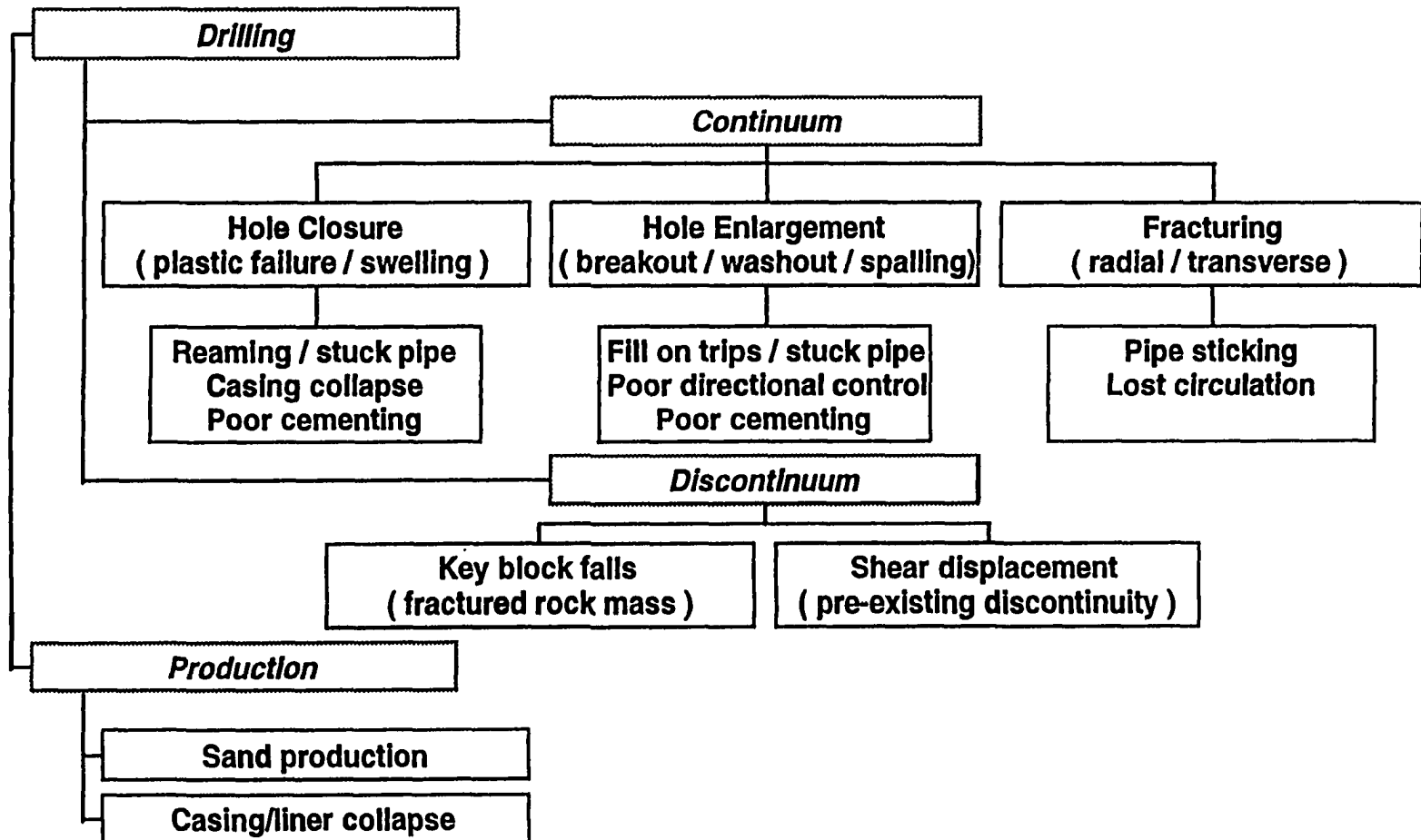


Figure 2.1: Commonly observed wellbore problems

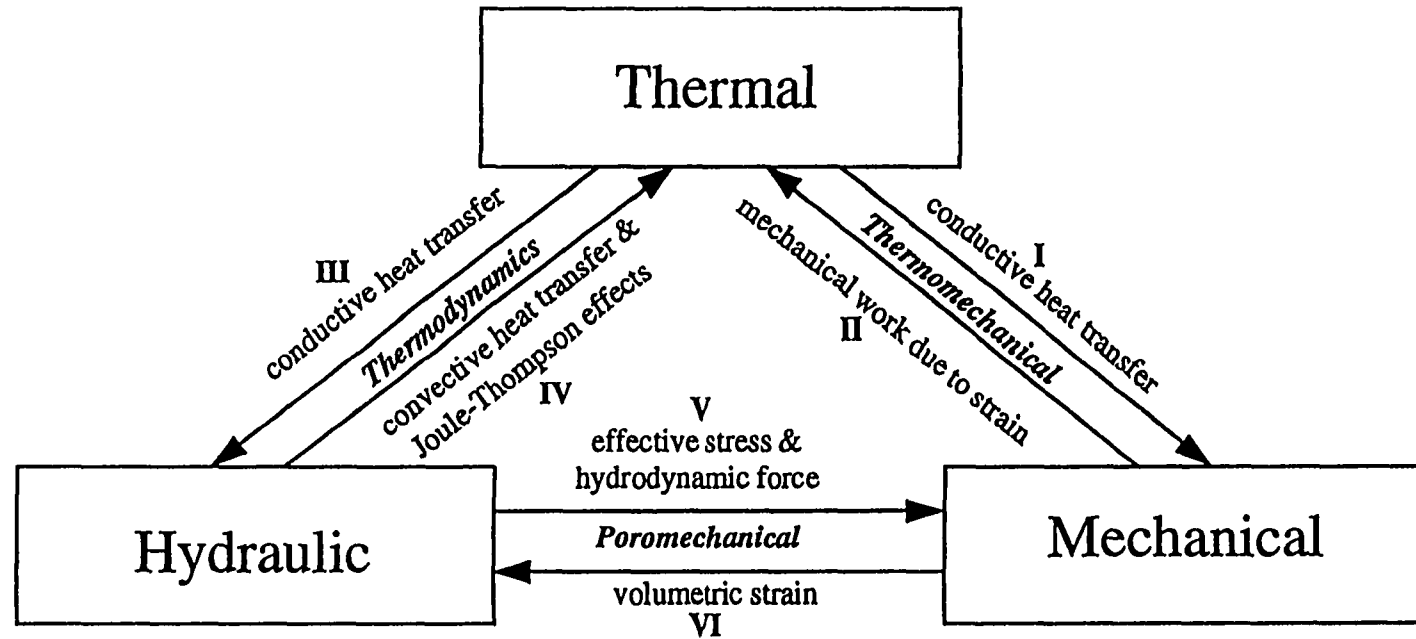


Figure 2.2: Schematic diagram of coupling mechanisms for a fully coupled thermal-hydraulic-mechanical system

## 3 Theoretical Background

### 3.1 Introduction

This chapter develops and summarizes the basic theories adopted in this dissertation. The developments are based on Biot's self-consistent theory [14, 15, 16] for fluid-saturated porous media. Small perturbation hypotheses are adopted, including infinitesimal deformations of the matrix so that the concept of the Eulerian strain tensor is applicable; infinitesimal matrix displacements so that Darcy's law can be defined in terms of absolute fluid velocity, instead of relative velocity of the fluid with respect to grains. This has been shown to be valid when grain displacements do not exceed 5% of the thickness of the compacting unit[62]. The fluid considered in this study is a single liquid phase. The potential phase changes, chemical and creep effects are ignored. The concept of effective heat transfer is adopted, *i.e.*, same temperature for both the matrix solid and pore fluid, which is based on an assumption that local heat exchanges between the solid and the fluid are rapid enough in comparison with global heat and fluid diffusions. Finally, the hypothesis of negligible inertia will be added so that the deformations are considered to be quasi-static.

### 3.2 Governing Equations

The governing equations for thermoporoelastic problems, within the context defined above, can be expressed in terms of the field equations governing the matrix deformations, fluid flow through pore space, and heat flow through both pore fluid

and porous matrix. These field equations can be derived based on the constitutive relations for the porous matrix, the pore space, the fluid and heat diffusions, together with the conservation laws for momentum, mass and energy. The derivations here closely follow the framework of Rice and Cleary[130] formulation, and Kurashigue's[88] approach for the inclusion of thermal effects. The total stress,  $\sigma_{ij}$  (tensile positive), pore pressure variation,  $p$  (compressive positive), and temperature variation,  $T$ , are chosen as the basic dynamic variables. The corresponding conjugate kinematic quantities are the solid strain,  $\varepsilon_{ij}$ , and fluid content change for unit volume pore fluid,  $\zeta$ .

### 3.2.1 Constitutive relations

Consider an elementary porous medium volume large enough to be considered the equivalence of the macroscopic porous medium, and a continuum assumption to be justified, the constitutive equations for the porous matrix and the pore space can be obtained based on the thermodynamics principles for fluid-saturated thermoelastic porous materials[37][88], *i.e.*

$$\varepsilon_{ij} = C_{ijkl}\sigma_{kl} + B_{ij}p + \alpha_{ij}^T T \quad (3.1)$$

$$\Delta\phi = B_{kl}\sigma_{kl} + Dp + \alpha_p^T T \quad (3.2)$$

where  $\sigma_{kl}, \varepsilon_{ij}, \Delta\phi, p, T$  are total stresses, average strains, change in porosity, and pore pressure and temperature changes from an initial equilibrium status, respectively.

The elastic parameters tensor  $C_{ijkl}, B_{ij}$ , for isotropic materials has the following form:

$$C_{ijkl} = \frac{1}{4G} \left( \delta_{ik}\delta_{jl} + \delta_{il}\delta_{kj} - \frac{2}{1+\nu}\delta_{ij}\delta_{kl} \right) \quad (3.3)$$

$$B_{ij} = \frac{3(\nu_u - \nu)}{2GB(1+\nu)(1+\nu_u)} \delta_{ij} \quad (3.4)$$

where  $B$  is Skempton's[139] pore pressure coefficient:

$$B = \frac{3(\nu_u - \nu)}{\alpha(1-2\nu)(1+\nu_u)} \quad (3.5)$$

D can be expressed as:

$$D = \frac{1}{B} \left( \frac{1}{K} - \frac{1}{K'_s} \right) - \frac{\phi}{K_f} \quad (3.6)$$

and  $K$  and  $\alpha_{ij}^T$  are the bulk modulus and the linear thermal expansion coefficient tensor, *i.e.*

$$K = \frac{2G(1 + \nu)}{3(1 - 2\nu)} \quad (3.7)$$

$$\alpha_{ij}^T = \alpha_m^{Tl} \delta_{ij} \quad (3.8)$$

In the above equations,  $\phi$  is the initial porosity,  $G$  is the shear modulus,  $K_f$  is the bulk modulus of the pore fluid,  $K'_s$  is the effective bulk modulus of the solid constituent,  $\alpha$  is Biot's coefficient of effective stress,  $\nu$  is Poisson's ratio,  $\nu_u$  is the undrained Poisson's ratio,  $\alpha_m^{Tl}$  is the linear thermal expansion coefficient of the porous matrix, and  $\alpha_p^T$  is the volumetric thermal expansion coefficient of the pore space.

Equation (3.1) can be re-arranged to present in a more convenient form:

$$\varepsilon_{ij} = \frac{1}{2G} \left( \sigma_{ij} - \frac{\nu}{1 + \nu} \sigma_{kk} \delta_{ij} \right) + \frac{\alpha(1 - 2\nu)}{2G(1 + \nu)} p \delta_{ij} + \frac{\alpha_m^T}{3} T \delta_{ij} \quad (3.9)$$

where  $\sigma_{kk}$  is the first invariant of the stress tensor and  $\alpha_m^T$  is the volumetric thermal expansion coefficient of the porous matrix.

Equation (3.9) can also be presented in terms of strain, *i.e.*

$$\sigma_{ij} = 2G \left( \varepsilon_{ij} + \frac{\nu}{1 - 2\nu} \varepsilon_{kk} \delta_{ij} \right) - \alpha p \delta_{ij} - \frac{2G(1 + \nu)}{(1 - 2\nu)} \frac{\alpha_m^T}{3} T \delta_{ij} \quad (3.10)$$

$$\sigma_{kk} = \frac{2G(1 + \nu)}{(1 - 2\nu)} \varepsilon_{kk} - 3\alpha p - \frac{2G(1 + \nu)}{(1 - 2\nu)} \alpha_m^T T \quad (3.11)$$

The change in fluid mass for the unit volume material  $m = \rho_f \phi$ , can be expressed as:

$$\Delta m = \rho_f \Delta \phi + \Delta \rho_f \phi \quad (3.12)$$

The change in fluid density due to pore pressure and temperature variations can be expressed as:

$$\Delta \rho_f = \frac{\Delta \rho_f}{p} \Big|_T p + \frac{\Delta \rho_f}{T} \Big|_p T \quad (3.13)$$

where, by definition,

$$\frac{\Delta\rho_f}{p} \Big|_T = \frac{\rho_f}{K_f}, \quad \frac{\Delta\rho_f}{T} \Big|_p = -\rho_f\alpha_f^T \quad (3.14)$$

where  $\alpha_f^T$  is the volumetric thermal expansion coefficient of the pore fluid. Substituting (3.14) into (3.13), and then into (3.12), one obtains:

$$\Delta m = \rho_f \left( \Delta\phi + \frac{p}{K_f}\phi - \alpha_f^T T\phi \right) \quad (3.15)$$

Substituting (3.4) and (3.6) into (3.2), one has:

$$\Delta\phi = \frac{3(\nu_u - \nu)}{2GB(1 + \nu)(1 + \nu_u)} \delta_{ij}\sigma_{ij} + \frac{1}{B} \left( \frac{1}{K} - \frac{1}{K'_s} \right) p - \frac{\phi}{K_f} p + \alpha_p^T T \quad (3.16)$$

Using (3.16) and (3.15), the following constitutive relations for the change of mass content per unit volume of fluid saturated porous material are obtained:

$$\Delta m = \rho_f \left[ \frac{3(\nu_u - \nu)}{2GB(1 + \nu)(1 + \nu_u)} \delta_{ij}\sigma_{ij} + \frac{1}{B} \left( \frac{1}{K} - \frac{1}{K'_s} \right) p + (\alpha_p^T - \alpha_f^T\phi)T \right] \quad (3.17)$$

or, presenting these equations in terms of the change of fluid content per unit reference volume:

$$\zeta = \frac{\Delta m}{\rho_f} = \frac{3(\nu_u - \nu)}{2GB(1 + \nu)(1 + \nu_u)} \delta_{ij}\sigma_{ij} + \frac{1}{B} \left( \frac{1}{K} - \frac{1}{K'_s} \right) p + (\alpha_p^T - \alpha_f^T\phi)T \quad (3.18)$$

Equation (3.18) can further be simplified as:

$$\zeta = \frac{3(\nu_u - \nu)}{2GB(1 + \nu)(1 + \nu_u)} \left( \sigma_{kk} + \frac{3}{B}p \right) + (\alpha_p^T - \alpha_f^T\phi)T \quad (3.19)$$

by applying the following relationship:

$$\frac{1}{B} \left( \frac{1}{K} - \frac{1}{K'_s} \right) = \frac{9(\nu_u - \nu)}{2GB^2(1 + \nu)(1 + \nu_u)} \quad (3.20)$$

Substituting Skempton's pore pressure coefficient,  $B$ , into (3.19), one finally obtains:

$$\zeta = \frac{\alpha(1 - 2\nu)}{2G(1 + \nu)} \left( \sigma_{kk} + \frac{3}{B}p \right) + (\alpha_p^T - \alpha_f^T\phi)T \quad (3.21)$$

By identifying the consequence of positive entropy production as implied by existing relationships between the fluxes and their driving forces[37], the following

constitutive relations for the coupled mass and heat diffusion processes can be obtained:

$$q_i = -\rho_f \kappa_{ij} p_{,j} + L_{ij} T_{,j} \quad (3.22)$$

$$h_i = -k_{ij}^T T_{,j} + L'_{ij} p_{,j} \quad (3.23)$$

where  $q_i$  and  $h_i$  denote the fluid mass and the heat flux, respectively, while  $L_{ij}$  and  $L'_{ij}$  are cross-effect coefficients. The former represents the thermo-osmosis effects, analogous to Soret's diffusion in a solution, the latter is analogous to the Dufour's effect in solutions.

For isotropic materials, the permeability coefficient tensor,  $\kappa_{ij}$ , and the thermal conductivity tensor,  $k_{ij}^T$ , can be reduced to:

$$\kappa_{ij} = \kappa \delta_{ij} \quad (3.24)$$

$$k_{ij}^T = k^T \delta_{ij} \quad (3.25)$$

Since the cross effects terms in (3.22) and (3.23) are much smaller in general compared to the first term, they are usually neglected. So one obtains the following form for the constitutive relations, or diffusion equations, by substituting (3.24) and (3.25) into (3.22) and (3.23):

$$q_i = -\rho_f \kappa p_{,i} \quad (3.26)$$

$$h_i = -k^T T_{,i} \quad (3.27)$$

### 3.2.2 Conservation Laws

There are three conservation laws in the present quasi-static non-isothermal context:

- The first is a momentum balance or equilibrium equation:

$$\sigma_{ij,j} = 0 \quad (3.28)$$

where body forces are neglected.

- The second is the local fluid mass conservation. Assuming no fluid mass supply, it has the general form of:

$$\frac{\partial \Delta m}{\partial t} + q_{j,j} = 0 \quad (3.29)$$

Substituting (3.26) into (3.29), one obtains:

$$\frac{\partial \Delta m}{\partial t} - \rho_f \kappa p_{,jj} = 0 \quad (3.30)$$

or,

$$\frac{\partial \zeta}{\partial t} - \kappa p_{,jj} = 0 \quad (3.31)$$

- The last one is the energy conservation equation. Neglecting the terms representing the interconvertibility of thermal and mechanical energy, and for the case of no heat source, the energy balance for an elementary volume yields the following equation[38] :

$$\frac{\partial (\rho_t C_t T)}{\partial t} = -h_{i,i} - (C_f T q_i)_{,i} \quad (3.32)$$

where  $\rho_t$  and  $C_t$  are the mass density and specific heat for the bulk material, and  $C_f$  is the specific heat of pore fluid. The first term on the right hand side of this last equation represents the conductive heat transfer through the bulk material. The second term on the right-hand side represents the convective heat transfer through the pore fluid flow.

Equation (3.32) is similar to the microscopic energy balance equation for a homogeneous fluid phase, and is established based on the concept of effective heat transfer, i.e., a uniform mean temperature gradient is imposed in a fluid-saturated, homogeneous porous medium. In other words, the mean temperature of the matrix solid and fluid phases are equal for an elementary volume.

An alternative way of expressing energy balance for fluid-saturated porous media is to distinguish the mean temperature between the matrix solid and the pore fluid. The energy balance equations will be established for each phases, and the heat flux

transferred from one phase to the other is expressed by means of a heat transfer coefficient [38][79]. This model is more difficult to use compared to the one that is adopted in this dissertation, because more parameters are involved, and some of them, such as the heat transfer coefficient between the two phases are difficult to determine accurately. But it is a more suitable model when the fluid velocity is high; hence, the occurrence of a significant temperature differences between the solid and fluid phases are possible.

### 3.2.3 Field Equations

#### 3.2.3.1 Deformation Field Equation

Substituting the geometric relationship for small deformations; *i.e.*

$$\varepsilon_{ij} = \frac{1}{2} (u_{i,j} + u_{j,i}) \quad (3.33)$$

$$\varepsilon_{kk} = u_{k,k} \quad (3.34)$$

into (3.10), one obtains the following modified Navier equation in terms of displacements:

$$G u_{i,jj} + \frac{G}{1-2\nu} u_{j,ji} - \alpha p_{,i} - \frac{2G\alpha_m^T (1+\nu)}{3(1-2\nu)} T_{,i} = 0 \quad (3.35)$$

#### 3.2.3.2 Fluid Diffusivity Field Equations

Differentiating equations (3.10) and (3.34) twice leads to:

$$\sigma_{ii,jj} = 2G \left( \frac{1+\nu}{1-2\nu} \varepsilon_{kk,jj} \right) - 3\alpha p_{,jj} - \frac{1+\nu}{1-2\nu} 2G\alpha_m^T T_{,jj} \quad (3.36)$$

$$\varepsilon_{kk,jj} = u_{i,ijj} \quad (3.37)$$

Differentiating (3.35) with respect to  $x_i$ , solving  $u_{i,ijj}$  and substituting into (3.37), then into (3.36), the following compatibility equation in terms of stresses is obtained:

$$\sigma_{ii,jj} + \frac{2\alpha(1-2\nu)}{(1-\nu)} p_{,jj} + \frac{4G(1+\nu)}{(1-\nu)} \frac{\alpha_m^T}{3} T_{,jj} = 0 \quad (3.38)$$

Differentiating (3.21) twice with respect to  $x_j$ , and substituting (3.38) into it, one obtains:

$$\begin{aligned} \zeta_{,jj} = & \frac{\alpha(1-2\nu)}{2G(1+\nu)} \left[ \left( \frac{3}{B} - \frac{2\alpha(1-2\nu)}{(1-\nu)} \right) p_{,jj} - \frac{4G(1+\nu)}{(1-\nu)} \frac{\alpha_m^T}{3} T_{,jj} \right] \\ & - (\alpha_p^T - \alpha_f^T \phi) T_{,jj} \end{aligned} \quad (3.39)$$

Solving  $p_{,jj}$  from (3.39) and substituting into (3.31), the fluid diffusivity equation can be obtained:

$$\frac{\partial \zeta}{\partial t} = c^f \left[ \zeta_{,jj} + \left( \frac{2\alpha(1-2\nu)}{(1-\nu)} \frac{\alpha_m^T}{3} - (\alpha_p^T - \alpha_f^T \phi) \right) T_{,jj} \right] \quad (3.40)$$

where,

$$c^f = \frac{2\kappa GB^2(1-\nu)(1+\nu_u)^2}{9(1-\nu_u)(\nu_u-\nu)} \quad (3.41)$$

is the fluid diffusivity coefficient.

If one differentiates (3.21) with respect to  $t$ , substitutes into (3.31) and rearrange the expression, the fluid diffusion field equation can be expressed in terms of pore pressure:

$$\frac{\partial p}{\partial t} = \frac{2\kappa GB^2(1+\nu)(1+\nu_u)}{9(\nu_u-\nu)} p_{,jj} - \frac{B}{3} \frac{\partial \sigma_{kk}}{\partial t} + \frac{2GB^2(1+\nu)(1+\nu_u)}{9(\nu_u-\nu)} (\alpha_f^T \phi - \alpha_p^T) \frac{\partial T}{\partial t} \quad (3.42)$$

Applying the relationship between  $\sigma_{kk}$  and  $\varepsilon_{kk}$ , equation (3.42) can alternatively be expressed as:

$$\frac{dp}{dt} = M \left[ \kappa p_{,jj} - \alpha \frac{\partial \varepsilon_{kk}}{\partial t} + (\alpha \alpha_m^T + \alpha_f^T \phi - \alpha_p^T) \frac{dT}{dt} \right] \quad (3.43)$$

where,

$$M = \frac{2G(\nu_u-\nu)}{\alpha^2(1-2\nu)(1-2\nu_u)} \quad (3.44)$$

is the Biot modulus.

### 3.2.3.3 Thermal Diffusivity Field Equation

Substituting (3.26) and (3.27) into (3.32), one obtains the thermal diffusivity field equation:

$$\frac{\partial T}{\partial t} = \frac{k^T}{\rho_t C_t} T_{,ii} + \frac{\kappa \rho_f C_f}{\rho_t C_t} (T p_{,i})_{,i}$$

$$= c^T T_{,ii} + \frac{\kappa \rho_f C_f}{\rho_t C_t} (T p_{,i})_{,i} \quad (3.45)$$

where,

$$c^T = \frac{k^T}{\rho_t C_t} \quad (3.46)$$

is the thermal diffusivity coefficient for the bulk material.

As one can see, the displacement, pore pressure and thermal field equations derived for a fluid-saturated, isotropic, thermoporoelastic body are completely coupled with each other through equations (3.35), (3.40) and (3.45), where pore pressure and temperature coupling involves non-linearity.

Choosing stress,  $\sigma_{ij}$ , to replace the displacements  $u_i$ , and pore pressure,  $p$ , to replace the change of fluid content,  $\zeta$ , as the field variables, the above field equations can alternatively be presented in the following form:

$$\sigma_{ij,j} = 0 \quad (3.47)$$

$$\frac{dp}{dt} = M \left[ \kappa p_{,jj} - \alpha \frac{\partial \varepsilon_{kk}}{\partial t} + (\alpha \alpha_m^T + \alpha_f^T \phi - \alpha_p^T) \frac{dT}{dt} \right] \quad (3.48)$$

$$\frac{dT}{dt} = c^T T_{,ii} + \frac{\kappa \rho_f C_f}{\rho_t C_t} (T_{,i} p_{,i} + T p_{,ii}) \quad (3.49)$$

### 3.2.4 Kurashige's Model

The above derivation closely follows Kurashige's[88] work. However, Kurashige adopted an assumption in his derivation that pores thermally expand with their shapes remaining similar; so the volumetric thermal expansion coefficient of pore space,  $\alpha_p^T$ , was expressed as:

$$\alpha_p^T = \phi \alpha_m^T \quad (3.50)$$

hence, the fluid diffusivity field equation had the following form:

$$\frac{\partial \zeta}{\partial t} = c^f \left\{ \zeta_{,jj} + \left[ \frac{2\alpha(1-2\nu)}{(1-\nu)} \frac{\alpha_m^T}{3} - (\alpha_m^T - \alpha_f^T) \phi \right] T_{,jj} \right\} \quad (3.51)$$

It should be pointed that the assumption (3.50) has not been substantiated by experiments. On the contrary, experiments on sandstone by Von Gonten and

Choudhary[152] showed that the pore volume will decrease with temperature at constant pressure because of the thermal expansion of mineral grains into the pore space. Results of tests by Ashqar[10], Janah[84] and Somerton[141] also showed that this is the case (also for sandstones). According to the existing experimental data, the contraction of pore volume is small until the temperature variation reaches about 100°C and this value varies with the initial porosity. The lower the initial porosity, the higher the critical temperature and the amount of the contraction due to the larger fraction of solid content. Above the critical temperature range, the thermal contraction increases at a nearly constant rate (see Figure 3.1).

The amount of the pore volume contraction may also be a function of mineral composition of porous matrix, and pore pressure. Especially, the effects of pore pressure on the amount of pore volume contraction is prominent. The high pore pressure limits the contraction of pore volume (see Figure 3.2). Because of this, shales may not have as significant pore volume contraction as it was observed for sandstones, or even behave otherwise (*i.e.* pore volume expands while heating).

Because of their high permeability, heating or pressurizing does not induce pore pressure in sandstone samples if the measurements last relatively long, and the test conditions are not strictly set up as undrained, which is most probably the case of those published experiments (the test conditions are, unfortunately, not described in details in the literature). However, due to the extremely low permeability of shales, the pore pressure induced in shales by heating can be very high as will be shown in the modelling section of this dissertation (Chapter 4). If the effects of pore pressure on pore volume change overwhelm the effects of solids expansion into the pore, the pore volume can expand instead of contracting. In this case, assumption (3.50) might be applicable. Nevertheless, the behavior of pore volume change with temperature depends upon the formation type and environmental conditions. It is more suitable to treat the volumetric thermal expansion coefficients for matrix and for pore space as two independent parameters. The accuracy of the model will rely on the accuracy of the parameters obtained from physical observations.

Another assumption that had been adopted by Kurashige[88], but eliminated in the model derived in this chapter, is the local heat balance assumption of:

$$\rho_t C_t T_t = \phi \rho_f C_f T_f \quad (3.52)$$

where  $T_t$  and  $T_f$  are bulk material and pore fluid temperature, respectively.

Even though applying this assumption can further simplify the energy balance equation (3.45), it does not physically represent the local heat balance condition correctly. The local heat balance should be represented simply by an equilibrium temperature between the fluid and solid phases[38].

### 3.3 Non-linear and Plastic Rock Behaviors

As indicated in the above section, the response of a coupled thermoporoelastic system is non-linear in nature if the convective heat transfer is significant enough, even if all the parameters involved in the system are linear. In addition, similar to a solid material, the constitutive relations change drastically and irreversible deformations occur when the elastic limit of effective stresses for a porous material are exceeded[33][138]. Even if the stresses remain within the elastic limit, many experimental observations have evidenced that the reaction of some material properties to the change of stress, pore pressure and temperature is non-linear [13][52][81][86][92][166]. The linear relations are applicable only to a limited range of stress and temperature variations.

#### 3.3.1 Stress- and Temperature-dependent Material Properties

##### 3.3.1.1 Porosity and Permeability

The dependency of porosity and permeability upon the effective stress or pore fluid pressure has been studied by many authors, both theoretically and experimentally.

Among them, Geertsma[65] suggested that, within the elastic range of matrix deformation, porosity is a linear function of confining pressure and fluid pressure:

$$\phi = \phi_n + \left( \frac{1}{K_s} - \frac{1 - \phi_n}{K} \right) (dp_c - dp) \quad (3.53)$$

where  $p_c$  is the confining pressure, and  $\phi_n$  is the porosity at the previous loading stage. Garg and Nur[63] proposed a non-linear expression for stress-dependent porosity as a power series in the volumetric strain of porous matrix and pore fluid. They also showed that their equation reduces to Equation (3.53) when the terms of second order or higher are neglected. Finol and Farouq Ali[60] derived the following linear relations for the porosity change with the oil pressure in a black oil system with an immobile water phase:

$$\phi = \phi_n (1 + c_p dp_o) \quad (3.54)$$

where  $c_p$  is the uniaxial compaction coefficient,  $p_o$  is the oil pressure. The above relationships are based on the experimental work. Recently, Cui[42] derived an expression for effective stress-dependent porosity following Carroll's[29] micromechanics model of porous material deformation and Mackenzie's[95] formula of bulk modulus for porous media with spherical-like pores:

$$\phi = \phi_n \exp \left[ \frac{3}{4G_s} (\sigma'_m - \sigma'_{mn}) \right] \quad (3.55)$$

where  $G_s$  is the shear modulus of matrix solids which can be considered to be stress independent[116]; and,

$$\sigma'_m = \frac{(\sigma_{xx} + \sigma_{yy} + \sigma_{zz})}{3} - p \quad (3.56)$$

is the mean effective stress. Assuming  $\sigma_{mn}$  to be the mean effective stress at a reference status, then  $\phi_n$  is the porosity with respect to this reference state.

Equation (3.55) can be extended to include the temperature effects (see Appendix A for the derivation):

$$\phi = \phi_n \exp \left[ \frac{3}{4G_s} (\sigma'_m - \sigma'_{mn}) + (\alpha_p^T - \alpha_m^T) (T - T_n) \right] \quad (3.57)$$

where  $T$  is the current temperature and  $T_n$  is the temperature at the reference state.

Equations (3.55) and (3.57) are based on the strict theoretical derivation, hence, they are universe relationships, and should not be limited to a certain rock or fluid type, or influenced by the environmental factors such as initial stress, pore pressure and temperature, like most of the experimentally obtained correlations do. However, these relationships are subject to certain assumptions and their applicability to a real rock-fluid system is yet to be substantiated. One of the two major assumptions on which the derivations are based are: (1) the pores are nearly spherical; and, (2) the volumetric response of the porous medium is linear elastic. For a real fluid-saturated porous system where the mechanical response is non-linear due to the existing of crack-like pores, or progressive pore collapse for rocks that have a very high porosity, Equations (3.55) and (3.57) might only be applicable to small ranges of stress and temperature variations; and hence, have to be used in incremental form.

Past investigations showed that permeability is also a complex function of effective stress and pore pressure[167]. A typical assumption in the literature is that permeability is primarily dependent upon the changes in porosity. For one-dimensional consolidation of soils, the relationships between the void ratio (the ratio of void volume to solid volume) and permeability are typically logarithmic as shown in Figure 3.3, according to the experimental studies[108][91].

For the rocks at greater depths, a well-known correlation between the porosity and permeability is Carman-Kozeny's relation[133]:

$$k = k_n \left( \frac{\phi}{\phi_n} \right)^3 \quad (3.58)$$

where  $k_n$  and  $\phi_n$  are reference values of permeability and porosity, respectively.

By assuming the permeability to be proportional to the  $b_{k\phi}$ -th ( $b_{k\phi}$  is a positive number) power of the porosity[24], the following relationship for the effective stress

and temperature-dependent permeability based on Equation (3.57) can be derived:

$$k = k_n \exp \left\{ b_{k\phi} \left[ \frac{3}{4G_s} (\sigma'_m - \sigma'_{mn}) + (\alpha_p^T - \alpha_m^T) (T - T_n) \right] \right\} \quad (3.59)$$

where  $k_n$  is the permeability at the reference state.

Equation (3.59) can be expressed in another form:

$$\ln k = \ln k_n + b_{k\phi} \left[ \frac{3}{4G_s} (\sigma'_m - \sigma'_{mn}) + (\alpha_p^T - \alpha_m^T) (T - T_n) \right] \quad (3.60)$$

By dropping the temperature-related term in (3.60), the equation qualitatively agrees with the relationship developed experimentally by McKee[101] where the permeability in logarithmic scale decreases linearly with the increase of the Terzaghi's effective compressive stress.

### 3.3.1.2 Poroelastic Parameters

Experimental results have shown that, even for hard rocks for which the rock matrix has a comparable compressibility compared to the rock grain, the mechanical properties for the rock grain, such as the bulk modulus  $K_s$ , can be taken as constant in the range of the stress change induced by drilling or production[116]. However, the poroelastic properties for the bulk material, such as the drained bulk modulus  $K$ , demonstrate highly non-linear effects[63][116]. According to the porosity relationship (3.57), the stress and temperature dependency of the poroelastic parameters can also be derived (see Appendix A):

$$\frac{1}{K} = \frac{1}{K_s} \frac{1}{1 - \phi_n e^x} (1 + a \phi_n e^x) \quad (3.61)$$

$$G = G_s \left[ 1 - \frac{15(1 - \nu_s)}{7 - 5\nu_s} \phi_n e^x \right] \quad (3.62)$$

$$\alpha = \frac{(1 + a) \phi_n e^x}{1 + a \phi_n e^x} \quad (3.63)$$

$$B = \frac{1 + a}{a + (1 - \phi_n e^x) K_s / K_f + \phi_n e^x} \quad (3.64)$$

where,

$$a = \frac{1 + \nu_s}{2(1 - 2\nu_s)} \quad (3.65)$$

$$x = -\frac{3}{4G_s}(\sigma'_m - \sigma'_{mn}) + (\alpha_p^T - \alpha_m^T)(T - T_n) \quad (3.66)$$

Similarly to porosity and permeability, this set of equations should be used in incremental form.

### 3.3.1.3 Thermoelastic Parameters

Although the study of the non-linear response of thermoelastic parameters to stress, pore pressure and temperature are far from complete, limited experimental studies on stress- and temperature-dependent thermoelastic parameters, such as thermal expansion, thermal conductivity and thermal diffusivity coefficients, for the dry or fluid saturated rocks (mainly sand stone) have been reported in the literature[141].

#### Thermal Expansion

The experiments on an outcrop sandstone under stress free conditions have shown that the thermal expansion coefficient increases non-linearly with the increase of temperature, as shown in Figure 3.4. Typically, it can approximately be treated as linear below a certain temperature (400°C), increases rapidly when temperature further increases beyond the linear range, then the thermal expansion stops at above a certain temperature (about 600°C). The results also show that cooling goes via a different path. However, if the rocks did not experience extremely high temperatures so that the permanent structure damage or plastic deformation did not occur, it can be expected that rock shrinkage during cooling follows the same path as heating.

On the other hand, it was reported that the thermal expansion coefficient of these rocks decreases with an increase in stresses[145][159]. Sweet[145] estimated that the volumetric thermal expansion of low permeability sandstones decreases by 25% upon rising the stress from atmospheric pressure to 100 MPa. Wong and Brace's[159] work showed that the thermal expansion of Cheshire quartzite decreased about 25% under much larger pressure variations ( from 100MPa to

500MPa).

### Thermal Conductivity

Somerton[141] developed the following empirical model for temperature-dependent thermal conductivity for sandstone, based on the experimental results and guided by Tikhomirov's[148] work:

$$k^T = k_{20}^T - 10^{-3} (T - 293) (k_{20}^T - 1.38) \quad (3.67)$$

$$\times \left[ k_{20}^T (1.8 \times 10^{-3} T)^{-0.25 k_{20}^T} + 1.28 \right] (k_{20}^T)^{-0.64} \quad (3.68)$$

where  $k_{20}^T$  is the thermal conductivity at 20°C, T is the temperature in Kelvin, and both  $k_{20}^T$  and  $k^T$  are in W/m-k. Both the study by Somerton[141] and Tikhomirov[148] have shown the moderate negative gradients of thermal conductivity with temperature for high conductivity rocks, but small positive gradients for low conductivity rocks, as shown in Figure 3.5.

Thermal conductivity increases with stresses because increases in stress improve the thermal contact between mineral grains and increases the density of the rock. The change in thermal conductivity with the added stress is generally small, and the magnitude decrease with the increase of the stresses as shown in Figure 3.6. For sandstones, Edmondson[55] reported from 10% to 13% increase in thermal conductivity for about 7 MPa stress increase at low environmental stress level (6 to 25 MPa). Woodside and Messmer[161] reported about 12% increase per 7 MPa at low stress ranges (0-7 MPa), and 2.5% increase per 7 MPa at higher stress ranges (14-28 MPa). The results reported by Somerton[141] are similar to Woodside's[161] work.

The effects of stress and temperature variation on thermal diffusivity exhibit the similar tendency as that of the thermal conductivity (Figure 3.7).

### 3.3.1.4 Fluid Properties

Some of the fluid properties such as density, viscosity, compressibility, thermal capacity and expansion, are very sensitive to temperature and pressure variations. The temperature- and pressure-dependent fluid properties, such as density, viscosity and compressibility have been studied by numerous authors for a wide range of fluid types, and temperature and pressure conditions, to cite a few [36][100]. A few studies on the thermal properties for some fluids have also been reported in the literature [122][124][125], but the data under reservoir or deep subsurface conditions is scanty.

Based on his experimental investigations, Fernandez [59] proposed the following state equation for water:

$$\rho_f = \rho_{fn} \exp \left[ -\alpha_f^T (T - T_n) + \frac{1}{K_f} (p - p_n) \right] \quad (3.69)$$

where  $\rho_{fn}$  is the fluid density at reference temperature and pore pressure  $T_n$  and  $p_n$ .

The above equation can be linearized by expanding the exponential function and keep only the first order terms:

$$\rho_f = \rho_{fn} \left[ 1 - \alpha_f^T (T - T_n) + \frac{1}{K_f} (p - p_n) \right] \quad (3.70)$$

Equation (3.70) has been used by Bear and Corapcioglu [13] in their modelling of consolidation of aquifers during hot water injection or pumping.

Bird *et al.* [17] proposed the following model for temperature-dependent dynamic viscosity of liquids:

$$\mu = \mu_n \exp \left[ A \left( \frac{1}{T} - \frac{1}{T_n} \right) \right] \quad (3.71)$$

where  $\mu_n$  is the viscosity of liquids at reference temperature  $T_n$ , and A is a constant. Huyakron and Pinder [82] suggested the following expression:

$$\mu = 10^{-6} \times 239.4 \times 10^{(248.37/T + 133.15)} \quad (3.72)$$

where T is in degrees Celsius and  $\mu$  is in (g/cm s).

Sorey[142] suggested the following formula for temperature-dependent thermal expansion coefficient:

$$\alpha_f^T = \frac{\rho_{fn} - \rho_f}{\rho_n (T - T_n)} \quad (3.73)$$

and Perry's handbook[124] proposed the following cubic equations for the temperature-dependent thermal expansion for liquids:

$$\alpha_f^T = \alpha T + \beta T^2 + \gamma T^3 \quad (3.74)$$

where  $\alpha$ ,  $\beta$  and  $\gamma$  are constants which vary for different materials. The temperature range for the above formula are from 0 to 160°C.

The temperature-dependent thermal conductivity and thermal capacity for some fluids are given in table form by Ozbeck and Phillips[122] and Phillips *et al.*[125]. In general, the influence of temperature on these properties are more significant for oils than for salt water. This is also true for all the other fluid properties. The temperature effects on fluid thermal conductivity seems to be small and can be treated linearly for most common subsurface conditions.

### 3.3.1.5 Summary

The majority of the information about the temperature- and stress-dependent thermoelastic properties is based on laboratory studies conducted on sandstones. The studies for other rock types (especially for shale, which is very important for well-bore stability studies) are basically non-existent. Besides, the data available so far, including the thermal properties for fluids, is relatively scanty, and does not reflect the response of systematic changes in temperature, effective stress and pore pressure, especially under subsurface high temperature and high pressure conditions. So, it is hard to come up with convincing general non-linear phenomenological models for these properties. For this reason, the non-linear analysis and discussion in this dissertation is mainly concentrated on the thermoporoplastic behavior. However, with the incremental algorithm for general non-linear problem developed in this dissertation, it is convenient to incorporate temperature, stress, pore pres-

sure, and even other factor-dependent parameters into the current model, once such information becomes available.

### 3.3.2 Thermoporoelastoplastic Constitutive Relations

#### 3.3.2.1 Plasticity in Geological Materials

Plasticity, or irreversible deformations often occur in ductile-type engineering materials, when stresses exceed the limits of elasticity of a material. An important characteristic of geomechanical problems at all scales is the occurrence of such deformations, because the plastic part of the total deformations is in general much larger than the elastic part. Besides, plastic analyses is the only way to give accurate failure prediction if a material is ductile enough to go through plastic deformations before its final failure. The behavior of a system is said to be elastoplastic when the elastic deformations of the system is not negligible, and thus included in the plastic analysis.

The plastic behavior of materials can generally be divided into three types: strain hardening (stress increase is required for an increase of strain), strain softening (stress decrease associated with strain increase) and ideal plasticity (stress is constant during the increase of plastic strain). Figure 3.8, which is a typical axial stress/axial strain curve from a triaxial compression test of a geological material, illustrates the hardening and softening processes at different loading stages. The recognized mechanism for strain hardening is that of microcracks initiation and frictional sliding at the grain-size level, (BC section in Figure 3.8). Once sufficient microcracks have formed to allow the formation of localized shear bands, strain softening occur (CD section in Figure 3.8).

A yield function defines the limits of elasticity under any possible combination of stresses. In a  $n$ -dimensional stress space, or loading space, a yield function represents a surface which separate the elastic state from an outer zone of impermissible stress states (Figure 3.9 ). This surface changes with increasing deformation in the

case of strain hardening/softening (Figure 3.9 (b) and (c)), and keeps unchanged in the case of ideal plastic deformation (Figure 3.9 (a)).

### 3.3.2.2 General Elastoplastic Constitutive Relations for Non-isothermal Fluid Saturated Porous Media

In a non-isothermal poromechanical system, the yield surface, presented in terms of macroscopic parameters, is a function of stresses, pore pressure, temperature and hardening/softening parameters:

$$F(\sigma_{ij}, p, T, \kappa^p) = 0 \quad (3.75)$$

where,

$$\kappa^p = \kappa^p(\varepsilon_{ij}^p, p, T) \quad (3.76)$$

is the hardening/softening parameter.

When the material first reaches its elastic limit, or the initial yield surface,  $\kappa^p = 0$ . During successive elastoplastic deformations, the size and position of the yield surface changes consistently as a function of  $\kappa^p$  during hardening or softening, but keeps unchanged during ideal plastic deformation (Figure 3.9). For isotropic hardening/softening, the yield surface in loading space simply expands/shrinks, homothetically and concentrically, from the initial yield surface, as shown in Figure 3.9, (d).

For a fluid-saturated porous medium, the plastic deformations include both the permanent matrix deformations as well as the permanent changes in fluid contents due to the permanent change in connected porosity. The magnitude and direction of the plastic strain and plastic porosity can be defined by the following flow rule based on the normality principle[41]:

$$(d\varepsilon_{ij}^p, d\phi^p) = d\lambda \left( \frac{\partial Q}{\partial \sigma_{ij}}, \frac{\partial Q}{\partial p} \right) \quad (3.77)$$

where  $Q$  is the plastic potential and  $d\lambda$  is a non-negative scalar factor called plastic multiplier[78]. Since plastic deformations are irreversible, they cannot be determined solely by the current loading, but rather are dependent upon the loading

history. So, the plastic strain and plastic porosity can only be calculated incrementally.

Assuming that the yield condition is continuously satisfied while the plastic deformations, and hence, the consistency condition  $dF = 0$  holds, the differentiation of Equation (3.75) gives:

$$\frac{\partial F}{\partial \sigma_{ij}} : d\sigma_{ij} + \left( \frac{\partial F}{\partial \kappa^p} \frac{\partial \kappa^p}{\partial p} + \frac{\partial F}{\partial p} \right) dp + \frac{\partial F}{\partial \kappa} \frac{\partial \kappa^p}{\partial \varepsilon_{ij}^p} : d\varepsilon_{ij}^p + \left( \frac{\partial F}{\partial \kappa^p} \frac{\partial \kappa^p}{\partial T} + \frac{\partial F}{\partial T} \right) dT = 0 \quad (3.78)$$

Substituting (3.77) into (3.78), solving  $d\lambda$ , and then substituting  $d\lambda$  back into (3.77), the plastic strain and plastic porosity can be solved :

$$d\varepsilon_{ij}^p = - \frac{\frac{\partial F}{\partial \sigma_{ij}} : d\sigma_{ij} + \left( \frac{\partial F}{\partial \kappa^p} \frac{\partial \kappa^p}{\partial p} + \frac{\partial F}{\partial p} \right) dp + \left( \frac{\partial F}{\partial \kappa^p} \frac{\partial \kappa^p}{\partial T} + \frac{\partial F}{\partial T} \right) dT}{\left( \frac{\partial F}{\partial \kappa^p} \frac{\partial \kappa^p}{\partial \varepsilon_{ij}^p} \right) : \frac{\partial Q}{\partial \sigma_{ij}}} \frac{\partial Q}{\partial \sigma_{ij}} \quad (3.79)$$

$$d\phi^p = - \frac{\frac{\partial F}{\partial \sigma_{ij}} : d\sigma_{ij} + \left( \frac{\partial F}{\partial \kappa^p} \frac{\partial \kappa^p}{\partial p} + \frac{\partial F}{\partial p} \right) dp + \left( \frac{\partial F}{\partial \kappa^p} \frac{\partial \kappa^p}{\partial T} + \frac{\partial F}{\partial T} \right) dT}{\left( \frac{\partial F}{\partial \kappa^p} \frac{\partial \kappa^p}{\partial \varepsilon_{ij}^p} \right) : \frac{\partial Q}{\partial p}} \frac{\partial Q}{\partial p} \quad (3.80)$$

Once  $F, Q$  and  $\kappa^p$  are specified, the thermoporoelastoplastic constitutive relations can be determined through:

$$\begin{aligned} d\varepsilon_{ij} &= d\varepsilon_{ij}^e + d\varepsilon_{ij}^p \\ &= C_{ijkl} d\sigma_{kl} + B_{ij} dp + \alpha_{ij}^T dT + d\varepsilon_{ij}^p \end{aligned} \quad (3.81)$$

$$\begin{aligned} d\phi &= d\phi^e + d\phi^p \\ &= B_{kl} d\sigma_{kl} + D dp + \alpha_p^T dT + d\phi^p \end{aligned} \quad (3.82)$$

When  $Q \equiv F$ , the flow rule is called associated. The associated flow rule are commonly used together with the failure functions that are independent of the hydrostatic stress component, such as Tresca and Von Mises failure criteria[78] to predict the ideal-plastic and hardening behavior of metals. For geomaterials, it has been observed that the associated flow rule overestimates the dilation; hence, non-associated flow rules are often required[96].

Very few studies has been found in the literature about the temperature dependency of yield surfaces and hardening parameters. Kosar[87] and Agar[6]'s

experimental studies on oil sands concluded that the peak strength is not sensitive to temperature change up to 225°C. Since the temperature variation during drilling is far below this level, only isothermal plastic behavior models are adopted in this study.

### 3.3.2.3 Mohr-Coulomb and Drucker-Prager Failure Criteria

A wide variety of isothermal yield functions and plastic potentials have been developed and used for geomaterials[35][165]. Among these, the most popularly used yield functions for relatively hard rock are Mohr-Coulomb and Drucker-Prager failure criteria.

The Mohr-Coulomb failure criterion in terms of principal stresses is:

$$F = (\sigma_3 - p) - N_{\phi_f} (\sigma_1 - p) + q_u \quad (3.83)$$

where,

$$N_{\phi_f} = \frac{1 + \sin \phi_f}{1 - \sin \phi_f} \quad (3.84)$$

where  $\phi_f$  is the angle of internal friction; and,

$$q_u = 2c\sqrt{N_{\phi_f}} \quad (3.85)$$

is the uniaxial compressive strength, where  $c$  is the cohesion. In the principal stress space, the Mohr-Coulomb criterion is a hexagonal pyramid with its axis coincident with the trisector of the space, and the three coordinates of the vertex equal to  $c \cot \phi_f$ , as shown in Figure 3.10. When the angle of internal friction reduces to zero, the Tresca failure criterion is restored from Equation (3.83), as shown in the same figure.

The Mohr-Coulomb failure function generally fits the experimental data better, but the gradient vector cannot be defined at the ridges of the yield surface which brings some practical difficulty in modelling. For this reason, the Drucker-Prager failure criterion which has the form of a right circular cone in principal stress space,

as shown in Figure 3.11, is often used. Presented in terms of the stress invariants, the Drucker-Prager failure criterion is:

$$F = \sqrt{J_2'} + 3\alpha_{dp} \left( \frac{I}{3} - p \right) - k_{dp} \quad (3.86)$$

where,

$$I = \sigma_{ii} \quad (3.87)$$

is the first invariable of total stress tensor; and,

$$J_2' = \frac{1}{2} s_{ij} s_{ij}, \quad \left( s_{ij} = \sigma_{ij} - \frac{I}{3} \delta_{ij} \right) \quad (3.88)$$

is the second invariable of deviatoric stresses.  $\alpha_{dp}$  and  $k_{dp}$  are functions of  $c$  and  $\phi_f$ , and can be determined by matching (3.86) with (3.83). When the Drucker-Prager cone surface is inscribed tangentially inside the Mohr-Coulomb pyramid[54] (Figure 3.12):

$$\alpha_{dp} = \frac{\sin \phi_f}{\sqrt{9 + 3 \sin^2 \phi_f}} \quad \text{and} \quad k_{dp} = \frac{3c \cos \phi_f}{\sqrt{9 + 3 \sin^2 \phi_f}} \quad (3.89)$$

When the Drucker-Prager cone surface graphically passes through the corners of the Mohr-Coulomb pyramid[164]:

$$\alpha_{dp} = \frac{2 \sin \phi_f}{\sqrt{3} (3 - \sin \phi_f)} \quad \text{and} \quad k_{dp} = \frac{6c \cos \phi_f}{\sqrt{3} (3 - \sin \phi_f)} \quad (3.90)$$

Equation (3.89) always gives a failure load equal to or less than that from Mohr-Coulomb failure criterion, and is thus a lower bound to the Mohr-Coulomb criterion. On the other hand, Equation (3.90) represents an upper bound by giving a collapse loads equal to or greater than that from Mohr-Coulomb criterion. In the case of  $\phi_f = 0$ , Equation (3.86) reduces to Von Mises's yield law.

#### 3.3.2.4 A Drucker-Prager Model for Strain Hardening and Softening

Even though the study of post-yield behavior of geological material has had a long history, almost no study has been conducted so far as to how the interactions of solid and fluid phases influence the post-failure behavior of fluid saturated porous

media, except the recent theoretical development by Coussy[41], who modified the solid mechanics flow rule for the application to porous media based on the principles of volumetric response (Equation (3.77)). Among the existing extensive post-yield constitutive models and plastic analyses for fluid saturated porous media, the extension of the solid mechanics plasticity theory to incorporate the effective stress law is the most common practice. Even though this type of constitutive models usually give reasonable prediction to the total stress-strain behavior, as they are evidenced by numerous experiments, they are not adequate to describe the pore pressure redistribution induced by the permanent pore deformations during the plastic deformation of the porous material. The attempt in this section is to derive the relations for both the elastoplastic deformation and plastic porosity according to a hardening/softening constitutive model for fluid saturated porous media, based on the concept of effective stress and theoretical work by Coussy[41], in trying to fill the above-mentioned gap.

By assuming an isotropic strain hardening rule, with the hardening parameter linked only to the plastic strain, a Drucker-Prager model extended to describe hardening/softening behaviors by allowing the cone angle to vary during the plastic deformation has been used previously for the elastoplastic analysis of the borehole stability and other geomechanical problems in solid phase materials exhibiting both hardening/softening behaviors[151][147][153]. Presented in terms of effective stresses, the loading function of the model is:

$$F = \sqrt{J_2'} - 3\alpha_{dp} \left[ a_{dp} - \left( \frac{I}{3} - p \right) \right] = 0 \quad (3.91)$$

where,

$$\alpha_{dp} = \alpha_{dp}^0 + \alpha_{dp}^1 \frac{\kappa_{dp}}{B_{dp} + \kappa_{dp}} \quad (3.92)$$

describes the cone angle variation during the post-failure plastic deformation; and,

$$\kappa_{dp} = \int d\bar{\epsilon}^p \quad (3.93)$$

is the hardening parameter defined by the isotropic strain hardening rule where  $\bar{\epsilon}^p$

is the second invariants of deviatoric plastic strains:

$$\bar{\epsilon}^p = 2e_{ij}^p e_{ij}^p \quad (3.94)$$

$$e_{ij}^p = \epsilon_{ij}^p - \frac{1}{3} \epsilon_v^p \delta_{ij} \quad (3.95)$$

$$\epsilon_v^p = \epsilon_{ii}^p \quad (3.96)$$

and  $a_{dp} = k_{dp}/3\alpha_{dp} = c \cot \phi_f$ . In the case of hardening,  $\alpha_{dp}^0$  is the apex angle of the initial failure cone, and  $\alpha_{dp}^0 + \alpha_{dp}^1$  is the apex angle of failure cone at peak strength. In the case of softening,  $\alpha_{dp}^0$  is the apex angle at peak strength and  $\alpha_{dp}^0 - |\alpha_{dp}^1|$  is the apex angle at residual strength.  $B_{dp}$  is a constant.

The following flow potential is adopted for non-associated flow rule. :

$$Q = \sqrt{J_2'} + 3\beta_{dp} \left( \frac{I}{3} - p \right) \quad (3.97)$$

where,

$$\beta_{dp} = \gamma \alpha_{dp} \quad (0 \leq \gamma \leq 1) \quad (3.98)$$

### 3.3.2.5 Thermoporoelastoplastic Constitutive Relations

To facilitate the implementation of the plastic model in the finite element solution in Chapter 5, matrix notations are adopted in the following derivations.

Substituting the elastic and plastic strain components into (3.81):

$$d\epsilon = d\epsilon^e + d\epsilon^p = D_e^{-1} (d\sigma + \alpha Idp + \alpha_m^T K IdT) + d\lambda b \quad (3.99)$$

where  $D_e$  is the elastic constant matrix; and  $b = \partial Q / \partial \sigma$  can be obtained by differentiating (3.97) with respect to the total stress tensor:

$$b = \frac{1}{2\sqrt{J_2'}} \left[ \begin{array}{cccccc} 2\beta_{dp}\sqrt{J_2'} + s_x & 2\beta_{dp}\sqrt{J_2'} + s_y & 2\beta_{dp}\sqrt{J_2'} + s_z & 2s_{xy} & 2s_{yz} & 2s_{zx} \end{array} \right]^T \quad (3.100)$$

Introducing the hardening modulus,  $A$ , the consistency relations  $dF = 0$  can be presented in the following form:

$$a^T d\sigma + a' dp - A d\lambda = 0 \quad A = -\frac{1}{d\lambda} \frac{\partial F}{\partial \kappa_{dp}} d\kappa_{dp} \quad (3.101)$$

where

$$\begin{aligned} \mathbf{a}^T &= \frac{\partial F}{\partial \boldsymbol{\sigma}} & (3.102) \\ &= \frac{1}{2\sqrt{J_2}} \left[ \begin{array}{ccc} 2\alpha_{dp}\sqrt{J_2} + s_x & 2\alpha_{dp}\sqrt{J_2} + s_y & 2\alpha_{dp}\sqrt{J_2} + s_z \\ 2s_{xy} & 2s_{yz} & 2s_{zx} \end{array} \right] \end{aligned}$$

and

$$a' = \frac{\partial F}{\partial p} = 3\alpha_{dp} \quad (3.103)$$

Multiplying both sides of (3.99) with  $\mathbf{a}^T \mathbf{D}_e$ , and eliminating  $\mathbf{a}^T d\boldsymbol{\sigma}$  by using (3.101):

$$\mathbf{a}^T \mathbf{D}_e d\boldsymbol{\varepsilon} = -a' dp + A d\lambda + \mathbf{a}^T \alpha \mathbf{I} dp + \mathbf{a}^T \alpha_m^T K \mathbf{I} dT + \mathbf{a}^T \mathbf{D}_e d\lambda \mathbf{b} \quad (3.104)$$

The plastic multiplier can be obtained by rearranging (3.104):

$$d\lambda = \frac{\mathbf{a}^T \mathbf{D}_e d\boldsymbol{\varepsilon} + (a' - \mathbf{a}^T \alpha \mathbf{I}) dp - \mathbf{a}^T \alpha_m^T K \mathbf{I} dT}{A + \mathbf{a}^T \mathbf{D}_e \mathbf{b}} \quad (3.105)$$

Substituting (3.105) into (3.99) and re-arranging, the poroelastoplastic constitutive relations for this model can be derived:

$$d\boldsymbol{\sigma} = (\mathbf{D}_e - \mathbf{D}_p) d\boldsymbol{\varepsilon} - (\alpha \mathbf{I} + \mathbf{D}_p^p) dp - (\alpha_m^T K \mathbf{I} + \mathbf{D}_p^T) dT \quad (3.106)$$

where,

$$\mathbf{D}_p = \frac{\mathbf{D}_e \mathbf{b} \mathbf{a}^T \mathbf{D}_e}{A + \mathbf{a}^T \mathbf{D}_e \mathbf{b}} \quad (3.107)$$

$$\mathbf{D}_p^p = \frac{\mathbf{D}_e \mathbf{b} (a' - \mathbf{a}^T \alpha \mathbf{I})}{A + \mathbf{a}^T \mathbf{D}_e \mathbf{b}} \quad (3.108)$$

$$\mathbf{D}_p^T = -\frac{\mathbf{D}_e \mathbf{b} \mathbf{a}^T \alpha_m^T K \mathbf{I}}{A + \mathbf{a}^T \mathbf{D}_e \mathbf{b}} \quad (3.109)$$

To determine A, one first substitutes (3.100) into (3.77) and obtains the deviatoric incremental plastic strains:

$$d\mathbf{e}^p = \frac{d\lambda}{2\sqrt{J_2}} \mathbf{s} \quad (3.110)$$

Then, using (3.93), (3.94) and (3.88), it can be shown that:

$$d\lambda = d\bar{\epsilon}^p = d\kappa_{dp} \quad (3.111)$$

Substituting (3.111) into (3.101) and using (3.91) and (3.92), A can be obtained:

$$A = -\frac{\partial F}{\partial \kappa_{dp}} = \frac{3\alpha_{dp}^1 B_{dp}}{(B_{dp} + \kappa_{dp})^2} \left[ a_{dp} - \left( \frac{I}{3} - p \right) \right] \quad (3.112)$$

From (3.77) one has:

$$d\phi^p = d\lambda b', \quad b' = \frac{\partial Q}{\partial p} = -3\beta_{dp} \quad (3.113)$$

Substituting (3.105) into (3.113):

$$d\phi^p = -3\beta_{dp} \times \frac{\mathbf{a}^T \mathbf{D}_e d\boldsymbol{\epsilon} + (a' - \mathbf{a}^T \boldsymbol{\alpha} \mathbf{I}) dp - \mathbf{a}^T \boldsymbol{\alpha}_m^T \mathbf{K} \mathbf{I} dT}{A + \mathbf{a}^T \mathbf{D}_e \mathbf{b}} \quad (3.114)$$

Replacing  $\sigma_{kk}$  in Equation (3.16) with  $\epsilon_{kk}$  by using (3.11), and representing (3.16) in incremental form :

$$d\phi^e = \frac{3(\nu_u - \nu)}{B(1 + \nu_u)(1 - 2\nu)} d\epsilon_{kk} - \frac{9(1 - \nu)(1 + 2\nu_u)(\nu_u - \nu)}{2GB^2(1 + \nu)(1 - 2\nu)(1 + \nu_u)^2} dp - \frac{\phi}{K_f} dp + \left( \alpha_p^T - \frac{3(\nu_u - \nu)\alpha_m^T}{B(1 + \nu_u)(1 - 2\nu)} \right) dT \quad (3.115)$$

Substituting both (3.114) and (3.115) into (3.82), and rearranging:

$$d\phi = \frac{3(\nu_u - \nu)}{B(1 + \nu_u)(1 - 2\nu)} d\epsilon_{kk} - 3\beta_{dp} \frac{\mathbf{a}^T \mathbf{D}_e d\boldsymbol{\epsilon}}{A + \mathbf{a}^T \mathbf{D}_e \mathbf{b}} - \left[ \frac{9(1 - \nu)(1 + 2\nu_u)(\nu_u - \nu)}{2GB^2(1 + \nu)(1 - 2\nu)(1 + \nu_u)^2} + 3\beta_{dp} \frac{(a' - \mathbf{a}^T \boldsymbol{\alpha} \mathbf{I})}{A + \mathbf{a}^T \mathbf{D}_e \mathbf{b}} + \frac{\phi}{K_f} \right] dp + \left[ \left( \alpha_p^T - \frac{3(\nu_u - \nu)\alpha_m^T}{B(1 + \nu_u)(1 - 2\nu)} \right) + 3\beta_{dp} \frac{\mathbf{a}^T \boldsymbol{\alpha}_m^T \mathbf{K} \mathbf{I}}{A + \mathbf{a}^T \mathbf{D}_e \mathbf{b}} \right] dT \quad (3.116)$$

The thermoporoelastoplastic constitutive relation for the change of fluid content per unit reference volume can be obtained by substituting (3.116) into (3.15) and rearranging:

$$\zeta = \frac{3(\nu_u - \nu)}{B(1 + \nu_u)(1 - 2\nu)} d\epsilon_{kk} - 3\beta_{dp} \frac{\mathbf{a}^T \mathbf{D}_e d\boldsymbol{\epsilon}}{A + \mathbf{a}^T \mathbf{D}_e \mathbf{b}}$$

$$\begin{aligned}
& - \left[ \frac{9(1-\nu)(1+2\nu_u)(\nu_u-\nu)}{2GB^2(1+\nu)(1-2\nu)(1+\nu_u)^2} + 3\beta_{dp} \frac{(a' - a^T \alpha I)}{A + a^T D_e b} \right] dp \\
& + \left[ \left( \alpha_p^T - \frac{3(\nu_u - \nu) \alpha_m^T}{B(1+\nu_u)(1-2\nu)} \right) + 3\beta_{dp} \frac{a^T \alpha_m^T KI}{A + a^T D_e b} - \alpha_f^T \phi \right] dT \quad (3.117)
\end{aligned}$$

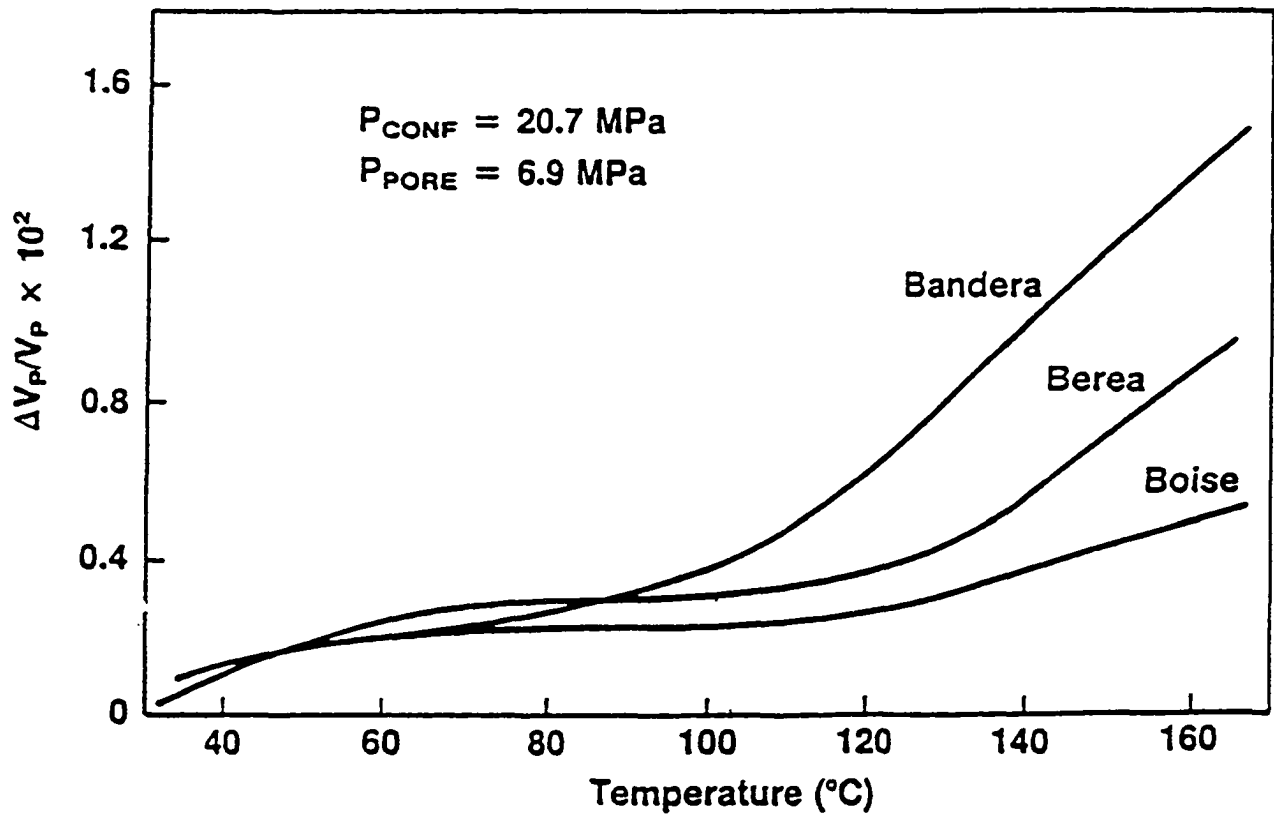


Figure 3.1: Pore volume contraction of three sand stones as function of temperature at constant stress conditions (after Somerton, 1992 )

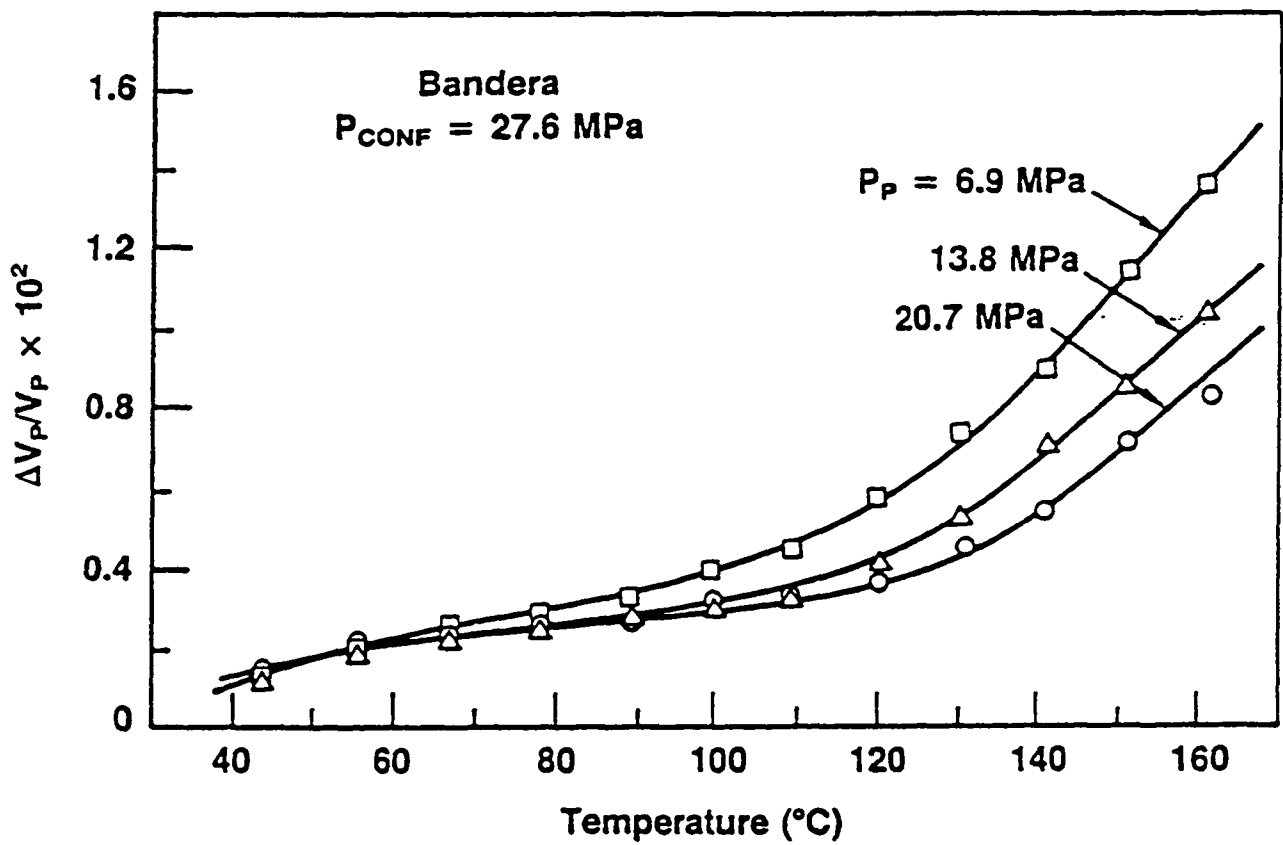


Figure 3.2: Effects of pore pressure on pore volume contraction during temperature change (after Somerton, 1992)

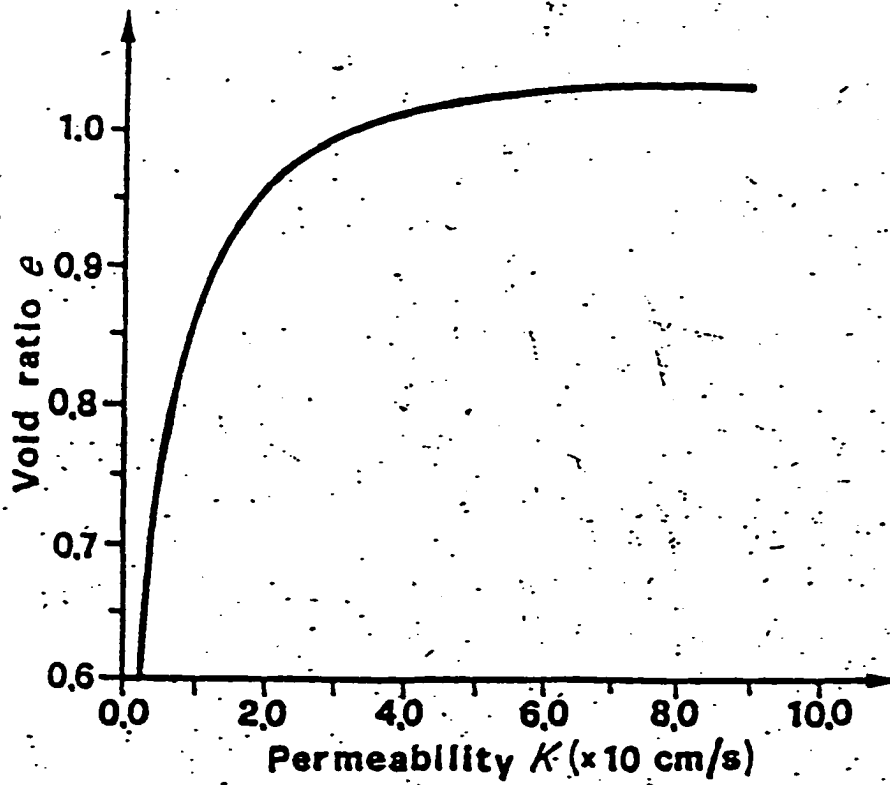


Figure 3.3: Experimentally obtained relationship between void ratio and permeability (after Lewis & Schrefler, 1987. Note that the permeability in this figure is the definition of original author)

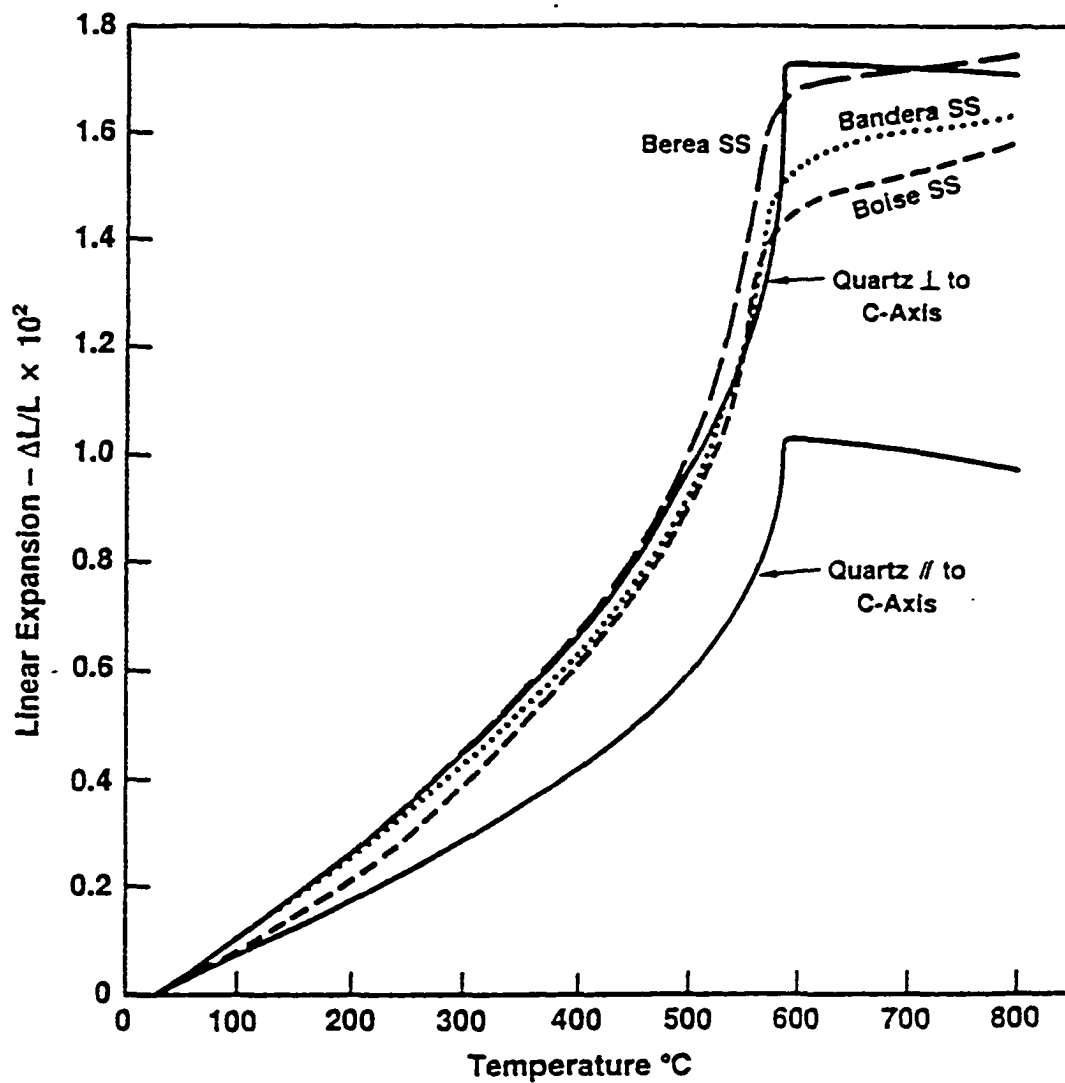


Figure 3.4: Linear thermal expansion as a function of temperature for some sandstones and quartz (after Somerton, 1992)

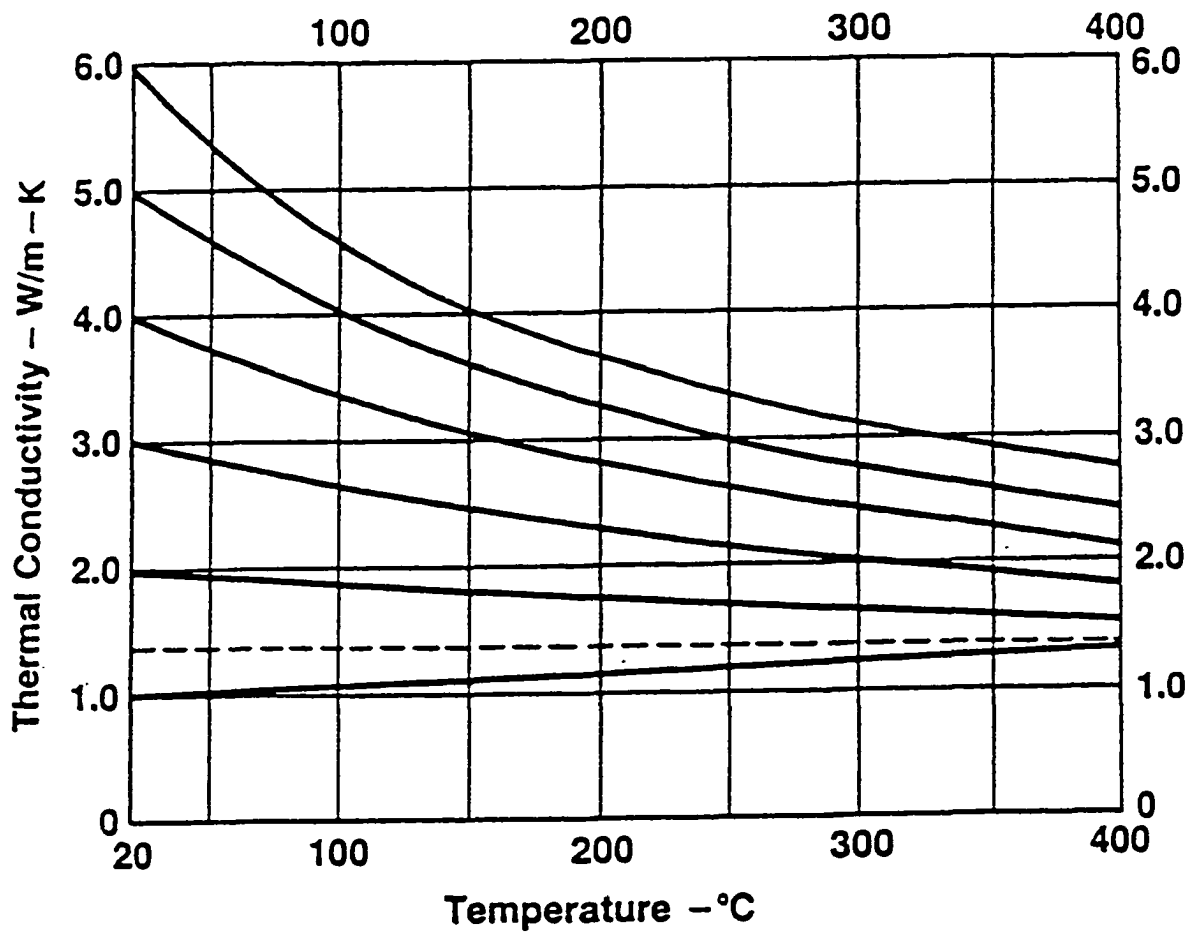


Figure 3.5: Thermal conductivity as a function of temperature (after Somerton, 1992)

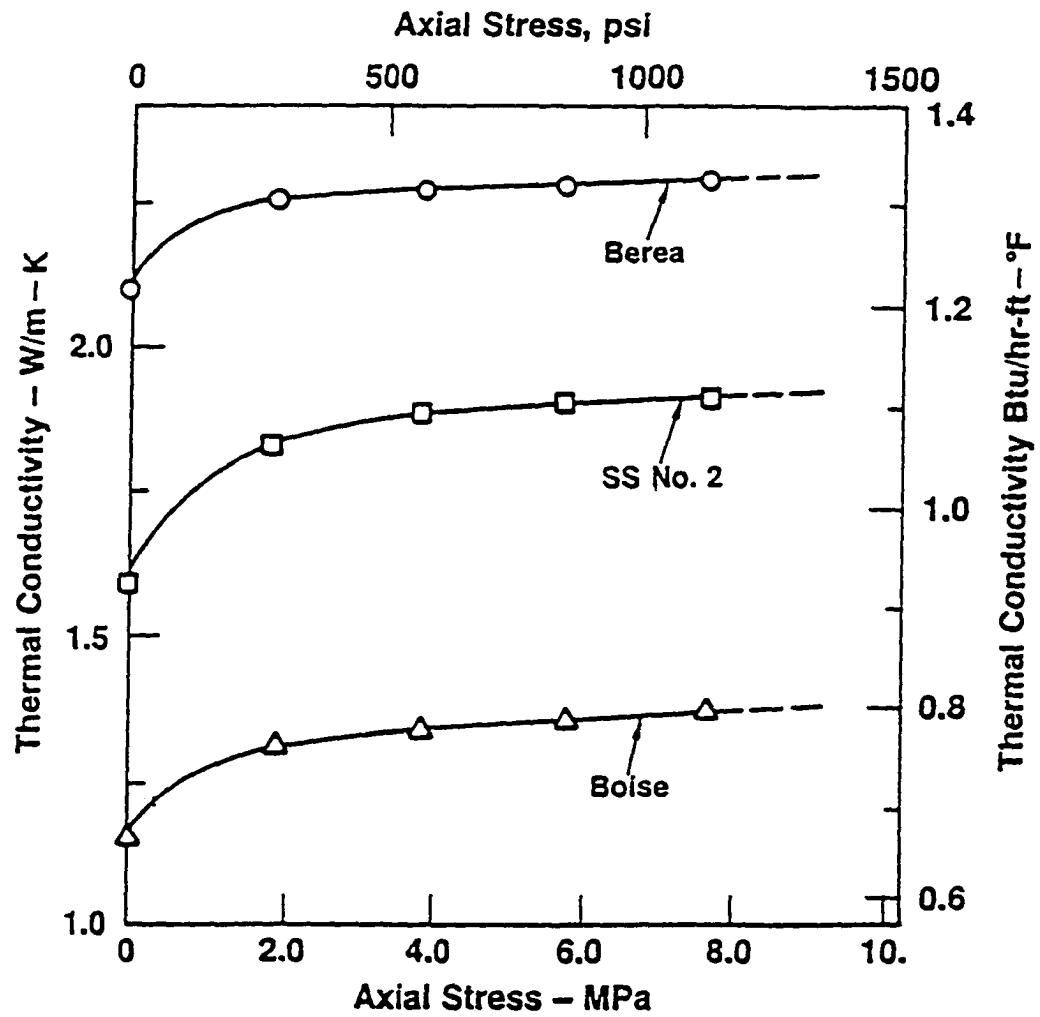


Figure 3.6: Thermoconductivity as a function of stress (after Somerton, 1992)

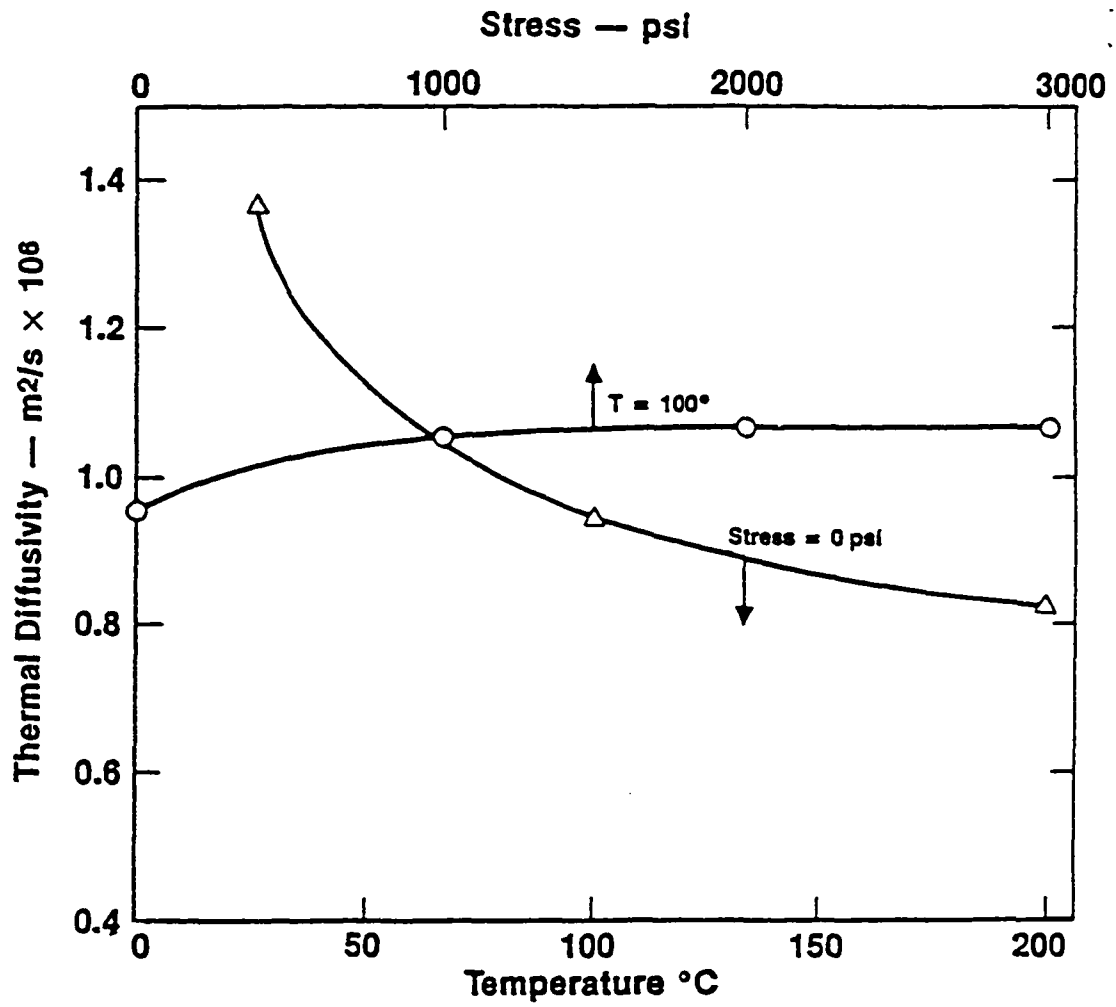


Figure 3.7: Thermal diffusivity as a function of temperature and stress for dry Berea sandstone (after Somerton, 1992)

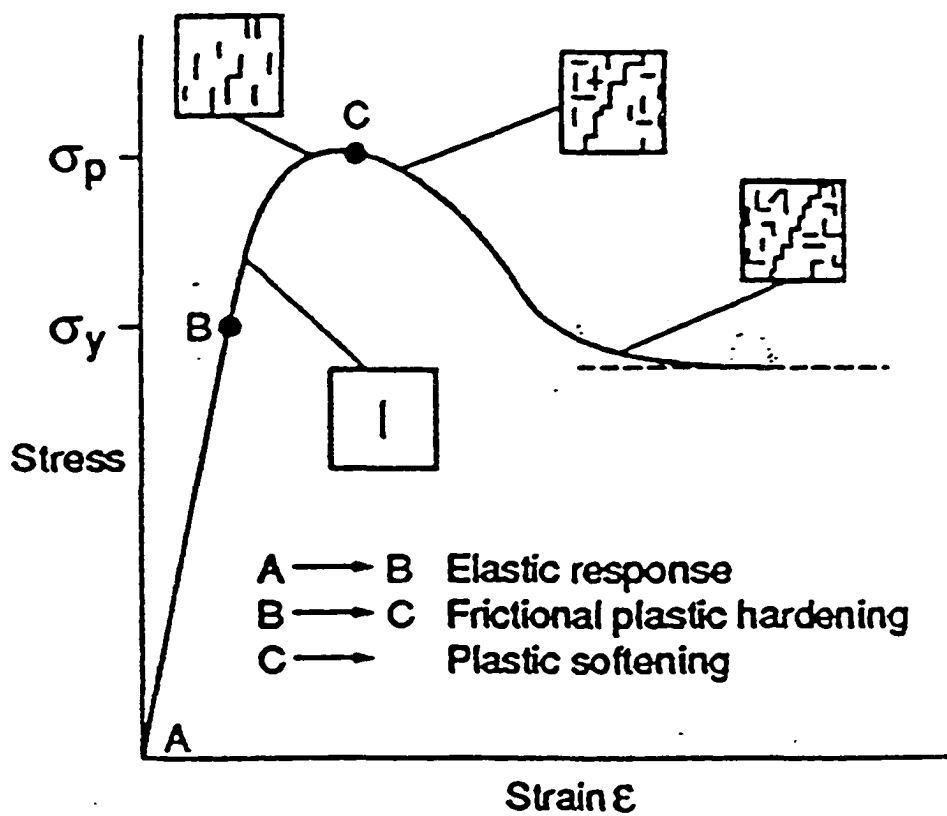


Figure 3.8: Typical rock behavior during tri-axial tests (after Veeken et al., 1989)

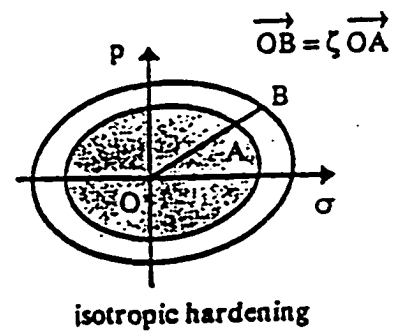
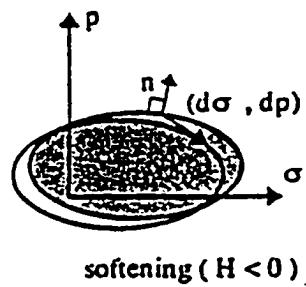
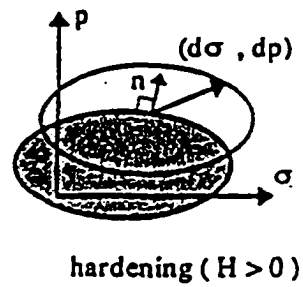
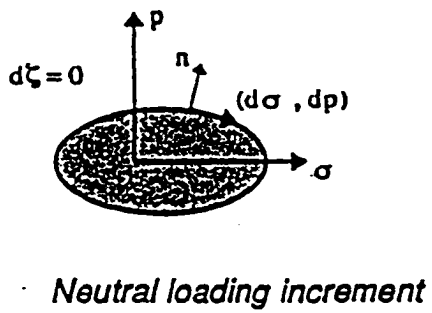


Figure 3.9: Geometric interpretation of hardening/softening models(after O. Coussy, 1995)

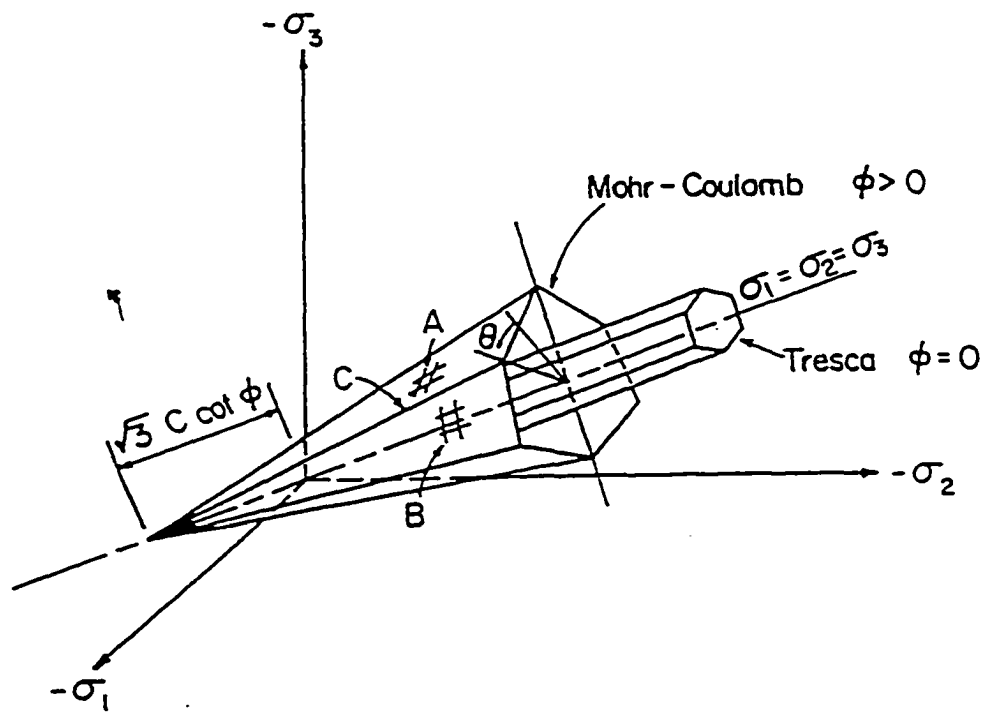


Figure 3.10: Mohr-Coulomb and Tresca yield functions in principal stress space (after R. D. Hart, 1981)

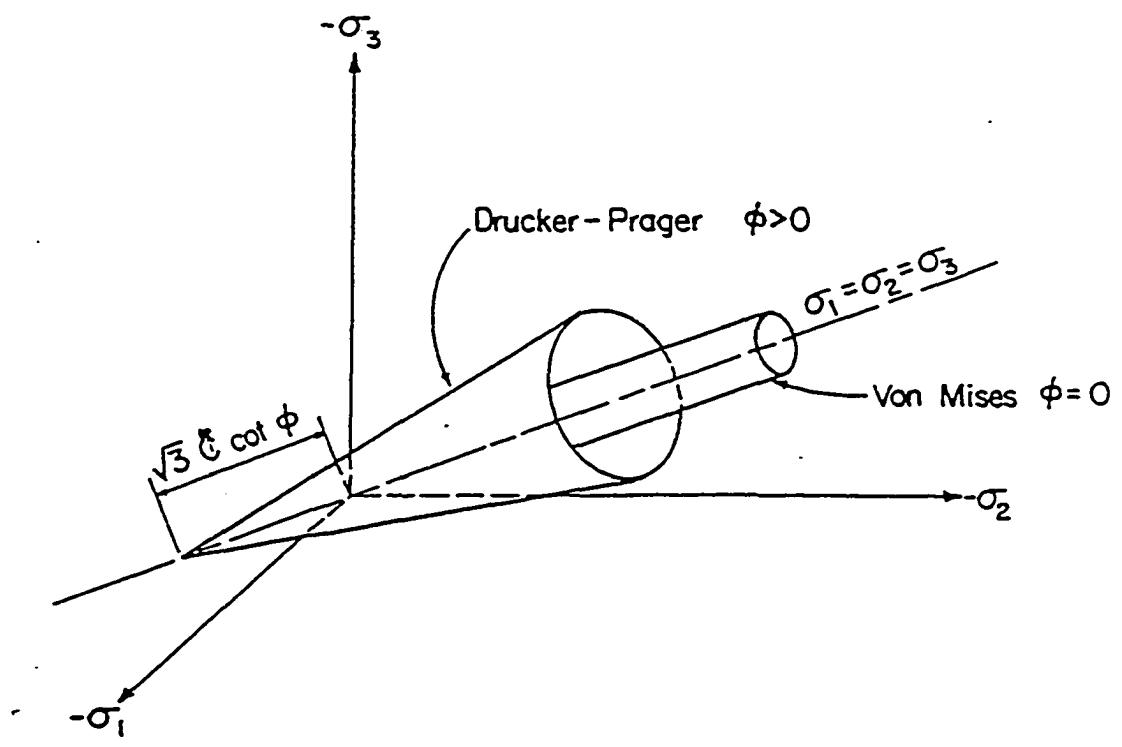


Figure 3.11: Drucker-Prager and Von Mises yield functions in principal stress space (after R. D. Hart, 1981)

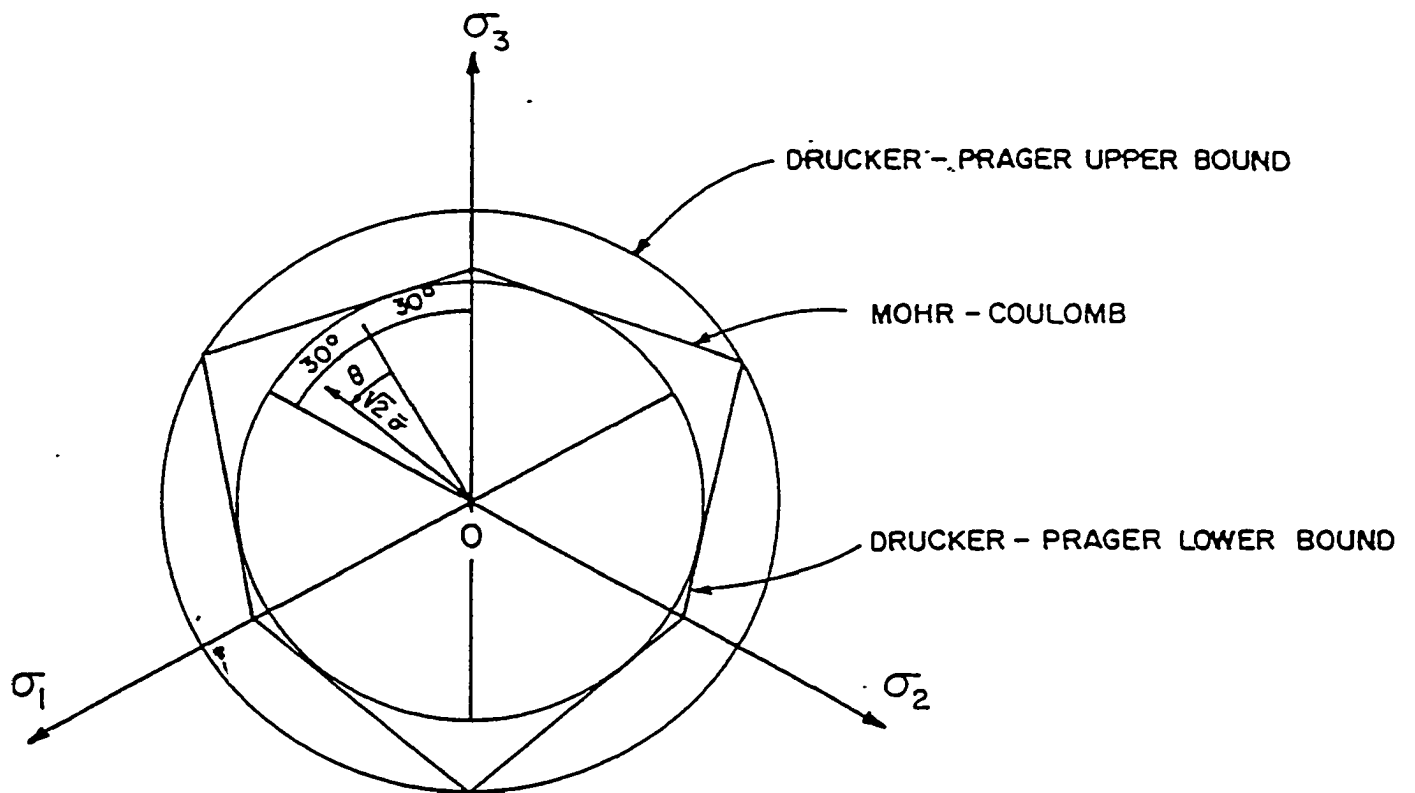


Figure 3.12: Upper and lower bound Drucker-Prager yield surfaces (after R. D. Hart, 1981)

## 4 Thermoporoelastic Solutions

### 4.1 Introduction

This chapter presents the analytical solutions obtained in this dissertation for the condition of fully-coupled thermoporoelasticity, including the general solution for axisymmetric loading condition; dimensionless solutions for some extreme boundary conditions; the solution for a borehole subjected to non-hydrostatic far-field loading and solution for inclined boreholes. In addition, the thermoelastic solution for inclined boreholes is also derived at the end of the chapter for the purpose of comparison.

### 4.2 General Solutions For Irrotational Displacement Field

The displacement field under the condition of axisymmetric loading is irrotational. This allows the decoupling of the displacement field from temperature and pore pressure fields, as it is presented in the following derivations. Decoupling greatly simplifies the solution procedure, and this section constitutes one of the important components for the solution of general borehole problems in which the displacement field is generally rotational.

### 4.2.1 Decoupling of Displacement Field from Temperature and Pore Pressure Fields

For the irrotational displacement field, the displacement can be expressed as the gradient of a scalar function,  $\Phi$  : *i.e.*

$$u_i = \Phi_{,i} = \frac{\partial \Phi}{\partial x_i} \quad (4.1)$$

$$u_{i,i} = \varepsilon_{ii} = \Phi_{,ii} \quad (4.2)$$

$$u_{i,jj} = \Phi_{,ijj} = \frac{\partial^2 \Phi}{\partial x^2} \frac{\partial \Phi}{\partial x_i} + \frac{\partial^2 \Phi}{\partial y^2} \frac{\partial \Phi}{\partial x_i} + \frac{\partial^2 \Phi}{\partial z^2} \frac{\partial \Phi}{\partial x_i} \quad (4.3)$$

$$\begin{aligned} \int u_{i,jj} dx &= \int \Phi_{,ijj} dx \\ &= \int \left( \frac{\partial^2 \Phi}{\partial x^2} \frac{\partial \Phi}{\partial x} + \frac{\partial^2 \Phi}{\partial y^2} \frac{\partial \Phi}{\partial x} + \frac{\partial^2 \Phi}{\partial z^2} \frac{\partial \Phi}{\partial x} \right) dx \\ &= \frac{\partial^2 \Phi}{\partial x^2} + \frac{\partial^2 \Phi}{\partial y^2} + \frac{\partial^2 \Phi}{\partial z^2} \\ &= \Phi_{,jj} = \varepsilon_{jj} \end{aligned} \quad (4.4)$$

Expanding Equation (3.35) according to the rectangular coordinate system notation:

$$G \left( \frac{\partial^2 u_x}{\partial x^2} + \frac{\partial^2 u_y}{\partial y^2} + \frac{\partial^2 u_z}{\partial z^2} \right) + \frac{G}{1-2\nu} \left( \frac{\partial^2 u_x}{\partial x^2} + \frac{\partial^2 u_y}{\partial y \partial x} + \frac{\partial^2 u_z}{\partial z \partial x} \right) \quad (4.5)$$

$$= \alpha \frac{\partial p}{\partial x} + \frac{2G\alpha_m^T (1+\nu)}{3(1-2\nu)} \frac{\partial T}{\partial x} \quad (4.6)$$

then replacing  $u_i$  with  $\Phi_{,i}$ :

$$\begin{aligned} G \left( \frac{\partial^3 \Phi}{\partial x^3} + \frac{\partial^3 \Phi}{\partial y^2 \partial x} + \frac{\partial^3 \Phi}{\partial z^2 \partial x} \right) + \frac{G}{1-2\nu} \left( \frac{\partial^3 \Phi}{\partial x^3} + \frac{\partial^3 \Phi}{\partial^2 y \partial x} + \frac{\partial^3 \Phi}{\partial^2 z \partial x} \right) \\ = \alpha \frac{\partial p}{\partial x} + \frac{2G\alpha_m^T (1+\nu)}{3(1-2\nu)} \frac{\partial T}{\partial x} \end{aligned} \quad (4.7)$$

Equation (4.7) can be re-arranged to have the following form:

$$\frac{2G(1-\nu)}{(1-2\nu)} \left( \frac{\partial^3 \Phi}{\partial x^3} + \frac{\partial^3 \Phi}{\partial y^2 \partial x} + \frac{\partial^3 \Phi}{\partial z^2 \partial x} \right) = \alpha \frac{\partial p}{\partial x} + \frac{2G\alpha_m^T (1+\nu)}{3(1-2\nu)} \frac{\partial T}{\partial x} \quad (4.8)$$

Integrating Equation (4.8) on both sides and using (4.4), one obtains:

$$\frac{2G(1-\nu)}{(1-2\nu)} \varepsilon_{jj} = \alpha p + \frac{2G\alpha_m^T(1+\nu)}{3(1-2\nu)} T + g(t) \quad (4.9)$$

where  $g(t)$  is an arbitrary function of time.

Substituting  $\varepsilon_{jj}$  into (3.11) and re-arranging:

$$\begin{aligned} \sigma_{kk} &= \frac{1+\nu}{1-\nu} \alpha p + \frac{2G\alpha_m^T(1+\nu)^2}{3(1-2\nu)(1-\nu)} T - 3\alpha p - \frac{2G(1+\nu)}{(1-2\nu)} \alpha_m^T T + \frac{1+\nu}{1-\nu} g(t) \\ &= -\frac{2(1-2\nu)}{1-\nu} \alpha p - \frac{4G(1+\nu)}{3(1-\nu)} \alpha_m^T T + \frac{1+\nu}{1-\nu} g(t) \end{aligned} \quad (4.10)$$

Formulations of the pore pressure and temperature diffusion equations for irrotational displacement field can be obtained through the following procedure:

Substituting (4.10) into (3.21) and re-arranging:

$$\begin{aligned} \zeta &= \frac{\alpha(1-2\nu)}{2G(1+\nu)} \left[ -\frac{2(1-2\nu)}{1-\nu} \alpha p - \frac{4G(1+\nu)}{3(1-\nu)} \alpha_m^T T + \frac{1+\nu}{1-\nu} g(t) + \frac{3}{B} p \right] \\ &\quad + (\alpha_p^T - \alpha_f^T \phi) T \end{aligned} \quad (4.11)$$

$$\begin{aligned} &= \frac{\alpha(1-2\nu)}{2G(1+\nu)} \left[ \frac{3}{B} - \frac{2(1-2\nu)}{1-\nu} \alpha \right] p - \left[ \frac{2\alpha(1-2\nu)\alpha_m^T}{3(1-\nu)} - (\alpha_p^T - \alpha_f^T \phi) \right] T \\ &\quad + \frac{\alpha(1-2\nu)}{2G(1-\nu)} g(t) \end{aligned} \quad (4.12)$$

Differentiating (4.12) with respect to  $t$  while keeping all the coefficients constant:

$$\begin{aligned} \frac{\partial \zeta}{\partial t} &= \frac{\alpha(1-2\nu)}{2G(1+\nu)} \left[ \frac{3}{B} - \frac{2(1-2\nu)}{1-\nu} \alpha \right] \frac{\partial p}{\partial t} - \left[ \frac{2\alpha(1-2\nu)\alpha_m^T}{3(1-\nu)} - (\alpha_p^T - \alpha_f^T \phi) \right] \frac{\partial T}{\partial t} \\ &\quad + \frac{\alpha(1-2\nu)}{2G(1-\nu)} \frac{\partial g(t)}{\partial t} \end{aligned} \quad (4.13)$$

Substituting (4.13) into (3.31):

$$\begin{aligned} \frac{\alpha(1-2\nu)}{2G(1+\nu)} \left[ \frac{3}{B} - \frac{2(1-2\nu)}{1-\nu} \alpha \right] \frac{\partial p}{\partial t} &= \kappa p_{,jj} + \left[ \frac{2\alpha(1-2\nu)\alpha_m^T}{3(1-\nu)} - (\alpha_p^T - \alpha_f^T \phi) \right] \frac{\partial T}{\partial t} \\ &\quad - \frac{\alpha(1-2\nu)}{2G(1-\nu)} \frac{\partial g(t)}{\partial t} \end{aligned} \quad (4.14)$$

and re-arranging:

$$\frac{\partial p}{\partial t} = \frac{2\kappa GB^2(1-\nu)(1+\nu_u)^2}{9(\nu_u - \nu)(1-\nu_u)} p_{,jj}$$

$$+ \frac{2GB^2(1-\nu)(1+\nu_u)^2}{9(\nu_u-\nu)(1-\nu_u)} \left[ \frac{2\alpha(1-2\nu)\alpha_m^T}{3(1-\nu)} - (\alpha_p^T - \alpha_f^T\phi) \right] \frac{\partial T}{\partial t} \quad (4.15)$$

$$\begin{aligned} & - \frac{B(1+\nu_u)}{3(1-\nu_u)} \frac{\partial g(t)}{\partial t} \\ = & c^f p_{,jj} + c^{\mathcal{J}T} \frac{\partial T}{\partial t} - c^g \frac{\partial g(t)}{\partial t} \end{aligned} \quad (4.16)$$

where,

$$c^{\mathcal{J}T} = \frac{c^f}{\kappa} \left[ \frac{2\alpha(1-2\nu)\alpha_m^T}{3(1-\nu)} - (\alpha_p^T - \alpha_f^T\phi) \right] \quad (4.17)$$

$$c^g = \frac{B(1+\nu_u)}{3(1-\nu_u)} \quad (4.18)$$

For infinite or semi-infinite domains, the function  $g(t)$  is identically zero, since  $\varepsilon$ ,  $p$  and  $T$  must vanish at infinity in Equation (4.9). Thus Equation (4.16) is decoupled from the displacement field and becomes:

$$\frac{\partial p}{\partial t} = c^f p_{,jj} + c^{\mathcal{J}T} \frac{\partial T}{\partial t} \quad (4.19)$$

This way, the displacement field has been decoupled from the pore pressure and temperature fields, but the pore pressure and temperature field are still coupled with each other through the convective heat transfer term.

## 4.2.2 Dimensionless Diffusivity Equations

To facilitate the parametric study, the following dimensionless variables are introduced:

- $T' = T/T_m$ ,  $T_m$  is the disturbance of the temperature at the boundary from the initial state;
- $p' = p/p_m$ ,  $p_m$  is the disturbance of the pore-pressure at the boundary from the initial state;
- $x'_i = x_i/r_0$ ,  $r_0$  is a representative length (wellbore radius in wellbore problem); and.

- $t' = t / (r_0^2 / c^f)$ .

Using the above introduced dimensionless variables:

$$\frac{\partial p}{\partial t} = \frac{p_m \partial p'}{\frac{r_0^2}{c^f} \partial t'} \quad (4.20)$$

$$\begin{aligned} p_{,jj} &= \frac{\partial^2 p}{\partial x^2} + \frac{\partial^2 p}{\partial y^2} + \frac{\partial^2 p}{\partial z^2} \\ &= \frac{p_m}{r_0^2} \left( \frac{\partial^2 p'}{\partial x'^2} + \frac{\partial^2 p'}{\partial y'^2} + \frac{\partial^2 p'}{\partial z'^2} \right) \\ &= \frac{p_m}{r_0^2} p'_{,jj} \end{aligned} \quad (4.21)$$

$$\frac{\partial T}{\partial t} = \frac{T_m \partial T'}{\frac{r_0^2}{c^f} \partial t'} \quad (4.22)$$

$$\begin{aligned} T_{,jj} &= \frac{\partial^2 T}{\partial x^2} + \frac{\partial^2 T}{\partial y^2} + \frac{\partial^2 T}{\partial z^2} \\ &= \frac{T_m}{r_0^2} \left( \frac{\partial^2 T'}{\partial x'^2} + \frac{\partial^2 T'}{\partial y'^2} + \frac{\partial^2 T'}{\partial z'^2} \right) \\ &= \frac{T_m}{r_0^2} T'_{,jj} \end{aligned} \quad (4.23)$$

$$\begin{aligned} (Tp_j)_{,j} &= \frac{\partial}{\partial x} \left( T \frac{\partial p}{\partial x} \right) + \frac{\partial}{\partial y} \left( T \frac{\partial p}{\partial y} \right) + \frac{\partial}{\partial z} \left( T \frac{\partial p}{\partial z} \right) \\ &= \frac{T_m p_m}{r_0^2} \left[ \frac{\partial}{\partial x'} \left( T' \frac{\partial p'}{\partial x'} \right) + \frac{\partial}{\partial y'} \left( T' \frac{\partial p'}{\partial y'} \right) + \frac{\partial}{\partial z'} \left( T' \frac{\partial p'}{\partial z'} \right) \right] \\ &= \frac{T_m p_m}{r_0^2} (T' p'_{,j})_{,j} \end{aligned} \quad (4.24)$$

Substituting Equations (4.20) to (4.24) into the diffusivity field equations (4.16) and (3.45), one obtains:

$$\frac{p_m \partial p'}{\frac{r_0^2}{c^f} \partial t'} = c^f \frac{p_m}{r_0^2} p'_{,jj} + c^f T \frac{T_m \partial T'}{\frac{r_0^2}{c^f} \partial t'} \quad (4.25)$$

$$\frac{T_m \partial T'}{\frac{r_0^2}{c^f} \partial t'} = c^T \frac{T_m}{r_0^2} T'_{,jj} + \frac{\kappa \rho_f C_f}{\rho_t C_t} \frac{T_m p_m}{r_0^2} (T' p'_{,j})_{,j} \quad (4.26)$$

Re-arranging Equations (4.25) and (4.26), the dimensionless temperature and pore pressure diffusion equations for the irrotational displacement field can be obtained ( note that the primes for the dimensionless variables have been dropped for simplicity ):

$$\frac{\partial T}{\partial t} = A_0 T_{,ii} + A_1 (T p_{,i})_{,i} \quad (4.27)$$

$$\frac{\partial p}{\partial t} = p_{,ii} + A_2 \frac{\partial T}{\partial t} \quad (4.28)$$

where,

$$A_0 = \frac{c^T}{c^f}, \quad A_1 = \frac{\kappa \rho_f C_f p_m}{\rho_t C_t c^f}, \quad A_2 = \frac{T_m}{p_m} c^{fT}$$

### 4.2.3 Diffusivity Equations in Cylindrical Coordinate System

According to the relationship between cylindrical and rectangular coordinate systems:

$$r^2 = x^2 + y^2, \quad \theta = \arctan \frac{y}{x}, \quad z = z \quad (4.29)$$

and applying the chain rule, the following transformation relationships (assume plane strain condition; so  $p$  and  $T$  are independent of  $z$ ) can be obtained:

$$\frac{\partial}{\partial x} = \frac{\partial}{\partial r} \cos \theta - \frac{1}{r} \frac{\partial}{\partial \theta} \sin \theta \quad (4.30)$$

$$\begin{aligned} \frac{\partial^2}{\partial x^2} &= \frac{\partial^2}{\partial r^2} \cos^2 \theta - 2 \frac{\partial^2}{\partial r \partial \theta} \frac{\sin \theta \cos \theta}{r} + \frac{\partial}{\partial r} \frac{\sin^2 \theta}{r} \\ &+ 2 \frac{\partial}{\partial \theta} \frac{\sin \theta \cos \theta}{r^2} + \frac{\partial^2}{\partial \theta^2} \frac{\sin^2 \theta}{r^2} \end{aligned} \quad (4.31)$$

$$\frac{\partial}{\partial y} = \frac{\partial}{\partial r} \sin \theta + \frac{1}{r} \frac{\partial}{\partial \theta} \cos \theta \quad (4.32)$$

$$\begin{aligned} \frac{\partial^2}{\partial y^2} &= \frac{\partial^2}{\partial r^2} \sin^2 \theta + 2 \frac{\partial^2}{\partial r \partial \theta} \frac{\sin \theta \cos \theta}{r} + \frac{\partial}{\partial r} \frac{\cos^2 \theta}{r} \\ &- 2 \frac{\partial}{\partial \theta} \frac{\sin \theta \cos \theta}{r^2} + \frac{\partial^2}{\partial \theta^2} \frac{\cos^2 \theta}{r^2} \end{aligned} \quad (4.33)$$

$$\frac{\partial^2}{\partial x^2} + \frac{\partial^2}{\partial y^2} = \frac{\partial^2}{\partial r^2} + \frac{1}{r} \frac{\partial}{\partial r} + \frac{1}{r^2} \frac{\partial^2}{\partial \theta^2} \quad (4.34)$$

$$\frac{\partial p}{\partial x} \frac{\partial T}{\partial x} = \left( \frac{\partial p}{\partial r} \cos \theta - \frac{1}{r} \frac{\partial p}{\partial \theta} \sin \theta \right) \left( \frac{\partial T}{\partial r} \cos \theta - \frac{1}{r} \frac{\partial T}{\partial \theta} \sin \theta \right) \quad (4.35)$$

$$= \frac{\partial p}{\partial r} \frac{\partial T}{\partial r} \cos^2 \theta - \frac{\partial p}{\partial r} \frac{\partial T}{\partial \theta} \frac{\cos \theta \sin \theta}{r} \quad (4.36)$$

$$- \frac{\partial p}{\partial \theta} \frac{\partial T}{\partial r} \frac{\sin \theta \cos \theta}{r} + \frac{\partial p}{\partial \theta} \frac{\partial T}{\partial \theta} \frac{\sin^2 \theta}{r^2} \quad (4.37)$$

$$\frac{\partial p}{\partial y} \frac{\partial T}{\partial y} = \left( \frac{\partial p}{\partial r} \sin \theta + \frac{1}{r} \frac{\partial p}{\partial \theta} \cos \theta \right) \left( \frac{\partial T}{\partial r} \sin \theta + \frac{1}{r} \frac{\partial T}{\partial \theta} \cos \theta \right) \quad (4.38)$$

$$= \frac{\partial p}{\partial r} \frac{\partial T}{\partial r} \sin^2 \theta + \frac{\partial p}{\partial r} \frac{\partial T}{\partial \theta} \frac{\cos \theta \sin \theta}{r} \quad (4.39)$$

$$+ \frac{\partial p}{\partial \theta} \frac{\partial T}{\partial r} \frac{\sin \theta \cos \theta}{r} + \frac{\partial p}{\partial \theta} \frac{\partial T}{\partial \theta} \cos^2 \theta \quad (4.40)$$

$$\frac{\partial p}{\partial x} \frac{\partial T}{\partial x} + \frac{\partial p}{\partial y} \frac{\partial T}{\partial y} = \frac{\partial p}{\partial r} \frac{\partial T}{\partial r} + \frac{1}{r^2} \frac{\partial p}{\partial \theta} \frac{\partial T}{\partial \theta} \quad (4.41)$$

Expanding the dimensionless thermal diffusivity Equation (4.27) in a rectangular coordinate system :

$$\begin{aligned} \frac{\partial T}{\partial t} &= A_0 T_{,ii} + A_1 (Tp_{,i})_{,i} \\ &= A_0 \left( \frac{\partial^2 T}{\partial x^2} + \frac{\partial^2 T}{\partial y^2} \right) + A_1 \left[ \frac{\partial}{\partial x} \left( T \frac{\partial p}{\partial x} \right) + \frac{\partial}{\partial y} \left( T \frac{\partial p}{\partial y} \right) \right] \\ &= A_0 \left( \frac{\partial^2 T}{\partial x^2} + \frac{\partial^2 T}{\partial y^2} \right) + A_1 \left( \frac{\partial T}{\partial x} \frac{\partial p}{\partial x} + \frac{\partial T}{\partial y} \frac{\partial p}{\partial y} + T \frac{\partial^2 p}{\partial x^2} + T \frac{\partial^2 p}{\partial y^2} \right) \end{aligned} \quad (4.42)$$

then applying (4.30) to (4.41):

$$\frac{\partial T}{\partial t} = A_0 \left( \frac{\partial^2 T}{\partial r^2} + \frac{1}{r} \frac{\partial T}{\partial r} + \frac{1}{r^2} \frac{\partial^2 T}{\partial \theta^2} \right) \quad (4.43)$$

$$+ A_1 \left[ \frac{\partial p}{\partial r} \frac{\partial T}{\partial r} + \frac{1}{r^2} \frac{\partial p}{\partial \theta} \frac{\partial T}{\partial \theta} + T \left( \frac{\partial^2 p}{\partial r^2} + \frac{1}{r} \frac{\partial p}{\partial r} + \frac{1}{r^2} \frac{\partial^2 p}{\partial \theta^2} \right) \right] \quad (4.44)$$

Assuming  $p = p(r, t)$  and  $T = T(r, t)$  for irrotational displacement field and thermal diffusion from a circular borehole, the above equation can further be simplified as:

$$\frac{\partial T}{\partial t} = A_0 \left( \frac{\partial^2 T}{\partial r^2} + \frac{1}{r} \frac{\partial T}{\partial r} \right) + A_1 \left[ \frac{\partial p}{\partial r} \frac{\partial T}{\partial r} + T \left( \frac{\partial^2 p}{\partial r^2} + \frac{1}{r} \frac{\partial p}{\partial r} \right) \right] \quad (4.45)$$

The pore pressure diffusion equation (4.28) can be expressed as:

$$\begin{aligned} \frac{\partial p}{\partial t} &= p_{,ii} + A_2 \frac{\partial T}{\partial t} \\ &= \left( \frac{\partial^2 p}{\partial r^2} + \frac{1}{r} \frac{\partial p}{\partial r} \right) + A_2 \frac{\partial T}{\partial t} \end{aligned} \quad (4.46)$$

## 4.2.4 Some Simplified Scenarios

Equations (4.27) and (4.28) are coupled with each other, with non-linearity in the temperature field so they are difficult to solve analytically. But in some cases, the coupled equations can be simplified by ignoring some terms according to the values of coefficients  $A_0$ ,  $A_1$ , and  $A_2$ .

### 4.2.4.1 Scenario 1

If  $A_1$  is very small compared to  $A_0$ , ( or  $c^T \gg c^f$  , which means the thermal diffusivity is much greater than the fluid diffusivity), it would be satisfactory enough to ignore the non-linear term in temperature diffusion equation (4.27). The physical meaning for this simplification is that the conductive heat transfer dominates the thermal diffusion process and that the convective heat transfer due to the pore fluids flow is negligible. This simplification further decouples Equations(4.27) from (4.28):

$$\frac{\partial T}{\partial t} = A_0 T_{,ii} \quad (4.47)$$

$$\frac{\partial p}{\partial t} = p_{,ii} + A_2 \frac{\partial T}{\partial t} \quad (4.48)$$

and thus, the analytical solutions for these equations under initial and boundary conditions can easily be obtained. This scenario is especially important for shale stability modelling.

### 4.2.4.2 Scenario 2

If both  $A_0$  and  $A_1$  are very small, which means the fluid diffusion is much faster than the thermal diffusion, it can be assumed that the fluid diffusion becomes steady before the temperature begins to change. So, the diffusion equations can be simplified into the following form:

$$p_{,ii} = 0 \quad (4.49)$$

$$\frac{\partial T}{\partial t} = A_0 T_{,ii} + A_1 (Tp_{,i})_{,i} \quad (4.50)$$

The fluid diffusion equation in this scenario can be readily resolved and the thermal diffusion equation can be solved numerically. This scenario is important for the modelling of short-term, high pressure fluid injection.

#### 4.2.4.3 Scenario 3

If  $A_1$  is very large compared with  $A_2$ , which means the convective heat transfer by pore fluids flow dominates the thermal diffusion process, the diffusion field equation can be simplified as:

$$\frac{\partial T}{\partial t} = A_1 (Tp_{,i})_{,i} \quad (4.51)$$

$$p_{,ii} = 0 \quad (4.52)$$

This scenario can be applied to the modelling of long-term fluid injection in highly porous media.

### 4.3 Solutions for Borehole Problems

This section presents two analytical solutions simulating the thermoporoelastic process triggered by drilling a borehole in saturated porous media, and subject to a step constant temperature change together with mud pressure acting on the borehole wall. The analysis bears a special meaning in wellbore stability control during drilling. The problems are solved by the Laplace transform method. The solution is closed-form in Laplace domain; and is then inverted to the time domain by using Stehfest's algorithm. For very small characteristic times where Stehfest's algorithm can not be applied, asymptotic solutions are derived. Thermoelastic solution for inclined boreholes is also obtained at the end of the section for the purpose of comparison.

## 4.3.1 Boreholes Subjected to Non-hydrostatic Stress Field

### 4.3.1.1 Problem Definition

The problem under consideration is an infinitely long circular borehole excavated in infinite poroelastic medium. The borehole is subjected to a non-hydrostatic far-field stresses, a borehole fluid pressure and a constant temperature on borehole wall as shown in Figure 4.1. Borehole fluid pressure is assumed to be applied immediately after the drilling, and the fluid temperature is different from the virgin formation temperature.

Coussy[40] and Wang and Papamichos[156] attempted to solve similar problems. Coussy[40] developed a model which superimposes the temperature induced pore pressure and stresses onto a pure elastic stress distribution due to non-hydrostatic stress field, which is not a coupled thermoporoelastic model. Whereas the model proposed by Wang and Papamichos[156] is based on an assumption that a steady-state of the stress and pore pressure have been reached before the heat and fluid exchange starts on the borehole wall. This assumption is suitable for the case of fluid injection but not for the case of modelling wellbore stability during drilling. In this section, a fully-coupled thermoporoelastic model without such limitations are developed. It is worth to note that the solution given by Wang and Papamichos[156] for the condition that fluid diffusivity equals to thermal diffusivity, which is a singularity in the solution for the general condition, is wrong. They demonstrated through their early-time asymptotic solution that the singularity term can be canceled out. But this renders the pore pressure diffusion at the singularity is completely independent of the temperature condition, which is not true physically. A complete solution will be presented in this section.

### 4.3.1.2 Solutions

By ignoring the non-linear convective heat transfer term in the thermal diffusivity equation (3.45), field equations (3.35), (3.40) and (3.45) are linear and the thermal

diffusivity equation is decoupled from the displacement and pore pressure diffusivity equations. Following Detournay and Cheng[51], the problem can be solved by dividing the load due to excavation and mud circulation disturbances into three loading modes, and superimposing the results from the three loading modes onto the virgin formation condition. Assuming that the wellbore is aligned along one of the in-situ principal stress directions, and that  $p_0$ ,  $T_0$  and  $\sigma_2 \neq \sigma_3$  are initial formation pore pressure, temperature, and in-situ principal stresses perpendicular to the borehole axis, the boundary conditions for each of the three loading modes are as following:

Mode 1:

$$\sigma_{rr}^{(1)} = H(t) (P_0 - p_m) \quad (4.53)$$

$$\sigma_{r\theta}^{(1)} = 0 \quad (4.54)$$

$$p^{(1)} = 0 \quad (4.55)$$

$$T^{(1)} = 0 \quad (4.56)$$

Mode 2:

$$\sigma_{rr}^{(2)} = 0 \quad (4.57)$$

$$\sigma_{r\theta}^{(2)} = 0 \quad (4.58)$$

$$p^{(2)} = H(t) (p_m - p_0) \quad (4.59)$$

$$T^{(2)} = H(t) (T_m - T_0) \quad (4.60)$$

Mode 3:

$$\sigma_{rr}^{(3)} = -S_0 H(t) \cos 2\theta \quad (4.61)$$

$$\sigma_{r\theta}^{(3)} = S_0 H(t) \sin 2\theta \quad (4.62)$$

$$p^{(3)} = 0 \quad (4.63)$$

$$T^{(3)} = 0 \quad (4.64)$$

where  $r, \theta, P_0, S_0$  are defined in Figure 4.1;  $p_m$  and  $T_m$  are wellbore pressure and mud

temperature during drilling, and  $H(t)$  denotes the Heaviside unit step function.

$$\begin{cases} H(t) = 0 & \text{for } t \leq 0 \\ H(t) = 1 & \text{for } t > 0 \end{cases} \quad (4.65)$$

For all the three loading modes, the induced stress, pore pressure and temperature vanish at infinity.

### Solutions for Loading Modes 1 and 3

In modes 1 and 3, the temperature boundary condition is zero, so the solutions given by Detournay and Cheng[51] can directly be adopted with a modification for taking into account the internal borehole pressure.

The solution for mode 1 is:

$$\sigma_{rr}^{(1)} = H(t) (P_0 - p_m) \frac{r^2}{a^2} \quad (4.66)$$

$$\sigma_{\theta\theta}^{(1)} = -H(t) (P_0 - p_m) \frac{r^2}{a^2} \quad (4.67)$$

The solution in the Laplace domain for mode 3 is:

$$\begin{aligned} \frac{s\bar{\sigma}_{rr}^{(3)}}{S_0 \cos 2\theta} &= \frac{B(1+\nu_u)}{3(1-\nu_u)} C_1 \left[ \frac{1}{\lambda r} K_1(\lambda r) + \frac{6}{(\lambda r)^2} K_2(\lambda r) \right] - \frac{C_2}{(1-\nu_u)} \frac{a^2}{r^2} \\ &\quad - 3C_3 \frac{a^4}{r^4} \end{aligned} \quad (4.68)$$

$$\begin{aligned} \frac{s\bar{\sigma}_{\theta\theta}^{(3)}}{S_0 \cos 2\theta} &= \frac{B(1+\nu_u)}{3(1-\nu_u)} C_1 \left[ \frac{1}{\lambda r} K_1(\lambda r) + \left( 1 + \frac{6}{(\lambda r)^2} \right) K_2(\lambda r) \right] \\ &\quad + 3C_3 \frac{a^4}{r^4} \end{aligned} \quad (4.69)$$

$$\begin{aligned} \frac{s\bar{\sigma}_{r\theta}^{(3)}}{S_0 \sin 2\theta} &= \frac{2B(1+\nu_u)}{3(1-\nu_u)} C_1 \left[ \frac{1}{\lambda r} K_1(\lambda r) + \frac{3}{(\lambda r)^2} K_2(\lambda r) \right] - \frac{C_2}{2(1-\nu_u)} \frac{a^2}{r^2} \\ &\quad - 3C_3 \frac{a^4}{r^4} \end{aligned} \quad (4.70)$$

$$\frac{s\bar{p}^{(3)}}{S_0 \cos 2\theta} = \frac{B^2(1-\nu)(1+\nu_u)^2}{9(1-\nu_u)(\nu_u-\nu)} C_1 K_2(\lambda r) + \frac{B(1+\nu_u)C_2}{3(1-\nu_u)} \frac{a^2}{r^2} \quad (4.71)$$

where  $\lambda^2 = s/c^f$ , and  $C_1, C_2, C_3$  are constants obtained from boundary conditions:

$$C_1 = \frac{12\lambda a (1 - \nu_u) (\nu_u - \nu)}{B (1 + \nu_u) (D_2 - D_1)} \quad (4.72)$$

$$C_2 = \frac{4(1 - \nu_u) D_2}{D_2 - D_1} \quad (4.73)$$

$$C_3 = \frac{\lambda a (D_2 + D_1) + 8(\nu_u - \nu) K_2(\lambda a)}{\lambda a (D_2 - D_1)} \quad (4.74)$$

## Solution for Loading Mode 2

### Temperature

By ignoring the non-linear coupling term in Equation (3.45), the thermal diffusivity equation deteriorates to a classical heat conduction equation which has the following form in a polar coordinate system:

$$\frac{\partial^2 T}{\partial r^2} + \frac{1}{r} \frac{\partial T}{\partial r} = \frac{1}{c^T} \frac{\partial T}{\partial t} \quad (4.75)$$

The equation is decoupled from the fluid and displacement field equations and can be solved with the following boundary and initial conditions:

$$T = (T_m - T_0)H(t) \quad \text{at } r = a, \quad (4.76)$$

$$T = 0 \quad \text{at } r = \infty, \quad (4.77)$$

Transforming (4.75) to (4.77) into the Laplace domain:

$$\frac{\partial^2 \bar{T}}{\partial r^2} + \frac{1}{r} \frac{\partial \bar{T}}{\partial r} - q^2 = 0 \quad (4.78)$$

$$\bar{T} = (T_m - T_0)/s, \quad \text{at } r = a \text{ and } t > 0 \quad (4.79)$$

$$\bar{T} = 0, \quad \text{at } r = \infty \text{ or } t \leq 0 \quad (4.80)$$

where  $q^2 = s/c^T$ .

The solution for this problem can be found in Carslaw and Jaeger[31]; *i.e.*

$$\bar{T}^{(2)} = \frac{H(t)(T_m - T_0)}{s} \frac{K_0(qr)}{K_0(qa)} \quad (4.81)$$

where  $K_n$  is the modified Bessel function of the second kind of order  $n$ .

Inverting this solution into the time domain,

$$T(r, t)^{(2)} = H(t)(T_m - T_0) \left[ 1 - \frac{2}{\pi} \int_0^\infty e^{-c^T \zeta^2 t} \frac{J_0(\zeta a) Y_0(\zeta r) - Y_0(\zeta a) J_0(\zeta r)}{J_0^2(\zeta a) + Y_0^2(\zeta a)} \frac{d\zeta}{\zeta} \right] \quad (4.82)$$

and introducing the dimensionless variables  $\tau = c^T t/a^2$  and  $R = r/a$ , the expression (4.82) becomes:

$$T(R, \tau)^{(2)} = H(t)(T_m - T_0) \left[ 1 - \frac{2}{\pi} \int_0^\infty e^{-\tau \zeta^2} \frac{J_0(\zeta) Y_0(\zeta R) - Y_0(\zeta) J_0(\zeta R)}{J_0^2(\zeta) + Y_0^2(\zeta)} \frac{d\zeta}{\zeta} \right] \quad (4.83)$$

For  $\tau < 0.3$ , and relatively small  $R$  values, the integral (4.83) can be evaluated by the following asymptotic solution[83]:

$$T(R, \tau)^{(2)} = H(t)(T_m - T_0) \left[ R^{-\frac{1}{2}} \operatorname{erf} c \frac{R-1}{2\tau^{\frac{1}{2}}} + \frac{\tau^{\frac{1}{2}}}{4R^{\frac{1}{2}}} \left( 1 - \frac{1}{R} \right) i \operatorname{erf} c \frac{R-1}{2\tau^{\frac{1}{2}}} - \left( \frac{7}{32} + \frac{1}{16R} - \frac{9}{32R^2} \right) \frac{\tau}{R^{\frac{1}{2}}} i^2 \operatorname{erf} c \frac{R-1}{2\tau^{\frac{1}{2}}} + \dots \right] \quad (4.84)$$

where,

$$i^n \operatorname{erf} cx = \int_x^\infty i^{n-1} \operatorname{erf} c\zeta d\zeta, \quad n = 1, 2, \dots, \quad (4.85)$$

$$i \operatorname{erf} cx = \frac{1}{\sqrt{\pi}} e^{-x^2} - x \operatorname{erf} cx \quad (4.86)$$

$$i^2 \operatorname{erf} cx = \frac{1}{4} \left[ (1 + 2x^2) \operatorname{erf} cx - \frac{2x}{\sqrt{\pi}} e^{-x^2} \right] \quad (4.87)$$

### Pore Pressure

Because of the axisymmetric loading condition in loading mode 2, the pore pressure diffusivity equation (3.40) can further be decoupled from the displacement field equation as derived in section 4.2.1. In a cylindrical coordinate system, the pore pressure diffusivity equation (4.16) (dimensionless form (4.46)) has the following form:

$$\frac{\partial^2 p}{\partial r^2} + \frac{1}{r} \frac{\partial p}{\partial r} = \frac{1}{c^f} \frac{\partial p}{\partial t} - \frac{c^f T}{c^f} \frac{\partial T}{\partial t} \quad (4.88)$$

For a given temperature distribution, the pore pressure induced by both excavation and applying the mud pressure can be obtained by solving the non-homogeneous pore pressure diffusivity equation with the following initial and boundary conditions:

$$p = (p_m - p_0) H(t) \quad \text{at } r = a, \quad (4.89)$$

$$p = 0 \quad \text{at } r = \infty, \quad (4.90)$$

Transforming Equations (4.88) to (4.90) into the Laplace domain:

$$\frac{\partial^2 \bar{p}}{\partial r^2} + \frac{1}{r} \frac{\partial \bar{p}}{\partial r} - \lambda^2 \bar{p} = -\xi^2 \bar{T} \quad (4.91)$$

where  $\xi^2 = sc^{fT}/c^f$ .

$$\bar{p} = (p_m - p_0)/s, \quad \text{at } r = a \text{ and } t > 0$$

$$\bar{p} = 0, \quad \text{at } r = \infty \text{ or } t \leq 0$$

The solution for the homogeneous equation of Equation (4.91) has the same form as (4.81):

$$\bar{p} = \frac{H(t) (p_m - p_0) K_0(\lambda r)}{s K_0(\lambda a)} \quad (4.92)$$

It can be verified that:

$$\bar{p}_p = \frac{c^{fT} \bar{T}}{1 - c^f/c^T} \quad (4.93)$$

is a special solution of Equation (4.91)[155]. The final solution for non-homogeneous equation (4.91) in the Laplace domain is the summation of the above two solutions.

By applying the boundary condition, the solution has the following form:

$$\bar{p}^{(2)} = \frac{H(t)}{s} \left[ (p_m - p_0) - \frac{c^{fT}(T_m - T_0)}{1 - c^f/c^T} \right] \frac{K_0(\lambda r)}{K_0(\lambda a)} + \frac{c^{fT} H(t)(T_m - T_0)}{(1 - c^f/c^T) s} \frac{K_0(qr)}{K_0(qa)} \quad (4.94)$$

Inverted into time domain, the following expression can be found:

$$p(r, t)^{(2)} = H(t) \left[ (p_m - p_0) - \frac{c^{fT}(T_m - T_0)}{1 - c^f/c^T} \right] \times \\ \left[ 1 - \frac{2}{\pi} \int_0^\infty e^{-c^f \zeta^2 t} \frac{J_0(\zeta a) Y_0(\zeta r) - Y_0(\zeta a) J_0(\zeta r)}{J_0^2(\zeta a) + Y_0^2(\zeta a)} \frac{d\zeta}{\zeta} \right] + \frac{c^{fT} H(t)(T_m - T_0)}{1 - c^f/c^T} \times$$

$$\times \left[ 1 - \frac{2}{\pi} \int_0^\infty e^{-c^T \zeta^2 t} \frac{J_0(\zeta a) Y_0(\zeta r) - Y_0(\zeta a) J_0(\zeta r) d\zeta}{J_0^2(\zeta a) + Y_0^2(\zeta a)} \frac{d\zeta}{\zeta} \right] \quad (4.95)$$

Introducing the dimensionless time  $\tau^f = c^f T / a^2$ , and for small value of  $\tau^f$ ,  $\tau$ , and  $R$ , the pore pressure distribution can be evaluated by the following formula:

$$\begin{aligned} p(R, \tau^f, \tau)^{(2)} &= H(t) \left[ (p_m - p_0) - \frac{c^f T (T_m - T_0)}{1 - c^f / c^T} \right] \left[ R^{\frac{1}{2}} \operatorname{erf} c \frac{R-1}{2\tau^{\frac{1}{2}}} + \frac{\tau^{\frac{1}{2}}}{4R^{\frac{1}{2}}} \left( 1 - \frac{1}{R} \right) \times \right. \\ &\quad \left. i \operatorname{erf} c \frac{R-1}{2\tau^{\frac{1}{2}}} - \left( \frac{7}{32} + \frac{1}{6R} - \frac{9}{32R^2} \right) \frac{\tau^f}{R^{\frac{1}{2}}} i^2 \operatorname{erf} c \frac{R-1}{2\tau^{\frac{1}{2}}} + \dots \right] \\ &\quad + \frac{c^f T H(t) (T_m - T_0)}{1 - c^f / c^T} \left[ R^{\frac{1}{2}} \operatorname{erf} c \frac{R-1}{2\tau^{\frac{1}{2}}} + \frac{\tau^{\frac{1}{2}}}{4R^{\frac{1}{2}}} \left( 1 - \frac{1}{R} \right) i \operatorname{erf} c \frac{R-1}{2\tau^{\frac{1}{2}}} \right. \\ &\quad \left. - \left( \frac{7}{32} + \frac{1}{6R} - \frac{9}{32R^2} \right) \frac{\tau}{R^{\frac{1}{2}}} i^2 \operatorname{erf} c \frac{R-1}{2\tau^{\frac{1}{2}}} + \dots \right] \quad (4.96) \end{aligned}$$

Note that in Equation (4.94), the factor  $(1 - c^f / c^T)$  appears in the denominator, which would appear to have a singular behavior when fluid diffusivity is identical to thermal diffusivity. However, taking the limit of Equation (4.94) :

$$\lim_{c^T \rightarrow c^f} \frac{H(t)}{s} \left[ (p_m - p_0) - \frac{c^f T (T_m - T_0)}{1 - c^f / c^T} \right] \frac{K_0(\lambda r)}{K_0(\lambda a)} + \frac{c^f T H(t) (T_m - T_0)}{(1 - c^f / c^T) s} \frac{K_0(qr)}{K_0(qa)} \quad (4.97)$$

yields the following finite solution for the pore pressure:

$$\bar{p}^{(2)} = \frac{H(t)}{s} (p_m - p_0) \frac{K_0(\lambda r)}{K_0(\lambda a)} + \frac{H(t) \xi^2 (T_m - T_0)}{s 2\lambda} \left( \frac{r K_1(\lambda r)}{K_0(\lambda a)} - \frac{a K_1(\lambda a) K_0(\lambda r)}{(K_0(\lambda a))^2} \right) \quad (4.98)$$

In fact, solution (4.94) goes smoothly through  $c^f / c^T = 1$ , which means no special physical phenomena will occur when thermal diffusivity and fluid diffusivity are identical.

Alternatively, the solution given by Equation (4.98) can be directly obtained from (4.91) as following:

Replacing  $q$  by  $\lambda$  in (4.81), then substituting into (4.91), one obtains:

$$\frac{\partial^2 \bar{p}}{\partial r^2} + \frac{1}{r} \frac{\partial \bar{p}}{\partial r} - \lambda^2 \bar{p} = -\xi^2 \frac{H(t) (T_m - T_0)}{s} \frac{K_0(\lambda r)}{K_0(\lambda a)} \quad (4.99)$$

The equation (4.99) is satisfied by a special solution of:

$$\bar{p}_{ps} = \frac{\xi^2 T_m - T_0}{2\lambda} \frac{r K_1(\lambda r)}{s K_0(\lambda a)} \quad (4.100)$$

A complete solution of pore pressure is obtained by combining the homogenous solution of Equation (4.99), with its special solution, Equation (4.100):

$$\bar{p}^{(2)} = AK_0(\lambda r) + \frac{H(t)\xi^2 (T_m - T_0)}{s} \frac{r K_1(\lambda r)}{2\lambda K_0(\lambda a)} \quad (4.101)$$

Substituting the boundary condition (4.59) into (4.101) yields exactly Equation (4.98).

### Stresses

Solving (3.35), the radial displacement  $u_r$  can readily be obtained:

$$u_r = \frac{A}{r} + \frac{(1-2\nu)\alpha}{2G(1-\nu)} \frac{1}{r} \int_a^r \varsigma p(\varsigma, t) d\varsigma + \frac{\alpha_m^T (1+\nu)}{3(1-\nu)} \frac{1}{r} \int_a^r \varsigma T(\varsigma, t) d\varsigma \quad (4.102)$$

The stress components in a polar coordinate system can be derived by obtaining the relevant strain components from Equation (4.102) and then substituting into constitutive equation (3.10):

$$\sigma_{rr} = -2G \frac{A}{r^2} - \frac{(1-2\nu)\alpha}{(1-\nu)} \frac{1}{r^2} \int_a^r \varsigma p(\varsigma, t) d\varsigma - \frac{2G\alpha_m^T (1+\nu)}{3(1-\nu)} \frac{1}{r^2} \int_a^r \varsigma T(\varsigma, t) d\varsigma \quad (4.103)$$

$$\begin{aligned} \sigma_{\theta\theta} = & 2G \frac{A}{r^2} + \frac{(1-2\nu)\alpha}{(1-\nu)} \frac{1}{r^2} \int_a^r \varsigma p(\varsigma, t) d\varsigma + \frac{2G\alpha_m^T (1+\nu)}{3(1-\nu)} \frac{1}{r^2} \int_a^r \varsigma T(\varsigma, t) d\varsigma \\ & - \frac{(1-2\nu)\alpha}{(1-\nu)} p - \frac{2G\alpha_m^T (1+\nu)}{3(1-\nu)} T \end{aligned} \quad (4.104)$$

$$\sigma_{r\theta} = 0 \quad (4.105)$$

By applying the boundary conditions (4.57) for mode 2 to Equation (4.103),  $A$  is zero. Laplace transforming Equations (4.103) and (4.104), then substituting Equations (4.81) and (4.94) or (4.98) into them, the stress distributions for mode 2 in the Laplace domain can be solved:

$$s\bar{\sigma}_{rr}^{(2)} = \frac{(1-2\nu)\alpha}{(1-\nu)} \left\{ \left[ (p_m - p_0) - \frac{c^f T (T_m - T_0)}{1 - c^f/c^T} \right] \left[ \frac{K_1(\lambda r)}{r\lambda K_0(\lambda a)} - \frac{a K_1(\lambda a)}{r^2 \lambda K_0(\lambda a)} \right] + \right.$$

$$\begin{aligned} & \left. \frac{c^{fT}(T_m - T_0)}{1 - c^f/c^T} \left[ \frac{K_1(qr)}{rqK_0(qa)} - \frac{aK_1(qa)}{r^2qK_0(qa)} \right] \right\} \\ & + \frac{2G\alpha_m^T(1 + \nu)}{3(1 - \nu)}(T_m - T_0) \left[ \frac{K_1(qr)}{rqK_0(qa)} - \frac{aK_1(qa)}{r^2qK_0(qa)} \right] \end{aligned} \quad (4.106)$$

$$\begin{aligned} s\bar{\sigma}_{\theta\theta}^{(2)} &= -\frac{(1 - 2\nu)\alpha}{(1 - \nu)} \left\{ \left[ (p_w - p_0) - \frac{c^{fT}(T_m - T_0)}{1 - c^f/c^T} \right] \left[ \frac{K_1(\lambda r)}{r\lambda K_0(\lambda a)} - \frac{aK_1(\lambda a)}{r^2\lambda K_0(\lambda a)} \right. \right. \\ & \left. \left. + \frac{K_0(\lambda r)}{K_0(\lambda a)} \right] + \frac{c^{fT}(T_m - T_0)}{1 - c^f/c^T} \left[ \frac{K_1(qr)}{rqK_0(qa)} - \frac{aK_1(qa)}{r^2qK_0(qa)} + \frac{K_0(qr)}{K_0(qa)} \right] \right\} \\ & - \frac{2G\alpha_m^T(1 + \nu)}{3(1 - \nu)}(T_m - T_0) \left[ \frac{K_1(qr)}{rqK_0(qa)} - \frac{aK_1(qa)}{r^2qK_0(qa)} + \frac{K_0(qr)}{K_0(qa)} \right] \end{aligned} \quad (4.107)$$

For  $c^f = c^T$ , one obtains:

$$\begin{aligned} s\bar{\sigma}_{rr}^{(2)} &= \left[ \frac{2G\alpha_m^T(1 + \nu)}{3(1 - \nu)}(T_m - T_0) - \frac{(1 - 2\nu)\alpha}{(1 - \nu)}(p_m - p_0) \right] \left[ \frac{K_1(\lambda r)}{r\lambda K_0(\lambda a)} - \frac{aK_1(\lambda a)}{r^2\lambda K_0(\lambda a)} \right] \\ & - \frac{(1 - 2\nu)\alpha\xi^2}{(1 - \nu)}(T_m - T_0) \left[ \frac{K_2(\lambda r)}{\lambda^2 K_0(\lambda a)} - \frac{a^2 K_2(\lambda a)}{r^2\lambda^2 K_0(\lambda a)} \right] \end{aligned} \quad (4.108)$$

$$\begin{aligned} s\bar{\sigma}_{\theta\theta}^{(2)} &= -\frac{(1 - 2\nu)\alpha}{(1 - \nu)} \left\{ (p_w - p_0) \left[ \frac{K_1(\lambda r)}{r\lambda K_0(\lambda a)} - \frac{aK_1(\lambda a)}{r^2\lambda K_0(\lambda a)} \right. \right. \\ & \left. \left. + \frac{K_0(\lambda r)}{K_0(\lambda a)} \right] + \xi^2(T_m - T_0) \left[ \frac{K_2(\lambda r)}{2\lambda^2 K_0(\lambda a)} - \frac{a^2 K_2(\lambda a)}{2r^2\lambda^2 K_0(\lambda a)} + \frac{rK_1(\lambda r)}{2\lambda K_0(\lambda a)} \right] \right\} \\ & - \frac{2G\alpha_m^T(1 + \nu)}{3(1 - \nu)}(T_m - T_0) \left[ \frac{K_1(\lambda r)}{r\lambda K_0(\lambda a)} - \frac{aK_1(\lambda a)}{r^2\lambda K_0(\lambda a)} + \frac{K_0(\lambda r)}{K_0(\lambda a)} \right] \end{aligned} \quad (4.109)$$

### Final Solution

The solutions in the time domain for large values of  $\tau$  and  $R$  for temperature and pore pressure distribution Equations (4.81), (4.94) and (4.98), and stress distributions for loading modes 2 and 3, can be obtained by directly applying numerical Laplace inversion methods such as Stehfest's algorithm[143].

The final solution for temperature, pore pressure and stress distribution for the problem defined in Figure 4.1 can be obtained by superimposing solutions from modes 1 to 3 onto the original stress and pore pressure fields:

$$\sigma_{rr} = -P_0 + S_0 \cos 2\theta + \sigma_{rr}^{(1)} + \sigma_{rr}^{(2)} + \sigma_{rr}^{(3)} \quad (4.110)$$

$$\sigma_{\theta\theta} = -P_0 - S_0 \cos 2\theta + \sigma_{\theta\theta}^{(1)} + \sigma_{\theta\theta}^{(2)} + \sigma_{\theta\theta}^{(3)} \quad (4.111)$$

$$\sigma_{zz} = \sigma_z + \nu \left( \sigma_{rr}^{(1)} + \sigma_{rr}^{(2)} + \sigma_{rr}^{(3)} + \sigma_{\theta\theta}^{(1)} + \sigma_{\theta\theta}^{(2)} + \sigma_{\theta\theta}^{(3)} \right) - \alpha (1 - 2\nu) \left( p^{(2)} + p^{(3)} \right) \quad (4.112)$$

$$\sigma_{r\theta} = -S_0 \sin 2\theta + \sigma_{r\theta}^{(3)} \quad (4.113)$$

$$p = p_0 + p^{(2)} + p^{(3)} \quad (4.114)$$

$$T = T_0 + T^{(2)} \quad (4.115)$$

where the superscript <sup>(i)</sup> represents the solution for loading modes i.

## 4.3.2 Inclined Boreholes

This section presents the analytical solution for the temperature, pore pressure and stress distribution around an inclined borehole, *i.e.*, a borehole with its axis arbitrarily oriented with respect to the in-situ principal stresses. The problem is solved by the superposition of three fundamental problems: a thermoporoelastic plane-strain problem; an elastic uni-axial stress problem; and an elastic anti-plane shear problem.

### 4.3.2.1 Problem Definition

Figure 4.2-(a) is the schematic diagram of an inclined borehole.  $S_{x'}$ ,  $S_{y'}$  and  $S_{z'}$  are the in-situ principal compressive stresses;  $p_0$  and  $T_0$  are virgin formation pore pressure and temperature; and  $p_m$  and  $T_m$  are the wellbore pressure and temperature applied by the drilling fluid, respectively. The local borehole coordinate system,  $xyz$ , with its  $z$ -axis coinciding with the borehole axis, are related to the global coordinate system,  $x'y'z'$ , by an azimuth angle,  $\varphi_{z'}$ , formed by rotating an angle  $\varphi_z$

about the  $z'$ -axis, and an inclination angle,  $\varphi_y$ , formed by further rotating an angle  $\varphi_y$  about the  $y$ -axis. The borehole coordinate system  $xyz$  is selected as the solution domain for the conveniences of borehole failure analyses. The in-situ principal stresses,  $S_{x'}, S_{y'}, S_{z'}$ , can be converted to the stresses under borehole coordinate system,  $S_x, S_y, S_z, S_{xy}, S_{yz}, S_{zx}$ , via the transformation given by Fjær *et al.*[61], as shown in Figure 4.2-(b).

The following boundary conditions are assumed at the instant after drilling:

In the far field ( $r \rightarrow \infty$ ):

$$\left\{ \begin{array}{l} \sigma_{xx} = -S_x \\ \sigma_{yy} = -S_y \\ \sigma_{zz} = -S_z \\ \sigma_{xy} = -S_{xy} \\ \sigma_{yz} = -S_{yz} \\ \sigma_{zx} = -S_{zx} \\ p = p_0 \\ T = T_0 \end{array} \right. \quad (4.116)$$

Along the borehole wall ( $r = a$ ):

$$\left\{ \begin{array}{l} \sigma_{rr} = -S_r H(-t) \\ \sigma_{r\theta} = -S_{r\theta} H(-t) \\ \sigma_{rz} = -S_{rz} H(-t) \\ p = -p_0 H(-t) + p_m H(t) \\ T = T_m H(t) - T_0 \end{array} \right. \quad (4.117)$$

where  $S_r$ ,  $S_{r\theta}$  and  $S_{rz}$  are the far-field compressive stress components in cylindrical coordinates.  $H(t)$  denotes the Heaviside unit step function (4.65), and  $H(-t)$  is defined as  $1 - H(t)$  such that:

$$\left\{ \begin{array}{ll} H(-t) = 1 & \text{for } t \leq 0 \\ H(-t) = 0 & \text{for } t > 0 \end{array} \right. \quad (4.118)$$

### 4.3.2.2 Loading Decomposition

For a linear thermoporoelastic system defined by (3.35), (3.40) to (3.45) without the convective heat transfer term, the problem defined in Figure 4.2 can be solved by the superposition technique. Similar to the procedures in Cui *et al.*[43], the original problem can be decomposed into three sub-problems as shown in Figure 4.3:

#### Problem I

As shown in Figure 4.3-(b), problem I is a thermoporoelastic plane-strain problem. The boundary conditions for this problem are:

In the far field ( $r \rightarrow \infty$ ):

$$\left\{ \begin{array}{l} \sigma_{xx} = -S_x \\ \sigma_{yy} = -S_y \\ \sigma_{zz} = -\nu(S_x + S_y) - \alpha(1 - 2\nu)p_0 - \frac{2G(1+\nu)}{3}\alpha_m^T T_0 \\ \sigma_{xy} = -S_{xy} \\ \sigma_{yz} = \sigma_{zx} = 0 \\ p = p_0 \\ T = T_0 \end{array} \right. \quad (4.119)$$

Along the borehole wall ( $r = a$ ):

$$\left\{ \begin{array}{l} \sigma_{rr} = -S_r H(-t) \\ \sigma_{r\theta} = -S_{r\theta} H(-t) \\ \sigma_{rz} = 0 \\ p = -p_0 H(-t) + p_m H(t) \\ T = T_m H(t) - T_0 \end{array} \right. \quad (4.120)$$

#### Problem II

Problem II, as shown in Figure 4.3-(c), is a uniaxial loading problem. The boundary conditions for this problem are:

In the far field ( $r \rightarrow \infty$ ) :

$$\begin{cases} \sigma_{zz} = -S_z + [\nu(S_x + S_y) + \alpha(1 - 2\nu)p_0 + \frac{2G(1+\nu)}{3}\alpha_m T_0] \\ \sigma_{xx} = \sigma_{yy} = \sigma_{xy} = \sigma_{yz} = \sigma_{zx} = p = T = 0 \end{cases} \quad (4.121)$$

Along the borehole wall ( $r = a$ ) :

$$\sigma_{rr} = \sigma_{r\theta} = \sigma_{rz} = p = T = 0 \quad (4.122)$$

### Problem III

Problem III, as shown in Figure 4.3-(d), is an anti-plane shear problem. The boundary conditions for this problem are:

In the far field ( $r \rightarrow \infty$ ) :

$$\begin{cases} \sigma_{xx} = \sigma_{yy} = \sigma_{zz} = \sigma_{xy} = p = T = 0 \\ \sigma_{yz} = -S_{yz} \\ \sigma_{xz} = -S_{xz} \end{cases} \quad (4.123)$$

Along the borehole wall ( $r = a$ ) :

$$\begin{cases} \sigma_{rr} = \sigma_{r\theta} = p = T = 0 \\ \sigma_{rz} = -S_{rz}H(-t) \end{cases} \quad (4.124)$$

Note that the summation of boundary conditions (4.119) to (4.124) reproduces the boundary conditions (4.116) and (4.117).

#### 4.3.2.3 Solutions

##### For Problem I:

The problem defined by boundary conditions (4.119) and (4.120) has the out-of-plane displacement  $u_z$ , fluid flux  $q_z$  and heat flux  $h_z$  vanish. It is a plane strain borehole subjected to a non-hydrostatic stress field, a constant borehole pressure and a constant temperature difference along the borehole wall. The problem can be solved by further decomposing the problem into three sub-loading modes as derived in the last section ((4.110) to (4.115)). Since solutions (4.110) to (4.115) are given in

a coordinate system, assully named as  $x''y''z''$ , with its  $x''$  axis coinciding with the in-plane (the plane that is perpendicular to the borehole axis) minimum principal stress  $\sigma_{x''x''}$  (Figure 4.4), there is an angular difference between the coordinate systems  $xyz$  and  $x''y''z''$ , i.e.

$$\theta_r = \theta - \theta'' \quad (4.125)$$

where  $\theta$  and  $\theta''$  are the polar angles in  $xyz$  and  $x''y''z''$  systems respectively, and,

$$\theta_r = \frac{1}{2} \tan^{-1} \frac{2S_{xy}}{S_x - S_y} \quad (4.126)$$

The in-plane maximum and minimum principal stresses in  $x''y''z''$  coordinates are:

$$\begin{aligned} \sigma_{y''y''} \\ \sigma_{x''x''} \end{aligned} = -\frac{S_x + S_y}{2} \pm \sqrt{\left(\frac{S_x - S_y}{2}\right)^2 + S_{xy}^2} \quad (4.127)$$

The final solution for problem I in a polar coordinate system, complying with the  $x''y''z''$  coordinates, can be expressed as:

$$T^{(I)} = T_0 + T^{(2)} \quad (4.128)$$

$$p^{(I)} = p_0 + p^{(2)} + p^{(3)} \quad (4.129)$$

$$\sigma_{rr}^{(I)} = -P_0 + S_0 \cos 2\theta'' + \sigma_{rr}^{(1)} + \sigma_{rr}^{(2)} + \sigma_{rr}^{(3)} \quad (4.130)$$

$$\sigma_{\theta\theta}^{(I)} = -P_0 - S_0 \cos 2\theta'' + \sigma_{\theta\theta}^{(1)} + \sigma_{\theta\theta}^{(2)} + \sigma_{\theta\theta}^{(3)} \quad (4.131)$$

$$\sigma_{zz}^{(I)} = -2\nu P_0 + \nu \left( \sigma_{rr}^{(1)} + \sigma_{rr}^{(2)} + \sigma_{rr}^{(3)} + \sigma_{\theta\theta}^{(1)} + \sigma_{\theta\theta}^{(2)} + \sigma_{\theta\theta}^{(3)} \right) \quad (4.132)$$

$$-\alpha (1 - 2\nu) p^{(I)} - \frac{2G(1 + \nu)}{3} \alpha_m^T T \quad (4.133)$$

$$\sigma_{r\theta}^{(I)} = -S_0 \sin 2\theta'' + \sigma_{r\theta}^{(3)} \quad (4.134)$$

$$\sigma_{rz}^{(I)} = \sigma_{\theta z}^{(I)} = 0 \quad (4.135)$$

where,

$$P_0 = -\frac{\sigma_{x''x''} + \sigma_{y''y''}}{2} \quad (4.136)$$

$$S_0 = \frac{\sigma_{x''x''} - \sigma_{y''y''}}{2} \quad (4.137)$$

In (4.128) to (4.135), the superscript  $(I)$  represents the solution for Problem I. The expressions for  $T^{(2)}$ ,  $p^{(1)-(2)}$  and  $\sigma_{ij}^{(1)-(3)}$  are the temperature, pore pressure

and stress distribution for sub-loading modes 1 to 3, according to the superscripts (1) to (3). The solution referring to the coordinate system  $xyz$  can be obtained by replacing  $\theta''$  with  $\theta - \theta_r$  in Equations (4.128) to (4.135).

### For Problem II:

Since the boundary conditions at the borehole wall are zero for this problem, as shown in Equation (4.122), the drilling and the following pressurization of the borehole do not arouse any disturbances for this specific problem. *i.e.* the solution is time independent, or, elastic[43]. In fact, it is given by a constant  $\sigma_{zz}$  prevailing everywhere:

$$\sigma_{zz}^{(II)} = -S_z + \left[ \nu (S_x + S_y) + \alpha (1 - 2\nu) p_0 + \frac{2G(1 + \nu)}{3} \alpha_m^T T_0 \right] \quad (4.138)$$

$$\sigma_{rr}^{(II)} = \sigma_{\theta\theta}^{(II)} = \sigma_{r\theta}^{(II)} = \sigma_{rz}^{(II)} = \sigma_{\theta z}^{(II)} = p^{(II)} = T^{(II)} = 0 \quad (4.139)$$

### For Problem III:

For this problem, the stress disturbance due to drilling is introduced by the sudden drop of surface traction  $\sigma_{rz}$  on the borehole wall from  $-S_{rz}$  to zero. Since normal stress is kept unchanged in this anti-plane shear problem, no pore pressure will be generated as a response to the unloading of  $\sigma_{rz}$ ; hence, the solution is again elastic. The solution for this problem can be found in [26]:

$$\sigma_{rz}^{(III)} = -(S_{xz} \cos \theta + S_{yz} \sin \theta) \left[ 1 - \frac{R^2}{r^2} \right] \quad (4.140)$$

$$\sigma_{\theta z}^{(III)} = -(S_{xz} \sin \theta - S_{yz} \cos \theta) \left[ 1 + \frac{R^2}{r^2} \right] \quad (4.141)$$

$$\sigma_{rr}^{(III)} = \sigma_{\theta\theta}^{(III)} = \sigma_{r\theta}^{(III)} = p^{(III)} = T^{(III)} = 0 \quad (4.142)$$

### The Final Solution

Superimposing the solutions from Problems I to III yields the final solution of the overall problem (omitting the zero components):

$$\sigma_{rr} = \sigma_{rr}^{(I)} \quad (4.143)$$

$$\sigma_{\theta\theta} = \sigma_{\theta\theta}^{(I)} \quad (4.144)$$

$$\sigma_{zz} = \sigma_{zz}^{(I)} + \sigma_{zz}^{(II)} \quad (4.145)$$

$$\sigma_{r\theta} = \sigma_{r\theta}^{(I)} \quad (4.146)$$

$$\sigma_{rz} = \sigma_{rz}^{(III)} \quad (4.147)$$

$$\sigma_{\theta z} = \sigma_{\theta z}^{(III)} \quad (4.148)$$

$$p = p^{(I)} \quad (4.149)$$

$$T = T^{(I)} \quad (4.150)$$

### 4.3.3 Thermoelastic Borehole Solutions

Thermoelastic solutions for the stress distributions around an inclined borehole defined in Figure 4.2 can be obtained by superimposing a transient stress distribution term induced by the transient temperature distribution onto Bradley's solution[26]:

$$\begin{aligned} \sigma_{rr} = & \left( \frac{S_x + S_y}{2} \right) \left( 1 - \frac{a^2}{r^2} \right) + \left( \frac{S_x - S_y}{2} \right) \left( 1 + \frac{3a^2}{r^4} - \frac{4a^2}{r^2} \right) \cos 2\theta \\ & + S_{xy} \left( 1 + \frac{3a^2}{r^4} - \frac{4a^2}{r^2} \right) \sin 2\theta + p_m \frac{a^2}{r^2} + \sigma_{rr}^{(T)} \end{aligned} \quad (4.151)$$

$$\begin{aligned} \sigma_{\theta\theta} = & \left( \frac{S_x + S_y}{2} \right) \left( 1 + \frac{a^2}{r^2} \right) - \left( \frac{S_x - S_y}{2} \right) \left( 1 + \frac{3a^2}{r^4} \right) \cos 2\theta \\ & - S_{xy} \left( 1 + \frac{3a^2}{r^4} \right) \sin 2\theta - p_m \frac{a^2}{r^2} + \sigma_{\theta\theta}^{(T)} + \sigma_{\theta\theta}^{(T)} \end{aligned} \quad (4.152)$$

$$\sigma_{zz} = S_z - \nu \left[ 2(S_x - S_y) \frac{a^2}{r^2} \cos 2\theta + 4S_{xy} \frac{a^2}{r^2} \sin 2\theta \right] + \sigma_{zz}^{(T)} \quad (4.153)$$

$$\begin{aligned} \sigma_{r\theta} = & \left( \frac{S_x - S_y}{2} \right) \left( 1 - \frac{3a^2}{r^4} + \frac{2a^2}{r^2} \right) \sin 2\theta + S_{xy} \left( 1 - \frac{3a^2}{r^4} + \frac{2a^2}{r^2} \right) \cos 2\theta \\ & + \sigma_{r\theta}^{(T)} \end{aligned} \quad (4.154)$$

$$\sigma_{\theta z} = (-S_{xz} \sin \theta + S_{yz} \cos \theta) \left( 1 + \frac{a^2}{r^2} \right) + \sigma_{\theta z}^{(T)} \quad (4.155)$$

$$\sigma_{rz} = (S_{xz} \cos \theta + S_{yz} \sin \theta) \left( 1 - \frac{a^2}{r^2} \right) + \sigma_{rz}^{(T)} \quad (4.156)$$

where  $\theta$  is the polar angle in borehole cylindrical coordinate system as shown in Figure 4.2: and:

$$\sigma_{rr}^{(T)} = -\frac{2G\alpha_m^T(1+\nu)}{3(1-\nu)} \frac{1}{r^2} \int_a^r \zeta T(\zeta, t) d\zeta \quad (4.157)$$

$$\sigma_{\theta\theta}^{(T)} = \frac{2G\alpha_m^T(1+\nu)}{3(1-\nu)} \frac{1}{r^2} \int_a^r \zeta T(\zeta, t) d\zeta - \frac{2G\alpha_m^T(1+\nu)}{3(1-\nu)} T \quad (4.158)$$

$$\sigma_{zz}^{(T)} = \nu (\sigma_{rr}^{(T)} + \sigma_{\theta\theta}^{(T)}) \quad (4.159)$$

$$\sigma_{r\theta}^{(T)} = \sigma_{\theta z}^{(T)} = \sigma_{rz}^{(T)} = 0 \quad (4.160)$$

Laplace transforming (4.157) and (4.158), substituting (4.81) into them and integrating, the analytical solutions for (4.157) and (4.158) in the Laplace domain can be obtained:

$$\bar{\sigma}_{rr}^{(T)} = \frac{2G\alpha_m^T(1+\nu)(T_m - T_0)}{3(1-\nu)qsK_0(qa)} \left[ \frac{K_1(qr)}{r} - \frac{aK_1(qa)}{r^2} \right] \quad (4.161)$$

$$\bar{\sigma}_{\theta\theta}^{(T)} = -\frac{2G\alpha_m^T(1+\nu)(T_m - T_0)}{3(1-\nu)qsK_0(qa)} \left[ \frac{K_1(qr)}{r} - \frac{aK_1(qa)}{r^2} \right] \quad (4.162)$$

$$-\frac{2G\alpha_m^T(1+\nu)(T_m - T_0)}{3(1-\nu)s} \frac{K_0(qr)}{K_0(qa)} \quad (4.163)$$

where  $q$  is the same as it was defined in (4.78).

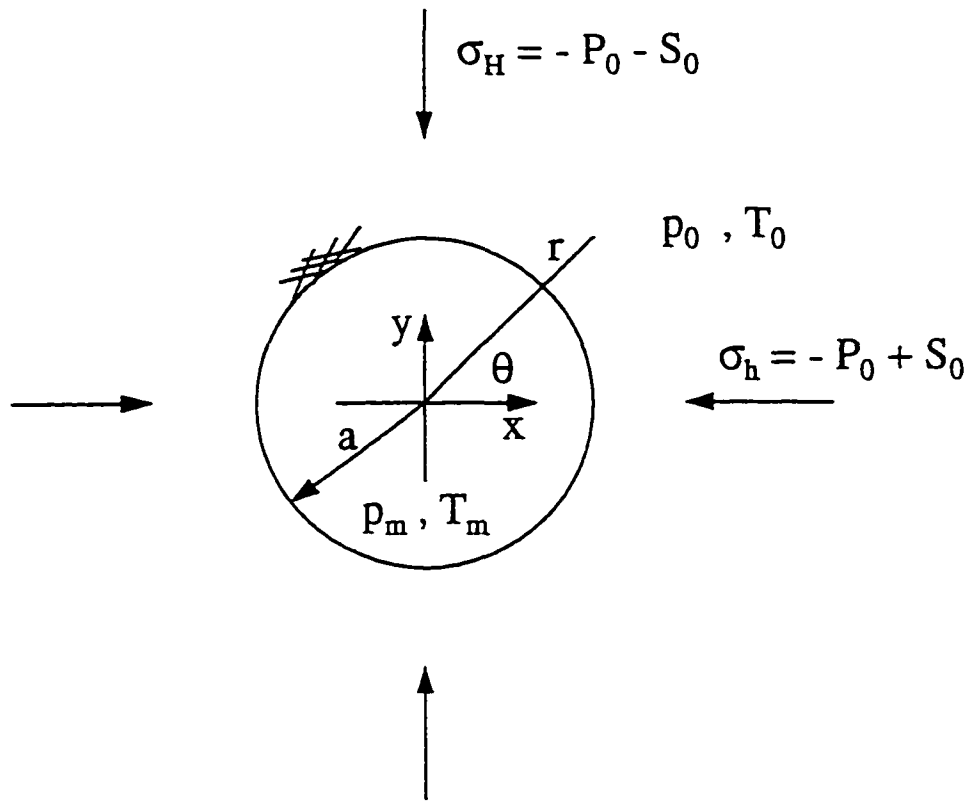
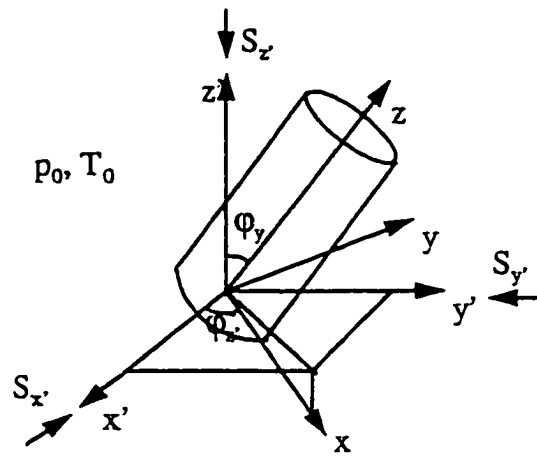
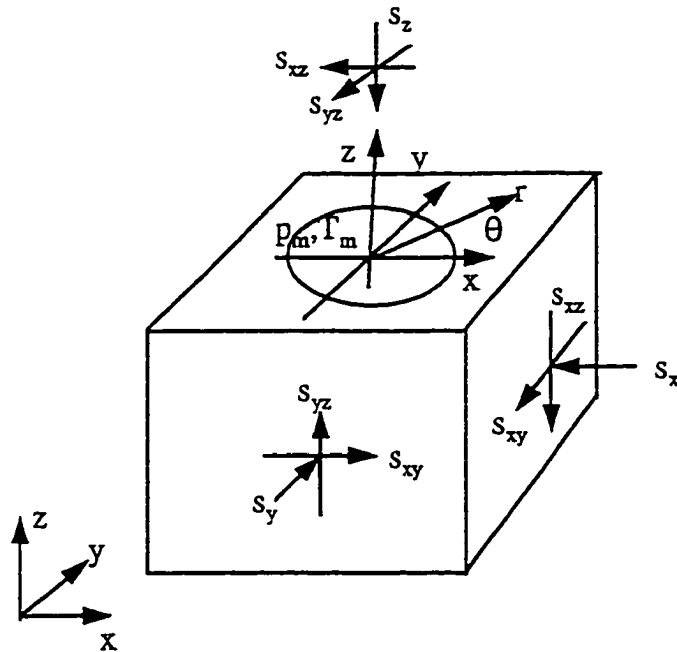


Figure 4.1: Schematic diagram for a borehole subjects to a non-hydrostatic stress fields and wellbore pressure and temperature which are different from initial formation pore pressure and temperature



(a) An inclined borehole



(b) Far-field stresses in borehole coordinate system

Figure 4.2: Schematic diagram of an inclined borehole

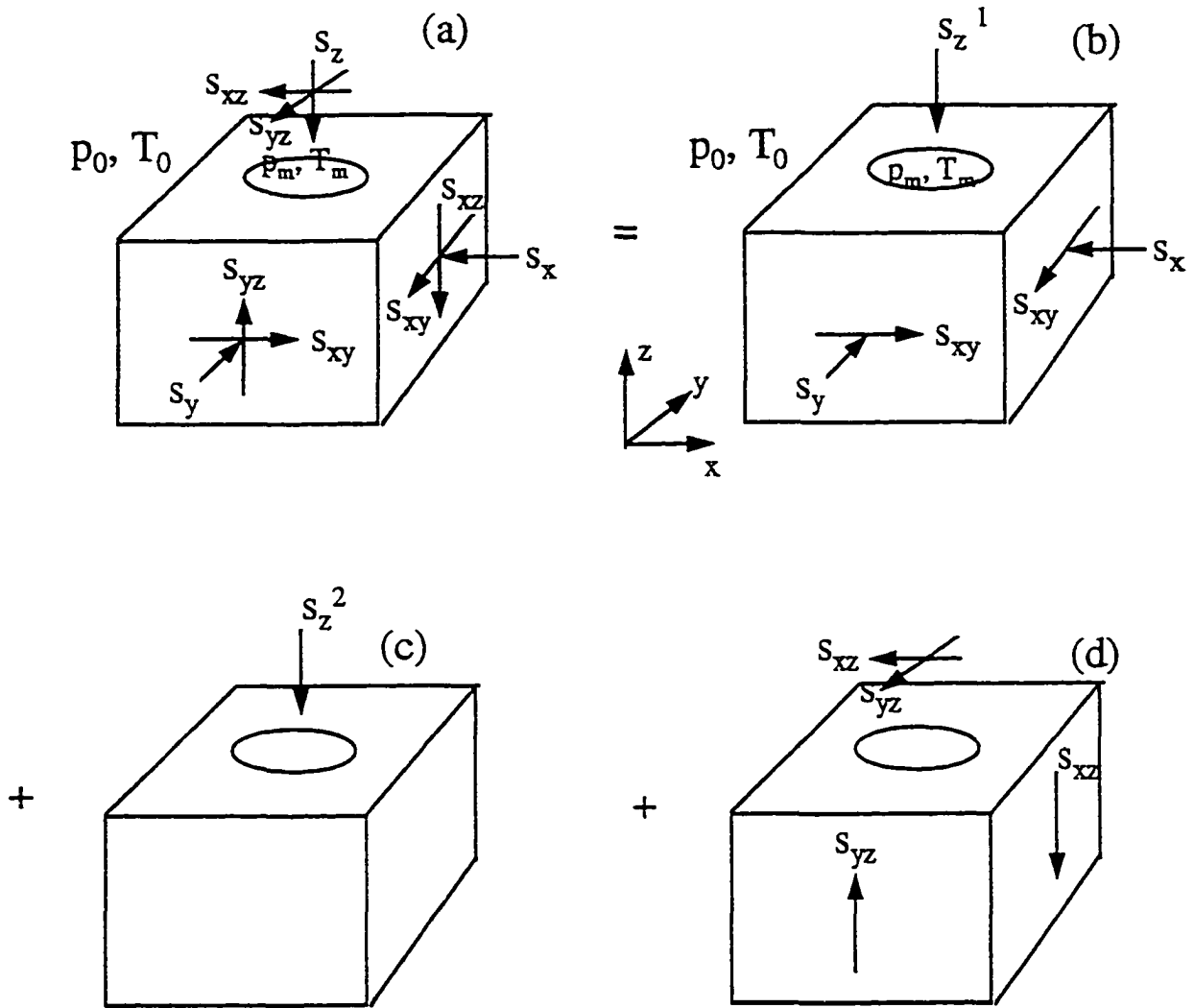


Figure 4.3: Loading decomposition scheme for inclined borehole problem

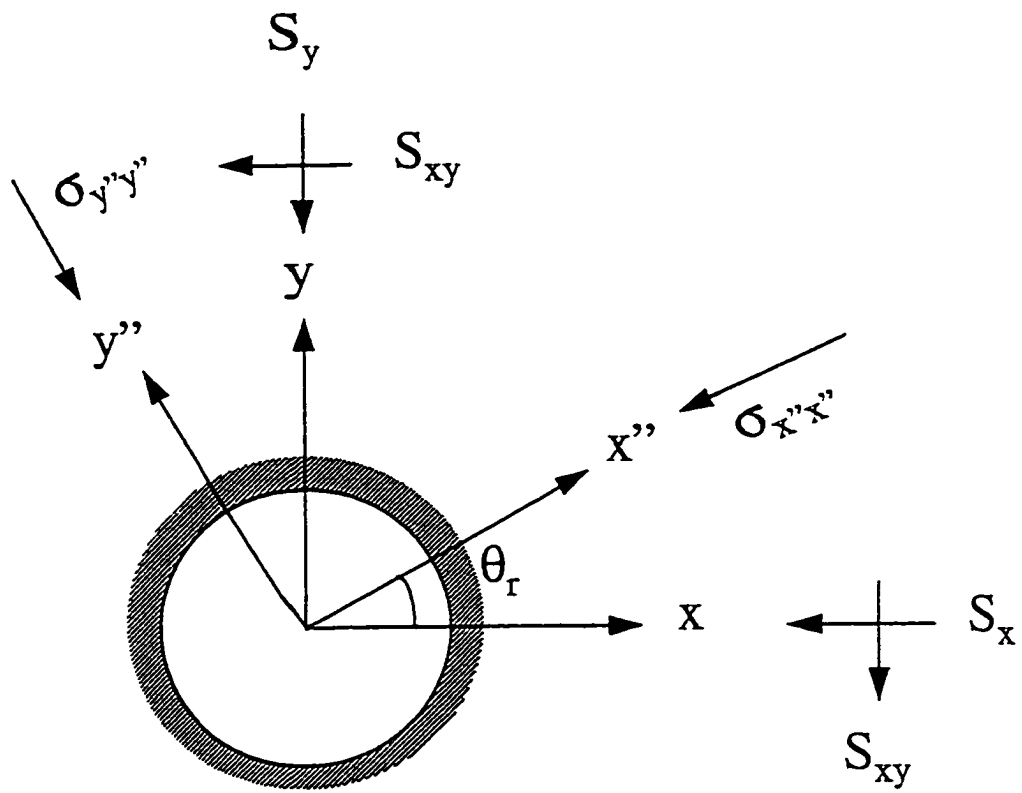


Figure 4.4: Relationship between the two local coordinate systems

# 5 Finite Element Model For Thermoporoelastoplasticity

## 5.1 Introduction

Analytical solutions have the advantages to be computationally stable, accurate and effective, compared to the numerical solutions, and thus, are convenient and cost effective to conduct parametric studies. Significant physical insights to most of the engineering problems are usually revealed from exercising such analytical solutions. They are also recognized as an indispensable tool to validate numerical solutions. However, analytical solutions are generally subjected to many strict assumptions, and only attainable for relatively simple geometries, initial/boundary conditions, and material properties; hence, their abilities to handle real application problems are very limited. When realistic physical conditions such as non-linearity, anisotropy, heterogeneity and complex geometries are to be taken into account, numerical solutions have to be sought.

Being one of the most popular numerical methods, the finite element method is widely used in solving stress/strain/deformation-related engineering problems, because of its better flexibility in dealing with arbitrary geometries, and greater capability of treating higher order boundary conditions, compared to the traditional finite difference method. In this chapter, three-dimensional finite element formulations and the algorithm for fully-coupled, non-linear, thermoporoelastoplastic models derived in Chapter 3 are developed. A two-dimensional version of the finite element program is implemented and extensively validated.

## 5.2 Finite Element Formulae

### 5.2.1 Weak Statement of Governing Equations

The problems posed by governing equations (3.47) to (3.49) with given boundary conditions for each fields can equivalently be expressed in the following integral form:

$$\int_{\Omega} W_i \sigma_{ij,j} d\Omega + \int_{\Gamma^{\sigma}} \bar{W}_i (\sigma_{ij} n_j - \hat{T}_i) d\Gamma = 0 \quad (5.1)$$

$$\begin{aligned} & \int_{\Omega} W_p \left[ \kappa p_{,ii} + \alpha \frac{\partial \varepsilon_{kk}}{\partial t} - (\alpha \alpha_m^T + \alpha_f^T \phi - \alpha_p^T) \frac{dT}{dt} + \frac{1}{M} \frac{dp}{dt} \right] d\Omega \\ & = - \int_{\Gamma^q} \bar{W}_p (\kappa p_{,i} n_i - \bar{q}) d\Gamma \end{aligned} \quad (5.2)$$

$$\begin{aligned} & \int_{\Omega} W_T \left[ k^T T_{,ii} + \kappa \rho_f C_f (T p_{,i})_{,i} + \rho_t C_t \frac{dT}{dt} \right] d\Omega \\ & = - \int_{\Gamma^h} \bar{W}_T [\kappa \rho_f C_f (T p_{,i})_{,i} n_i - k^T T_{,i} n_i - \bar{h}] d\Gamma \end{aligned} \quad (5.3)$$

where  $\Omega$  represents the solution domain;  $\Gamma$  represents the boundary of the solution domain;  $W_x$  and  $\bar{W}_x$  are arbitrary scalar functions;  $\sigma_{ij} n_j = \hat{T}_i$  is the stress boundary condition:  $\kappa p_{,i} n_i = \bar{q}$  and  $\kappa \rho_f C_f (T p_{,i})_{,i} n_i - k^T T_{,i} n_i = \bar{h}$  are, respectively, fluid and heat (both convective and conductive) flow across the boundary.

Using Green's formulae and selecting  $\bar{W}_x = -W_x$ , the weak form of (5.1) to (5.3) are written as:

$$\int_{\Omega} W_{i,j} \sigma_{ij} d\Omega - \int_{\Gamma^{\sigma}} W_i \hat{T}_i d\Gamma = 0 \quad (5.4)$$

$$\begin{aligned} & \int_{\Omega} W_{p,i} \kappa p_{,i} d\Omega + \int_{\Omega} W_p \left[ \alpha \frac{\partial \varepsilon_{kk}}{\partial t} - (\alpha \alpha_m^T + \alpha_f^T \phi - \alpha_p^T) \frac{dT}{dt} + \frac{1}{M} \frac{dp}{dt} \right] d\Omega \quad (5.5) \\ & = \int_{\Gamma^q} W_p \bar{q} d\Gamma \end{aligned} \quad (5.6)$$

$$\int_{\Omega} \left( W_{T,i} k^T T_{,i} + W_{T,i} \kappa \rho_f C_f T p_{,i} + W_T \rho_t C_t \frac{dT}{dt} \right) d\Omega - \int_{\Gamma^h} W_T \bar{h} d\Gamma = 0 \quad (5.7)$$

## 5.2.2 Spatial Discretization

The essence of the finite element method is to discretize the solution domain into an assembly of elements, each with  $n$  nodals; and then approximate the displacement, pressure and temperature fields within each element according to their nodal values and via spatial interpolation functions (shape functions). Adopting the matrix and vector notations, this approximation can be expressed as:

$$\mathbf{u} = \mathbf{N}_u \bar{\mathbf{u}} \quad (5.8)$$

$$p = \mathbf{N}_p \bar{p} \quad (5.9)$$

$$T = \mathbf{N}_T \bar{T} \quad (5.10)$$

where  $\mathbf{u} = \{u_x, u_y, u_z\}^T$ ,  $p$ , and  $T$  are displacement, pore pressure and temperature field variables;

$$\bar{\mathbf{u}} = \left[ \bar{u}_x^{(1)} \quad \bar{u}_y^{(1)} \quad \bar{u}_z^{(1)} \quad \dots \quad \bar{u}_x^{(n_u)} \quad \bar{u}_y^{(n_u)} \quad \bar{u}_z^{(n_u)} \right]^T \quad (5.11)$$

$$\bar{p} = \left[ \bar{p}^{(1)} \quad \dots \quad \bar{p}^{(n_p)} \right]^T \quad (5.12)$$

$$\bar{T} = \left[ \bar{T}^{(1)} \quad \dots \quad \bar{T}^{(n_T)} \right]^T \quad (5.13)$$

are nodal values of displacement, pore pressure and temperature: and.

$$\mathbf{N}_u = \begin{bmatrix} N_u^{(1)} & 0 & 0 & \dots & N_u^{(n_u)} & 0 & 0 \\ 0 & N_u^{(1)} & 0 & \dots & 0 & N_u^{(n_u)} & 0 \\ 0 & 0 & N_u^{(1)} & \dots & 0 & 0 & N_u^{(n_u)} \end{bmatrix} \quad (5.14)$$

$$\mathbf{N}_p = \left[ N_p^{(1)} \quad \dots \quad N_p^{(n_p)} \right] \quad (5.15)$$

$$\mathbf{N}_T = \left[ N_T^{(1)} \quad \dots \quad N_T^{(n_T)} \right] \quad (5.16)$$

are shape function matrices. Superscript  $T$  for a vector or matrix denotes their transposition; and  $n_u$ ,  $n_p$  and  $n_T$  are the nodal numbers in each element for the interpolation of displacement, pore pressure and temperature, respectively.

The gradient relationships can be expressed as:

$$\boldsymbol{\varepsilon} = \mathbf{B}_u \{\bar{u}\} \quad (5.17)$$

$$\nabla \mathbf{p} = \mathbf{B}_p \{\bar{p}\} \quad (5.18)$$

$$\nabla \mathbf{T} = \mathbf{B}_T \{\bar{T}\} \quad (5.19)$$

where  $\mathbf{B}_u$ ,  $\mathbf{B}_p$  and  $\mathbf{B}_T$  are matrices of the gradients:

$$\mathbf{B}_u = \begin{bmatrix} N_{u,x}^{(1)} & 0 & 0 & \dots & N_{u,x}^{(n_u)} & 0 & 0 \\ 0 & N_{u,y}^{(1)} & 0 & \dots & 0 & N_{u,y}^{(n_u)} & 0 \\ 0 & 0 & N_{u,z}^{(1)} & \dots & 0 & 0 & N_{u,z}^{(n_u)} \\ N_{u,y}^{(1)} & N_{u,x}^{(1)} & 0 & \dots & N_{u,y}^{(n_u)} & N_{u,x}^{(n_u)} & 0 \\ 0 & N_{u,z}^{(1)} & N_{u,y}^{(1)} & \dots & 0 & N_{u,z}^{(n_u)} & N_{u,y}^{(n_u)} \\ N_{u,z}^{(1)} & 0 & N_{u,x}^{(1)} & \dots & N_{u,z}^{(n_u)} & 0 & N_{u,x}^{(n_u)} \end{bmatrix} \quad (5.20)$$

$$\mathbf{B}_p = \begin{bmatrix} N_{p,x}^{(1)} & \dots & N_{p,x}^{(n_p)} \\ N_{p,y}^{(1)} & \dots & N_{p,y}^{(n_p)} \\ N_{p,z}^{(1)} & \dots & N_{p,z}^{(n_p)} \end{bmatrix} \quad (5.21)$$

$$\mathbf{B}_T = \begin{bmatrix} N_{T,x}^{(1)} & \dots & N_{T,x}^{(n_T)} \\ N_{T,y}^{(1)} & \dots & N_{T,y}^{(n_T)} \\ N_{T,z}^{(1)} & \dots & N_{T,z}^{(n_T)} \end{bmatrix} \quad (5.22)$$

Substituting into (5.4) to (5.7):

- the constitutive relation for stress and strain ( equation (3.10) in matrix notation):

$$\boldsymbol{\sigma} = \mathbf{D}\boldsymbol{\varepsilon} - \alpha \mathbf{I} p - \alpha_m^T \mathbf{K} \mathbf{T} \quad (5.23)$$

where,

$$\mathbf{I} = [1, 1, 1, 0, 0, 0] \quad (5.24)$$

- the approximate relations (5.8) to (5.10);
- the gradient relations (5.17) to (5.19);

and transforming (5.4) to (5.7) into matrix notations, one obtains the following approximated weak formulae of the governing equations:

$$\int_{\Omega} \nabla \mathbf{W}^T (\mathbf{D}\mathbf{B}_u \bar{\mathbf{u}} - \alpha \mathbf{I} \mathbf{N}_p \bar{\mathbf{p}} - \alpha_m^T \mathbf{K} \mathbf{I} \mathbf{N}_T \bar{\mathbf{T}}) d\Omega - \int_{\Gamma^{\sigma}} \mathbf{W}^T \hat{\mathbf{T}} d\Gamma = 0 \quad (5.25)$$

$$\begin{aligned} & \int_{\Omega} \nabla \mathbf{W}_p^T \kappa \mathbf{B}_p \bar{\mathbf{p}} d\Omega + \int_{\Omega} W_p \alpha \mathbf{I}^T \frac{\partial \bar{\mathbf{u}}}{\partial t} d\Omega - \int_{\Omega} W_p (\alpha \alpha_m^T + \alpha_f^T \phi - \alpha_p^T) \mathbf{N}_T \frac{d\bar{\mathbf{T}}}{dt} d\Omega \\ = & - \int_{\Omega} \frac{W_p}{M} \mathbf{N}_p \frac{d\bar{\mathbf{p}}}{dt} d\Omega + \int_{\Gamma^q} W_p \bar{q} d\Gamma \end{aligned} \quad (5.26)$$

$$\begin{aligned} & \int_{\Omega} \nabla \mathbf{W}_T^T k^T \mathbf{B}_T \bar{\mathbf{T}} d\Omega + \int_{\Omega} \nabla \mathbf{W}_T^T \kappa \rho_f C_f \mathbf{B}_p \bar{\mathbf{p}} \mathbf{N}_T \bar{\mathbf{T}} d\Omega = - \int_{\Omega} W_T \rho_t C_t \mathbf{N}_T \frac{d\bar{\mathbf{T}}}{dt} d\Omega \\ & + \int_{\Gamma^h} W_T \bar{h} d\Gamma \end{aligned} \quad (5.27)$$

Adopting Galerkin's method by which the original shape functions for displacement, pore pressure and temperature are selected as weighting functions  $W$ ,  $W_p$  and  $W_T$ , respectively, the equations (5.25) to (5.27) are converted into the following form:

$$\int_{\Omega} \mathbf{B}_u^T (\mathbf{D}\mathbf{B}_u \bar{\mathbf{u}} - \alpha \mathbf{I} \mathbf{N}_p \bar{\mathbf{p}} - \alpha_m^T \mathbf{K} \mathbf{I} \mathbf{N}_T \bar{\mathbf{T}}) d\Omega - \int_{\Gamma^{\sigma}} \mathbf{N}_u^T \hat{\mathbf{T}} d\Gamma = 0 \quad (5.28)$$

$$\begin{aligned} & \int_{\Omega} \mathbf{B}_p^T \kappa \mathbf{B}_p \bar{\mathbf{p}} d\Omega + \int_{\Omega} \mathbf{N}_p^T \alpha \mathbf{I}^T \mathbf{B}_u \frac{\partial \bar{\mathbf{u}}}{\partial t} d\Omega \\ = & \int_{\Omega} \mathbf{N}_p^T (\alpha \alpha_m^T + \alpha_f^T \phi - \alpha_p^T) \mathbf{N}_T \frac{d\bar{\mathbf{T}}}{dt} d\Omega - \int_{\Omega} \mathbf{N}_p^T \frac{1}{M} \mathbf{N}_p \frac{d\bar{\mathbf{p}}}{dt} d\Omega \end{aligned} \quad (5.29)$$

$$+ \int_{\Gamma^q} \mathbf{N}_p^T \bar{q} d\Gamma \quad (5.30)$$

$$\begin{aligned} & \int_{\Omega} \mathbf{B}_T^T k^T \mathbf{B}_T \bar{\mathbf{T}} d\Omega + \int_{\Omega} \mathbf{B}_T^T \kappa \rho_f C_f \mathbf{B}_p \bar{\mathbf{p}} \mathbf{N}_T \bar{\mathbf{T}} d\Omega + \int_{\Omega} \mathbf{N}_T^T \rho_t C_t \mathbf{N}_T \frac{d\bar{\mathbf{T}}}{dt} d\Omega \\ = & \int_{\Gamma^h} \mathbf{N}_T^T \bar{h} d\Gamma \end{aligned} \quad (5.31)$$

The above system can be re-arranged to present in the following concise form:

$$\mathbf{K}_u \bar{\mathbf{u}} + \mathbf{C}_{up} \bar{\mathbf{p}} + \mathbf{C}_{uT} \bar{\mathbf{T}} = \mathbf{F}_u \quad (5.32)$$

$$\mathbf{K}_p \bar{\mathbf{p}} + \mathbf{C}_{pu} \frac{d\bar{\mathbf{u}}}{dt} + \mathbf{C}_{pT} \frac{d\bar{\mathbf{T}}}{dt} + \mathbf{C}_{pp} \frac{d\bar{\mathbf{p}}}{dt} = \mathbf{F}_p \quad (5.33)$$

$$\mathbf{K}_{cdT}\bar{\mathbf{T}} + \mathbf{K}_{cvT}\bar{\mathbf{T}} + \mathbf{C}_{TT}\frac{d\bar{\mathbf{T}}}{dt} = \mathbf{F}_h \quad (5.34)$$

where.

$$\mathbf{K}_u = \int_{\Omega} \mathbf{B}_u^T \mathbf{D} \mathbf{B}_u d\Omega \quad (5.35)$$

$$\mathbf{C}_{up} = - \int_{\Omega} \mathbf{B}_u^T \alpha \mathbf{I} \mathbf{N}_p d\Omega \quad (5.36)$$

$$\mathbf{C}_{uT} = - \int_{\Omega} \mathbf{B}_u^T \alpha_m^T \mathbf{K} \mathbf{I} \mathbf{N}_T d\Omega \quad (5.37)$$

$$\mathbf{F}_u = \int_{\Gamma^q} \mathbf{N}_u^T \hat{\mathbf{T}} d\Gamma \quad (5.38)$$

$$\mathbf{K}_p = - \int_{\Omega} \mathbf{B}_p^T \kappa \mathbf{B}_p d\Omega \quad (5.39)$$

$$\mathbf{C}_{pu} = - \int_{\Omega} \mathbf{N}_p^T \alpha \mathbf{I}^T \mathbf{B}_u d\Omega = \mathbf{C}_{up}^T \quad (5.40)$$

$$\mathbf{C}_{pt} = \int_{\Omega} \mathbf{N}_p^T (\alpha \alpha_m^T + \alpha_f^T \phi - \alpha_p^T) \mathbf{N}_T d\Omega \quad (5.41)$$

$$\mathbf{C}_{pp} = - \int_{\Omega} \mathbf{N}_p^T \frac{1}{M} \mathbf{N}_p d\Omega \quad (5.42)$$

$$\mathbf{F}_q = - \int_{\Gamma^q} \mathbf{N}_p^T \bar{q} d\Gamma \quad (5.43)$$

$$\mathbf{K}_{cdT} = \int_{\Omega} \mathbf{B}_T^T k^T \mathbf{B}_T d\Omega \quad (5.44)$$

$$\mathbf{K}_{cvT} = \int_{\Omega} \mathbf{B}_T^T \kappa \rho_f C_f \mathbf{B}_p \bar{p} \mathbf{N}_T d\Omega \quad (5.45)$$

$$\mathbf{C}_{TT} = \int_{\Omega} \mathbf{N}_T^T \rho_t C_t \mathbf{N}_T d\Omega \quad (5.46)$$

$$\mathbf{F}_h = \int_{\Gamma^h} \mathbf{N}_T^T \bar{h} d\Gamma \quad (5.47)$$

Differentiating both sides of (5.32) with time and re-arranging, the system (5.32) to (5.34) can be expressed as:

$$\begin{bmatrix} \mathbf{K}_u & \mathbf{C}_{up} & \mathbf{C}_{uT} \\ \mathbf{C}_{pu} & \mathbf{C}_{pp} & \mathbf{C}_{pT} \\ 0 & 0 & \mathbf{C}_{TT} \end{bmatrix} \frac{1}{dt} \begin{bmatrix} d\bar{\mathbf{u}} \\ d\bar{\mathbf{p}} \\ d\bar{\mathbf{T}} \end{bmatrix} + \begin{bmatrix} 0 & 0 & 0 \\ 0 & \mathbf{K}_p & 0 \\ 0 & 0 & \mathbf{K}_{cdp} + \mathbf{K}_{cvp} \end{bmatrix} \begin{bmatrix} \bar{\mathbf{u}} \\ \bar{\mathbf{p}} \\ \bar{\mathbf{T}} \end{bmatrix} = \begin{bmatrix} \frac{\mathbf{F}_u}{dt} \\ \mathbf{F}_q \\ \mathbf{F}_h \end{bmatrix} \quad (5.48)$$

or in a more concise form:

$$\mathbf{B} \frac{d\bar{\mathbf{X}}}{dt} + \mathbf{C}\bar{\mathbf{X}} = \mathbf{F} \quad (5.49)$$

### 5.2.3 Temporal Discretization

Adopting the two-level recurrence scheme for the temporal discretization, the field variables at time  $t$  can be obtained by:

$$\begin{bmatrix} \bar{\mathbf{u}} & \bar{\mathbf{p}} & \bar{\mathbf{T}} \end{bmatrix} = \begin{bmatrix} 1 - \varpi & \varpi \end{bmatrix} \begin{bmatrix} \bar{\mathbf{u}}^{t_k} & \bar{\mathbf{p}}^{t_k} & \bar{\mathbf{T}}^{t_k} \\ \bar{\mathbf{u}}^{t_k + \Delta t_k} & \bar{\mathbf{p}}^{t_k + \Delta t_k} & \bar{\mathbf{T}}^{t_k + \Delta t_k} \end{bmatrix} \quad (5.50)$$

where  $\varpi = (t - t_k) / \Delta t_k$ . When  $\varpi = 0, 1/2, 2/3$ , and  $1$ , the above recurrence scheme corresponds to an explicit, Crank-Nicolson, Galerkin or an implicit schemes in finite difference method, respectively.

Substituting (5.50) into (5.51), replacing  $dt$  by  $\Delta t_k$ , multiplying both sides of (5.51) by  $\Delta t_k$  and re-arranging:

$$\begin{aligned} & \begin{bmatrix} \mathbf{K}_u & \mathbf{C}_{up} & \mathbf{C}_{uT} \\ \mathbf{C}_{pu} & \mathbf{C}_{pp} & \mathbf{C}_{pT} \\ 0 & 0 & \mathbf{C}_{TT} \end{bmatrix} \begin{bmatrix} d\bar{\mathbf{u}} \\ d\bar{\mathbf{p}} \\ d\bar{\mathbf{T}} \end{bmatrix} + \begin{bmatrix} 0 & 0 & 0 \\ 0 & \varpi \mathbf{K}_p \Delta t_k & 0 \\ 0 & 0 & \varpi (\mathbf{K}_{cdp} + \mathbf{K}_{cvp}) \Delta t_k \end{bmatrix} \begin{bmatrix} \bar{\mathbf{u}} \\ \bar{\mathbf{p}} \\ \bar{\mathbf{T}} \end{bmatrix}_{t_k + \Delta t_k} \\ = & \begin{bmatrix} 0 & 0 & 0 \\ 0 & -(1 - \varpi) \mathbf{K}_p \Delta t_k & 0 \\ 0 & 0 & -(1 - \varpi) (\mathbf{K}_{cdp} + \mathbf{K}_{cvp}) \Delta t_k \end{bmatrix} \begin{bmatrix} \bar{\mathbf{u}} \\ \bar{\mathbf{p}} \\ \bar{\mathbf{T}} \end{bmatrix}_{t_k} + \begin{bmatrix} \mathbf{F}_u \\ \mathbf{F}_q \Delta t_k \\ \mathbf{F}_h \Delta t_k \end{bmatrix} \end{aligned} \quad (5.51)$$

Using:

$$\begin{bmatrix} d\bar{\mathbf{u}} \\ d\bar{\mathbf{p}} \\ d\bar{\mathbf{T}} \end{bmatrix} = \begin{bmatrix} \bar{\mathbf{u}}^{t_k + \Delta t_k} - \bar{\mathbf{u}}^{t_k} \\ \bar{\mathbf{p}}^{t_k + \Delta t_k} - \bar{\mathbf{p}}^{t_k} \\ \bar{\mathbf{T}}^{t_k + \Delta t_k} - \bar{\mathbf{T}}^{t_k} \end{bmatrix} \quad (5.52)$$

and re-arranging, (5.51) can finally be presented as:

$$\begin{aligned} & \begin{bmatrix} \mathbf{K}_u & \mathbf{C}_{up} & \mathbf{C}_{uT} \\ \mathbf{C}_{pu} & \mathbf{C}_{pp} + \varpi \mathbf{K}_p \Delta t_k & \mathbf{C}_{pT} \\ 0 & 0 & \mathbf{C}_{TT} + \varpi (\mathbf{K}_{cdp} + \mathbf{K}_{cvp}) \Delta t_k \end{bmatrix} \begin{bmatrix} \bar{\mathbf{u}} \\ \bar{\mathbf{p}} \\ \bar{\mathbf{T}} \end{bmatrix}_{t_k + \Delta t_k} \\ = & \begin{bmatrix} \mathbf{K}_u & \mathbf{C}_{up} & \mathbf{C}_{uT} \\ \mathbf{C}_{pu} & \mathbf{C}_{pp} - (1 - \varpi) \mathbf{K}_p \Delta t_k & \mathbf{C}_{pT} \\ 0 & 0 & \mathbf{C}_{TT} - (1 - \varpi) (\mathbf{K}_{cdp} + \mathbf{K}_{cvp}) \Delta t_k \end{bmatrix} \begin{bmatrix} \bar{\mathbf{u}} \\ \bar{\mathbf{p}} \\ \bar{\mathbf{T}} \end{bmatrix}_{t_k} \end{aligned}$$

$$+ \begin{Bmatrix} \mathbf{F}_u \\ \mathbf{F}_q \Delta t_k \\ \mathbf{F}_h \Delta t_k \end{Bmatrix} \quad (5.53)$$

or in a more concise form:

$$[\mathbf{B} + \varpi \Delta t_k \mathbf{C}] \mathbf{X}_{t_k + \Delta t_k} = [\mathbf{B} - \Delta t_k (1 - \varpi) \mathbf{C}] \mathbf{X}_{t_k} + \mathbf{F} \quad (5.54)$$

### 5.2.4 Partitioned Solution Procedure

Since the coefficient matrix  $[\mathbf{B} + \varpi \Delta t_k \mathbf{C}]$  in (5.54) is not symmetric, a partitioned solution procedure proposed by Schrefler[135] is introduced to restore the symmetry of the coefficients so that a simpler solver can be used and the computation is more effective. Moreover, the partitioned system of equations are better conditioned.

Separating  $\mathbf{B}$  as:

$$\mathbf{B} = \mathbf{B}^I + \mathbf{B}^E \quad (5.55)$$

where,

$$\mathbf{B}^I = \begin{bmatrix} \mathbf{K}_u & \mathbf{C}_{up} & 0 \\ \mathbf{C}_{pu} & \mathbf{C}_{pp} & 0 \\ 0 & 0 & \mathbf{C}_{TT} \end{bmatrix} \quad (5.56)$$

$$\mathbf{B}^E = \begin{bmatrix} 0 & 0 & \mathbf{C}_{uT} \\ 0 & 0 & \mathbf{C}_{pT} \\ 0 & 0 & 0 \end{bmatrix} \quad (5.57)$$

substituting (5.56) and (5.57) into (5.54) and re-arranging, one has:

$$[\mathbf{B}^I + \varpi \Delta t_k \mathbf{C}] \mathbf{X}_{t_k + \Delta t_k} = [\mathbf{B} - \Delta t_k (1 - \varpi) \mathbf{C}] \mathbf{X}_{t_k} + \mathbf{F} - \mathbf{B}^E \mathbf{X}_{t_k + \Delta t_k} \quad (5.58)$$

The solution proceeds by separating the solution of temperature fields from (5.58). The  $T_{t_k + \Delta t_k}$  is first predicted by the formula:

$$\bar{T}_{t_k + \Delta t_k}^p = (1 + \varpi) \bar{T}_{t_k} - \varpi \bar{T}_{t_k - \Delta t_k} \quad (5.59)$$

Then the isothermal displacement and pore pressure fields are solved by the following formulae:

$$\begin{bmatrix} \mathbf{K}_u & \mathbf{C}_{up} \\ \mathbf{C}_{pu} & \mathbf{C}_{pp} + \varpi \mathbf{K}_p \Delta t_k \end{bmatrix} \begin{Bmatrix} \bar{\mathbf{u}} \\ \bar{p} \end{Bmatrix}_{t_k + \Delta t_k} \quad (5.60)$$

$$= \begin{bmatrix} \mathbf{K}_u & \mathbf{C}_{up} & \mathbf{C}_{uT} \\ \mathbf{C}_{pu} & \mathbf{C}_{pp} - (1 - \varpi) \mathbf{K}_p \Delta t_k & \mathbf{C}_{pT} \end{bmatrix} \begin{Bmatrix} \bar{\mathbf{u}} \\ \bar{p} \\ \bar{T} \end{Bmatrix}_{t_k} \quad (5.61)$$

$$+ \begin{Bmatrix} \mathbf{F}_u \\ \mathbf{F}_q \Delta t_k \end{Bmatrix} - \begin{Bmatrix} \mathbf{C}_{uT} \\ \mathbf{C}_{pT} \end{Bmatrix} \bar{T}_{t_k + \Delta t_k} \quad (5.62)$$

Then the temperature field is solved:

$$[\mathbf{C}_{TT} + \varpi (\mathbf{K}_{cdp} + \mathbf{K}_{cvp}) \Delta t_k] \bar{T}_{t_k + \Delta t_k} \quad (5.63)$$

$$= [\mathbf{C}_{TT} - (1 - \varpi) (\mathbf{K}_{cdp} + \mathbf{K}_{cvp}) \Delta t_k] \bar{T}_{t_k} + \mathbf{F}_h \Delta t_k \quad (5.64)$$

## 5.2.5 Algorithm for Non-linear and Elastoplastic Analysis

Many computational techniques for non-linear and elasto-plastic finite element analyses have now become widely accepted in practical engineering applications. Detailed assessments of these techniques can be found in a wide range of publications[121][162][48][149][117][8][9]. Their application in geomechanics has also received considerable attention and has been the subject of many texts and conferences[49][69][50][158].

There are three basic solution techniques for non-linear finite element analyses: iterative, incremental, and mixed procedures[48][149]. In a purely iterative method, the total load is applied in one step and successive corrections are performed until equilibrium is satisfied. Among the many iterative schemes, the initial stress method implements the corrections by transferring the unequilibrium stresses. Assuming a material satisfying the following general non-linear constitutive relations:

$$\boldsymbol{\sigma} = \bar{\mathbf{D}}_{ep}(\boldsymbol{\varepsilon}) \boldsymbol{\varepsilon} \quad (5.65)$$

$$= (\bar{\mathbf{D}}_e - \bar{\mathbf{D}}_p) \boldsymbol{\varepsilon} \quad (5.66)$$

$$= \sigma_e - \sigma_p \quad (5.67)$$

A direct iteration scheme obtains the final results through the following procedures:

$$\mathbf{K}_0 \mathbf{u}^1 = \mathbf{F} \quad (5.68)$$

$$\dots \quad (5.69)$$

$$\mathbf{K}_{i-1} \mathbf{u}^i = \mathbf{F}, \quad i = 1, 2, \dots \quad (5.70)$$

until  $\mathbf{u}_i \approx \mathbf{u}_{i-1}$ ; where

$$\mathbf{K}_i = \int \mathbf{B}^T \bar{\mathbf{D}}_{ep}(\epsilon_i) \mathbf{B} dV \quad (5.71)$$

and

$$\mathbf{u}^0 = 0 \quad (5.72)$$

Substituting (5.66) into (5.71):

$$\mathbf{K}_i = \int \mathbf{B}^T \bar{\mathbf{D}}_e \mathbf{B} dV - \int \mathbf{B}^T \bar{\mathbf{D}}_p \mathbf{B} dV \quad (5.73)$$

$$= \mathbf{K}_e - \mathbf{K}_p \quad (5.74)$$

In the initial stress method, the stiffness matrix  $\mathbf{K}_i$  is kept constant throughout the iteration:

$$\mathbf{K}_i = \mathbf{K}_e \quad (5.75)$$

and the error induced by such an approximation will be gradually corrected by redistributing the extra stresses  $\sigma_p$ , which is determined by the constitutive relations (5.66), in a way that is mathematically similar to the treatment of initial stresses:

$$\mathbf{K}_e \mathbf{u}^i = \mathbf{F} + \mathbf{R}^{i-1}, \quad i = 1, 2, \dots \quad (5.76)$$

where,

$$\mathbf{R}^{i-1} = \int \mathbf{B}^T \sigma_p^{i-1} dV \quad (5.77)$$

$$= \mathbf{K}_p \mathbf{u}^{i-1} \quad (5.78)$$

The iteration will be terminated when  $\mathbf{u}_{n-1} \approx \mathbf{u}_n$ .

In a sub-incremental initial stress method:

$$\mathbf{K}_e \Delta \mathbf{u}^i = \mathbf{R}^{i-1}, \quad i = 1, 2, \dots \quad (5.79)$$

where,

$$\mathbf{R}^0 = \mathbf{F}, \quad \mathbf{u} = \sum_{i=1}^n \Delta \mathbf{u}^i \quad (5.80)$$

and the iteration will be terminated when  $\Delta \mathbf{u}^i \approx 0$ .

In non-linear and plastic analyses, an incremental formulation is considered essential for dealing with general loading paths and the history dependent properties of plastic deformation. A purely incremental scheme (tangent stiffness method) generates the solution as a sequence of piecewise linear steps:

$$\mathbf{K}_T^i \Delta \mathbf{u}^i = \Delta \mathbf{F}^i, \quad i = 1, 2, \dots, n \quad (5.81)$$

$$\mathbf{u} = \sum_{i=1}^n \Delta \mathbf{u}_i \quad (5.82)$$

where  $\mathbf{K}_T^i$  is a tangent stiffness matrix which needs to be evaluated explicitly at the beginning of each load increments. Since the basic equilibrium equations are never completely satisfied at any stage, the results tends to exhibit cumulative errors.

A mixed procedure, which is the one that is adopted in this dissertation, consists in loading incrementally, and taking into account the non-linearity by iteration at each load level. The additional effort in such a procedure is offset by the fact that the accuracy can be assessed at each loading stage.

## 5.2.6 Program Flow Chart

Figure 5.1 is a flow chart of the calculation sequences for the algorithms developed in this chapter. As a matter of fact, the coupled THM analysis is realized by combining virtually two independent programs: a thermal analyzer which calculates the change of temperature field with time, and an isothermal consolidation tool which takes care of the non-linear and elastoplastic analysis of stress/strain/displacement during the temperature and pore pressure diffusion. Two sub-iteration processes

are involved in a completed analysis cycle (*i.e.* within one time step): iteration for plastic analysis and iteration induced by the partitioned solution procedure. The iteration procedure required for the non-linearity due to both the field variable-dependent material properties and convective heat transfer is accomplished at the same time during the seek of equilibrium of the partitioned system. When the system non-linear feature is strong, load can be incrementally applied within each time step so that the influence of loading path can be reflected more realistically.

## 5.3 Implementation and Validation of FE Model

The numerical scheme developed in this chapter has been programmed using Fortran language and implemented on a personal computer. Since the major purpose of this chapter is to develop and validate an effective finite element model which can conduct the THM coupled, non-linear and poroelastoplastic analysis for the investigation of wellbore instability in fluid-saturated porous media, only a two-dimensional plane strain model was actually implemented at this stage to avoid unnecessary computational efforts inherently associated with three-dimensional model. Once the two-dimensional algorithm is validated, extension to the three-dimensional model is just a matter of increase one more DOF in each node for the displacement, which should not have any major technical obstacle. Four-node linear isoparametric elements are adopted, and the performance of the code is extensively validated in the following sections.

### 5.3.1 Steady State and Transient Temperature Distribution

The testing of the thermal analyzer started with comparing the finite element model output of steady state temperature distribution in the cross-section of an infinitely long thick-walled tube subjected to a constant temperature potential at the inner face of the tube, as shown in Figure 5.2. The problem and its analytical solution

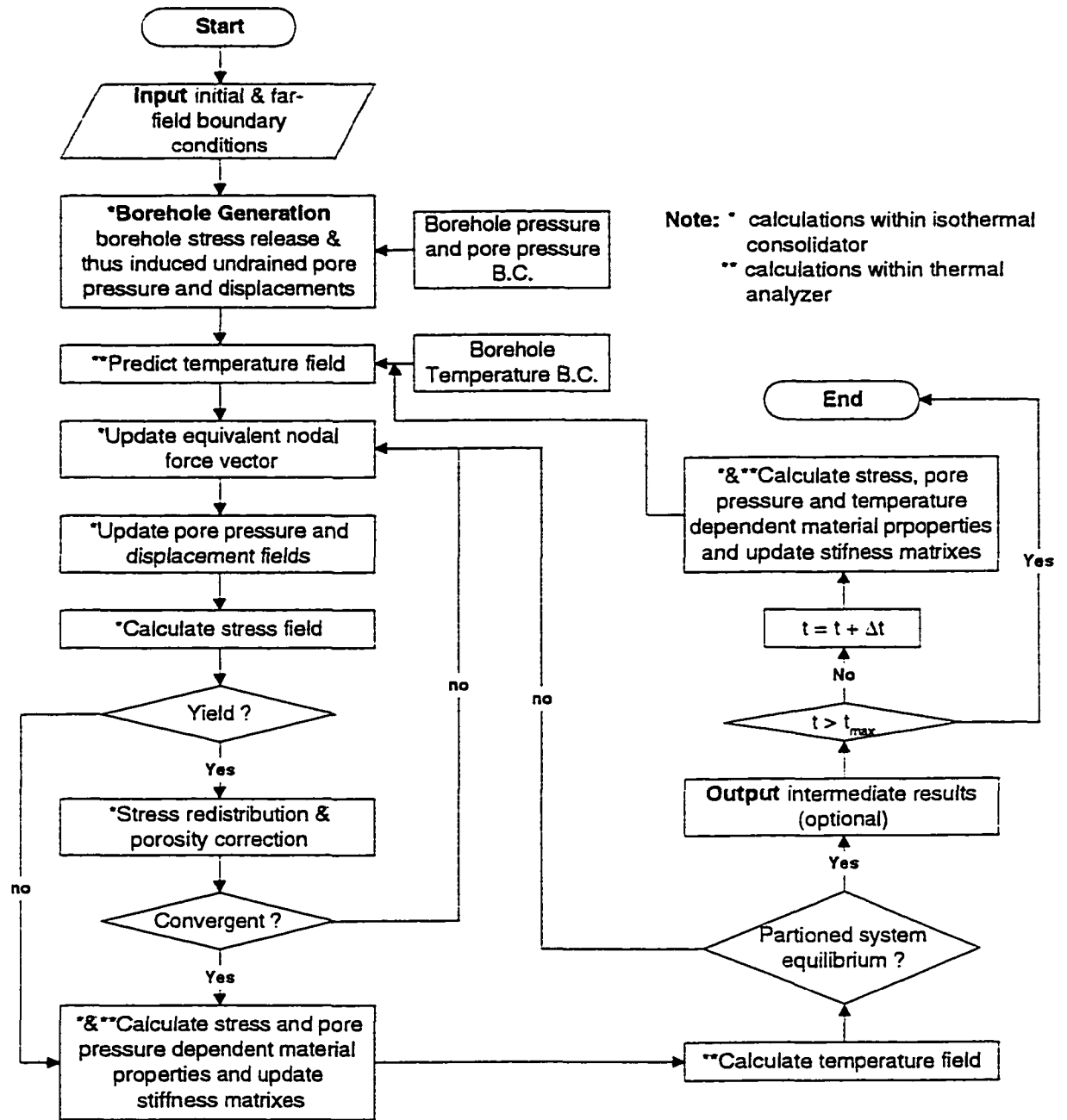


Figure 5.1: Calculation sequences for non-linear and thermoporoelastoplastic algorithms

are given in equations (5.83) to (5.85), respectively.

$$\frac{\partial^2 T}{\partial r^2} + \frac{1}{r} \frac{\partial T}{\partial r} = 0 \quad (5.83)$$

$$\begin{cases} T |_{r=a} = T_a \\ T |_{r=b} = T_b \end{cases} \quad (5.84)$$

$$T_r = \frac{T_b \log r_a - T_a \log r_b}{\log (r_a/r_b)} \quad (5.85)$$

The finite element mesh for the problem is shown in Figure 5.3 and the comparison of the numerical solution with the analytical one is shown in Table 5.1. As one can see, excellent agreement between the two solutions was obtained.

The accuracy of the time-dependent temperature distribution was tested by a linear heat conduction problem with a known analytical solution as shown in Figure 5.4. It is a three-side insulated plate (infinitely long in the direction perpendicular to the cross-section shown in Figure 5.4) with a zero initial temperature. For any time  $t > 0$ , a unit temperature is applied at the left hand side of the plate. The problem can be presented by a non-dimensional linear heat conduction equation:

$$\frac{\partial^2 T}{\partial x^2} = \frac{\partial T}{\partial t} \quad (5.36)$$

with the boundary and initial conditions:

$$\left. \begin{aligned} T = 1 \text{ at } x = 0, \quad \frac{\partial T}{\partial x} = 0 \text{ at } x = 4: \quad t > 0 \\ T(x, 0) = 0, \quad 0 < x \leq 4 \end{aligned} \right\} \quad (5.87)$$

The exact solution for the problem is given by Carslaw and Jaeger[31]:

$$T = 1 - \sum_{k=1}^{\infty} \frac{4}{\pi(2k-1)} \exp \left\{ - \left[ \frac{(2k-1)\pi}{8} \right]^2 t \right\} \sin \left[ \frac{(2k-1)\pi x}{8} \right] \quad (5.88)$$

As shown in Figure 5.4, the problem was discretized into four elements. Figure 5.5, Tables 5.2 and 5.3 are the comparison of numerical and analytical solutions for the transient temperature distribution at  $x = 1.0$  for different recurrence schemes. They show that for all the recurrence schemes, the numerical solutions give excellent

r = 0.1157 (m)			r = 0.1714 (m)		
T (°C)			T (°C)		
Node	Num.	Ana.	Node	Num.	Ana.
89	46.8903	46.9	67	38.5068	38.5
90	46.8853	46.9	68	38.5039	38.5
91	46.8903	46.9	69	38.5075	38.5
92	46.8888	46.9	70	38.5067	38.5
93	46.8865	46.9	71	38.5052	38.5
94	46.8914	46.9	72	38.5085	38.5
95	46.8865	46.9	73	38.5053	38.5
96	46.8889	46.9	74	38.5068	38.5
97	46.8904	46.9	75	38.5076	38.5
98	46.8854	46.9	76	38.5041	38.5
99	46.8905	46.9	77	38.5072	38.5
r = 0.2934 (m)			r = 0.7469 (m)		
T (°C)			T (°C)		
Node	Num.	Ana.	Node	Num.	Ana.
45	27.4309	27.4	12	7.28479	7.3
46	27.4292	27.4	13	7.28400	7.3
47	27.4313	27.4	14	7.28492	7.3
48	27.4309	27.4	15	7.28471	7.3
49	27.4301	27.4	16	7.28433	7.3
50	27.4320	27.4	17	7.28517	7.3
51	27.4301	27.4	18	7.28435	7.3
52	27.4310	27.4	19	7.28474	7.3
53	27.4315	27.4	20	7.28497	7.3
54	27.4294	27.4	21	7.28407	7.3
55	27.4312	27.4	22	7.28488	7.3

Table 5.1: Comparison of the numerical with the analytical solutions for the steady state temperature distribution in thick-walled tube example

approximation to the analytical solution except at very early times. The relative errors monotonically decrease with the increasing of time for all the recurrence schemes. The accuracy of the numerical solutions, including the early time solution, improves with the decreasing time step as shown in Table 5.4. However, even when the time step is very small, the noise in the early time solution still exists as shown in the same table.

The finite difference solution for the problem in question is unconditionally stable for any size of time step if  $1/2 \leq \varpi \leq 1$ . Whereas in finite element method, the stability of the solution is also dictated by the size of the smallest element[163] and the total DOF of the problem[160]. Since the increase of the total DOF and the decrease of the element size will commensurately reduce the maximum allowable time-step size[160][163], the discussion of improving the solution quality via increase the element numbers are not conducted here. The time step of 0.187 adopted in Figure 5.5 and Tables 5.2 and 5.3 are the theoretically derived maximum time step allowable[160] for a stable solution of the above defined problem. and for the recurrence schemes that  $1/2 \leq \varpi \leq 1$ . However, as one can see, noise exists in very early times for all the recurrence schemes, and for even very small time step size.

According to [163], this early time noise is associated with the physically unrealistic initial condition, *i.e.*, step loading, such as the suddenly applied temperature at  $t = 0$  in this example. Traditionally recommended way of reducing this noise is to replace the step loading with ramp loading, such as the two-step start in [160] (*i.e.*, apply the temperature through the first two, instead of one, time steps ). Since ramp loading brings in errors of replacing a step function with a weighted loading function, it may or may not be necessary, depending on how well the assumed step function approximates the real loading condition, and the interested solutions reside in what time range.

t	Ana.	C-N	err. (%)	Galerkin	err. (%)	Implicit	err. (%)
0.19	0.10199	-0.08635	-184.66	-0.00249	-102.44	0.01955	-80.83
0.37	0.24755	0.17606	-28.88	0.18638	-24.71	0.19242	-22.27
0.56	0.34510	0.30569	-11.42	0.30400	-11.91	0.30491	-11.65
0.75	0.41356	0.38812	-60.15	0.38397	-7.16	0.38329	-7.32
0.94	0.46458	0.44648	-3.9	0.44216	-4.83	0.44104	-5.07
1.12	0.50439	0.49076	-2.7	0.48671	-3.51	0.48554	-3.74
1.31	0.53654	0.52586	-1.99	0.55214	-2.68	0.52105	-2.89
1.50	0.56321	0.55450	-1.55	0.55118	-2.14	0.55021	-2.31
1.68	0.58582	0.57843	-1.26	0.57555	-1.75	0.57472	-1.90
1.87	0.60536	0.59882	-1.08	0.59641	-1.48	0.59572	-1.59
2.06	0.62252	0.61652	-0.96	0.61458	-1.28	0.61404	-1.36
2.24	0.63781	0.63214	-0.89	0.63065	-1.12	0.63025	-1.19
2.43	0.65161	0.64615	-0.84	0.64507	-1.00	0.64480	-1.05
2.62	0.66421	0.65889	-0.80	0.65818	-0.91	0.65801	-0.93
2.81	0.67584	0.67062	-0.77	0.67021	-0.83	0.67013	-0.84
2.99	0.68665	0.68152	-0.75	0.68136	-0.77	0.68137	-0.77
3.18	0.69679	0.69176	-0.72	0.69179	-0.72	0.69186	-0.71
3.37	0.70636	0.70142	-0.70	0.70160	-0.67	0.70173	-0.66
3.55	0.71544	0.71062	-0.67	0.71090	-0.64	0.71106	-0.61
3.74	0.72410	0.71939	-0.65	0.71974	-0.60	0.71994	-0.57

Table 5.2: Comparison of the numerical and analytical solutions for the transient temperature distribution for different recurrence schemes (  $dt = 0.187$ ,  $x = 1.0$  )

t	Ana.	C-N	err. (%)	Galerkin	err. (%)	Implicit	err. (%)
3.93	0.73238	0.72780	-0.63	0.72820	-0.57	0.72840	-0.54
4.11	0.74032	0.73588	-0.60	0.73630	-0.54	0.73652	-0.51
4.30	0.74796	0.74367	-0.57	0.74408	-0.52	0.74432	-0.49
4.49	0.75533	0.75119	-0.55	0.75158	-0.50	0.75182	-0.46
4.68	0.76244	0.75846	-0.52	0.75882	-0.47	0.75905	-0.44
4.86	0.76931	0.76549	-0.50	0.76582	-0.45	0.76603	-0.43
5.05	0.77596	0.77230	-0.47	0.77258	-0.44	0.77279	-0.41
5.24	0.78240	0.77890	-0.45	0.77913	-0.42	0.77933	-0.39
5.42	0.78864	0.78530	-0.42	0.78548	-0.40	0.78566	-0.38
5.61	0.79469	0.79151	-0.40	0.79163	-0.38	0.79180	-0.36
5.80	0.80055	0.79753	-0.38	0.79759	-0.37	0.79775	-0.35
5.98	0.80625	0.80337	-0.36	0.80338	-0.36	0.80325	-0.34
6.17	0.81177	0.80905	-0.34	0.80900	-0.34	0.80912	-0.33
6.36	0.81714	0.81445	-0.32	0.81445	-0.33	0.81456	-0.32
6.54	0.82235	0.81990	-0.30	0.81975	-0.32	0.81984	-0.30
6.73	0.82741	0.82509	-0.28	0.82489	-0.30	0.82496	-0.30
6.92	0.83232	0.83013	-0.26	0.82988	-0.29	0.82994	-0.29
7.11	0.83709	0.83502	-0.25	0.83473	-0.28	0.83477	-0.28

Table 5.3: Comparison of the numerical and analytical solutions for transient temperature distribution for different recurrence schemes (  $dt = 0.187$ ,  $x = 1.0$  )(cont.)

t	Ana.	dt = 0.01	err. (%)	dt = 0.1	err. (%)	dt = 0.5	err. (%)
0.1	0.02540	-0.56794	-2335.59	-0.15586	-713.51		
0.2	0.11382	0.08802	-22.67	0.02707	-76.22		
0.3	0.19668	0.18832	-4.25	0.14637	-25.58		
0.4	0.26352	0.26203	-0.57	0.23151	-12.15		
0.5	0.31728	0.31879	0.48	0.29520	-6.96	0.0718	-77.37
0.6	0.36128	0.36413	0.79	0.34517	-4.46		
0.7	0.39799	0.40142	0.86	0.38573	-3.08		
0.8	0.42917	0.43280	0.85	0.41953	-2.25		
0.9	0.45603	0.45969	0.80	0.44827	-1.70		
1.0	0.47947	0.48306	0.75	0.47312	-1.32	0.44486	-7.22
1.1	0.50016	0.50362	0.69	0.49487	-1.06		
1.2	0.51858	0.52187	0.63	0.51411	-0.86		
1.3	0.53513	0.53820	0.57	0.53128	-0.72		
1.4	0.55010	0.55294	0.52	0.54672	-0.61		
1.5	0.56373	0.56631	0.46	0.56070	-0.54	0.52809	-6.32
1.6	0.57622	0.57852	0.40	0.57343	-0.48		
1.7	0.58772	0.58973	0.34	0.58509	-0.45		
1.8	0.59836	0.60008	0.29	0.59583	-0.42		
1.9	0.60826	0.60969	0.23	0.60578	-0.41		
2.0	0.61751	0.61865	0.18	0.61504	-0.40	0.59917	-2.97

Table 5.4: Influence of time-step size on the numerical solutions (  $x=1.0$  )

### 5.3.2 One-dimensional Consolidation

The classical one-dimensional consolidation problem of Terzaghi[146] considers a soil layer of height  $H$ , resting on a rigid impermeable base; and a constant loading  $\sigma_z$  is applied on top of the layer under drained conditions (Figure 5.6). Recently, Detournay and Cheng[52] re-analyzed the problem in light of the Biot theory. The mathematical model and its analytical solution for the transient displacement and pore pressure distribution can be found in [52]:

$$\frac{\partial p}{\partial t} - c^f \frac{\partial^2 p}{\partial z^2} = 0 \quad (5.89)$$

$$p(t, z) = \frac{\eta \sigma_z}{GS} [1 - F_1(\chi, \tau)] \quad (5.90)$$

$$u(t, z) = \frac{\sigma_z H (1 - 2\nu_u)}{2G(1 - \nu_u)} \left[ 1 - \chi + \frac{\nu_u - \nu}{(1 - \nu)(1 - 2\nu_u)} F_2(\chi, \tau) \right] \quad (5.91)$$

where,

$$\eta = \alpha \frac{1 - 2\nu}{2(1 - \nu)} \quad (5.92)$$

is a poroelastic constant, and,

$$S = \frac{(1 - \nu_u)(1 - 2\nu)}{M(1 - \nu)(1 - 2\nu_u)} \quad (5.93)$$

is the storage coefficient. The dimensionless coordinate and time,  $\chi$  and  $\tau$ , are defined as:

$$\chi = \frac{z}{H}; \quad \tau = \frac{c^f t}{4H^2}; \quad (5.94)$$

and,

$$F_1(\chi, \tau) = 1 - \sum_{m=1,3,\dots}^{\infty} \frac{4}{m\pi} \sin\left(\frac{m\pi\chi}{2}\right) \exp(-m^2\pi^2\tau) \quad (5.95)$$

$$F_2(\chi, \tau) = \sum_{m=1,3,\dots}^{\infty} \frac{8}{m^2\pi^2} \cos\left(\frac{m\pi\chi}{2}\right) [1 - \exp(-m^2\pi^2\tau)] \quad (5.96)$$

This problem has been selected to test the displacement-pore pressure coupling function in the isothermal consolidation tool. The soil layer is discretized into ten 4-node isoparametric elements. The finite element mesh and the boundary conditions

are shown in Figure 5.7. The material properties for the problem are listed in Table 5.5.

Figure 5.8 is the comparison of the transient displacement at the top of the soil layer. Figures 5.9 and 5.10 represent pore pressure distributions along the layer depth at certain times. As one can see, excellent agreements between the analytical and numerical solutions are obtained for all the cases.

E (GPa)	$\nu$	G(GPa)	M (GPa)
20.6	0.189	8.66	48.2
$\alpha$	$\nu_u$	$\eta$	$\kappa$ (m <sup>2</sup> /MPa/day)
0.733	0.3086	0.281	$8.64 \times 10^{-6}$

Table 5.5: Material properties for one-dimensional consolidation problem

### 5.3.3 Temperature-induced Pore Pressure and Stresses

The Case I in Chapter 6, pore pressure and stresses induced by the temperature variations only in a fully-coupled THM system, was selected to validate the three-field coupling function in the finite element code. The finite element mesh for this case and their thermal and hydraulic boundary conditions are shown in Figure 5.11.

Figures 5.12 to 5.15 are the comparisons of temperature distributions along the borehole radius at different times. It can be seen that the numerical solution gives an excellent approximation to the analytical solution at times less than 1 day. Starting from 1 day, the two results begin to separate at the outer boundary. At 10 days, the prediction by the numerical solution is totally different from the analytical solution. This is because the influence of different outer boundary conditions between the numerical model and analytical model start to interfere the comparison at later times. In the numerical model, the calculation domain is predetermined as a finite domain, whereas the analytical model is obtained assuming an infinite outer boundary. Starting at the time when the developing temperature front hits the outer boundary of numerical model, the temperature at the outer boundary is not a fixed value anymore, but changes with time, because the outer boundary is

set as a free boundary in the numerical model in this example. Even if the outer boundary was prescribed as a fixed far-field temperature, *i.e.*  $T_b = 0$ , in the numerical model, the problem considered in the numerical model is still not the same problem as the analytical model described. So the two results cannot be compared after the temperature front hit the outer boundary of the numerical model.

Figures 5.16 to 5.19 are temperature induced pore pressures. Similarly to the temperature profiles, good agreement between the analytical and numerical solutions are obtained at times less than 1 day, but the outer boundary conditions come into play at later times and the two results start to deviate at times greater than 1 day.

Figures 5.20 to 5.23 are the comparisons of the total radial and circumferential stresses along the borehole radius (note that the Biot coefficient,  $\alpha$ , adopted in this example is different from what is adopted in Case I in Chapter 6 ). Figures 5.20 to 5.23 show that the numerical results for the stresses start to deviate away from the analytical results in earlier times compared to that of the temperature and pore pressure. This is because, on the one hand, in finite element method, displacements, rather than stresses, are adopted as the field variables as it is shown in Equation (5.25), hence, the accuracy of stresses is a level lower compared to that of first level field variables such as pore pressure, temperature and displacement; on the other hand, detailed analysis of the change of displacement field had been conducted for this example and the results showed that the disturbances of the displacement reach the outer boundary at an earlier time compared to that of the temperature and pore pressure, which is the major reason for the lower accuracy of stresses in this example.

It is worth to mention that once the finite element mesh for a certain example is predetermined, the output point for the stresses are fixed, if a peak value is in between the two output points, this important information could be missed, and adjusting the mesh to accommodate all the important information is not a straight forward work. As a matter of fact, the same problem exists for the outputs of all

transient numerical models. Since the purpose of running examples in this section is to compare the results with existing analytical solutions and validate the functions of the program, no analyses regarding the peak value in each time are conducted at the present stage.

From the comparison of the last example in this section one can see that either a large enough simulation domain, or an exact time-dependent outer boundary condition are essential to obtain reliable results from the numerical models for transient analysis.

### 5.3.4 Elastoplastic Analysis of Thick-walled Tube

The elastoplastic algorithm in the program is tested via the classical thick-walled tube problem.

Assuming a thick-walled tube with an inner diameter,  $a$ , of 2 meters and an outer diameter,  $b$ , of 8 meters; subjected to an internal pressure,  $p$ , of 230 kg/cm<sup>2</sup>; and has the following material properties:

$$\left\{ \begin{array}{ll} \text{Young's modulus} & E = 2.1 \times 10^5 \text{ kg/cm}^2 \\ \text{Poisson's ratio} & \nu = 0.17 \\ \text{Uniaxial compressive strength} & q_u = 200 \text{ kg/cm}^2 \end{array} \right. \quad (5.97)$$

The material is ideal elastoplastic and the plastic deformation conform with the Von Mises law. The analytical solutions for the problem are[121]:

- Plastic radius  $r_s$  is determined from the following formula:

$$p = \frac{2q_u}{\sqrt{3}} \left[ \ln \frac{r_s}{a} + \frac{1}{2} \left( 1 - \frac{r_s^2}{b^2} \right) \right] \quad (5.98)$$

- Stresses inside the plastic area:

$$\sigma_r = \sigma_2 = -p + \frac{2}{\sqrt{3}} q_u \ln \frac{r}{a} \quad (5.99)$$

$$\sigma_\theta = \sigma_1 = -p + \frac{2}{\sqrt{3}} q_u \left( 1 + \ln \frac{r}{d} \right) \quad (5.100)$$

- Stresses inside the elastic area:

$$\sigma_r = \sigma_3 = -\frac{q_u r_s^2}{\sqrt{3} b^2} \left( \frac{b^2}{r^2} - 1 \right) \quad (5.101)$$

$$\sigma_\theta = \sigma_1 = \frac{q_u r_s^2}{\sqrt{3} b^2} \left( \frac{b^2}{r^2} + 1 \right) \quad (5.102)$$

- The radial displacement at the interface of elastic and plastic area:

$$u_{rs} = \frac{1 + \nu}{E} \frac{q_u r_s}{b^2 - r_s^2} \left[ (1 - 2\nu) + \frac{b^2}{r_s^2} \right] \quad (5.103)$$

According to the symmetric condition, a quarter of the structure was selected, and discretized into 360 elements and 399 nodes. The comparison of the analytical and numerical solutions are listed in Table 5.6 and 5.7. As one can see, the numerical model produce good approximation to the analytical solutions.

	$r_s$ (m)	$u_{rs}$ (cm)
Analytical	3.64	0.2459
Numerical	3.60	0.2602
Relative Error	-1.1%	5.82%

Table 5.6: Comparison of numerical and analytical solutions for the radius of plastic zone and the radial displacement at the interface of elastic and plastic zone

Radius(m)	$\sigma_\theta$ (kg/cm <sup>2</sup> )			$\sigma_r$ (kg/cm <sup>2</sup> )		
	Ana.	FE	Err.(%)	Ana.	FE	Err.(%)
2.1	12.21	16.20	32.70	-218.7	-213.0	2.61
2.5	52.47	55.93	6.59	-178.5	-173.4	2.90
2.9	86.75	90.69	4.54	-144.19	-139.56	3.21
3.5	130.18	120.80	-7.20	-100.76	-110.0	-9.17
3.9	124.5	120.70	-3.05	-76.68	-74.96	3.00
4.6	96.21	93.41	-2.90	-48.40	-46.96	3.00
5.4	76.37	74.12	-2.90	-28.56	-27.70	3.00
6.2	63.71	61.82	-3.00	-15.9	-15.4	3.10
7.0	55.13	53.49	-3.00	-7.32	-7.09	3.10
7.8	49.05	47.59	-3.00	-1.24	-1.19	4.00

Table 5.7: Comparison of the numerical and analytical solutions for the stress distribution along the borehole radius

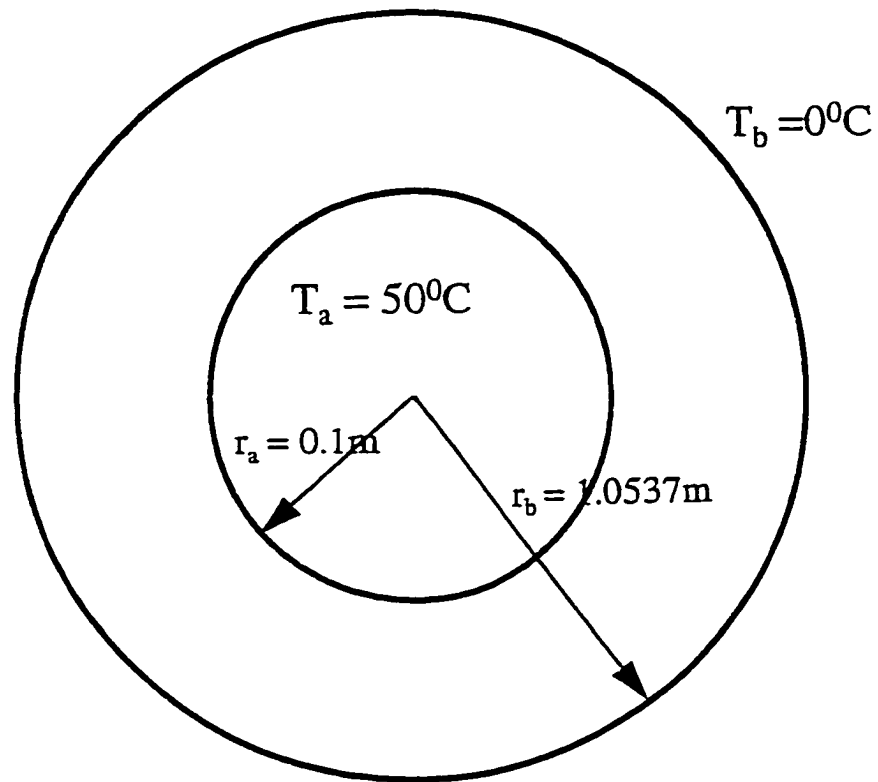


Figure 5.2: The schematic diagram of a thick-walled tube subjected to a constant temperature potential at the inner face of the tube

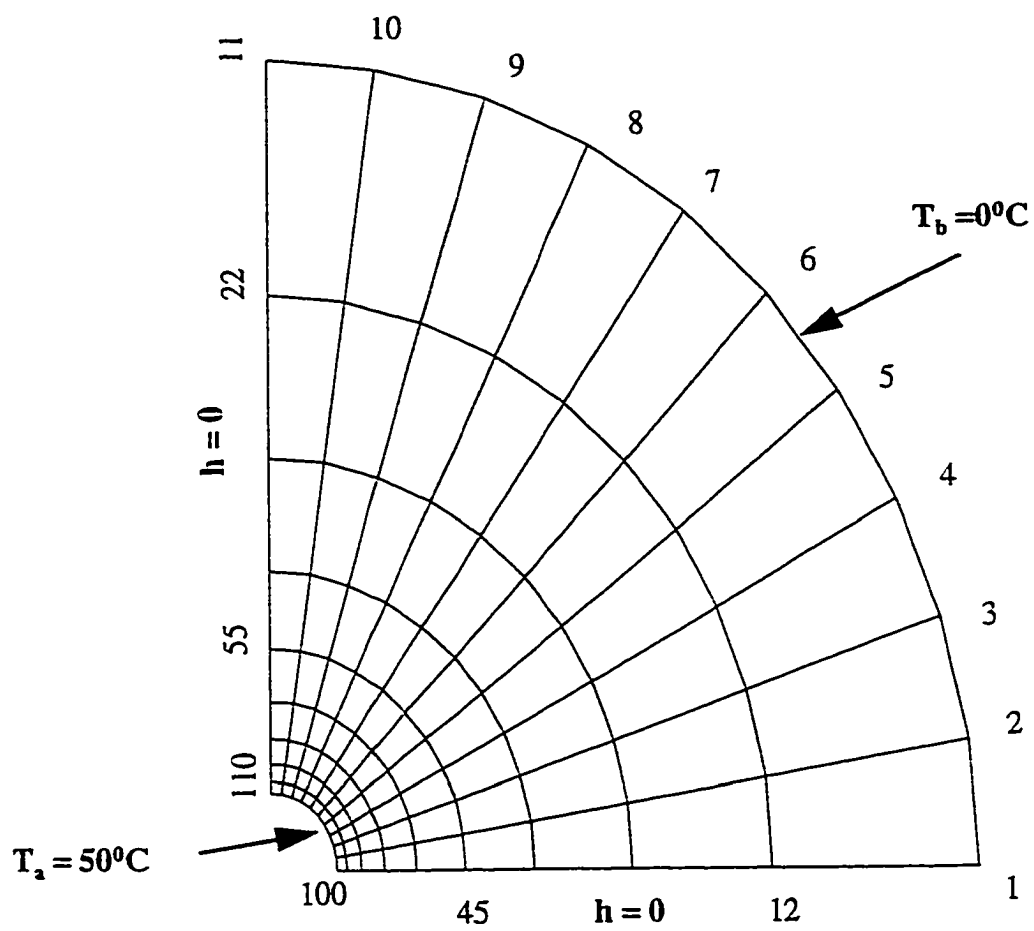


Figure 5.3: The FE mesh for the thick-walled tube example

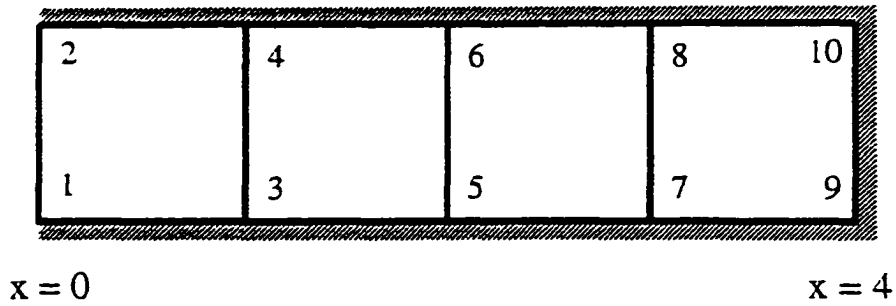


Figure 5.4: The schematics and FE mesh for a three-side insulated plate with a zero initial temperature and a unit temperature at the left-hand side of the plate ( for  $t > 0$  )

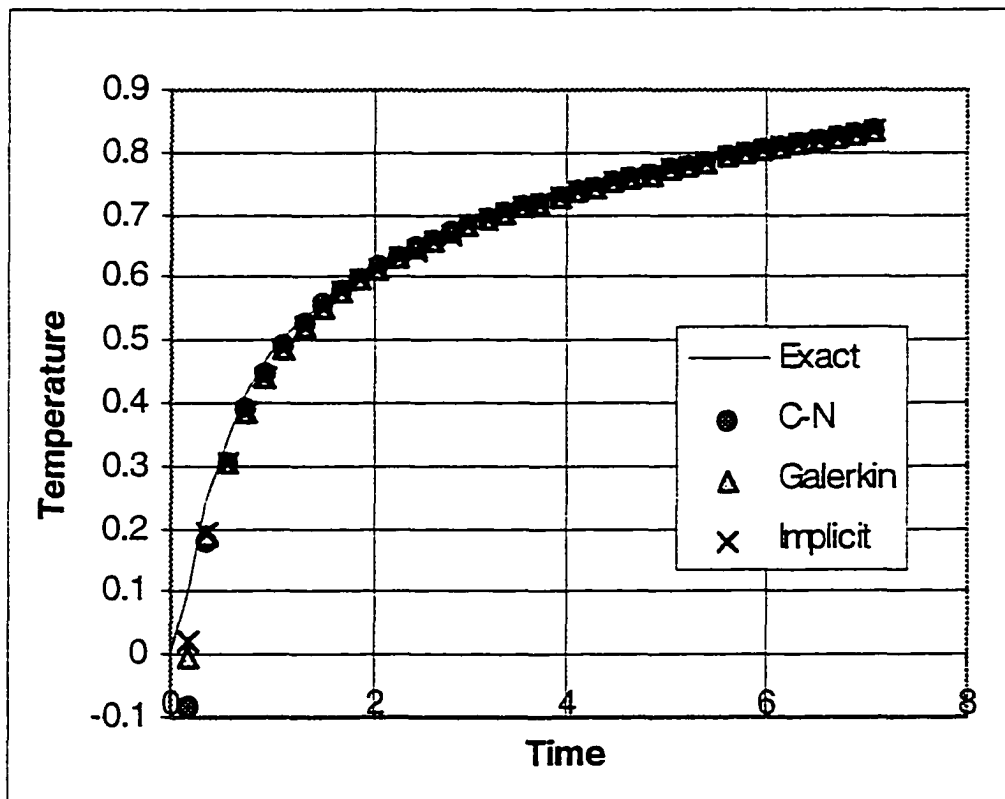


Figure 5.5: Comparison of numerical and analytical solutions for transient temperature distribution for different recurrence schemes ( @  $x = 1.0$  )

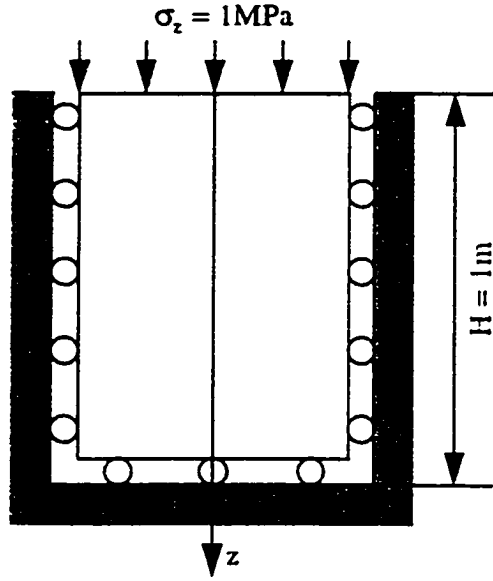


Figure 5.6: Schematic diagram of one-dimensional consolidation problem

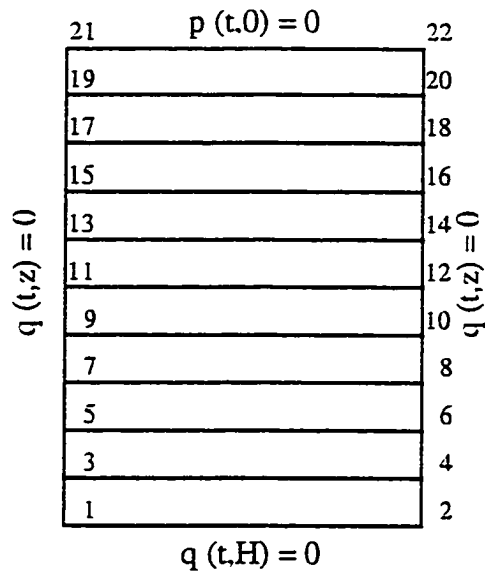


Figure 5.7: The FE mesh for one-dimensional consolidation problem

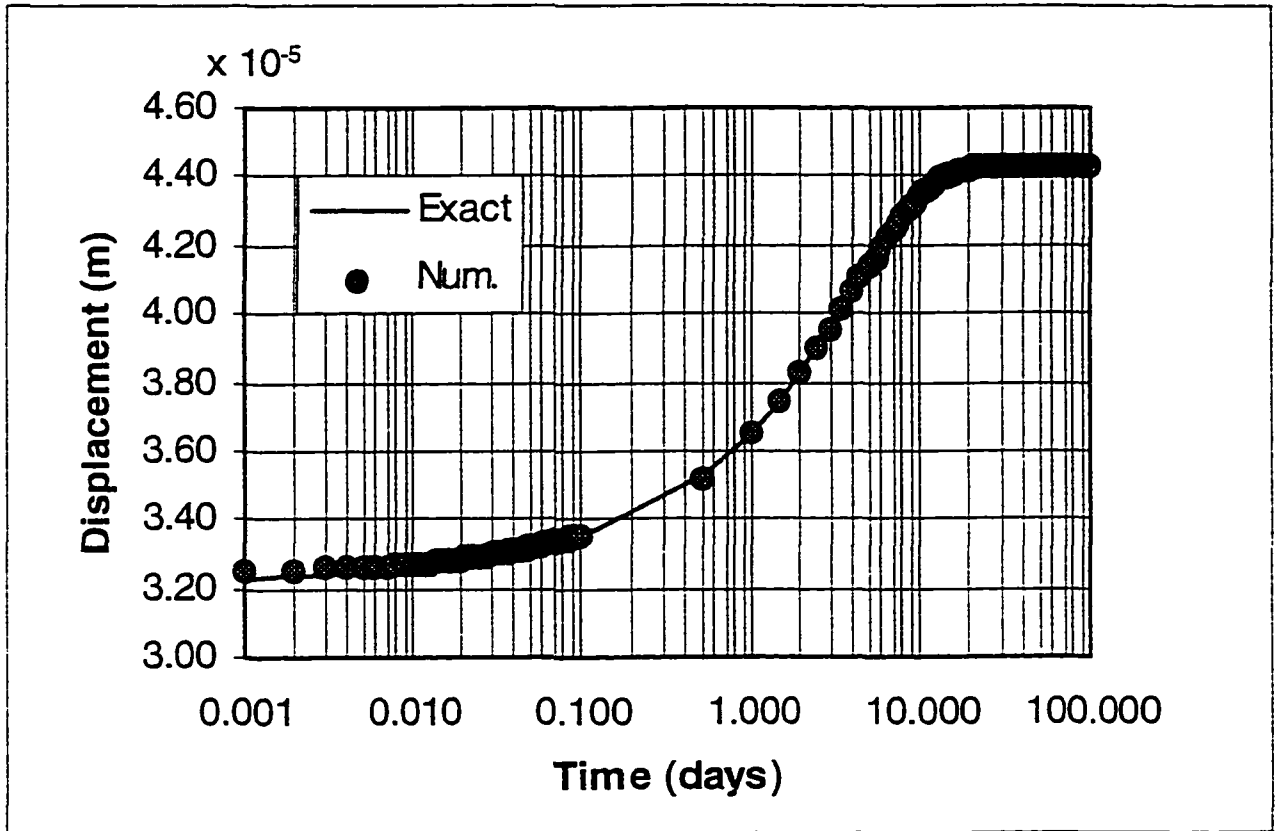


Figure 5.8: Comparison of numerical and analytical solutions for the transient displacement at the top of the soil layer

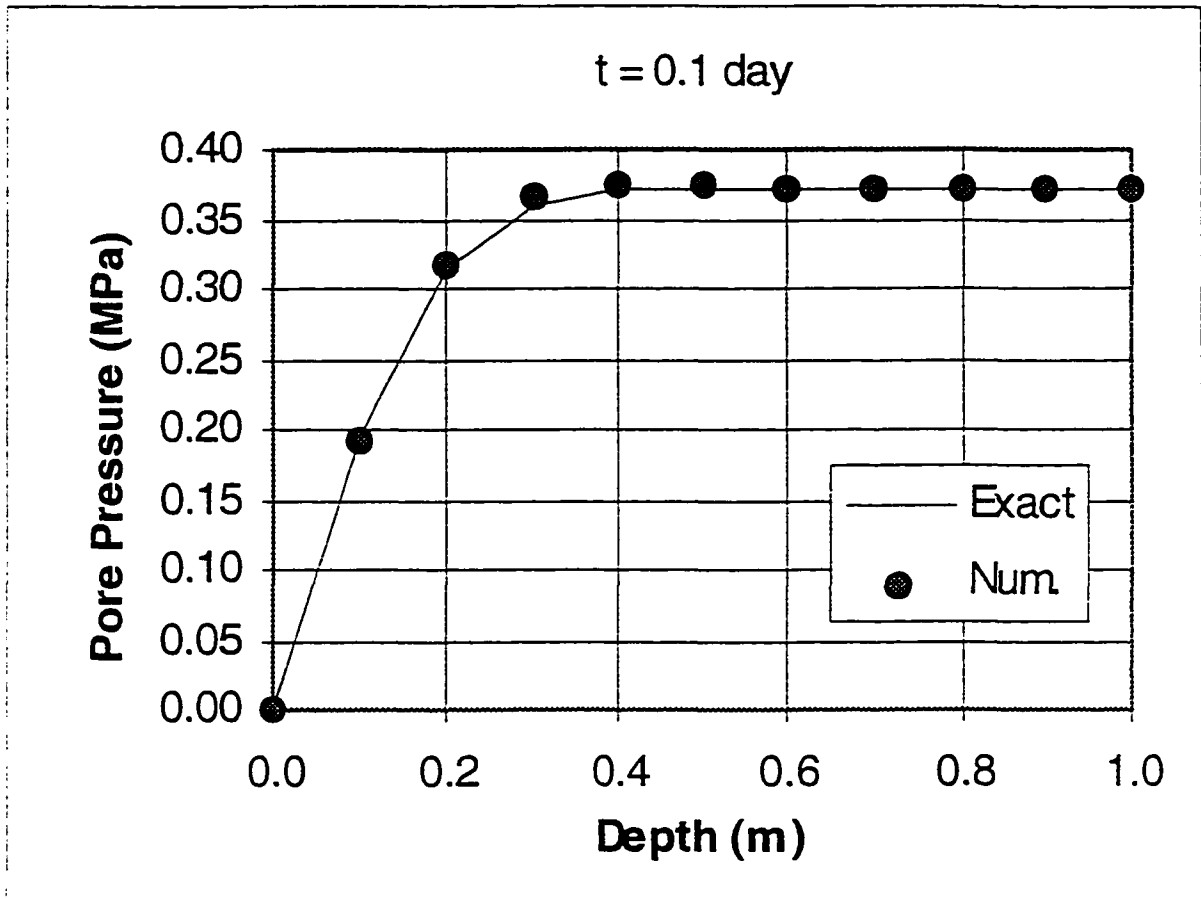


Figure 5.9: Comparison of numerical and analytical solutions for the pore pressure distribution along the layer depth ( $t = 0.1$  day)

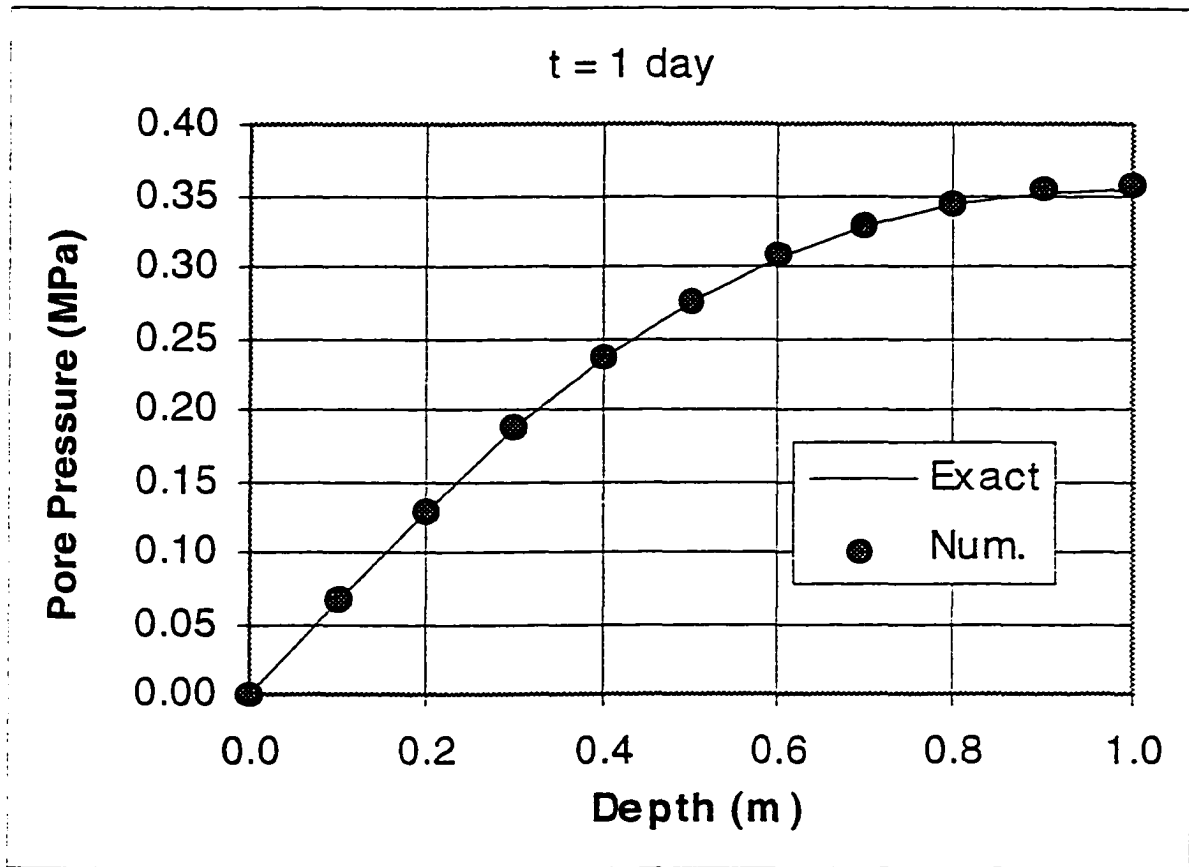


Figure 5.10: Comparison of numerical and analytical solutions for the pore pressure distribution along the layer depth ( $t = 1$  day)

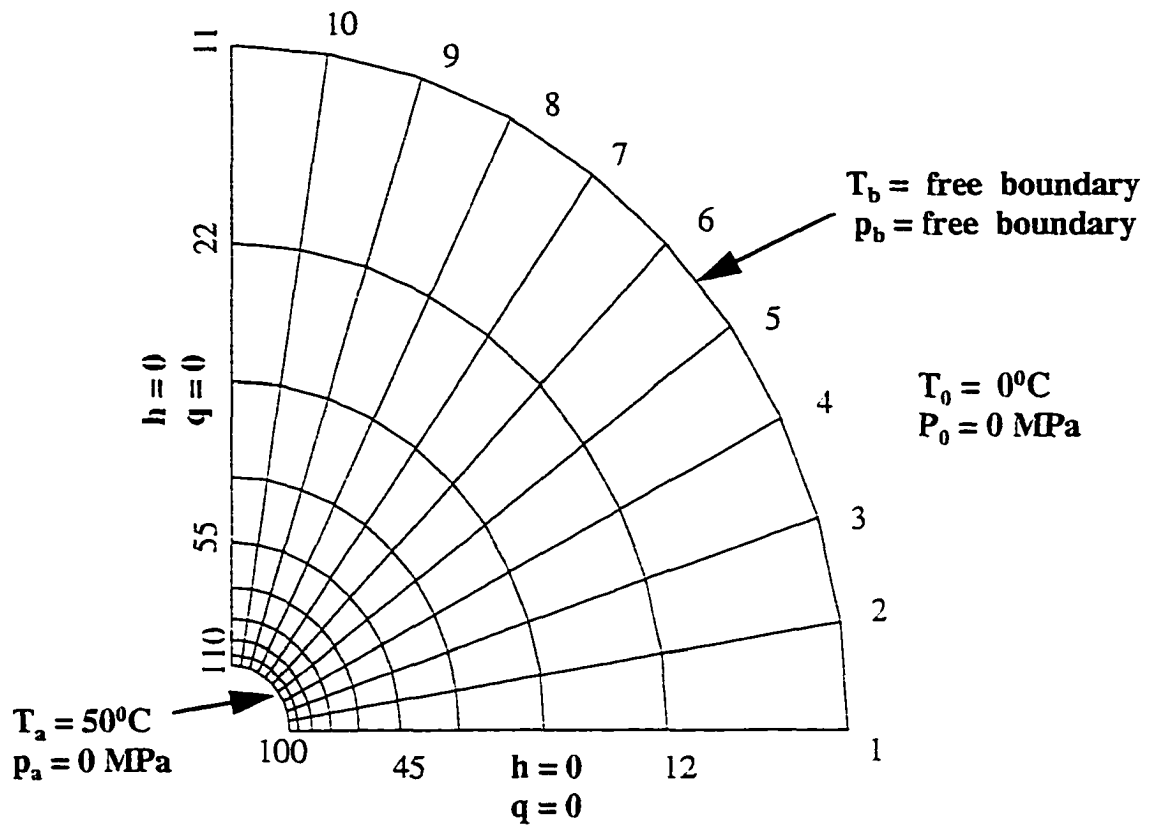


Figure 5.11: The FE mesh and the thermal and hydraulic boundary conditions for the Case I in Chapter 6

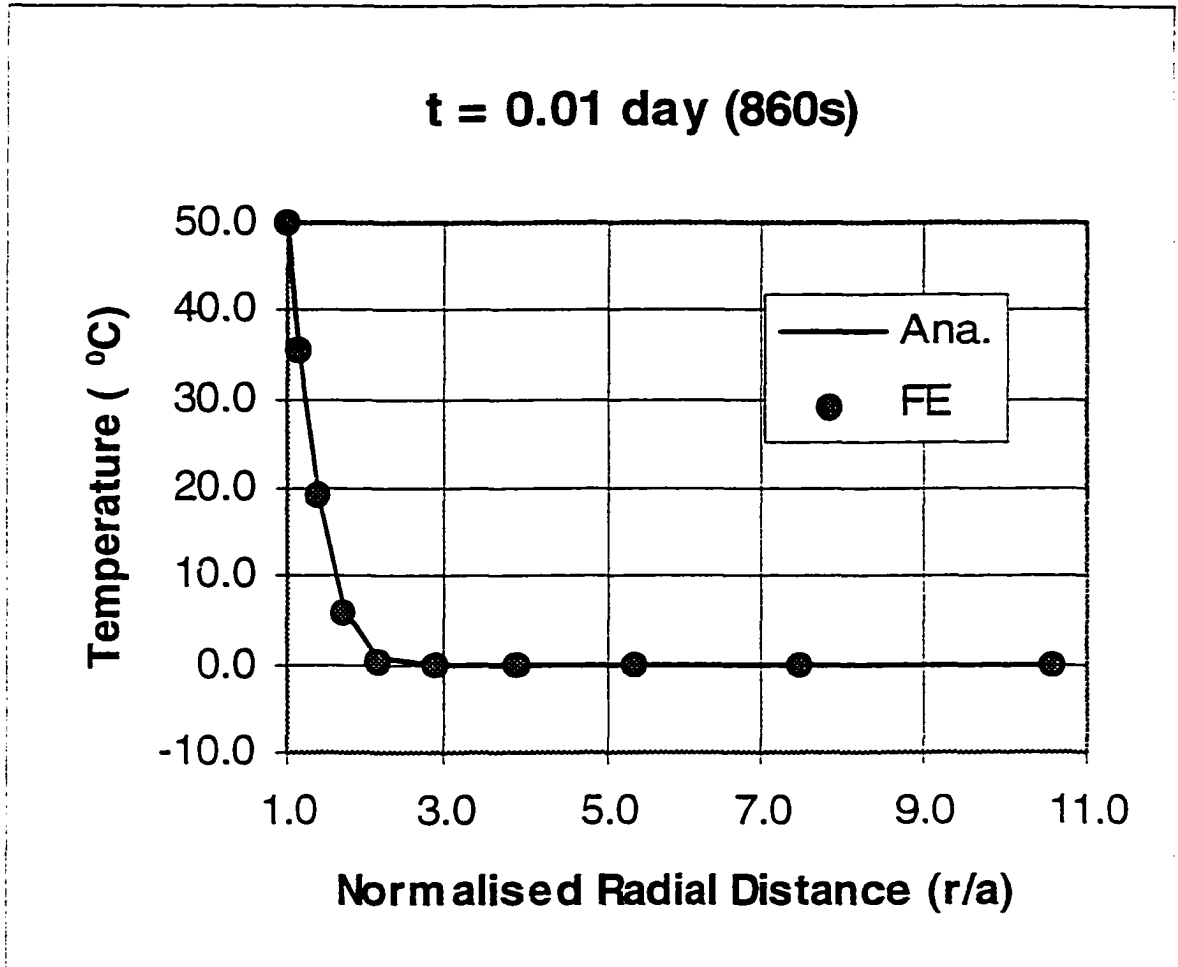


Figure 5.12: Comparison of numerical and analytical solutions for temperature distribution along the borehole radius ( t = 0.01 day )

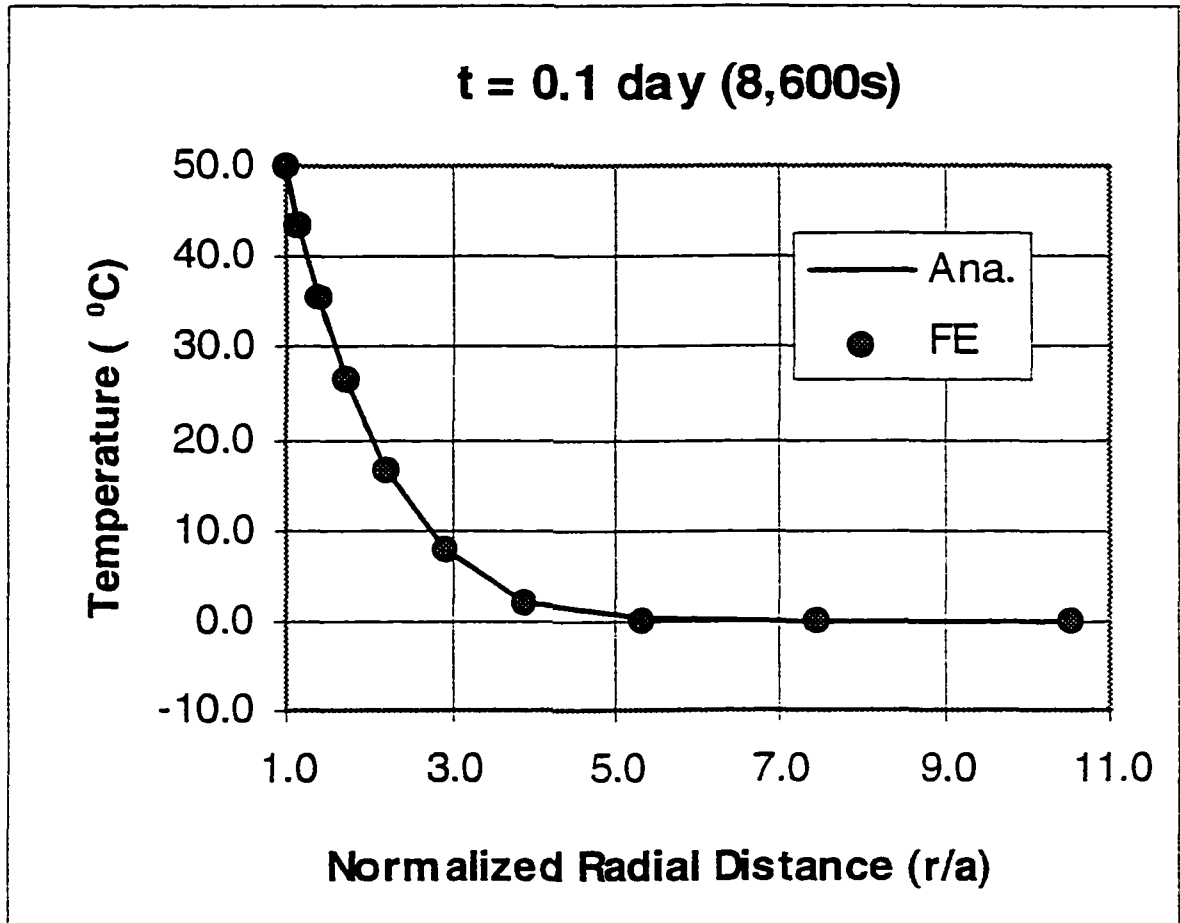


Figure 5.13: Comparison of numerical and analytical solutions for temperature distribution along the borehole radius ( t = 0.1 day )

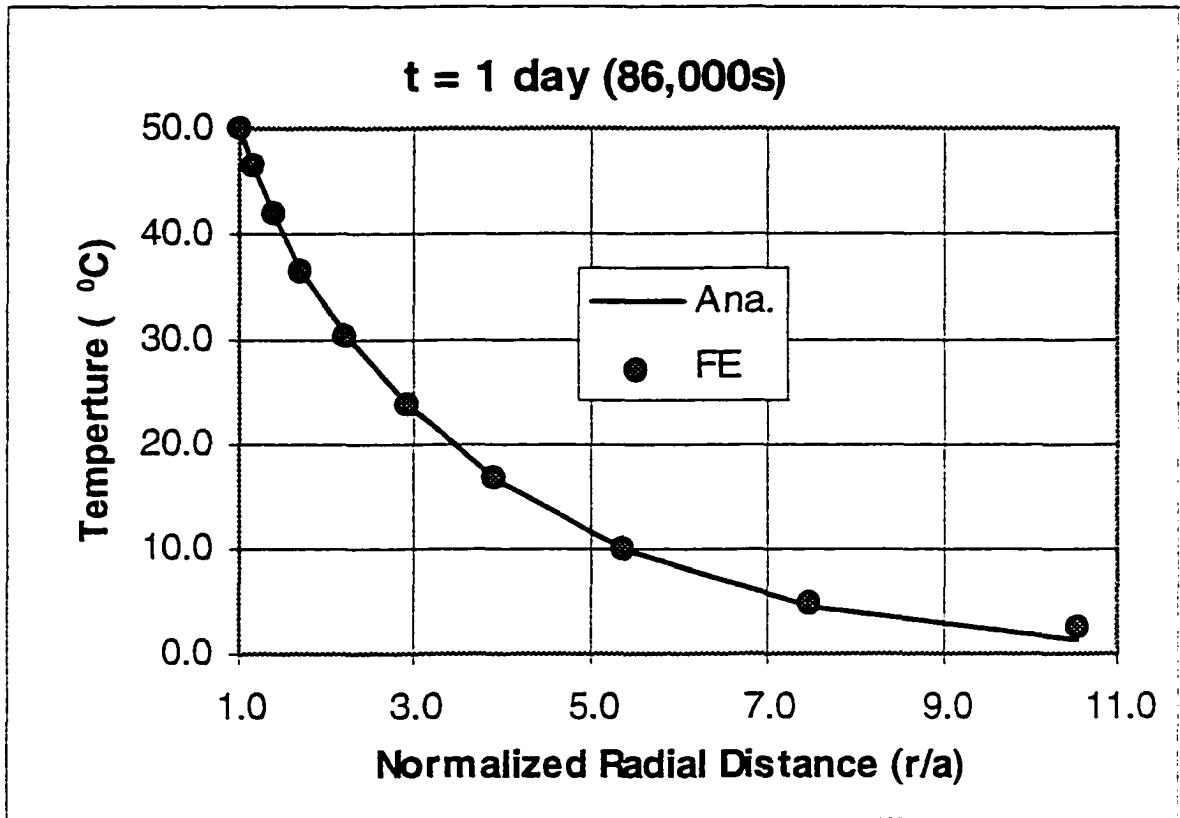


Figure 5.14: Comparison of numerical and analytical solutions for temperature distribution along the borehole radius ( $t = 1$  day)

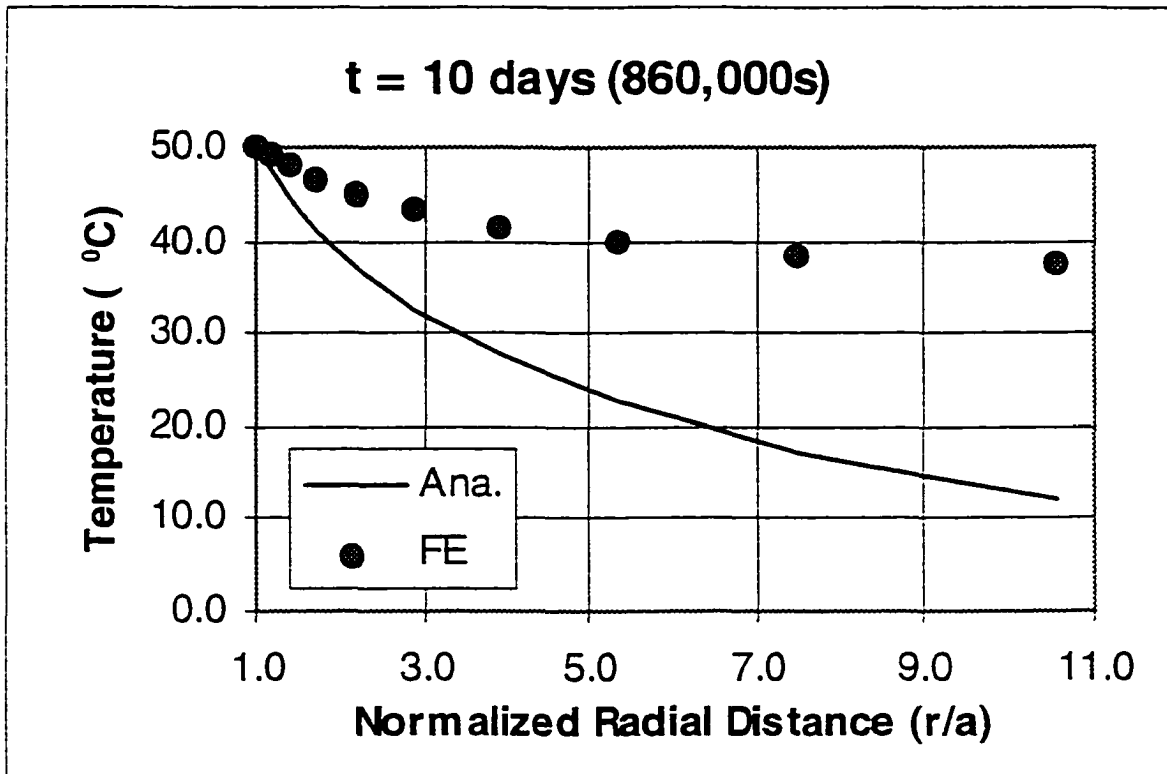


Figure 5.15: Comparison of numerical and analytical solutions for temperature distribution along the borehole radius ( t = 10 day )

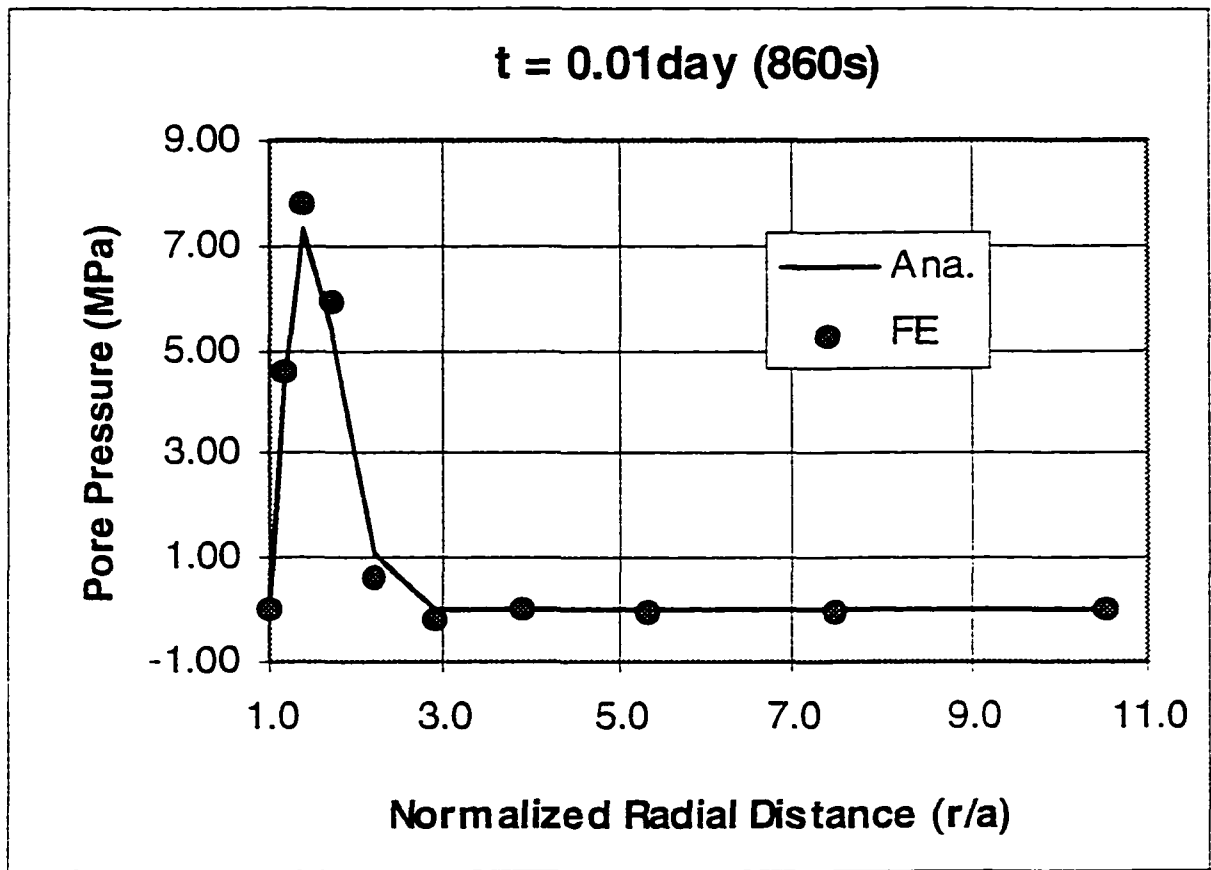


Figure 5.16: Comparison of numerical and analytical solutions for temperature induced pore pressure along the borehole radius ( t = 0.01 day )

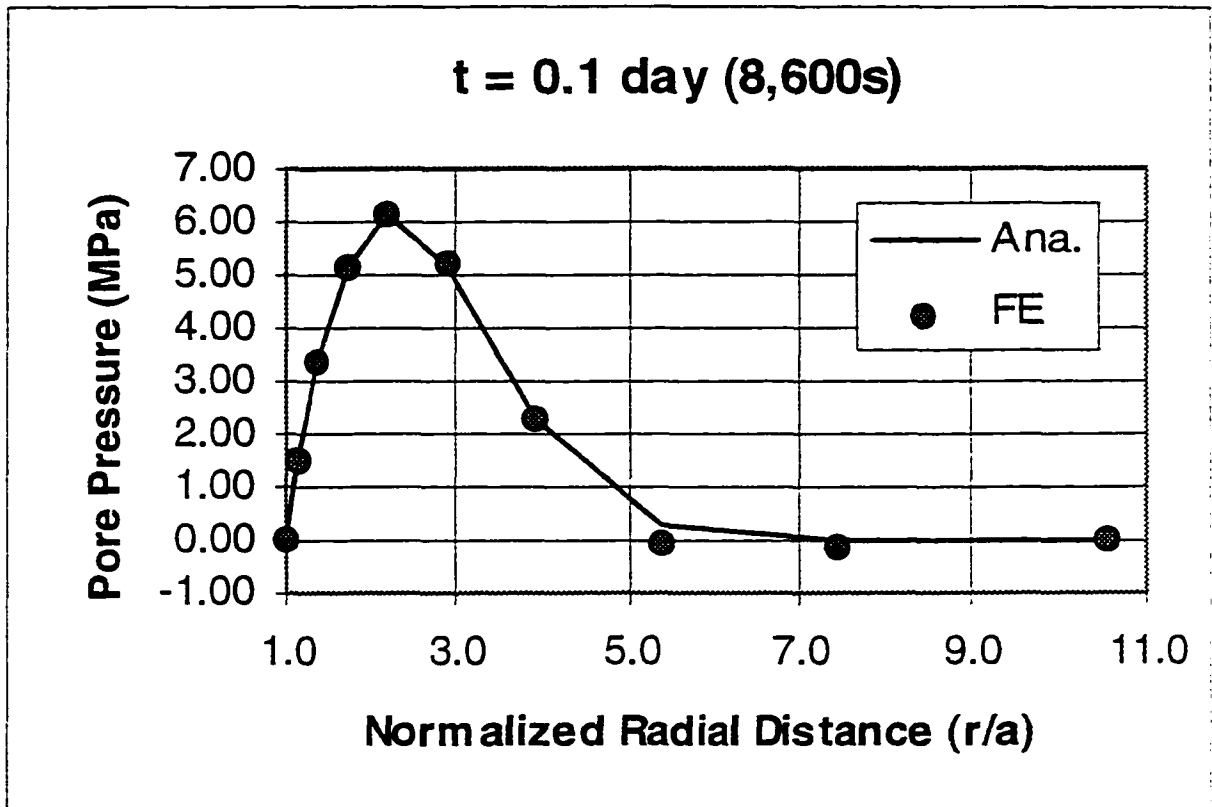


Figure 5.17: Comparison of numerical and analytical solutions for temperature induced pore pressure along the borehole radius ( t = 0.1 day )

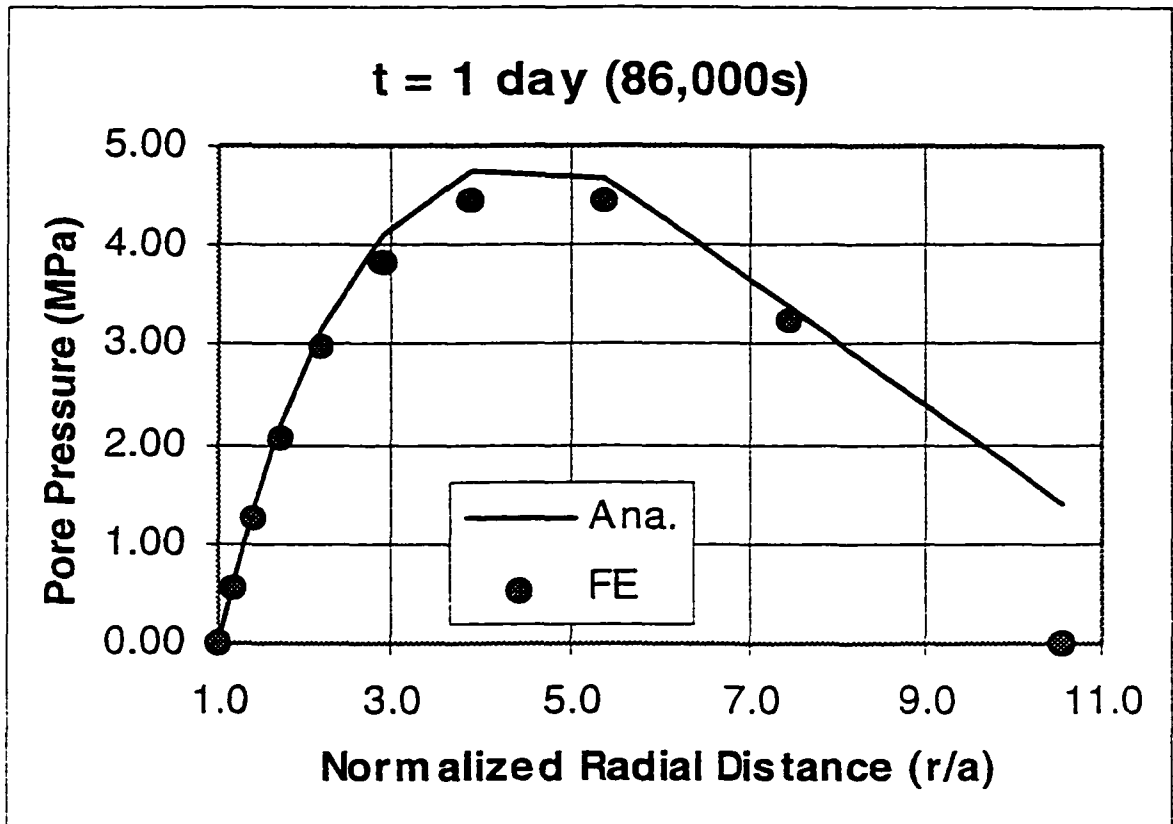


Figure 5.18: Comparison of numerical and analytical solutions for temperature induced pore pressure along the borehole radius ( t = 1 day )

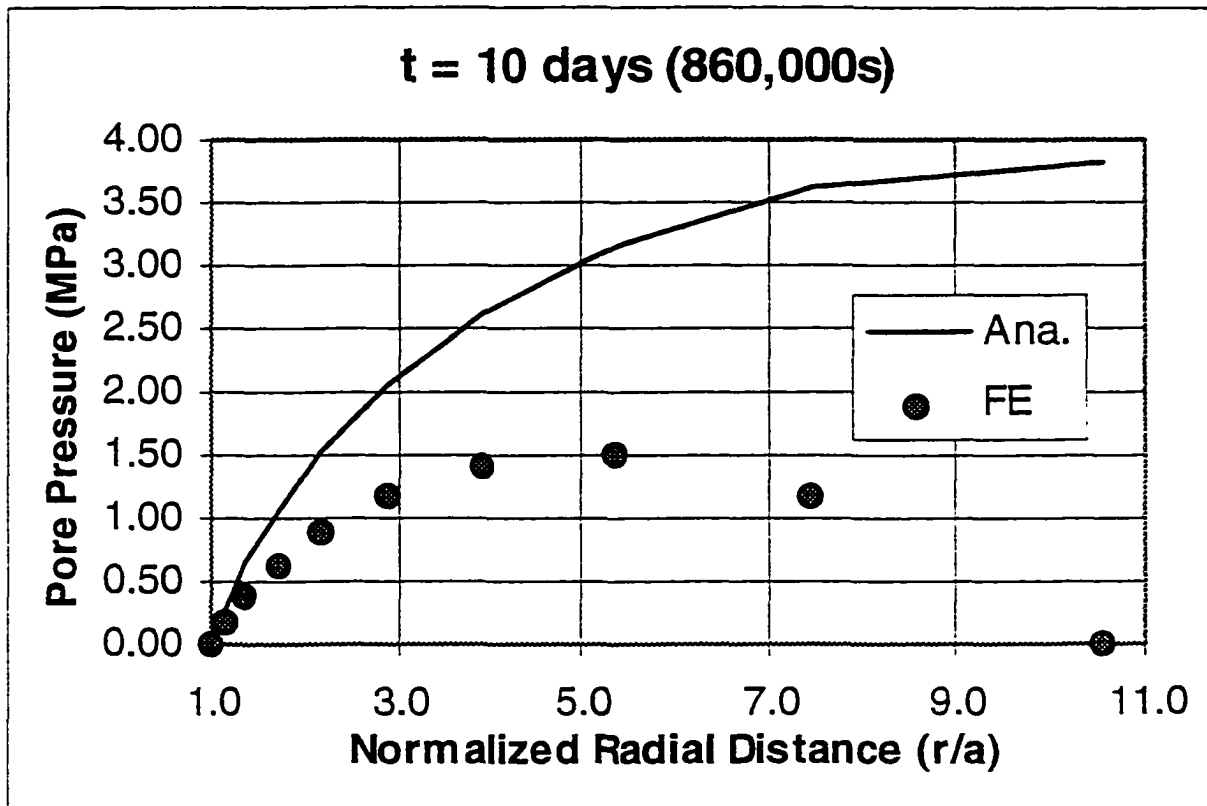


Figure 5.19: Comparison of numerical and analytical solutions for temperature induced pore pressure along the borehole radius ( t = 10 day )

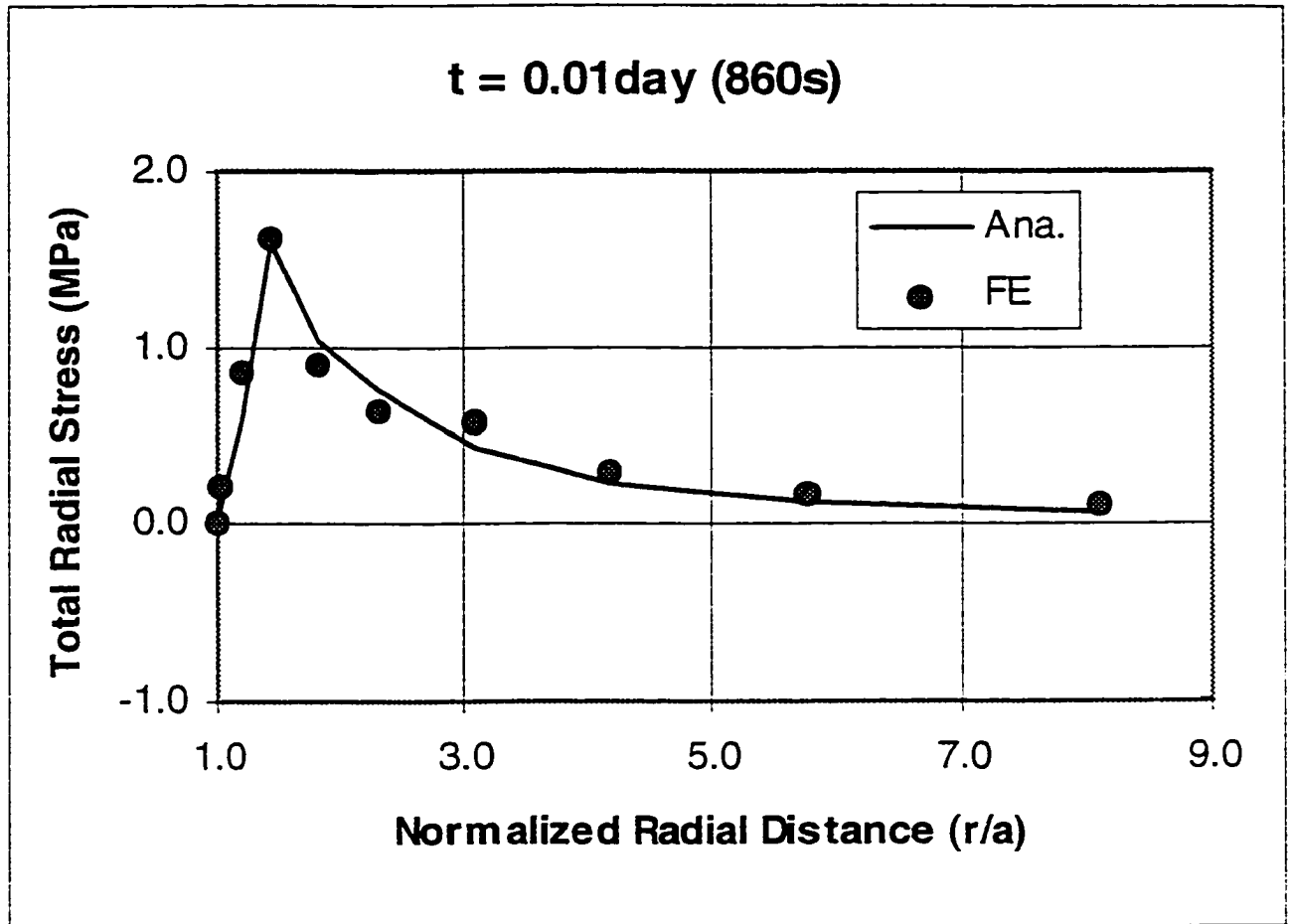


Figure 5.20: Comparison of numerical and analytical solutions for the total radial stress distribution along the borehole radius ( t = 0.01 day )

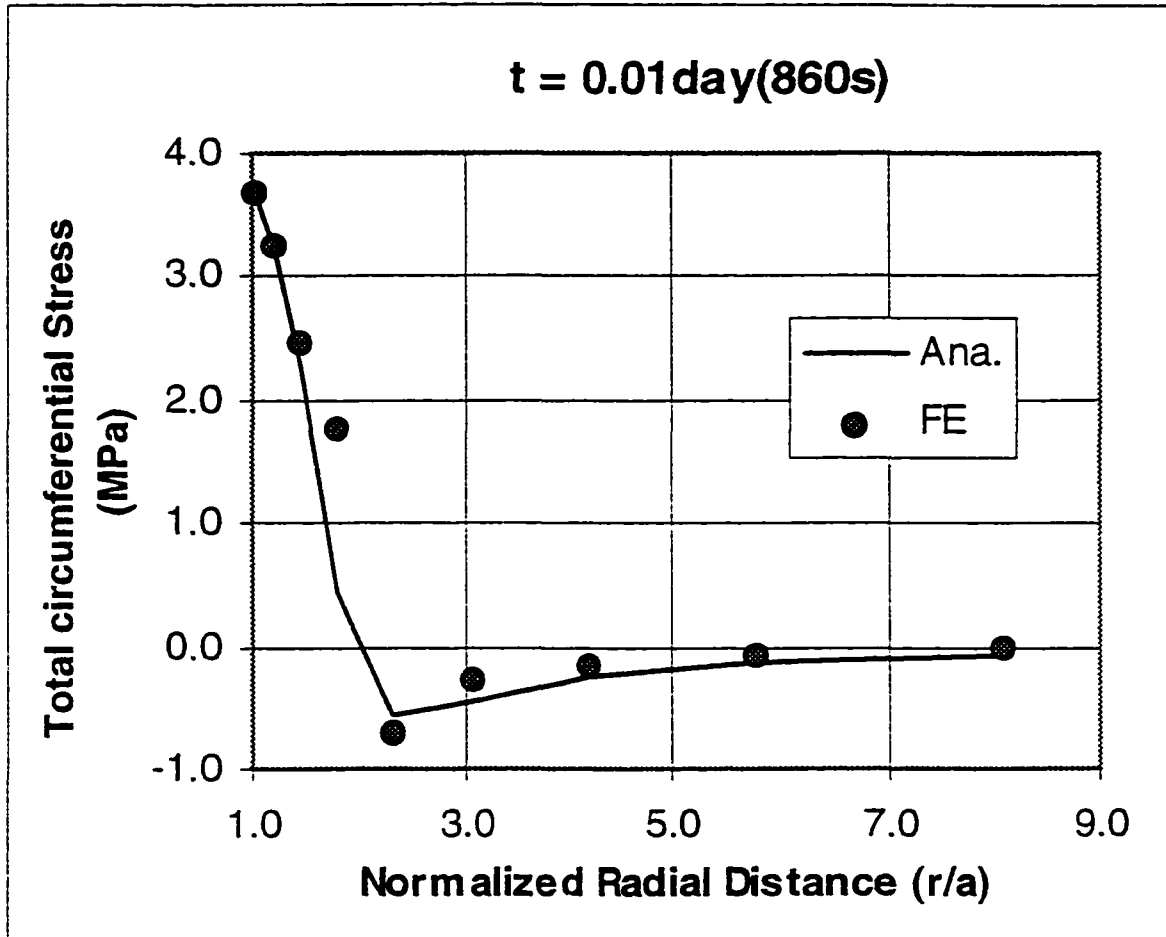


Figure 5.21: Comparison of numerical and analytical solutions for the total circumferential stress distribution along the borehole radius ( t = 0.01 day )

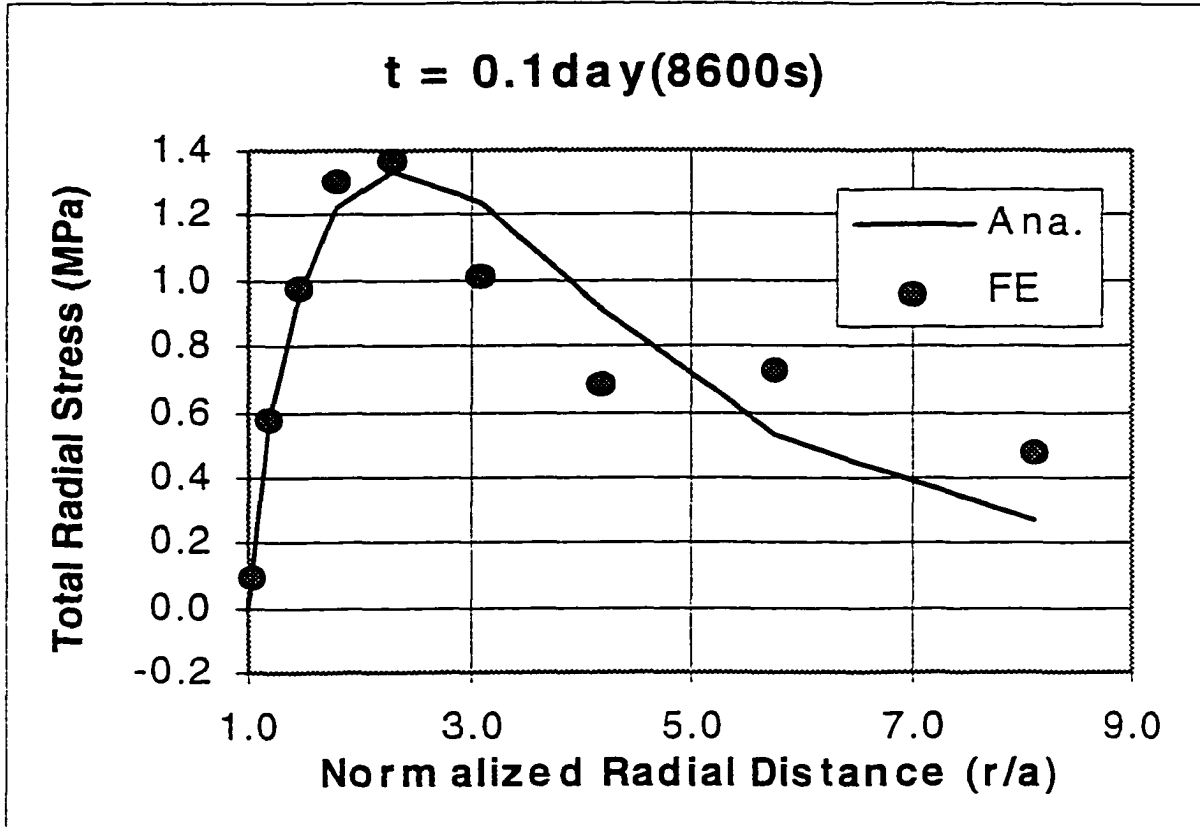


Figure 5.22: Comparison of numerical and analytical solutions for total radial stress distribution along the borehole radius ( t = 0.1 day )

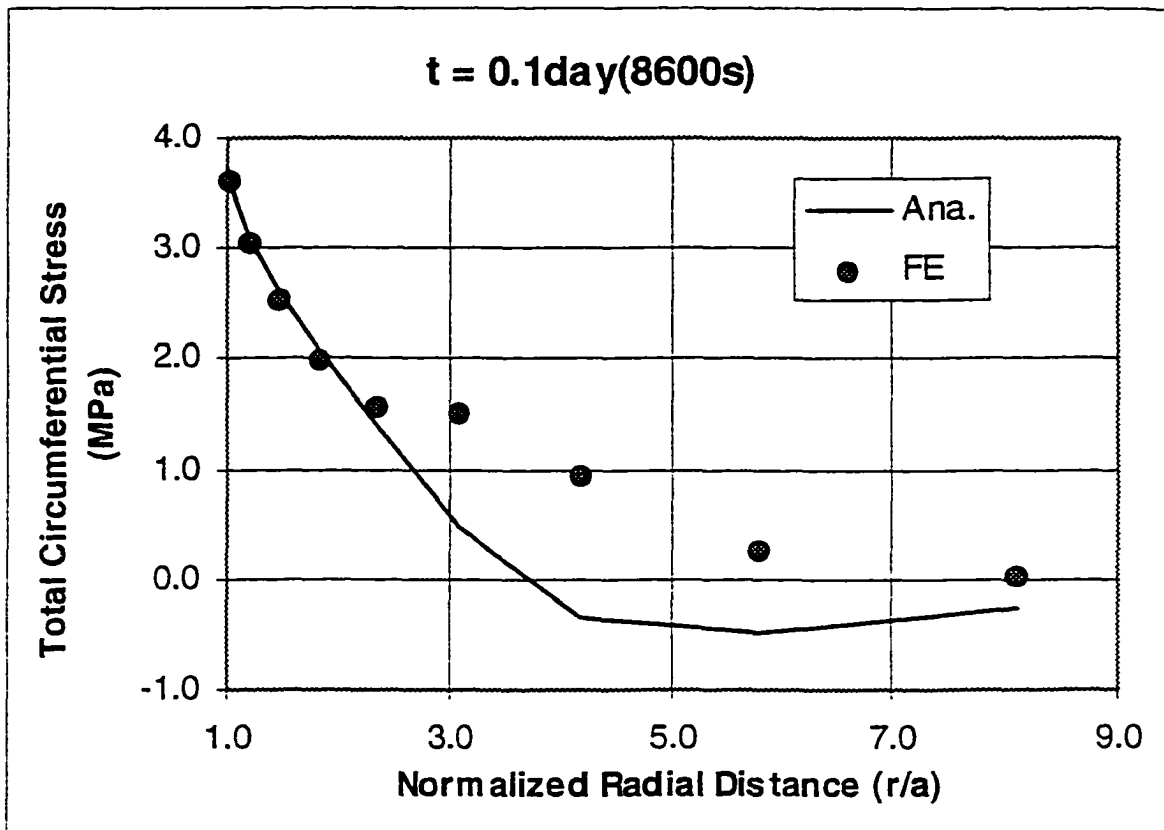


Figure 5.23: Comparison of numerical and analytical solutions for total circumferential stress distribution along the borehole radius ( t = 0.1 day )

## 6 Applications

This chapter discusses the applications of the thermoporoelastic solutions obtained in this dissertation. Clear physical insight into how the coupled THM process influences borehole stability will be provided through the analyses conducted. The potential significant impacts of non-isothermal drilling on the stability of inclined boreholes will be illustrated through a couple of numerical examples. Note that assumption (3.50) is applied in the following analyses due to lack of pore contraction data for shale for a more accurate model.

### 6.1 Basic Mechanisms of Thermoporoelastic Processes Affecting Borehole Stability

#### 6.1.1 Case I

In the following subsection, the basic mechanisms of thermoporoelastic processes affecting borehole stability will be illustrated through a diagnostic example: a section of a vertical borehole drilled in a shale, and subjected to trivial initial and boundary conditions except for the fact that a  $50^{\circ}\text{C}$  temperature difference is imposed on the borehole wall (Figure 6.1). The formation properties adopted for this example are listed in Table 6.1. Note that the sign of the total stress tensor has been changed to compressive positive in this section, to comply with the traditional rock mechanics convention.

$G$ ( $\times 10^9$ Pa)	$B$	$\kappa$ (darcy/cp)	$\nu$	$\nu_u$
3.82	0.78	$0.766 \times 10^{-7}$	0.24	0.31
$\alpha_m^T$ ( $^{\circ}\text{C}^{-1}$ )	$\alpha_f^T$ ( $^{\circ}\text{C}^{-1}$ )	$c^T$ ( $\text{m}^2/\text{s}$ )	$c^{fT}$ (Pa/ $^{\circ}\text{C}$ )	$\phi_0$
$18 \times 10^{-6}$	$300 \times 10^{-6}$	$1.6 \times 10^{-6}$	$5.2 \times 10^5$	0.14

Table 6.1: Thermoporoelastic Properties for Case I

### 6.1.2 Temperature-induced pore pressure and stresses

Figure 6.2 shows the transient temperature distribution, a typical conductive heat transfer case. The formation is gradually heated up while keeping the wellbore temperature constant. The temperature gradient at a fixed point decreases with time after the heat front reaches this point. At a fixed time, the temperature gradient decreases with distance. For the case of cooling, one could see that the formation will gradually be cooled off, by reversing the sign of the y-value in Figure 6.2.

Figure 6.3 is the temperature-induced transient pore pressure distribution. Because of the assumed permeable boundary conditions, the pore pressure is kept equal to zero along the borehole wall, but a significant pore pressure peak is generated near the borehole at early times. The peak decays with time, and moves away from the borehole. If, on the other hand, one considers the pore pressure history at a fixed point inside the formation, one would observe a gradual increase at the beginning, a peak, and then subsidence. In the case of cooling, the significant pore pressure drop near the borehole will occur at the beginning of the cooling. With time, the originally decreased pore pressure will gradually recover towards its original state.

Figures 6.4 and 6.5 present total radial and circumferential stresses induced by borehole temperature variations, respectively. The solid lines indicate the results from the thermoporoelastic model and the dotted lines indicate the exact thermoelastic results. As one can see, the impact of pore pressure on the stress distribution is significant. At early times, substantial differences between the results from the two models are observed near the borehole, especially for the circumfer-

ential stress. A significant compressive stress peak is initiated inside the formation for the thermoporoelastic model, but not for the thermoelastic model. At later times, the difference moves inside the formation and the two results converge toward each other near the borehole wall. This is because heating induces significant pore pressure near the borehole at early times. With time, the pore pressure near the borehole gradually dissipates, and the peak moves into the formation. Note that a tensile circumferential stress zone is generated inside the formation, at the back of the compressive stress zone. This is because the expansion of the material at the inner face of the borehole geometry, due to heating, imposes a tension on the outer side material, a mechanism similar to the fracturing of a glass when hot water is suddenly poured into it. For weak formations subjected to low initial stresses, this could imply a potential of fracture initiation from inside the formation.

### **6.1.3 Implications for Wellbore Stability**

#### **6.1.3.1 Shear Failure Potential**

##### **Heating**

The second feature revealed by Figures 6.4 and 6.5 is that the maximum difference between the circumferential and radial stresses occurs at the borehole wall for the thermoelastic model, but inside the formation for the thermoporoelastic model, and the difference for the thermoporoelastic model is almost double the value of the thermoelastic one. This implies that heating the borehole will greatly increase the potential of instantaneous shear failure, especially when combined with the significant pore pressure rising, as shown in Figure 6.6. The failure is much more severe in the thermoporoelastic case, and tends to initiate from inside the formation, rather than on the borehole wall. With time, the stress difference gradually decreases, and pore pressure gradually decays, so the borehole becomes more stable as far as shear failure is concerned.

## Cooling

The tendency is reversed in the case of cooling. Instantaneously, both the stress differences and the pore pressure will be decreased by the wellbore cooling, so the borehole is temporarily stabilized as far as shear failure is concerned. However, time-delayed failure could occur with the recovery of both stress difference and pore pressure with time, as shown in Figure 6.7. Note that for the case of a permeable boundary condition, the borehole wall always has the highest shear failure potential during cooling, and this potential does not change with time. In other words, the permeable boundary condition implies that the thermoporoelastic process does not come into play on the borehole wall.

### 6.1.3.2 Axial Failure Potential

Figures 6.8 and 6.9 present comparisons of the different stress components. It is observed that the axial stress is greater than the circumferential stress at both early and later times. This feature is unique for the temperature induced stresses. For a borehole in plane strain condition, the axial stress is always much smaller compared to the circumferential stress in the case of isothermal disturbances, such as borehole drilling and following pressurization. This implies a higher potential for the shifting of the shear failure plane from a transverse to axial direction under non-isothermal condition, as shown in Figure 6.8-(b).

### 6.1.3.3 Tensile Failure Potential

#### Spalling

Figure 6.10 displays the effective radial stress distribution at various times. For the case of wellbore heating, significant effective tensile radial stresses are developed near the borehole at early times, implying a high potential of borehole spalling (*spalling* here is defined as the radial tensile failure). This is due to the high pore pressure combined with the negligible increase in radial compressive stress induced by heating the wellbore. In the case of cooling, there is a slight potential for time-

delayed spalling to occur from inside the formation.

### **Fracturing**

Figure 6.11 plots the transient effective circumferential stress distribution. It can be seen that heating imposes a potential of fracture initiation from inside the formation at early times. Based on the conventional thermoelastic analysis, it is known that heating increases the potential of borehole shear failure, because the expansion of the material around the borehole during heating increases the compressive stress as well as the stress difference. Cooling, on the other hand, increases the potential of fracturing because of the circumferential tensile stress induced by the material shrinkage. In a thermoporoelastic process, heating could increase the potential of fracture initiation because of the high pore pressure generated. In the case of cooling, the maximum tensile stress always occurs on the borehole wall, so the fracture will always be initiated from the boundary. However, a tensile stress zone will develop into the formation with time, which can facilitate time-delayed fracture development.

#### **6.1.3.4 Time-delayed Heating-type of Problems**

Because of the geothermal gradient, the drilling fluid is always cooler than the formation when it first reaches the bottom hole, so the bottom hole will be stabilized at the beginning of drilling. When the borehole further deepens, the same section will be gradually heated up, as shown in Figure 6.12, implying a potential of time-delayed heating-type of problems, such as shear failure and spalling, occurring at the upper section of the borehole.

#### **6.1.3.5 Failure Potential for Different Formations**

Assuming Kurashige's assumption (3.50) is applicable for shale, and substituting (3.50) into Equation (3.42), one can see that the pore pressure induced by the temperature variation is proportional to two factors: (i) the differential thermal ex-

pansion between the porous matrix and pore fluid; and (ii) the formation porosity. It is also commonly known that the pore pressure accumulation in a poroelastic system is significantly affected by the formation permeability. Whereas the differential thermal expansion is more or less typical for a general rock-fluid system, the porosity and permeability can be quite different for different formations. The high pore pressure generation and accumulation in a thermoporoelastic process requires a high formation porosity and a low permeability, and shale is right in this category. Figure 6.13 plotted the pore pressure generated for different formations while keeping all other conditions constant. It can be seen that the pore pressure generated in shale is much higher compared to other formations. This could be a new explanation why shale is so problematic compared to other formations.

## 6.2 Application Examples

In this subsection, the impact of the thermoporoelastic process on borehole stability will be further illustrated through a couple of application examples.

### 6.2.1 Case II

The first example is a vertical well drilled in shale, subjected to a non-hydrostatic stress field, internal borehole pressure and temperature difference, as shown in Figure 6.14. The formation thermoporoelastic properties are the same as those listed in Table 6.1, and it is characterized by a uniaxial compressive strength of 20 MPa and an internal friction angle of  $30^\circ$ .

#### 6.2.1.1 Shear Failure

The Mohr-Coulomb failure criterion is adopted here for the shear failure analysis. The criterion can be expressed in terms of the maximum shear stress  $S$  as:

$$S = -\frac{1}{2}\sqrt{(\sigma_{\theta\theta} - \sigma_{rr})^2 + 4\sigma_{r\theta}^2} \quad (6.1)$$

and the mean effective stress  $P'$  :

$$P' = -\frac{1}{2}(\sigma_{\theta\theta} + \sigma_{rr}) - p \quad (6.2)$$

In the  $S - P'$  space, the Mohr-Coulomb criterion is expressed by a straight line:

$$S = P' \sin \phi_f - \frac{1 - \sin \phi}{2} q_u \quad (6.3)$$

where  $\phi_f$  is the internal friction angle, and  $q_u$  is the uniaxial compressive strength of the material. The stress points above the straight line indicate that shear failure will occur (Figure 6.15) . This analysis assumed that failure is independent of the out-of-plane stress  $\sigma_z$ .

Figure 6.15 presents the stress profiles along the  $\sigma_h$ -direction at various times. The solid lines denote the thermoporoelastic solutions for the condition of heating a borehole up to 50°C. The dotted lines represent the poroelastic solutions. Heating the borehole obviously increases the potential of shear failure significantly. For a mud weight that happens to be safe for the case of an isothermal poroelastic process, shear failure near the borehole region exists under non-isothermal conditions. As it is stated in the last subsection, this is a direct consequence of significant pore pressure and stress changes induced by heating the borehole. Figure 6.15 also indicates that instantaneous failure may occur from inside the formation and this potential decreases with time (note the peak point in stress profile at  $t = 0.001$  day). In addition, the failure potential increases with time along the borehole wall, indicating a mechanism for time-delayed shear failure. However, this mechanism is actually due to the mode 3 poroelastic effects[51]. As it was mentioned earlier, the thermoporoelastic process does not come into play on the borehole wall for the permeable boundary models.

Figure 6.16 presents the stress histories of two points along the  $\sigma_h$ -direction, one point on the borehole wall and one slightly inside the formation, and for heating the borehole at different temperatures while keeping the wellbore pressure constant. Again, it clearly indicates that heating increases the potential of shear failure, and this potential increases monotonically with the increase of temperature. As it is

showed in Figure 6.15. Figure 6.16 again indicated the potential of instantaneous shear failure inside the formation (notice the stress at earlier time for  $\Delta T = 30^\circ\text{C}$ ), and the decrease of this potential with time; as well as the increase of failure potential on the borehole wall with time.

Figure 6.17 displays the isochrones of stress distribution around the borehole, at  $r = 1.1a$ , for heating, cooling and isothermal conditions. While heating the borehole increases the potential of shear failure, cooling the borehole stabilizes the borehole at the early stages after drilling. However, time-delayed failure will occur at later time, as indicated in the figure (after cooling the borehole for 10 days). Note that in the case of heating, the highest failure potential occurs along the minor horizontal stress direction (Figure 6.18-(a)), which means the shear failure is an active one and it can be prevented by increasing the mud weight. Whereas the time-delayed shear failure during cooling occurs along the major horizontal stress direction, which means a passive shear failure (Figure 6.18-(b)); hence, increasing the mud weight will worsen the situation. As a matter of fact, the time-delayed failure during cooling is a combined effect of wellbore cooling and higher mud weight. This mechanism will be explained further when discussing Case III.

#### 6.2.1.2 Tensile Failure

##### Spalling

Figure 6.19 plotted the isochrones of effective radial stress profiles along the  $\sigma_h$  direction for the condition of heating the wellbore by  $50^\circ\text{C}$ . It can be seen that instantaneously after drilling, large tensile stresses developed near the borehole wall. As it is stated before, this is due to the high pore pressure combined with the negligible increase in radial compressive stress induced by heating the wellbore and the phenomena implies a spalling failure, or chip formation, during drilling.

According to the report by Salisbury [132], a series of test on shale samples simulating downhole temperature and pressure condition has been conducted and the data revealed that spalling is one of the major failure mode in shales. Prior to that,

a case of heating induced borehole spalling was also observed in an exhaust passage of an underground diesel-powered electric generator installation[68]. However, the traditional elastic/plastic wellbore stability models does not predict spalling as a major potential failure mode.

### Fracturing

Figure 6.20 shows the isochrones of the circumferential stress distribution around the borehole, slightly inside the formation, for both poroelastic and thermoporoelastic solutions. In this case, the thermoporoelastic solution gives a higher fracture initiation pressure than the poroelastic solution under the condition of borehole heating and a lower fracture initiation pressure under the condition of borehole cooling, which complies with the common concept that heating decreases, but cooling increases the fracture potential. This is a case where the thermoelastic effects overwhelm the thermoporoelastic effects, *i.e.*, the change of effective stress due to the change of pore pressure with temperature is less prominent than the change of effective stress due to the change of thermoelastic stress. In other words, the change of pore pressure is not significant enough to reverse the sign of the effective stress. Theoretically, if the increase/decrease of pore pressure due to the rise/lower of the temperature dominates the circumferential effective stress response, heating can increase, and cooling can decrease the potential of fracture initiation, as it will be illustrated in case III.

Since pore pressure due to the cooling/heating recovers/decays with time, fracture potential increases/decreases with time for the case of cooling/heating, as shown in the figure, implying the potential of time-delayed lost circulation in the case of cooling, and an improved condition for the case of heating.

### 6.2.2 Case III

The last example is an inclined borehole drilled in shale (Figure 6.21), and in a tectonically stressed area with a strike-slip fault type in-situ stress regime, where:

$$S_x = 29\text{MPa}, \quad S_y = 20\text{MPa}, \quad S_z = 25\text{MPa}.$$

The initial pore pressure was assumed to be 9.8MPa, the wellbore radius is 0.1m, and the temperature difference applied on the borehole wall is 30°C. The formation thermoporoelastic properties are given in Table 6.2.

$G$ (Pa)	$B$	$\nu$	$\nu_u$	$\kappa$ (darcy/cp)
$8.88 \times 10^9$	0.596	0.189	0.314	$0.5 \times 10^{-7}$
$\phi_0$	$\alpha_m^T$ ( $^{\circ}\text{C}^{-1}$ )	$\alpha_f^T$ ( $^{\circ}\text{C}^{-1}$ )	$c^T$ ( $\text{m}^2/\text{s}$ )	$c^{JT}$ ( $\text{Pa}/^{\circ}\text{C}$ )
0.14	$3.5 \times 10^{-5}$	$3.0 \times 10^{-4}$	$1.5 \times 10^{-8}$	$5.2 \times 10^5$

Table 6.2: Thermoporoelastic properties for Cases II and III

### 6.2.2.1 Shear Failure

Figure 6.22 presents the movement of stress clouds with temperature and time changes in  $\sigma'_m - \tau_m$  space, where:

$$\sigma'_m = \frac{\sigma_1 + \sigma_3}{2} - p \quad (6.4)$$

is the effective 2D mean stress; and,

$$\tau_m = \frac{\sigma_1 - \sigma_3}{2} \quad (6.5)$$

is the maximum shear stress. The stress clouds plotted are for the stresses around the borehole at  $r = 1.1a$ , for a fixed wellbore azimuth  $\varphi_z = 30^{\circ}$ , and a deviation angle  $\varphi_y = 60^{\circ}$ . The straight line in the plot is the Mohr-Coulomb failure criterion for a material that is characterized by a uniaxial compressive strength  $q_u = 25\text{MPa}$  and an effective internal friction angle  $\phi_f = 30^{\circ}$ . The part of the stress clouds residing above the straight line means failure will occur in a certain portion of the wellbore.

Again, as indicated in the figure, heating or cooling of a wellbore can significantly change its stability condition, especially at the early stage of the temperature variation. At  $t = 0.001$  day after drilling, the stress clouds for heating, isothermal and cooling conditions are far apart from each other. While the isothermal stress

cloud is located near the failure criterion, 95% of the stress cloud for the heating condition resides above the failure criterion implying an almost complete failure of the wellbore. Whereas the stress cloud for the cooling condition moves farther below the failure criterion, implying a significantly stabilized wellbore condition. At 10 days after drilling, the stress clouds for the non-isothermal condition move close to the stress cloud assuming an isothermal condition. Note that under the same temperature conditions, the movement of the stress clouds is basically along the  $\sigma'_m$  axis, indicating that the dominant reason for the stress change with time in a non-isothermal poroelastic process is due to the pore pressure diffusion. Under the heating condition, the highest pore pressure appears at the beginning, and it gradually decays with time. Hence, the effective stress increases, and the wellbore becomes more stable with time. Under cooling condition, the pore pressure is lowered at the beginning, and gradually recovers with time. Hence, a borehole will be stabilized at the beginning of cooling but failure potential will increase with time, as indicated in the figure. Since the stress clouds for the different temperatures is aligned along a direction neither parallel to the  $\sigma'_m$  nor to the  $\tau_m$  axis, it means that the thermoporoelastic process effects not only the pore pressure, but also the total stresses around the borehole - a phenomenon that can only be captured by a coupled thermoporoelastic model. Also note that the time-dependent effects are much more significant under non-isothermal conditions compared to that under an isothermal condition.

Figure 6.23 shows the change of the maximum effective collapse stress around the borehole as a function of borehole deviation angles and wellbore temperature. The effective collapse stress is defined by:

$$\tau_{col} = \tau_m - \left( \sigma'_m \sin \phi_f - \frac{1 - \sin \phi_f}{2} q_u \right) \quad (6.6)$$

A positive value of  $\tau_{col}$  represents failure. So, Figure 6.23 provides an illustration of how close the wellbore is to shear failure at different wellbore temperatures, and for different deviation angles.

The curves in Figure 6.23 can be divided into two groups: one for small times

and one for longer time periods. The curves within the small time group are parallel to each other, implying that the instantaneous temperature effect itself is independent of the borehole deviation angle. In fact, for the two-dimensional plane strain model adopted here, the temperature effects is clearly independent of the borehole azimuth and deviation angles, disregarding time. The unparallel curves during cooling for the large times are due to the change of the maximum shear failure location compared to the heating and isothermal conditions. If the failure location happens to be fixed for all the temperature conditions, the curves within each time group will be parallel to each other, as shown in Figures 6.24 and 6.25. Within each temperature group, the stability condition changes slightly with the borehole deviation angle and with time. For example, the collapse stress decreases more for the low deviation angle boreholes and decreases less for the high deviation angles in the case of heating, but it increases less for low deviation angle boreholes and increases more for the high deviation angle boreholes under wellbore cooling conditions. However, these effects are due to the time-dependent pore pressure and stress changes induced by mode 3 loading in problem I, which is a function of the in-plane stress difference; hence, it varies with the borehole deviation angles.

A general tendency presented for all the temperature conditions is that the failure potential decreases with an increase of the wellbore deviation angle; indicating that horizontal wells have the most stable wellbore condition. This is due to the strike-slip in-situ stress regime in this example where horizontal well sees a smaller in-plane stress difference than a vertical well.

Similar as presented in Figure 6.22, heating greatly increases the potential of shear failure, whereas cooling imposes a potential of time-delayed failure, for all the borehole deviation angles.

### 6.2.2.2 Fracturing

Figure 6.24 plotted the effective fracturing stress

$$\sigma_{frc} = \sigma'_{\theta \min} - T_{ens} \quad (6.7)$$

as a function of borehole deviation angle; where  $\sigma'_{\theta \min}$  is the minimum circumferential stress around the borehole, and  $T_{ens}$  is the tensile strength of the material which is assumed to be zero in this example.  $\sigma_{frc} > 0$  represents a safe wellbore condition, and  $\sigma_{frc} \leq 0$  represents radial fractures will be initiated on the borehole wall.

Figure 6.24 shows that, instantaneously, heating increased the potential of fracture initiation. As it is stated in the last example, this reversion from the common knowledge that heating will decrease the potential of fracturing is because of the significant pore pressure variation induced by the non-isothermal poroelastic process. With time, the fracturing potentials change slightly with the borehole deviation angle with time, for the same reason given in Figure 6.23. Note that the time-dependent effects are much more prominent for the condition of cooling compared to the condition of heating. As it is mentioned in the last case, this is actually a combined effect of high-pressure and high-temperature.

The pore pressure diffusion process induced by the over-balanced mud weight is analogous to the process of temperature diffusion via conductive heat transfer while keeping the borehole temperature constant: the pore pressure inside the formation gradually rises with time. When it is combined with the pore pressure decaying process during the wellbore heating, the two effects will cancel each other. When it is combined with the pore pressure recovering process during wellbore cooling, the two effects will add to each other, which results in a significant difference in time-dependent effects during heating and cooling.

In high-temperature, high-pressure and deep wells, high mud weight are usually required to counteract the high formation pressure, and cooling effects can be significant at the beginning of the drilling. Therefore, it is necessary to be aware of the potential time-delayed lost circulation in these wells, as shown in Figure 6.24, especially if over-balanced mud weights are used for some reason.

The most common practice of preventing wellbore instability is to increase the mud weight. However, in a poroelastic system, one has to be cautious with the long

term effects of increasing mud weight. Besides the time-delayed lost circulation, overly high mud weights can also induce time-delayed passive shear failure, as it is shown in Figures 6.17 and 6.18. and time-delayed spalling, as it will be explained in Figure 6.26.

### 6.2.2.3 Spalling

Figure 6.25 presents the effective radial stress as a function of borehole deviation angle and temperature. Again, assuming the formation tensile strength to be zero. A positive effective radial stress means a safe wellbore; otherwise, the borehole spalling, or chip formation, will occur.

Figure 6.25 shows that heating the wellbore imposes a high potential of instantaneous wellbore spalling, and the potential decreases with time; whereas cooling the wellbore tends to induce time-delayed borehole spalling. This tendency is more or less unaffected by the borehole deviation angle because the effective radial stress near the borehole is dominated by the wellbore and formation pressures, both of which are independent of the borehole deviation angles.

Figure 6.26 is a further illustration of the combined effects of highly overbalanced mud pressure and high-temperature on wellbore problems. When the mud weight is low, the non-isothermal and the unloading process dominate the pore pressure diffusion process; hence, borehole spalling occur at early times, but the wellbore becomes more stable with time, which is normal for the case of borehole heating. When the mud weight is abnormally high (an unpractical high mud weight was intentionally selected to demonstrate the mechanism), the over-balanced mud weight will dominate the pore pressure diffusion process. Under this condition, the wellbore is very stable at early times as far as the borehole spalling is concerned. However, the effective radial stresses substantially decrease with time, and time-delayed spalling will finally occur.

### 6.3 Summary

A conventional mud weight stability profile which is used in drilling design for the prediction of safe operating mud weight window comprises the critical mud weights for active, passive shear failures, and fracturing. If considering the formation as a thermoporoelastic system, it is indispensable to include the critical mud weights for borehole spalling in mud weight stability profiles, because high mud weight is usually required to prevent the heating-induced borehole spalling, but high mud weights also impose higher potential of passive shear failure and fracturing as well. The mud weight required to prevent borehole spalling could be higher than the mud weight required to prevent the active shear failure under the same temperature conditions. In this case, the safe operating mud weight window will be narrowed.

In addition, the long-term safe operating mud weight windows which take into account the disadvantageous long-term effects such as wellbore cooling, high mud weight, and temperature evolution along the borehole, are also necessary for the prevention of time-delayed failures, and the right selection of the casing points.

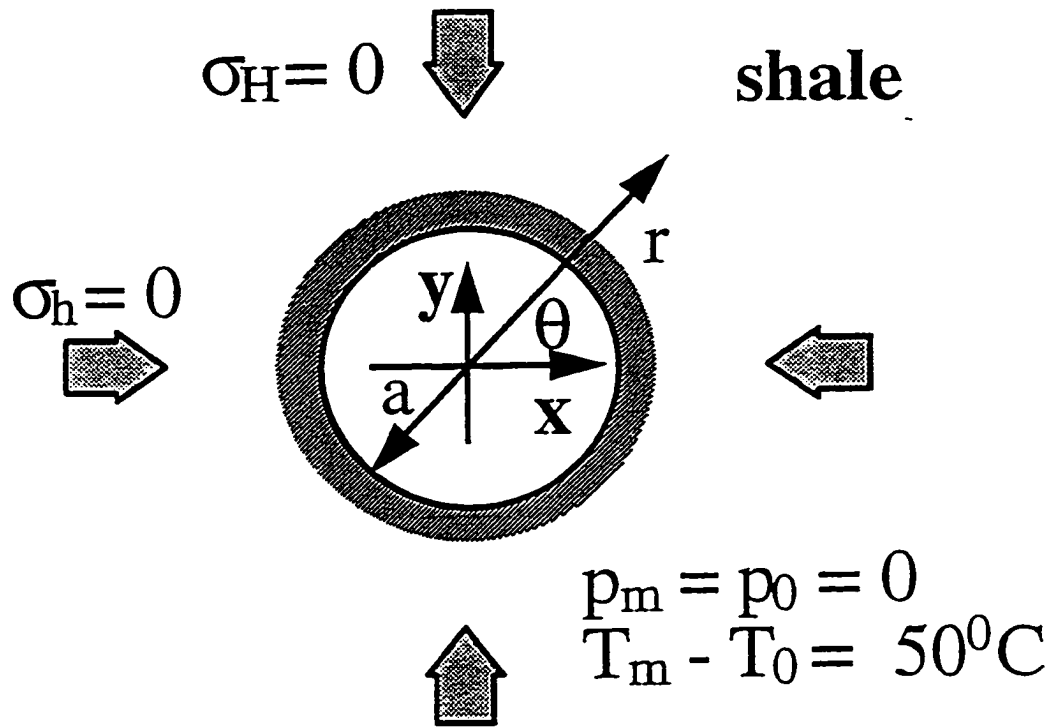


Figure 6.1: Boundary and initial conditions for Case I

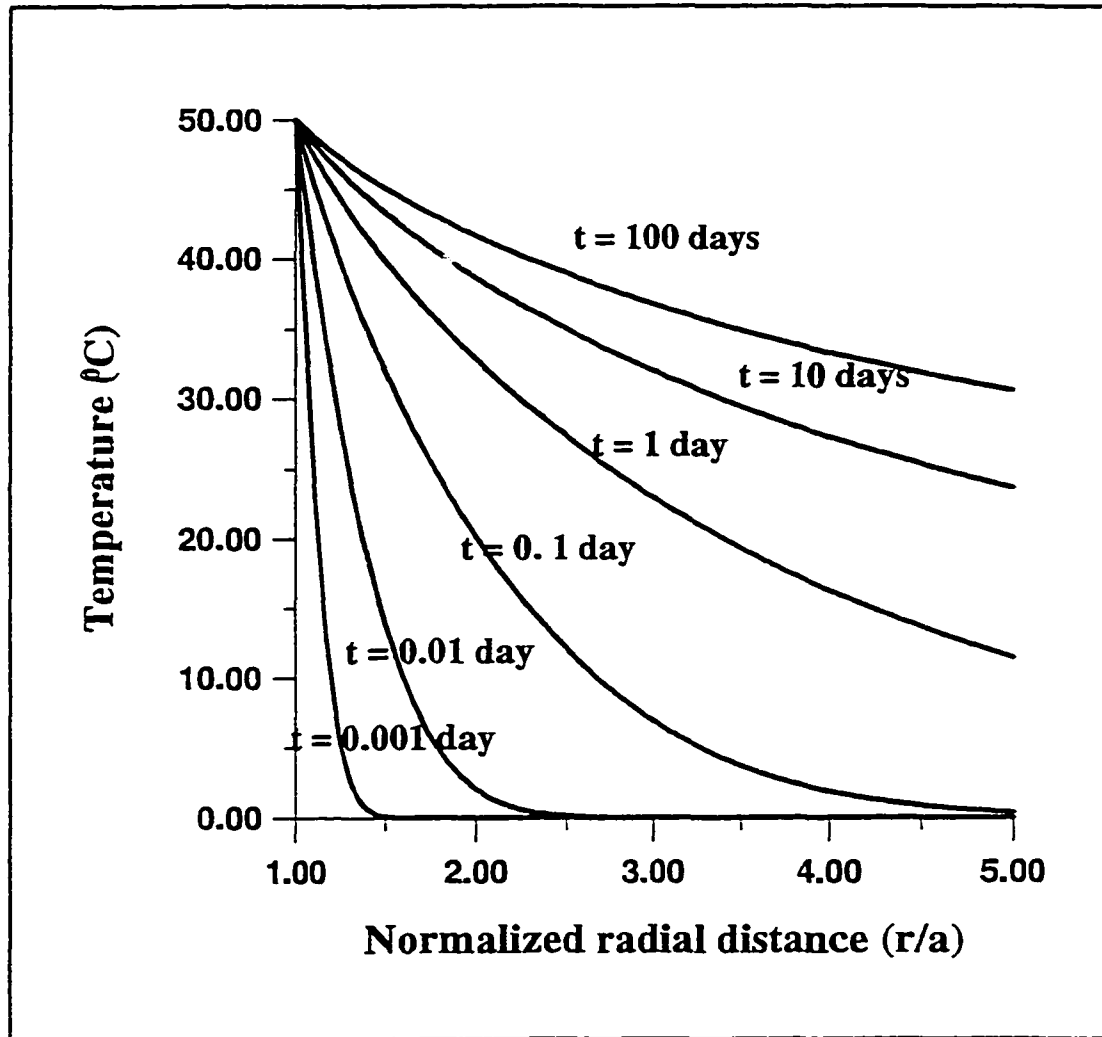


Figure 6.2: Transient temperature distribution

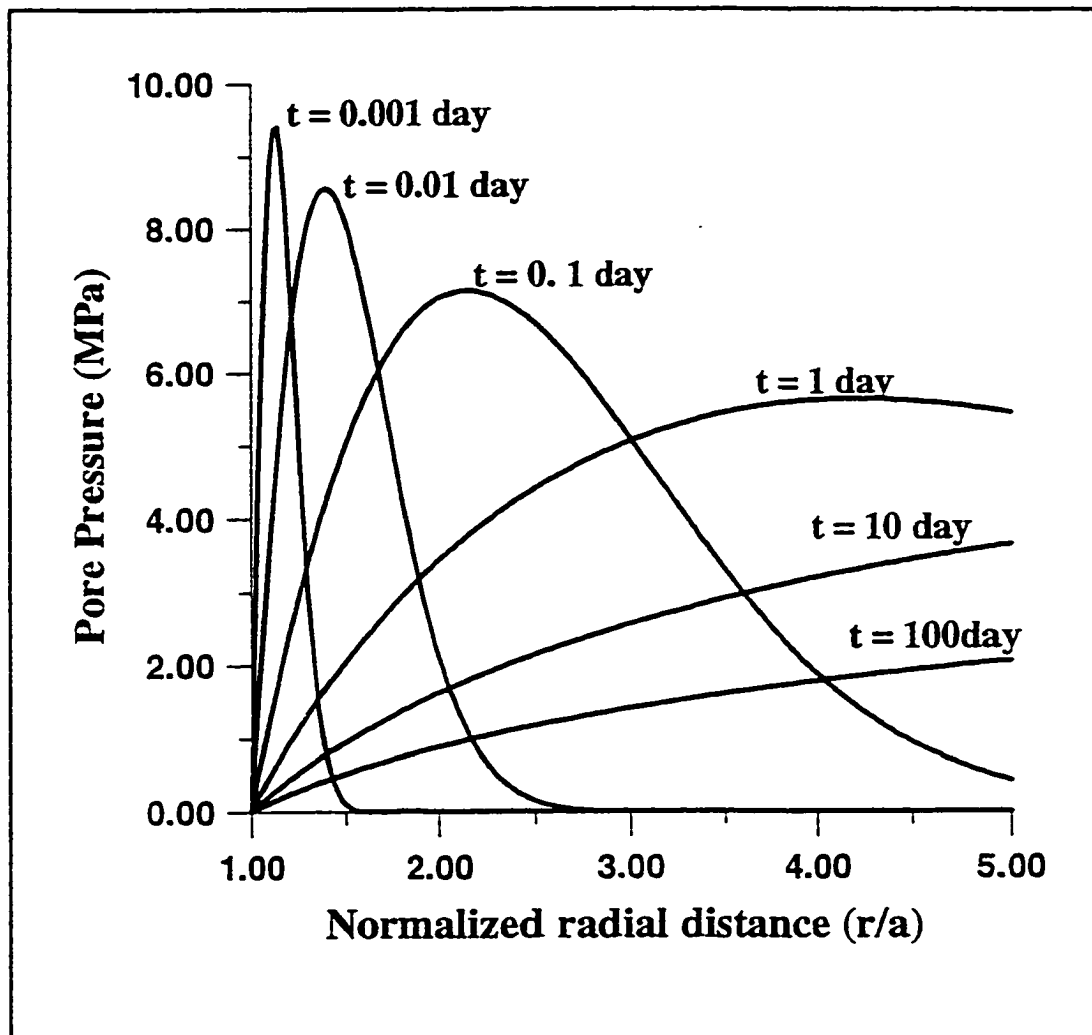


Figure 6.3: Temperature-induced pore pressure

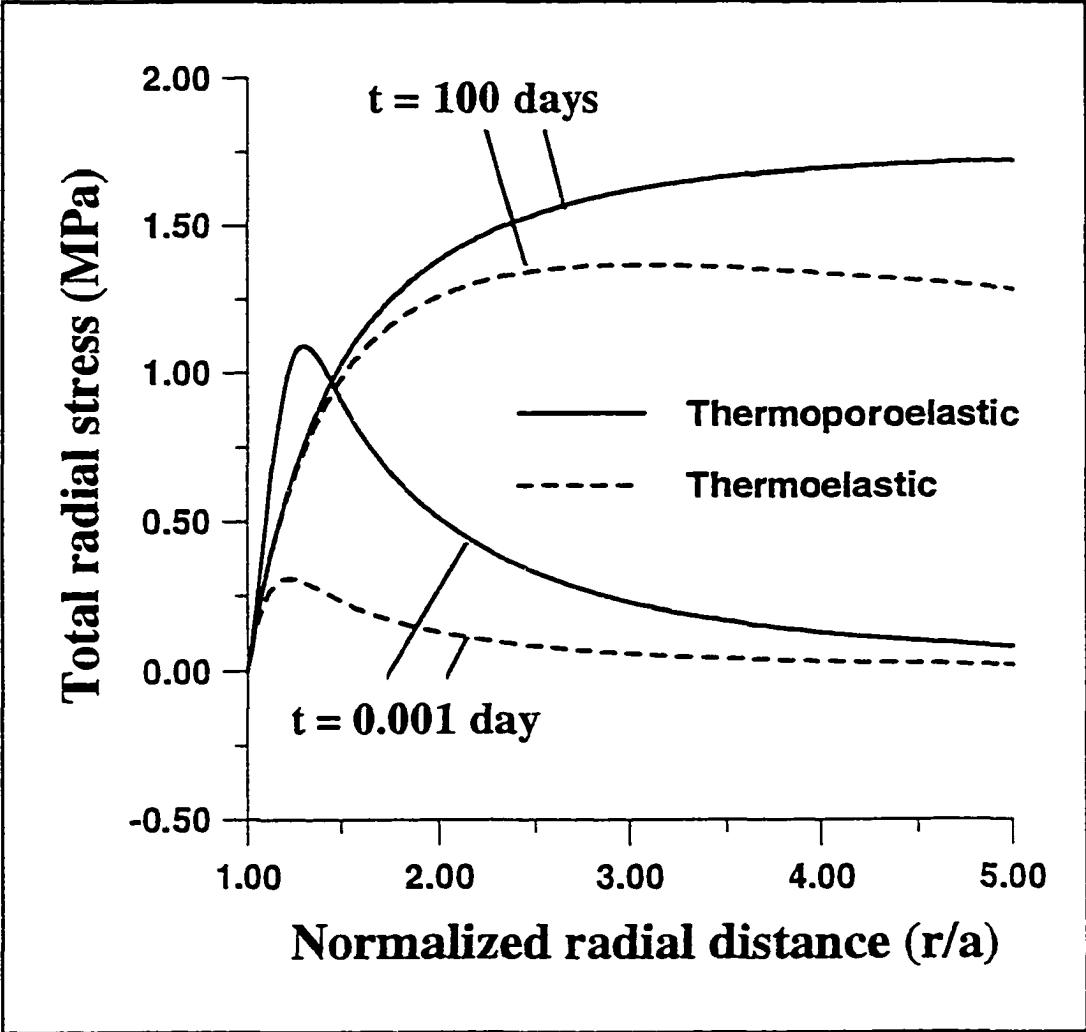


Figure 6.4: Total radial stress profile

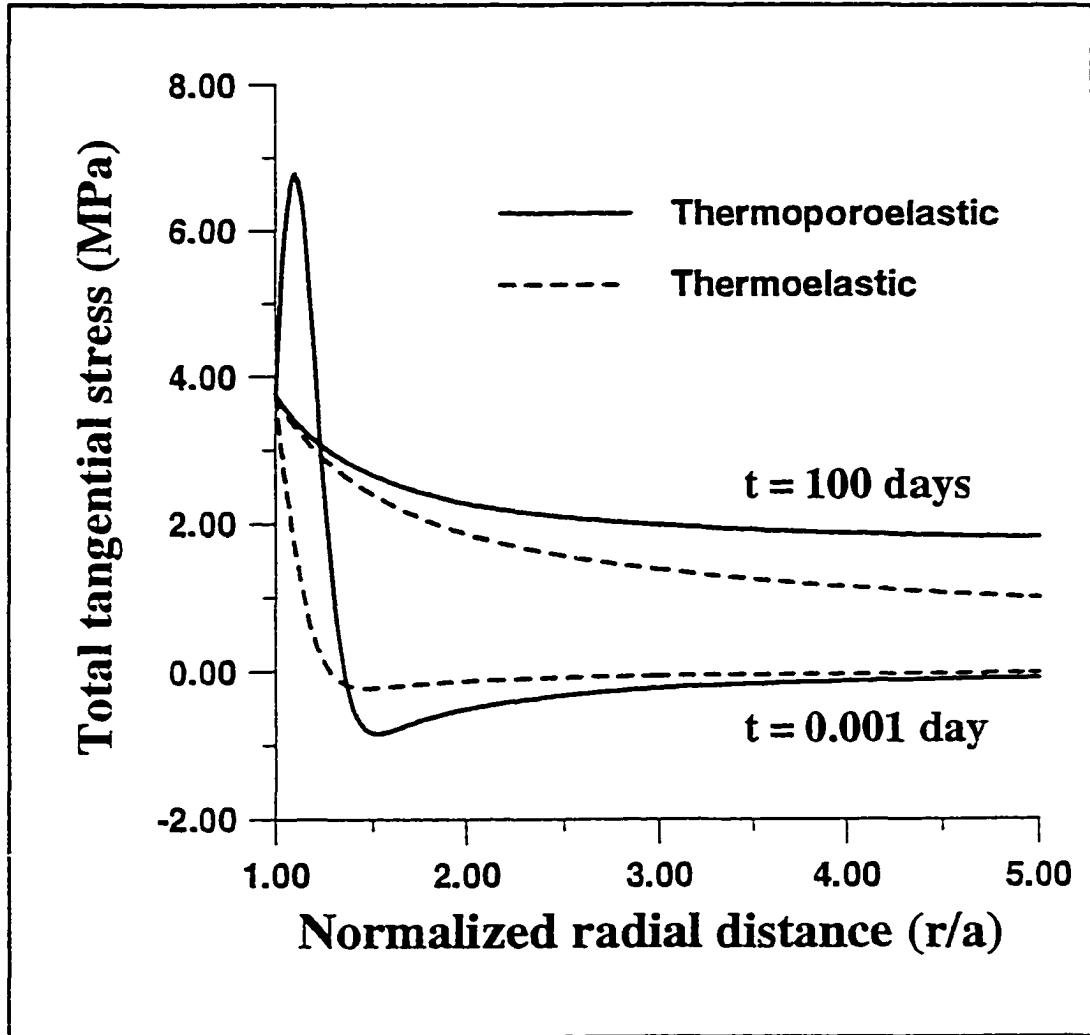


Figure 6.5: Total circumferential stress profile

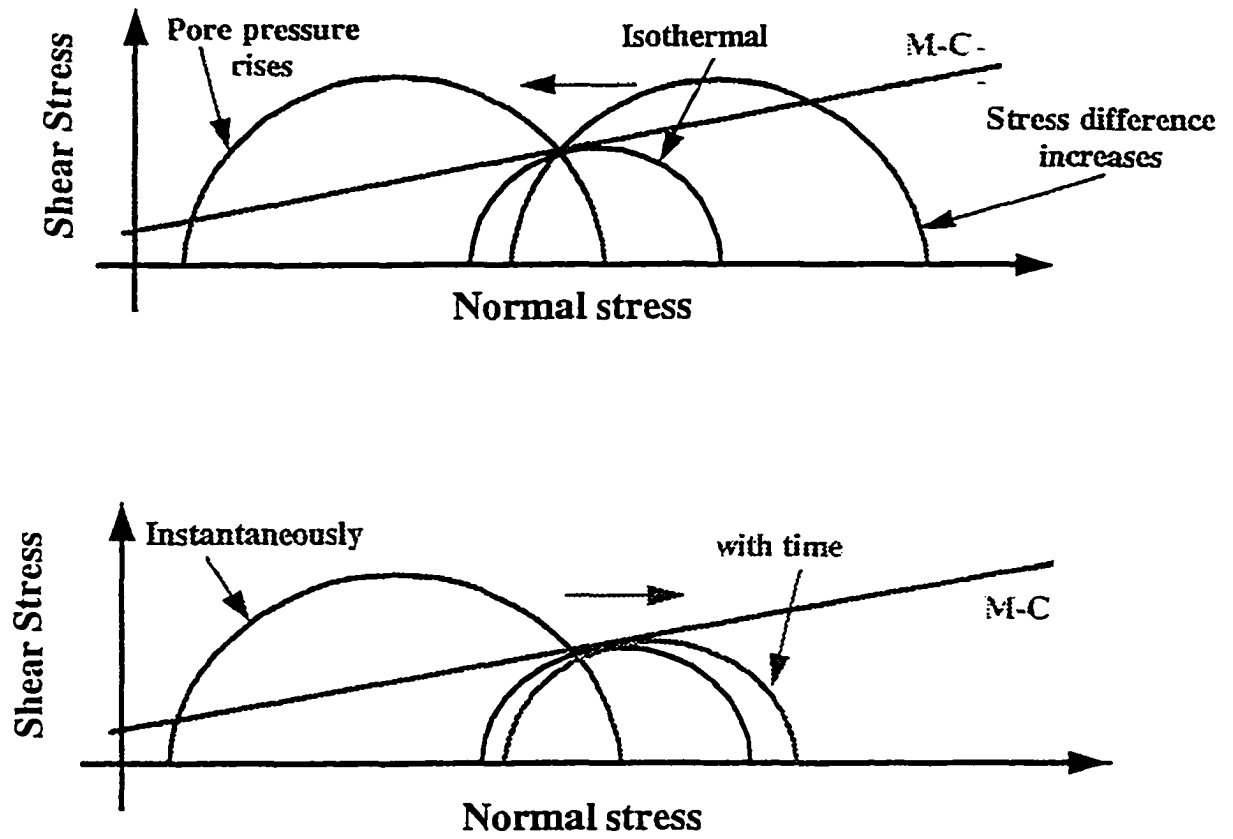


Figure 6.6: Heating induced shear failure potential

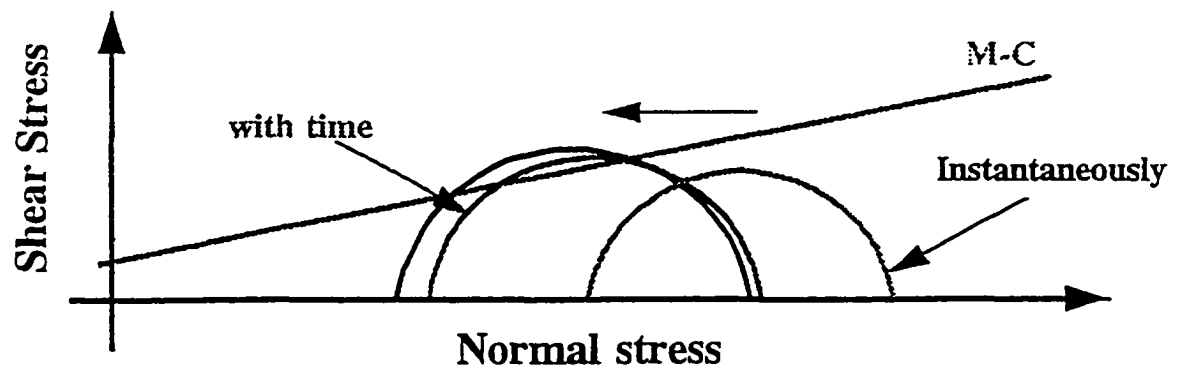
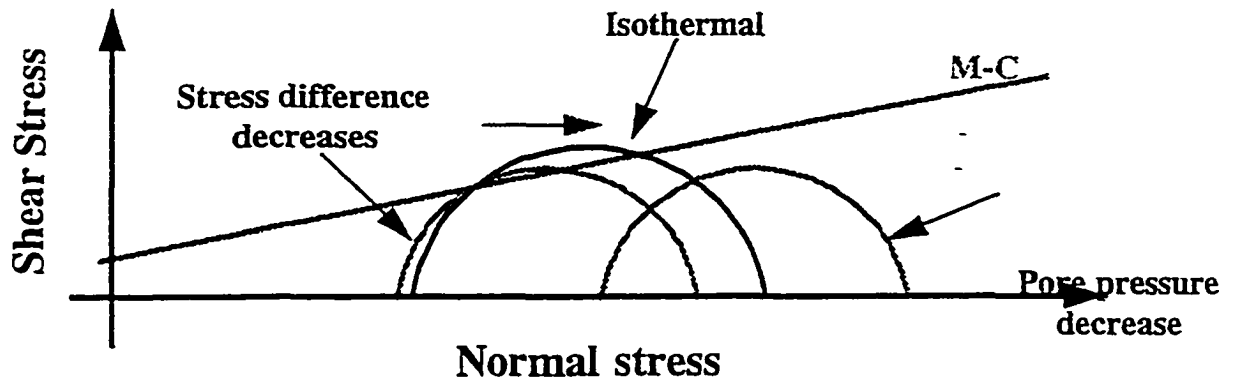
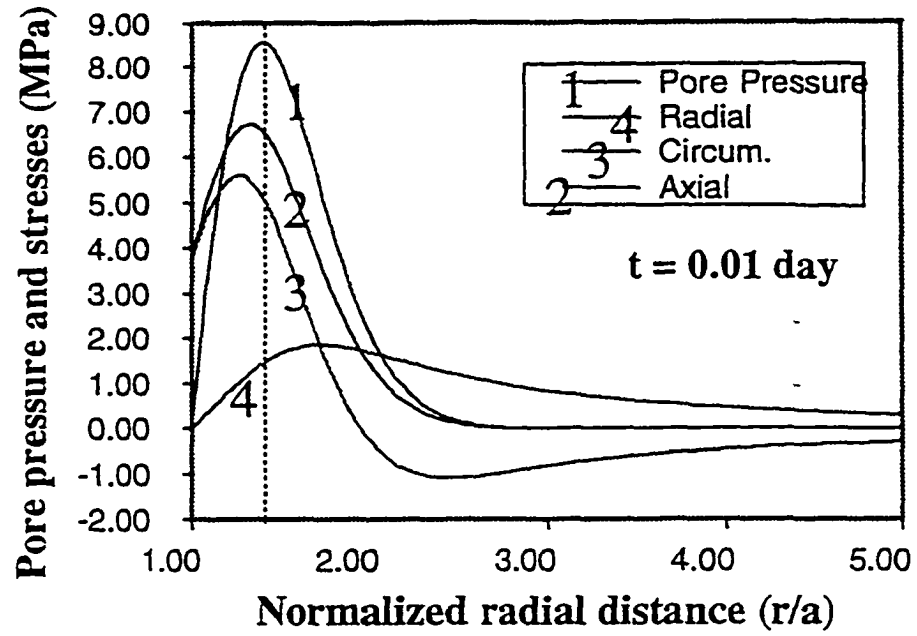
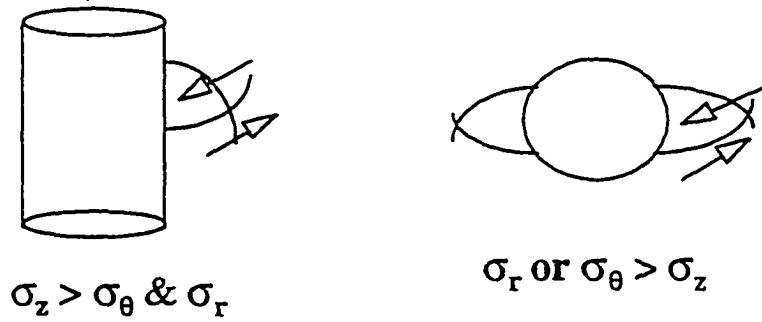


Figure 6.7: Cooling induced shear failure potential



(a) Comparison of stresses



(b) Different axial failure mode

Figure 6.8: Comparison of the magnitude of different stresses

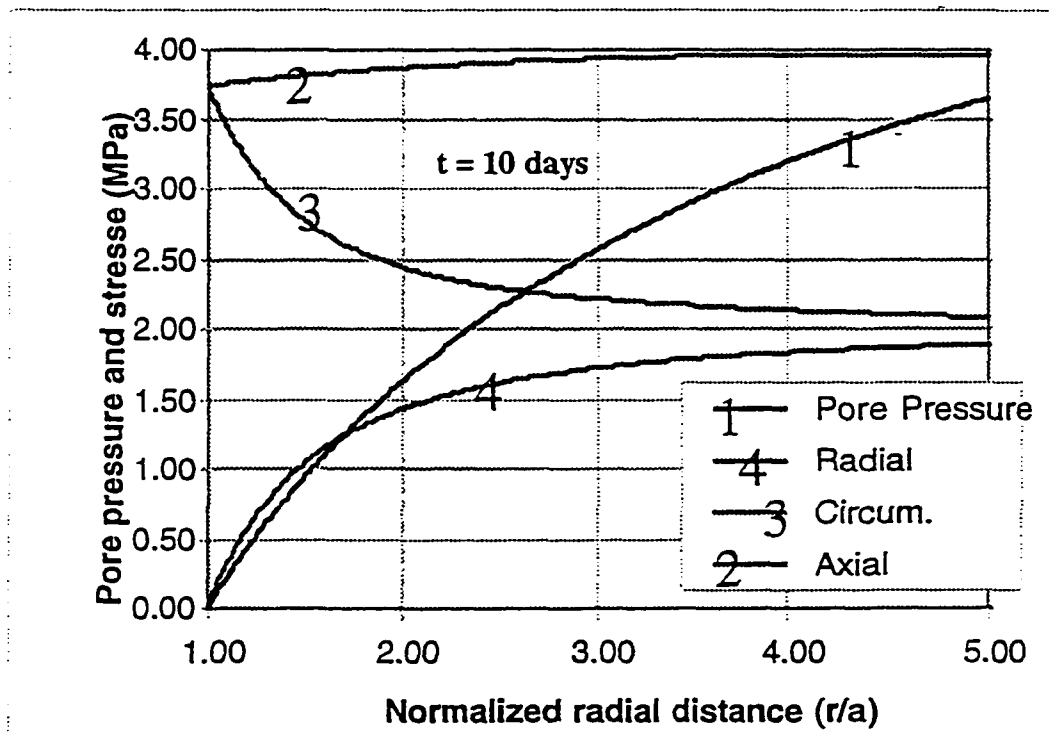


Figure 6.9: Comparison of stress magnitudes at 10 days

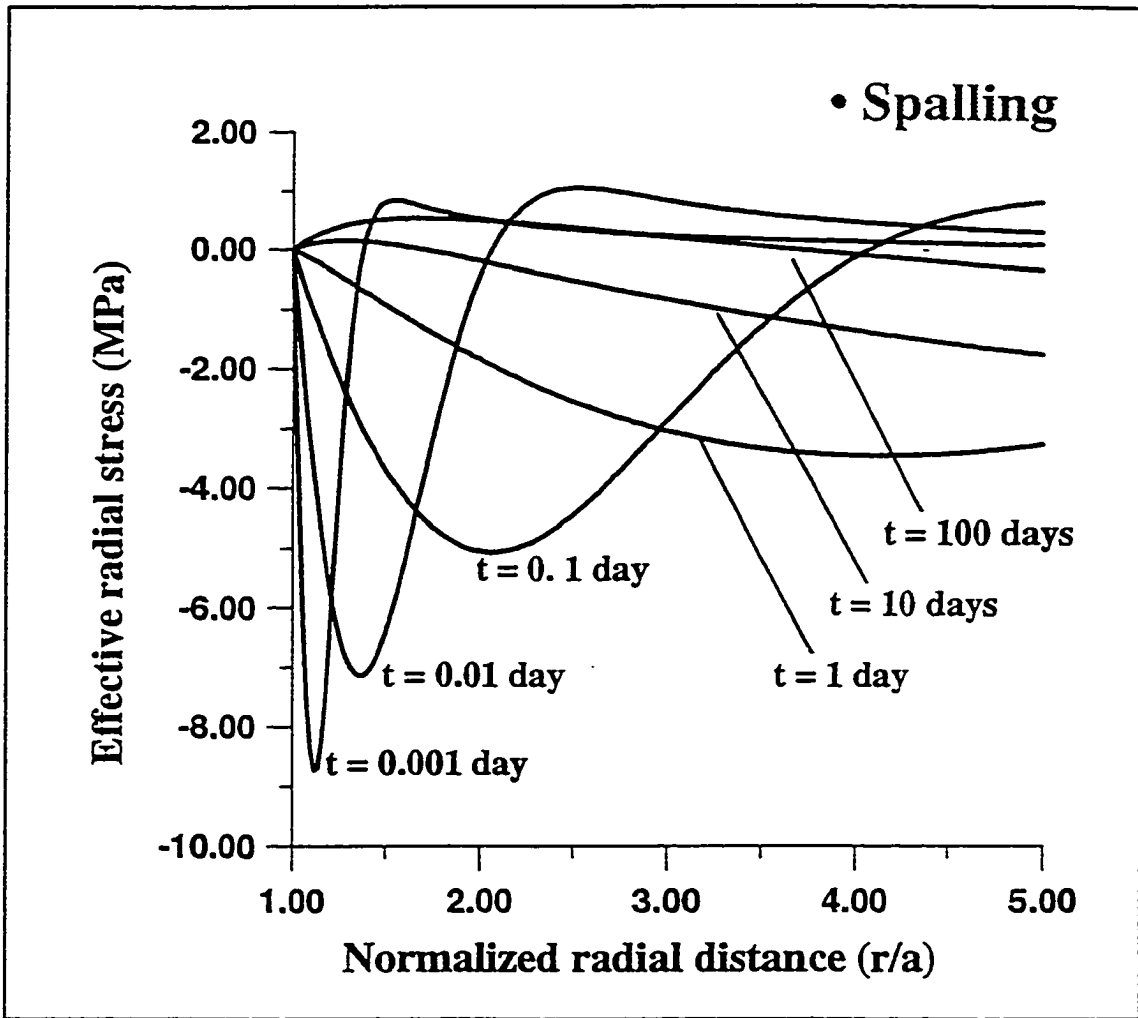


Figure 6.10: Transient effective radial stress profiles

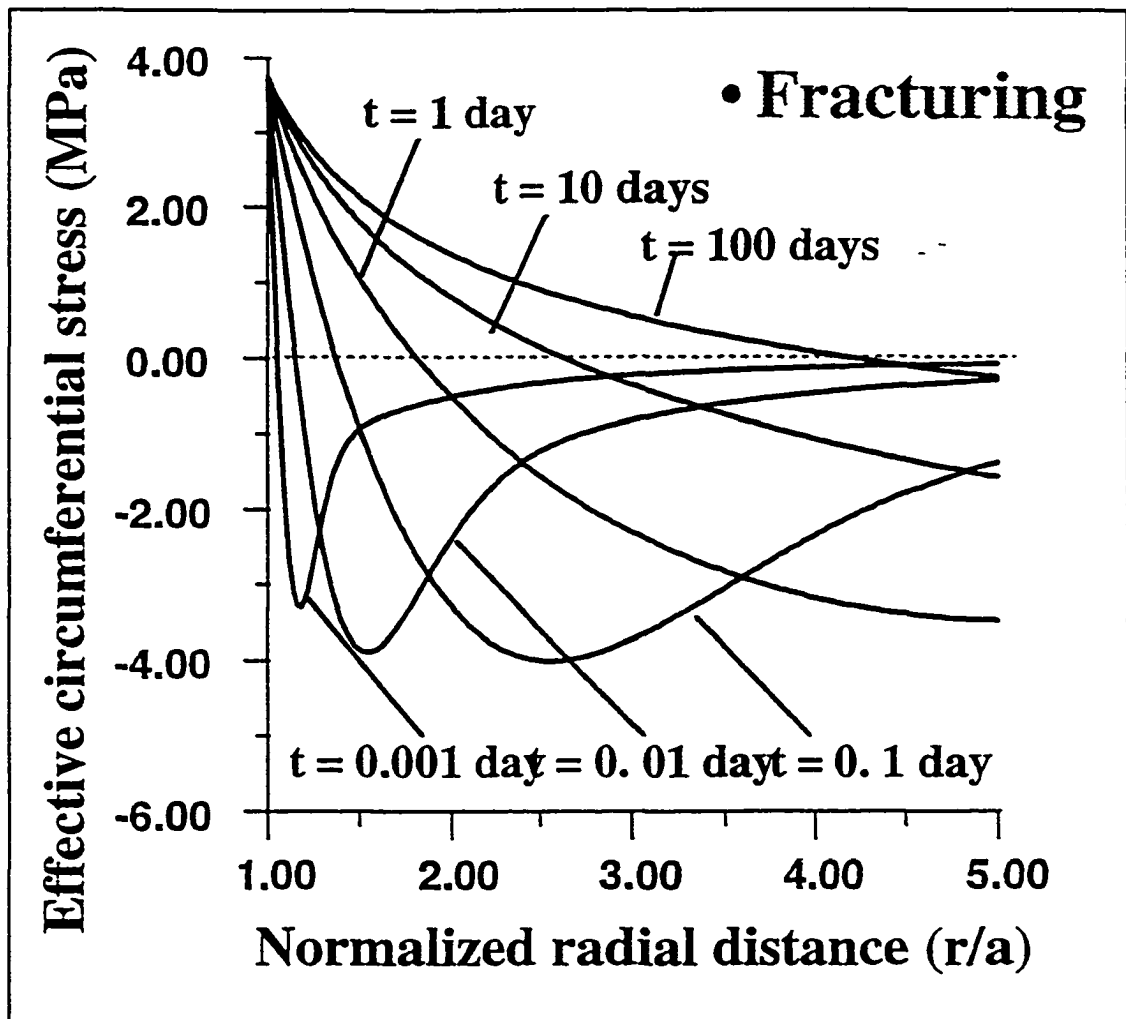


Figure 6.11: Transient effective circumferential stress profile

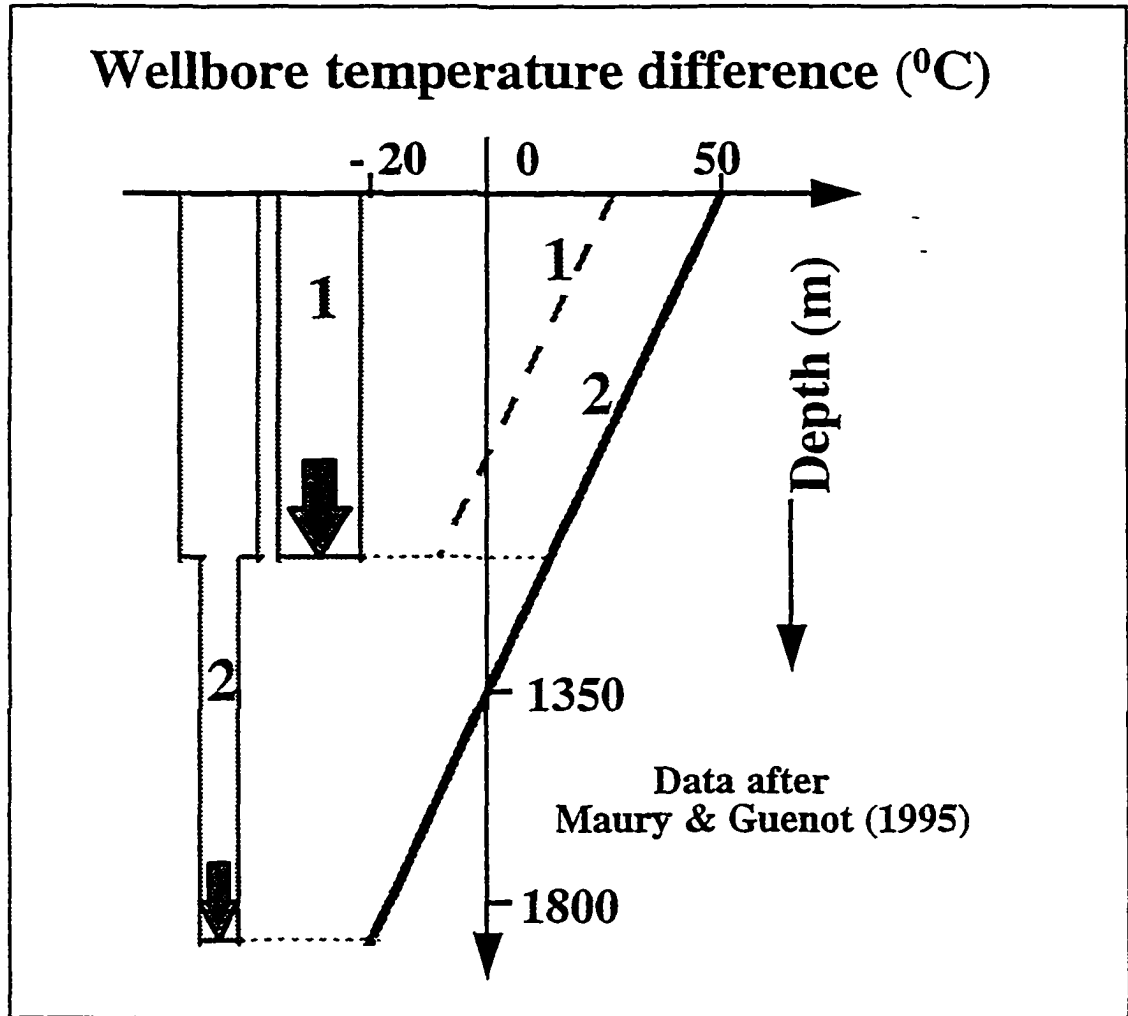
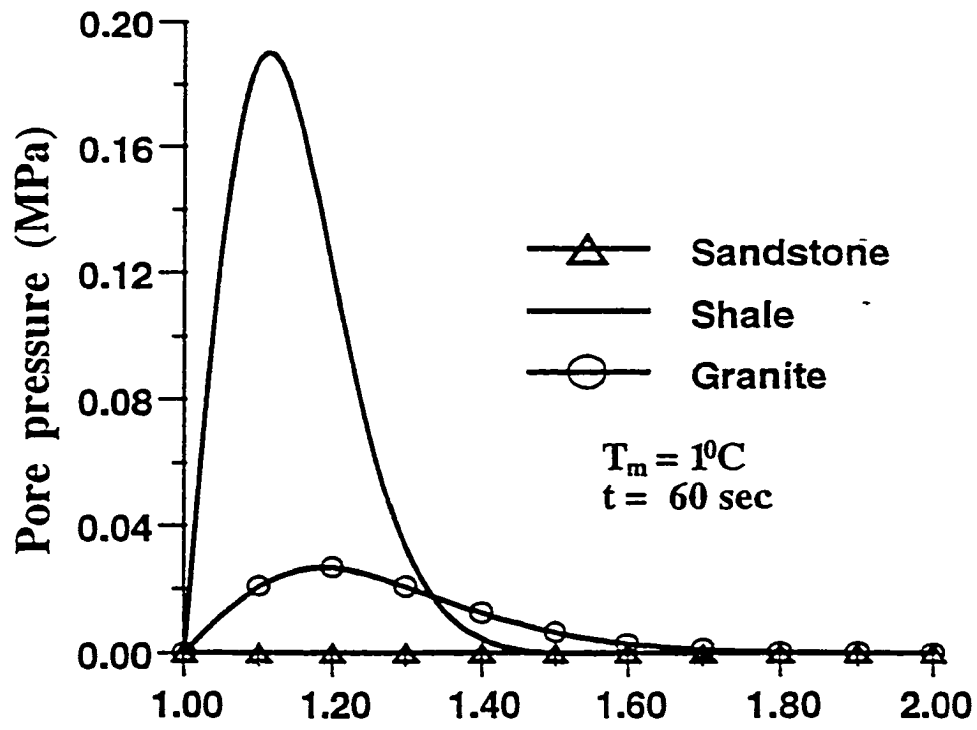


Figure 6.12: Schematic diagram of borehole temperature potential at different drilling phase



	$k$ (md)	$\phi$
ss	10	0.2
shale	$3.6\text{E-}5$	0.14
Gran.	$1\text{E-}4$	0.02

Figure 6.13: Failure potential at different formations

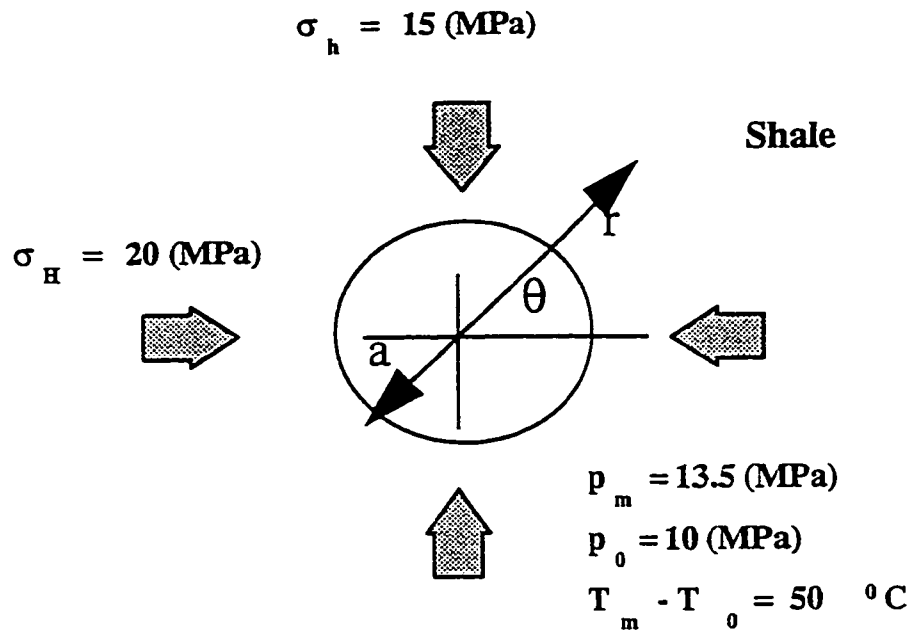


Figure 6.14: Boundary and initial conditions for Case II

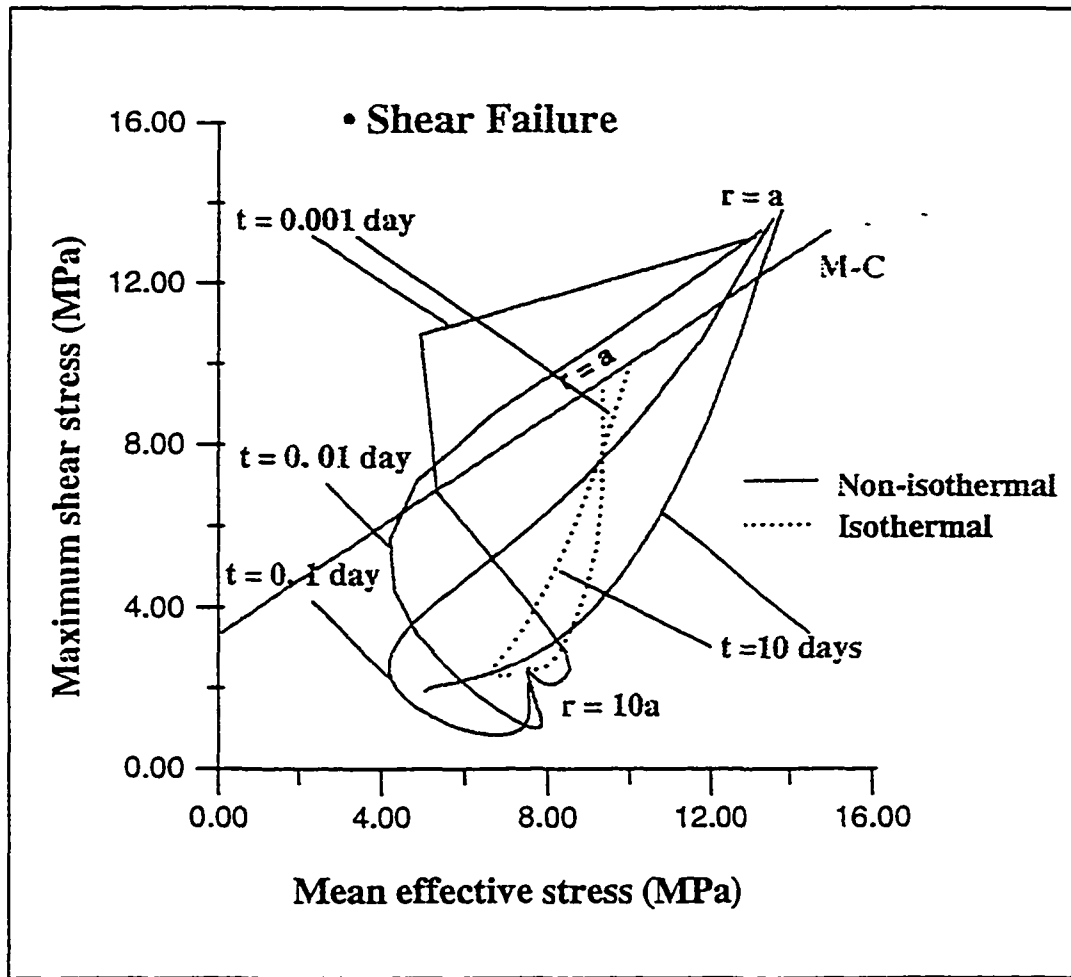


Figure 6.15: Isochrones of stress profile along  $\sigma_h$  direction

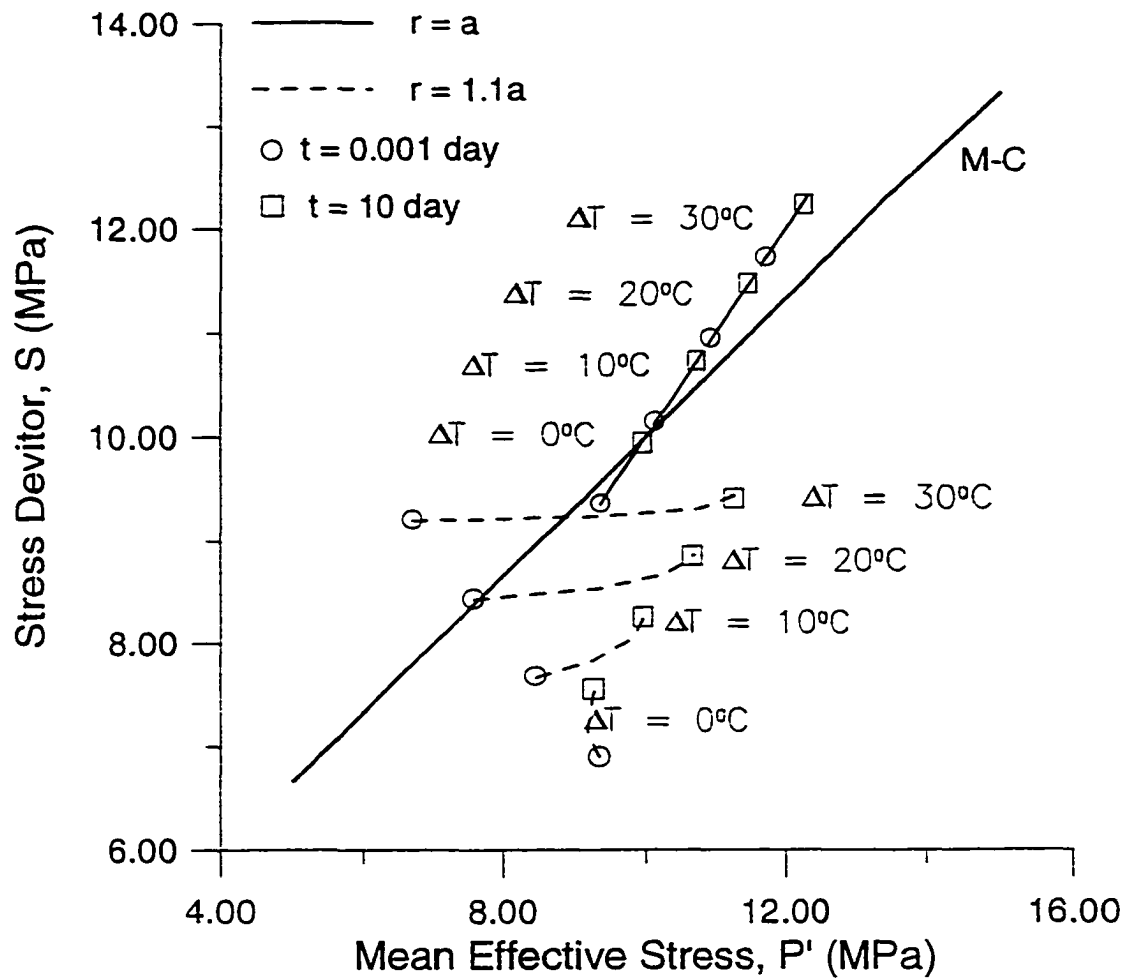


Figure 6.16: Stress history at some points around the borehole for different temperature condition

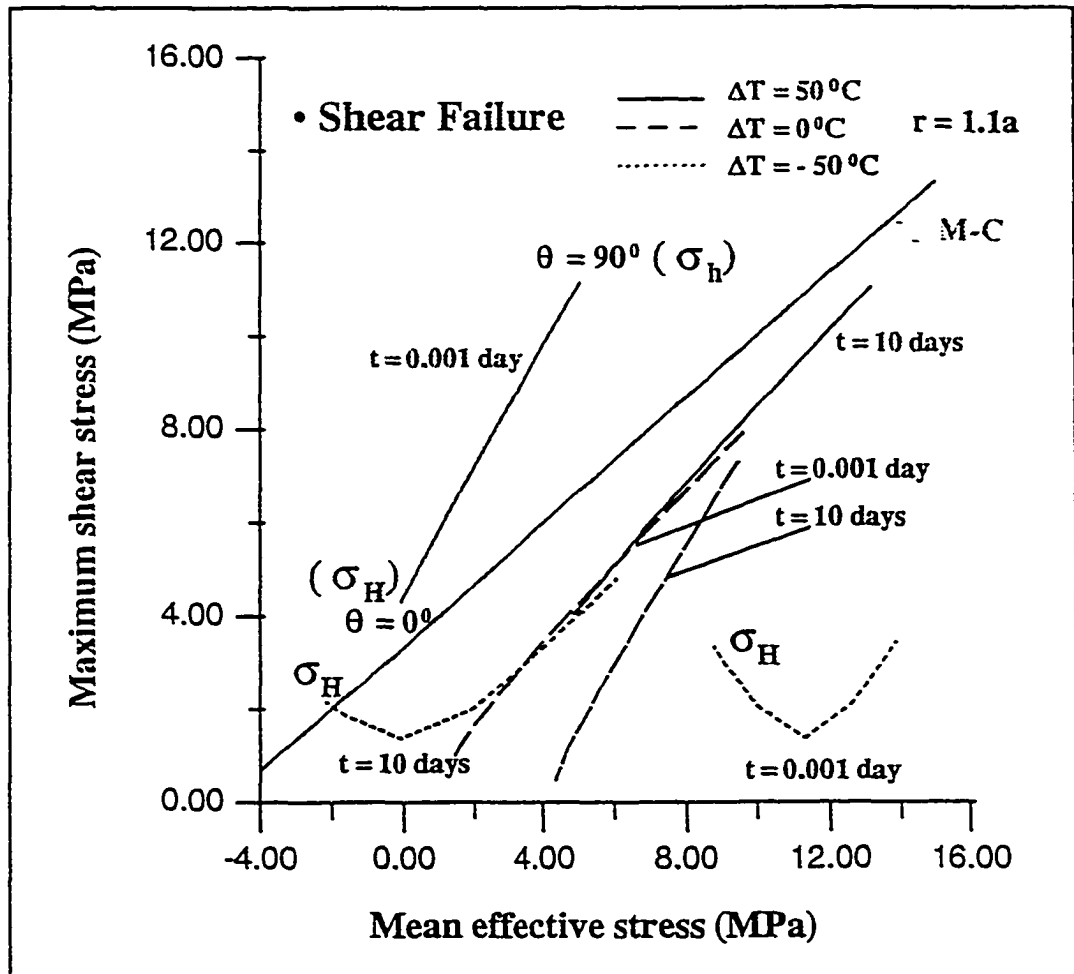


Figure 6.17: Stress distribution around the borehole for different temperature conditions and at different times

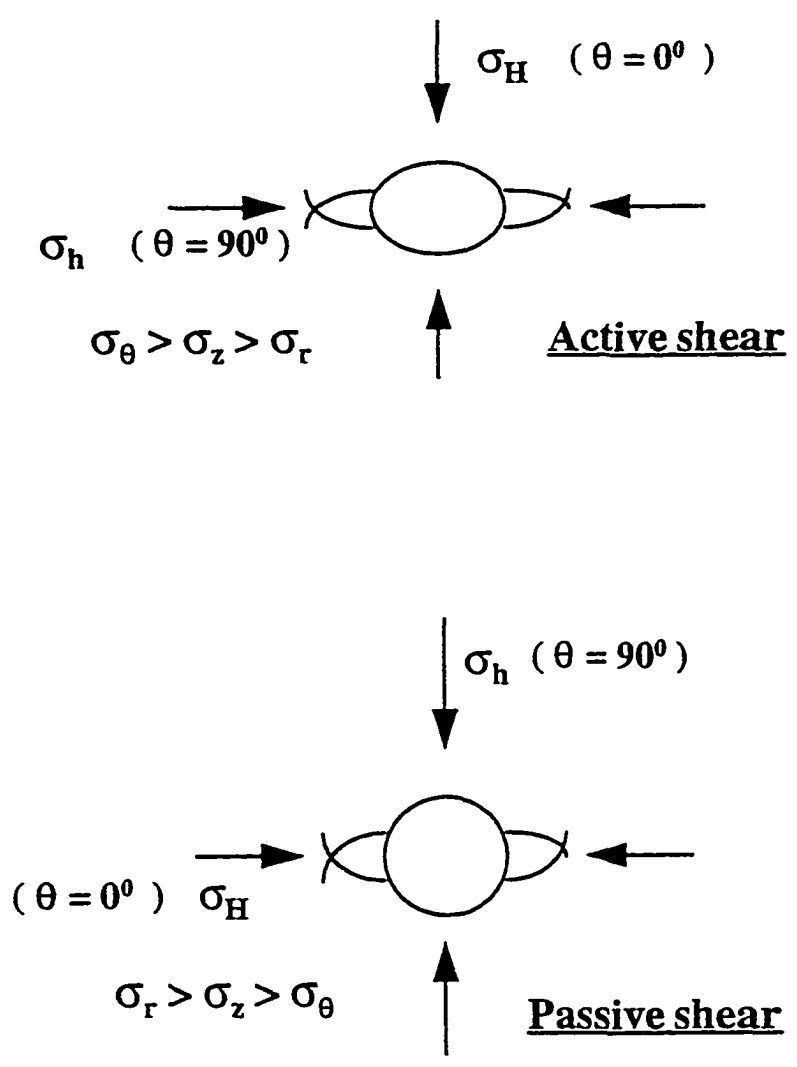


Figure 6.18: Different failure modes at different time

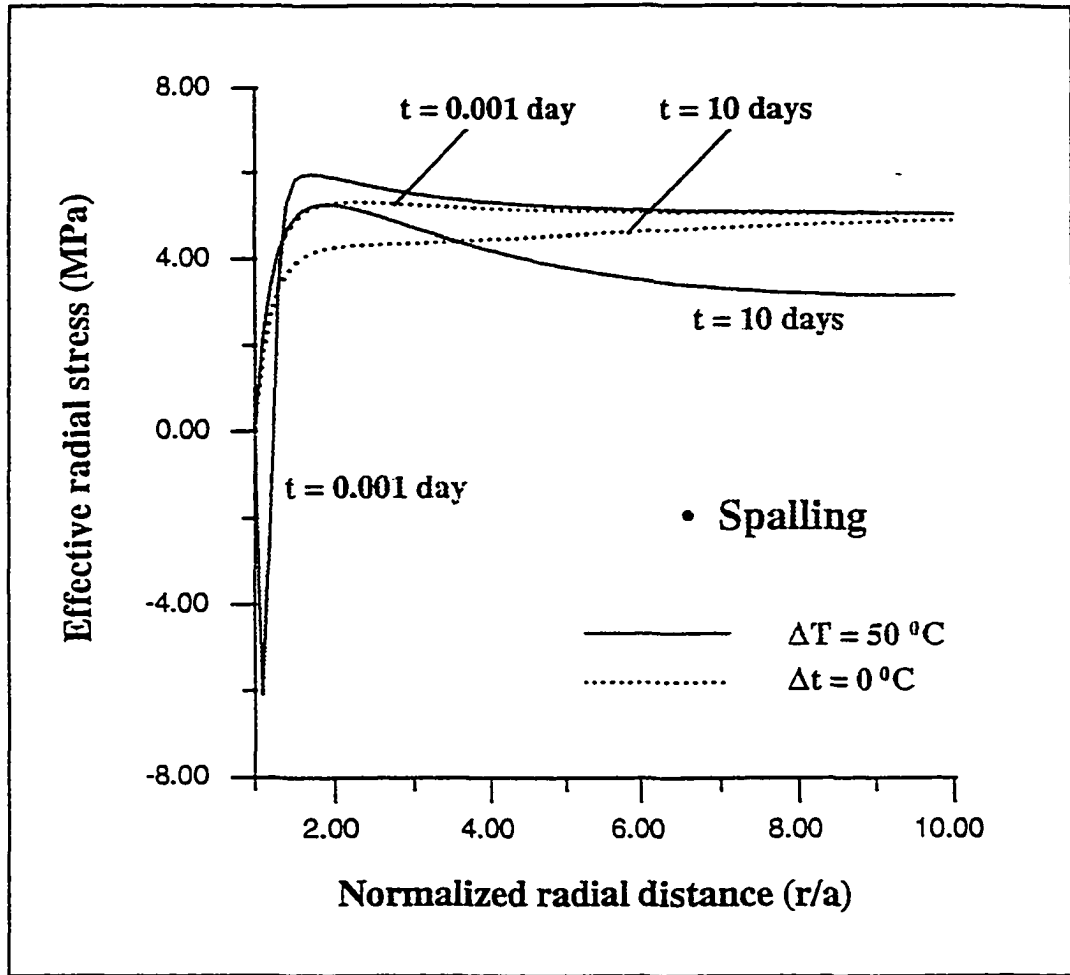


Figure 6.19: Effective radial stress profile along  $\sigma_h$  direction

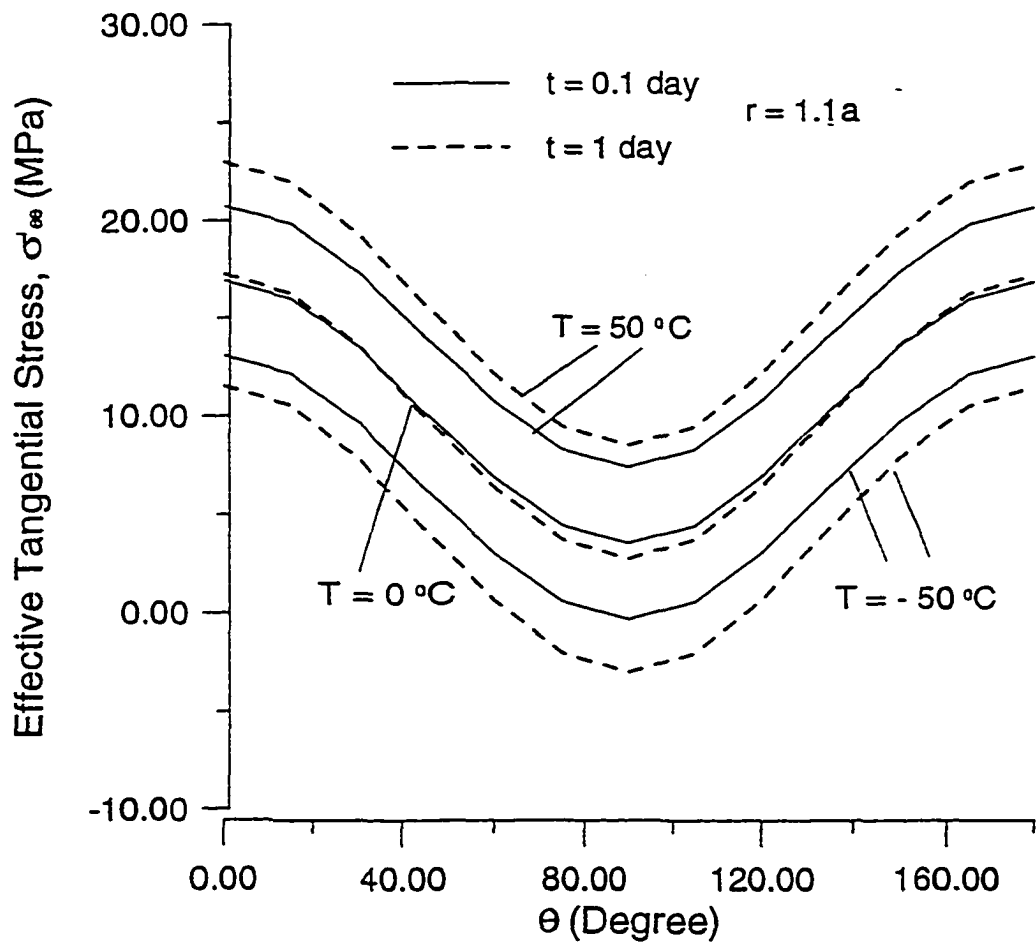


Figure 6.20: Effective circumferential stress at different temperature conditions

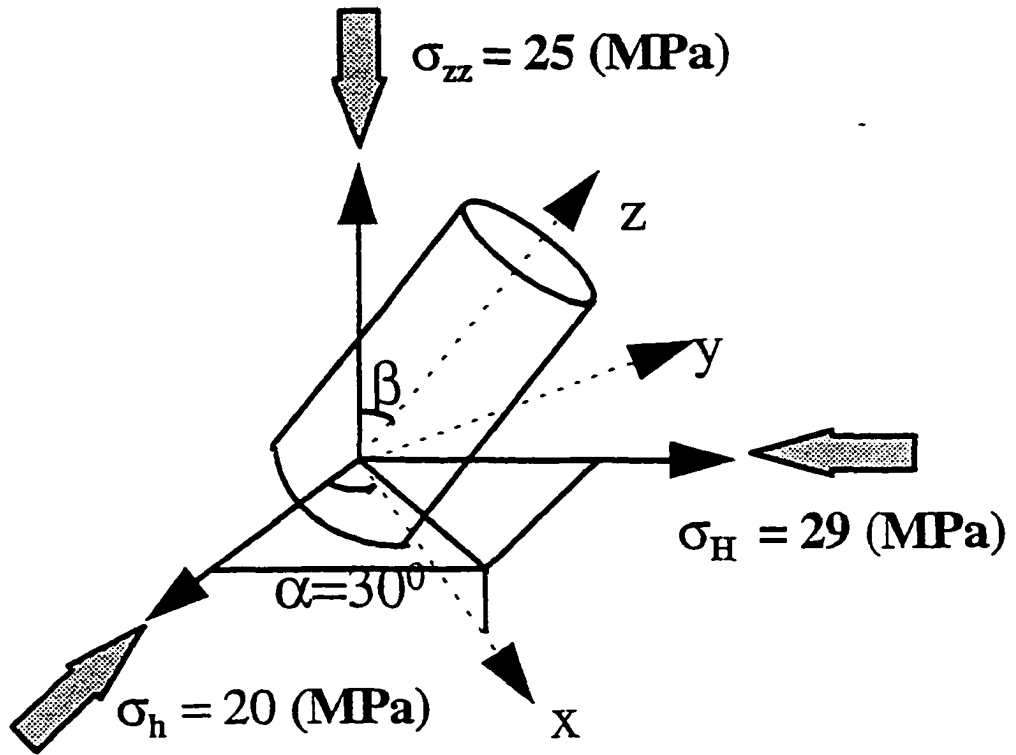


Figure 6.21: Boundary and initiation conditions for Case III

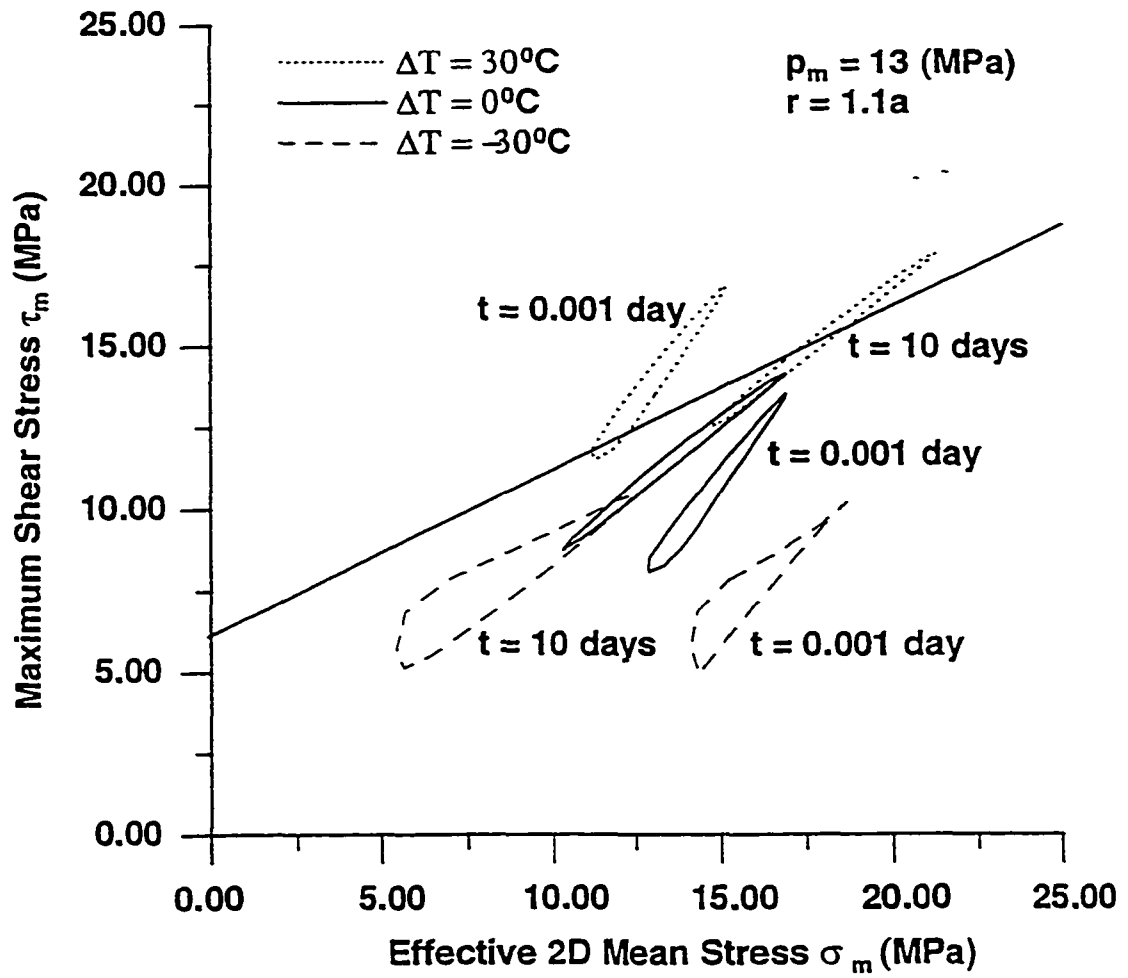


Figure 6.22: Stress clouds for different temperature condition and at different times

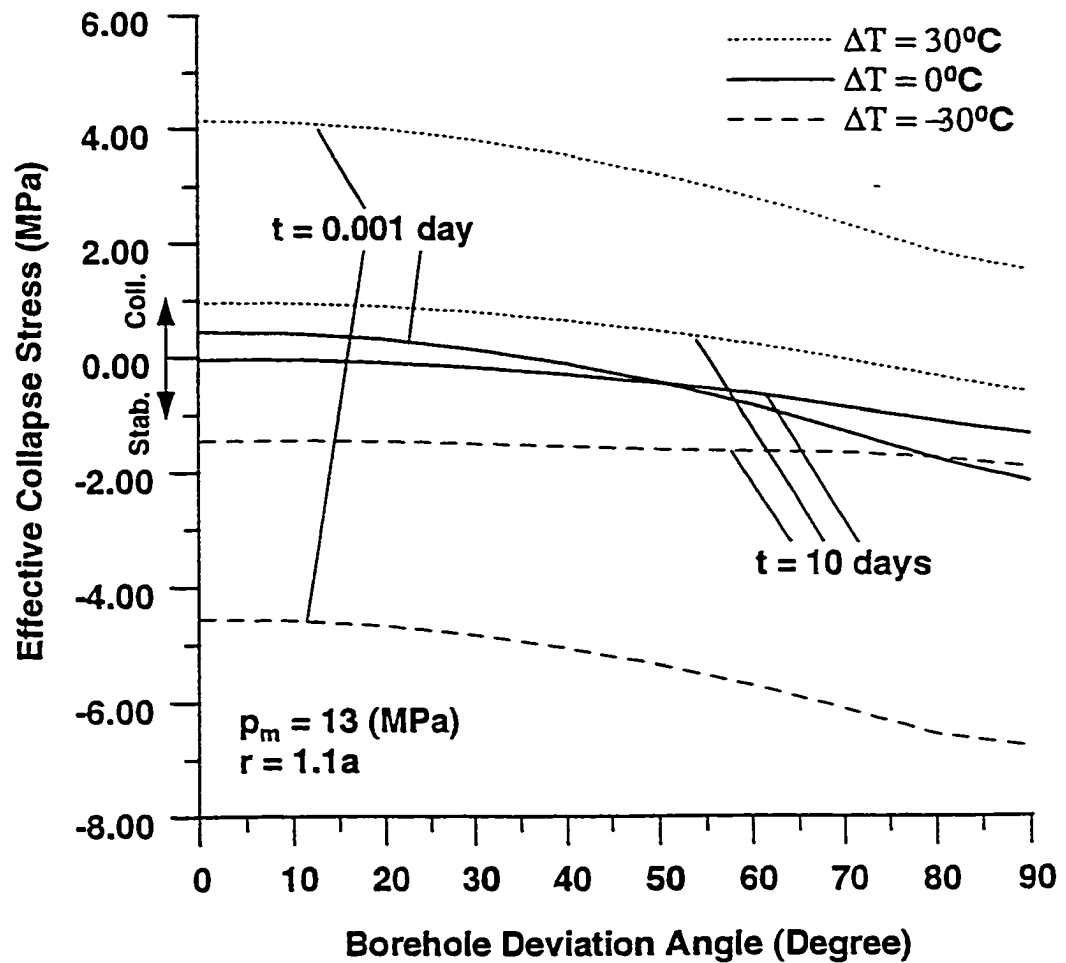


Figure 6.23: Effective collapse stress as a function of borehole deviation angle and temperature ( $\varphi_z = 30^\circ$ )

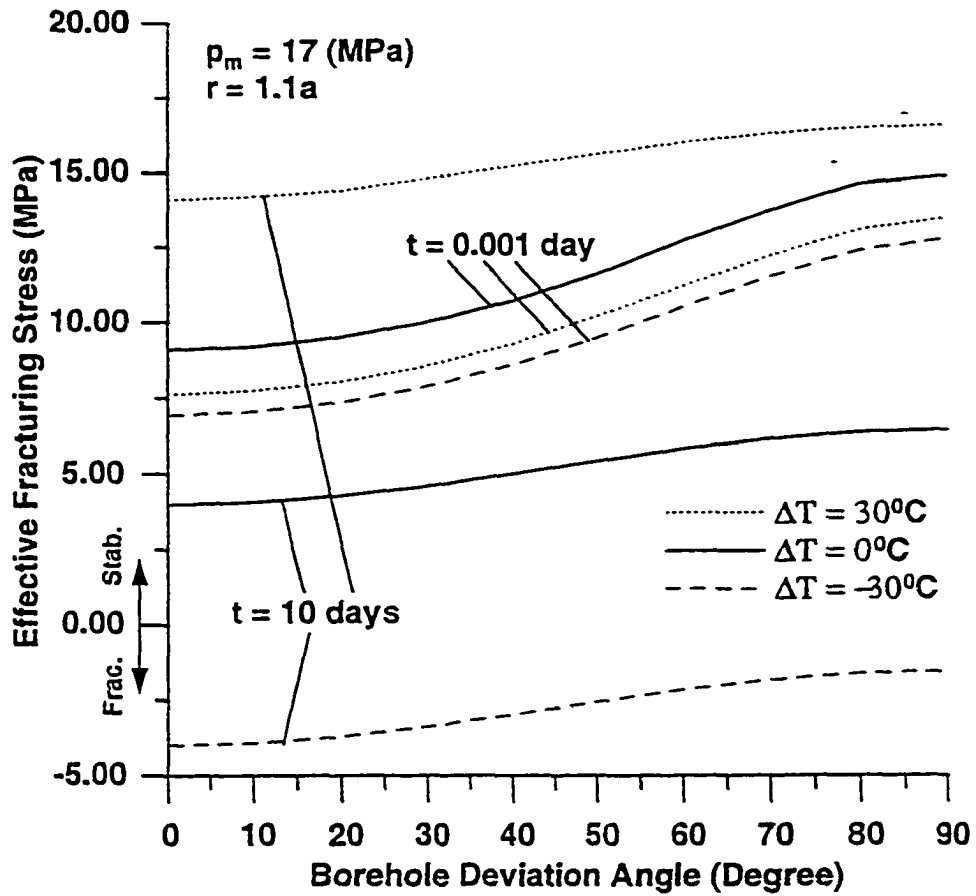


Figure 6.24: Effective fracturing stress as a function of borehole deviation angle and temperature ( $\varphi_2' = 30^\circ$ )

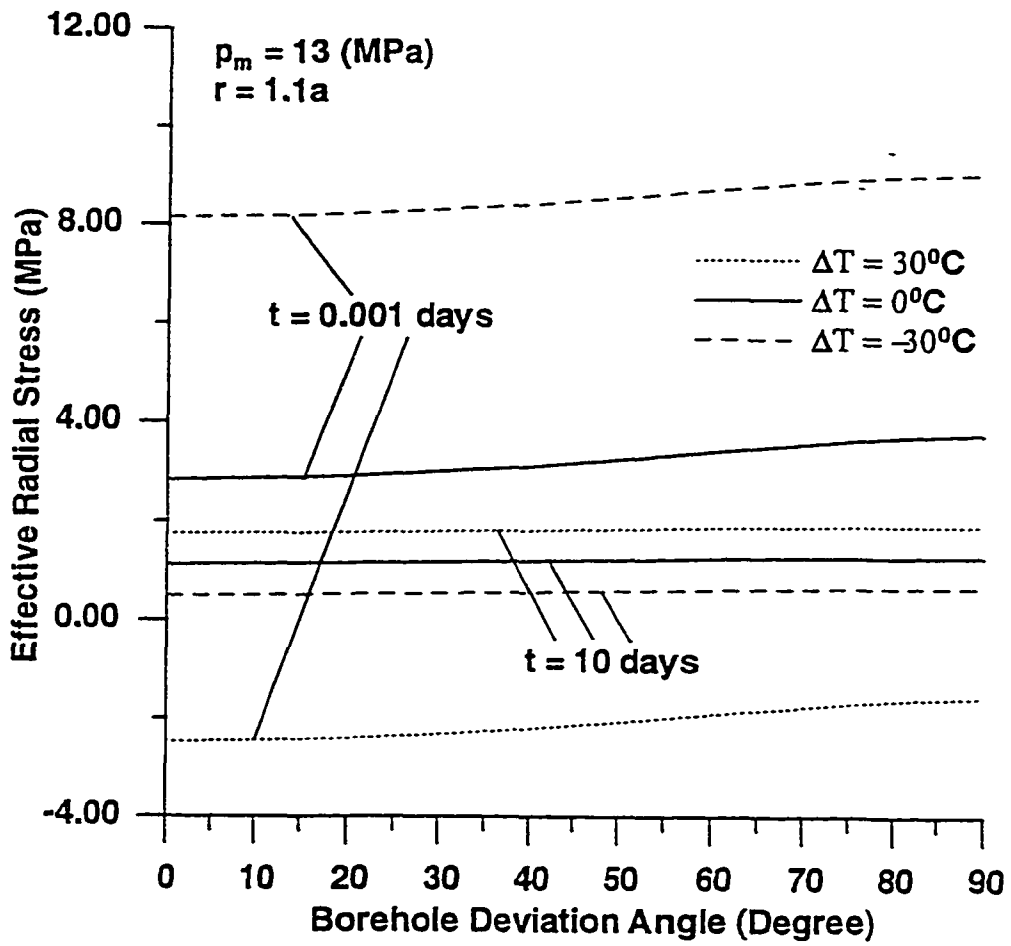


Figure 6.25: Effective radial stress as a function of wellbore deviation angle and temperature ( $\varphi_{z'} = 30^\circ$ )

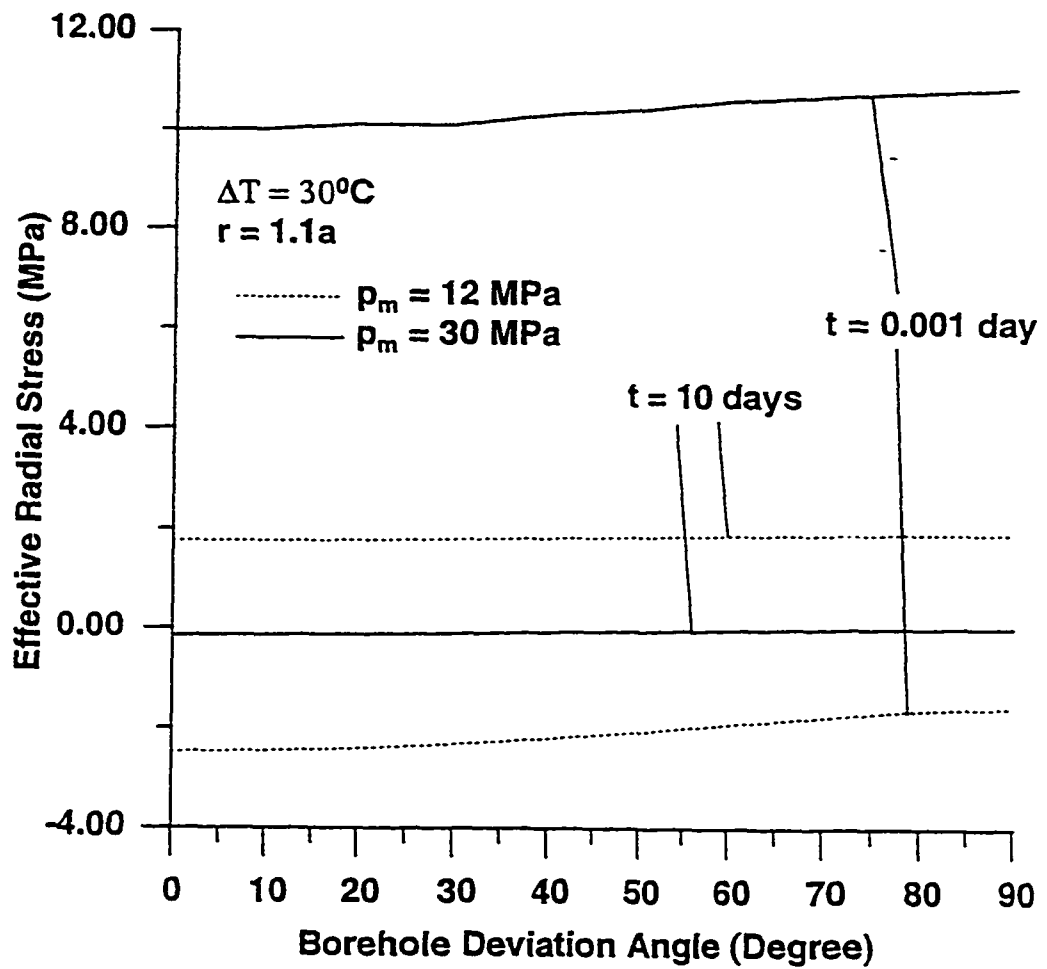


Figure 6.26: Effective radial stress as a function of borehole deviation angle and mud weight ( $\varphi_{z'} = 30^\circ$ )

# 7 Conclusions, Contributions and Recommendations

## 7.1 Conclusions

Coupled THM behavior is one of the most complicated physical phenomena in rock mechanics. The accurate prediction of such behavior is important for many engineering disciplines including wellbore instability control during drilling, completion and production of oil or gas wells.

This dissertation was aimed at developing fully-coupled thermoporomechanical models for the prediction of borehole behaviors during non-isothermal drilling, and quantitatively investigating the impacts of the non-isothermal drilling processes on wellbore instability.

Thermoporoelastic models (THM coupling) for the prediction of the stability of an inclined borehole subjected to non-isothermal drilling conditions were developed. The role of the thermoporoelastic process on the condition leading to borehole shear failure, spalling, and breakdown following drilling under non-isothermal conditions were illustrated through several examples. It showed that heating the borehole can significantly increase the potential of near-wellbore shear failure at early times. Heating also imposes a high potential of borehole spalling. On the other hand, cooling the borehole tends to stabilize the borehole at the beginning of the drilling; but with time, it could induce time-delayed lost circulation, wellbore spalling, and passive and active shear failures, especially when the cooling effects is combined with the high mud weight. In particular, if an originally cooled borehole is gradually

heated up during deepening, time-delayed failure could occur in the upper sections.

By assuming a two-dimensional plane strain model, the thermoporoelastic process itself is independent of the borehole deviation angle. But the combination of the thermoporoelastic effects with the effects of in-situ stress regime and borehole direction complicates the stability analysis.

The coupled thermoelastic solution (TM coupling) for the prediction of inclined borehole stability were also derived and the thermal induced stresses compared with the ones obtained from the coupled THM model. While the stress peak always appears inside the formation in a thermoporoelastic solution, the maximum tangential stress appears on the borehole wall for thermoelastic solution, and the magnitude of both tangential and radial stresses are much smaller compared with the thermoporoelastic solution. This means that pore pressure plays a critical role in thermal-related borehole problems in porous media. The thermoelastic solution can not adequately describe the real physical phenomena occur downhole.

A parametric study was also conducted and the effects of formation properties such as porosity and permeability on the thermoporoelastic effects were discussed. Whereas the thermoporoelastic effects is significant in shale formations, it is negligible for porous but permeable formations such as sandstones. Thermal effects are significant only in shaley formations, because of their high porosity and low permeability.

In addition to the thermoporoelastic analyses, work on the investigation of non-linear and elastoplastic poromechanical behavior were also conducted. A set of temperature- and stress-dependent formation and poromechanical parameters were derived, and non-linearity of other variables also studied and discussed. A finite element model with the capability of conducting fully-coupled non-linear and thermoporoelastoplastic behavior was developed and thoroughly validated.

## 7.2 Contributions

The fully-coupled thermoporomechanical analytical models for wellbore stability analysis developed in this dissertation furthered the current technologies in this field by taking into account the complete THM coupling mechanism and arbitrary borehole orientations with respect to the in-situ stress field, compared to the existing work. The theoretical study on the non-linear, stress- and temperature-dependent thermoporomechanical parameters, and the development of non-linear thermoporoelastoplastic finite element model for borehole stability study are entirely new application attempts in the area of fully-coupled THM modelling. Both the analytical and numerical models could be effective tools to predict, more accurately, the impacts of non-isothermal drilling processes on wellbore stability for boreholes drilled in fluid-saturated porous media. The work conducted in this dissertation can also be applied to the investigation of other non-isothermal geomechanics problems such as fluid injection and compaction/consolidation.

The findings from the thermoporoelastic analyses provide clear physical insights into the mechanisms for four types of time-delayed borehole failures; an additional mechanism for the high failure rate in shales; and the potential for the failure to initiate inside the formation. The results have shown that the impacts of thermal effects on the wellbore stability could be significant. It could provide solutions for those wellbore problems that cannot be predicted solely by isothermal analyses. These findings are especially important for offshore high-temperature, high-pressure and deep wells, where high mud weight are usually required to manage the high pressure. A small amount of temperature change on the wellbore wall could bring in various time-delayed borehole problem. It also implied that cooling the borehole could be an effective way to stabilize the wellbore in these wells, as long as the upper part of the wellbore are cased in time.

## 7.3 Recommendations

Based on the current studies, the following recommendations are made for potential important future developments.

- As stated in Chapter 3 (section 3.2.4), the expansion of pore volume in a fluid-saturated, non-isothermal system is one of the critical parameters for accurate modelling. The current observation on sandstones revealed a contrary tendency from past assumption, and the data for shales have not been looked upon yet. Further laboratory investigation on this parameter is necessary to improve the quality of modelling.
- The formulae derived in this dissertation for temperature and stress-dependent formation and poroelastic properties (Chapter 3, sections 3.3.1.1, 3.3.1.2, and Appendix A) are purely theoretical derivations and have not been substantiated by laboratory experiments. Validation of these relationships via reliable laboratory tests are necessary and important before applying them to any modelling and predictions.
- Generally, the information on both temperature- and stress-dependent thermoporoelastic properties (including matrix and fluid properties) are very scanty, especially for shale, and under deep subsurface conditions. The study on thermoporoelastoplastic constitutive relations and failure criteria are also very limited. The lack of thorough study on this aspect limited both the model development as well as their validation and field application. With the ever improving modelling technologies, systematic laboratory and field investigations on non-linear and plastic thermoporomechanical rock behavior will become more and more an indispensable key for successful predictions.
- Investigation of the impacts of non-linear and thermoporoelastoplastic behavior on wellbore stability has not been conducted in this dissertation and this is a major direction for the future work in this field. No study has been

conducted in this regard before, and as it is stated in Chapter 2, the experience from the comparison of elastic and elastoplastic analyses revealed great discrepancies in the predicted borehole behavior.

- An important simplification for the obtaining of two-dimensional borehole solutions is the assumption of uniform temperature distribution along the borehole axis. In reality, temperature distribution along the borehole axis changes with time constantly due to the circulation of drilling fluid. This means the temperature in a fixed point on the borehole wall is a function of time, and so are the borehole stability conditions. Because of this, the development of an effective borehole temperature evolution model and the incorporation of such a model into the borehole stability analysis model would be a key improvement to the current work.
- There are two common assumptions adopted in the analytical thermoporoe-lastic wellbore models developed in this dissertation: the completely permeable wellbore boundary condition and the step loading of temperature on the borehole wall. These assumptions could affect the accuracy of early-time, near-wellbore analysis because the start of fluid exchange between the wellbore and formation lags behind the application of wellbore pressure and temperature, especially for low permeable formations such as shales, and the quantity of the exchange are also dependent on many conditions. Besides, heating or cooling the wellbore cannot physically be realized instantly. The reasons that hinder the application of more realistic boundary conditions are the lack of knowledge about the fluid exchange condition on the borehole wall, and the time-dependent temperature rising/lowering during heating/cooling of the wellbore. Studies on these issues are imperative to the further improvement of the current models.

## References

- [1] B. A. Aadnøy and M. E. Chenevert. Stability of highly inclined boreholes. *SPE Drilling Engineering*, 12:364–374, 1987.
- [2] B. S. Aadnøy. Modelling of the stability of highly inclined boreholes in anisotropic rock formations. *SPE 16526, 1987 SPE Offshore European Conf., Aberdeen*, 1987.
- [3] A. Abou-Sayed. Personal communication. 1997.
- [4] Y. Abousleiman, L. Cui, A. H.-D. Cheng, and J. C. Roegiers. Poroelastic solution of an inclined borehole in a transversely isotropic medium. In J. J. K. Daeman and R. A. Schultz, editors, *Proc. 35th US Symp. Rock Mech.*, pages 313–318. Rotterdam. 1995. Balkema.
- [5] T. Addis, D. Boulter, L. Roca-Ramisa, and D. Plumb. The quest for borehole stability in the cusiana field, colombia. *Schlumberger Oilfield Review*, April/July:33–43, 1993.
- [6] J. G. Agar, N. R. Morgenstern, and J. D. Scott. Shear strength and stress-strain behavior of athabasca oil sands at elevated temperature and pressures. *Can. Geotech. J.*, 24:1–10, 1987.
- [7] D. Antheunis and et. al. Perforation collapse: failure of perforated friable sandstones. In *Proc. SPE-European spring meeting*, Amsterdam, 1976. SPE 5750.
- [8] J. H. Argyris and D. W. Scharpf. Methods of elastoplastic analysis. *J. Appl. Maths. Physics (Z.A.M.P.)*, 23:517–552, 1972.
- [9] H. Armen, H. S. Levine, and A. B. Pifco. Plasticity - theory and finite element applications. In J. T. Oden, R. W. Clough, and Y. E. Yamamoto, editors, *Advances in computational methods in structural mechanics and design*, pages 393–437, 1972.
- [10] P. Ashqar. Thermal expansion of porous rocks under stress. Technical report, The University of Carlifornia, Berkeley, 1979.

- [11] L. E. Baker, R. S. Sandhu, and W. H. Shieh. Application of elasto-plastic analysis of rock mechanics by finite element method. In *Proc. 11th Symp. on Rock Mech.*, Berkeley.
- [12] S. C. Bandis and N. Barton. Failure modes of deep boreholes. In *Proc. 27th. U.S. Symp. Rock Mech.*, pages 599–605, 1986.
- [13] J. Bear and M. Y. Corapcioglu. A mathematical model for consolidation in a thermoelasticity aquifer due to hot water injection or pumping. *Water resources research*, 17:3:723–736, 1981.
- [14] M. A. Biot. General theory of three-dimensional consolidation. *J. Appl. Phys.*, Vol. 12:155–164, 1941.
- [15] M. A. Biot. Theory of elasticity and consolidation for a porous anisotropic solid. *J. Appl. Phys.*, 26:182–185, 1955.
- [16] M. A. Biot. Thermoelasticity and irreversible thermodynamics. *J Appl. Phys.*, Vol. 27:240, 1956.
- [17] R. B. Bird, W. E. Stewart, and E. N. Lightfoot. *Transport phenomena*. John Wiley and Sons, Inc., N.Y., 1960.
- [18] D. R. Bland. Elastoplastic thick-walled tubes of work-hardening material subjected to internal and external pressures and to temperature gradients. *J. Appl. Phys.*, 12:209–229, 1956.
- [19] F. Bliard, F. Deleruyelle, A. Millard, and A. Stietel. Decovalex bmt1. final report. Technical Report Rapport DMT/92/644, CEA/DMT. Commissariat à L'énergie Atomique, Direction des Réacteurs Nucléaires. Département de Mécanique et de Technologie, 1992.
- [20] J. R. Booker and C. Savvidou. Consolidation around a spherical heat source. *Int. J. Solids Structures*, Vol. 20:1079–1090, 1984.
- [21] J. R. Booker and C. Savvidou. Consolidation around a point heat source. *Int. J. Num. Anal. Method in Geome.*, Vol. 9:173–184, 1985.
- [22] A. P. Boresi and K. P. Chong. *Elasticity in engineering mechanics*. Elsevier, 1974.
- [23] A. Bougnoux and G. Vouille. International project decovalex bmt1 - far field model. Technical report, ENSMP/CGES, CEA/IPSN, 1992.
- [24] T. Bourbie, O. Coussy, and B. Zinszner. *Acoustics of porous media*. 1987.
- [25] I. D. R. Bradford and J. M. Cook. A semi-analytical elastoplastic model for wellbore with applications to sanding. In *Rock Mechanics in Petroleum Engineering, Proc. of Eurock'94*, Rotterdam, 1994. Balkema. Proc. of Eurock'94.

- [26] W. B. Bradley. Failure of inclined boreholes. *J. Energy Res. Tech., Transactions of ASME*, 101:232–239, 1979.
- [27] W. E. Brigham and W. B. Morrow. P/z behavior for geothermal steam reservoir. In *Paper SPE 4899*, 1974.
- [28] E. T. Brown, J. W. Bray, and E. Hoek. Groundresponse curves for rock tunnels. *J. Geotech. Engng. ASCE*, 109:1:15–39, 1983.
- [29] M. M. Carroll. Mechanics response of fluid-saturated porous material. In F. P. J. Rintott and B. Tabarrok, editors, *Theoretical and Applied Mechanics, Proc. 15th IUTAM*, Noth-Holland, New York, 1980.
- [30] M. M. Carroll and N. Katsube. The role of terzaghi effective stress in linearly elastic deformation. *J. Energy Resour Tech.*, 105:509–511, 1983.
- [31] H. S. Carslaw and J. C. Jaeger. *Conduction of heat in solids*. Oxford, Amen House, London, 1959.
- [32] T. Chan and K. Khair. Simulation and results of the multiple fracture model. Technical Report DECOVALEX Project-phase I, Bench mark test 2, AECL Research, Applied Geoscience Branch, Whiteshell Laboratories, 1992.
- [33] P. Charlez. *Mechanics of porous media*. A.A. Balkema, Rotterdam, 1995.
- [34] L. Chin, R. R. Boade, J. H. Prevost, and G. H. Landa. Numerical simulation of shear-induced compaction in the ekofisk reservoir. *Int. J. Rock Min. Sci. & Geomech. Abstr.*, 30:7:1193–1200, 1993.
- [35] J. T. Christian and C. S. Desai. Constitutive laws for geologic media. In C. S. Desai and J. T. Christian, editors, *Numerical Methods in Geotechnical Engineering*, New York, 1977. McGraw-Hill.
- [36] S. P. Clark. *Handbook of Physical Constants*. The Geological Society of America, Inc., New York, 1966.
- [37] M. P. Cleary. *Fundamental solutions for fluid-saturated porous media and application to localised rupture phenomena*. Ph.D. dissertation, University Microfilms International, Ann Arbor, MI, 1976.
- [38] N. A. Combarous and S. A. Bories. Hydrothermal convection in saturated porous media. *Advances in Hydroscience*, 10:231–307, 1975.
- [39] B. Corre, R. Eymard, and A. Guenot. Numerical computation of temperature distribution in a wellbore while drilling. *SPE 13208*, 1984.
- [40] O. Coussy. Réponse thermoporoélastique d'un forage. In W. Wittke, editor, *Proc. 7th Int. Cong. Rock Mecha.*, pages 699–702, A. A. Balkema, Roterdam, Brookfield, 1993.

- [41] O. Coussy. *Mechanics of porous continua*. John Wiley & Sons, England, 1995.
- [42] L. Cui. *Poroelasticity with application to rock mechanics*. Ph.D. dissertation. The University of Delaware, 1995.
- [43] L. Cui, A. H.-D. Cheng, and Y. Abousleiman. Poroelastic solution for an inclined borehole. *J. Appl. Mech., Transactions of ASME*, 64:32–38, 1997.
- [44] L. Cui, A. H.-D. Cheng, V. N. Kaliakin, Y. Abousleiman, and J. C. Roegiers. Finite element analysis of anisotropic poroelasticity: a generalized mandel's problem and an inclined borehole problem. *Int. J. Num. Ana. Meth. Geomech.*, 20:381–401, 1996.
- [45] P. A. Cundall. A computer model for simulating progressive large scale movements in blocky rock systems. In *Rock Fracture (Proc. Symp. of the intl. Soc. of Rock Mechanics)*, Nancy, France, 1971. paper No. II-8.
- [46] P. A. Cundall. Udec-a generalized distinct element program for modelling fractured rock. Technical Report Rep. PCAR-1-80, Peter Cundall Assocs., European Research Office, US Army, Contract No. DAJA37-79-C-0548, 1980.
- [47] S. A. B. da Fontoura. Bore-3d version 1.02, release alpha, user's manual. Technical Report RMC-92-13, RMI,OU, Norman, OK, 1992.
- [48] C. S. Desai and J. F. Abel. *Introduction to the finite element method*. Von Nostrand Reinhold Co., New York, 1972.
- [49] C. S. Desai and J. T. Christian. *Numerical methods in geotechnical engineering*. McGraw-Hill, New York, 1977.
- [50] C. S. E. Desai. *Proc. 2nd int. conf. numerical methods in geomechanics*. ASCE, Blacksburg, Virginia, 1976.
- [51] E. Detournay and A. H.-D. Cheng. Poroelastic response of a borehole in a non-hydrostatic stress field. *Int. J. Rock. Mech. Min. & Geomech. Abstr.*, 25:3:171–182, 1988.
- [52] E. Detournay and A. H.-D. Cheng. Fundamentals of poroelasticity. In J. A. Hudson, editor, *Comprehensive rock engineering, Vol. II*, pages 113–171. Pergamon press, 1993.
- [53] E. Detournay and C. Fairhurst. Two-dimensional elastoplastic analysis of a long, cylindrical cavity under non-hydrostatic loading. *Int. J. Rock. Mech. Min. & Geomech. Abstr.*, 24:4:197–211, 1987.
- [54] D. C. Drucker and W. Prager. Soil mechanics and plasticity analysis or limit design. *Q. Appl. Math.*, 10:2:157–165, 1952.

- [55] T. Edmondson. Thermal diffusivity of sedimentary rocks subjected to simulated overburden pressure. Master's thesis. University of California, Berkeley. 1961.
- [56] R. T. Ewy. Yield and closure of directional and horizontal wells. *Int. J. Rock Mech. Min. Sci. & Geomech. Abstr.*, 30:7:1061-1067, 1993.
- [57] C. Fairhurst. Methods of determining in-situ rock stresses at great depth. Technical Report TRI-68 Missouri River Div., Corps of Engineer, Feb. 1968.
- [58] R. Fenner. Untersuchungen zur erkenntnis des gebiegsdruckes. *Gluckauf*, pages 681-695,705-715, 1938.
- [59] R. T. Fernandez. *Natural convection from cylinders buried in porous media*. Ph.D. dissertation, The University of California, Berkeley, 1972.
- [60] A. Finol and S. M. Farouq Ali. Numerical simulation of oil production with simultaneous ground subsidence. *SPE J.*, 15:411-424, 1975.
- [61] E. Fjær, R. M. Holt, P. Horsrud, A. M. Raaen, and R. Risnes. *Petroleum Related Rock Mechanics*. Elsevier, New York, 1992.
- [62] G. Gambolati. Equation for one-dimensional vertical flow of groundwater, 2, validity range of the diffusion equation. *Wat. Res. Research*, 9(5):1385-95, 1973.
- [63] S. K. Garg. Effective stress laws for fluid-saturated porous rocks. *J. Geophys. Res.*, 78(26):5911-5921, 1973.
- [64] S. K. Garg, J. W. Prichett, and D. H. J. Brownell. Transport of mass and energy in porous media. In *Proc. Second United Nation Symp. on the Devel. and Use of Geothermal Resource*, volume 3, pages 1651-1656. San Francisco, California, 1975.
- [65] J. Geertsma. The effects of fluid pressure decline on volumetric changes of porous rocks. *Petroleum Transactions, AIME*, 210:331-340, 1957.
- [66] R. E. Goodman and G. Shi. *Block theory and its application to engineering*. Prentice-Hall, Englewood, NJ, 1985.
- [67] R. E. Goodman and C. M. St John. Finite element analysis for discontinuous rocks. In C. S. Desai and J. T. Christian, editors, *Numerical methods in geotechnical engineering*, pages 148-175, New York, 1977. McGraw-Hill.
- [68] W. M. Gray. Surface spalling by thermal stresses in rocks. In *Proceedings of the rock mechanics symposium*, pages 85-98, 1965.

- [69] G. E. Gudehus. *Finite element methods in geomechanics*. Wiley, Chichester, 1977.
- [70] A. Guenot and F. J. Santarelli. Borehole stability: a new challenge for an old problem. In C. et. al. (eds), editor, *Key questions in rock mechanics*, pages 453–460, Rotterdam, 1988. Balkema.
- [71] A. Guenot and F. J. Santarelli. Influence of mud temperature on deep borehole behavior. In V. Maury and D. Fourmaintraux, editors. *Rock at great depth*, pages 809–817, Rotterdam, Balkema, 1989. Proc. Int. ISRM/SPE Symp. (3).
- [72] B. C. Haimson and C. Fairhurst. Hydraulic fracturing in porous-permeable materials. *Soc. Pet. Eng. J.*, pages 811–817, 1969.
- [73] O. Halonen. Bench mark test 2 without fluid flow. Technical Report Report of DECOVALEX, phase I, Bench Mark Test 2, Technical research center of Finland, Road, Traffic and Geotechnical Laboratory, 1992.
- [74] K. S. Hanse, M. Prats, and C. K. Chan. Finite-element modeling of depletion-induced reservoir compaction and surface subsidence in the south belridge oil field, california. Anchorage, 1993. Paper SPE 26074. SPE Western Regional Meeting.
- [75] K. Hara and A. Kobayashi. Analysis of the problem of bmt1 with thames. Technical Report Report of DECOVALEX, phase I. Bench Mark Test 1. 1993.
- [76] R. D. Hart and C. M. S. John. Formulation of fully-coupled thermal-mechanical-fluid flow model for nonlinear geologic systems. *Int. J. Rock. Mech. Min. Sci. & Geomech. Abstr.*, 23:3:213–224, 1986.
- [77] G. W. Herbert. Cold waterflooding a warm reservoir. *SPE 5083*, 1974.
- [78] R. Hill. *The mathematical theory of plasticity*. Oxford University Press. Oxford, 1950.
- [79] K. Hojka and M. B. Dusseault. Analytical solutions for transient thermoelastic stress fields around a borehole during fluid injection into permeable media. *JCPT*, Vol. 32, NO.4:49–57, 1993.
- [80] M. K. Hubbert and D. G. Willis. Mechanics of hydraulic fracturing. *JPT*. Trans. AIME 210:153–166, 1957.
- [81] D. S. Hughes and C. E. Cooke. The effects of pressure on the reduction of pore volume of consolidated sandstones. *Geophysics*, 18:298–309, 1953.
- [82] P. Huyakorn and G. F. Pinder. A pressure-enthalpy finite element model for simulating hydrothermal reservoirs. *Math. Comput. Simul.*, 20:167–178, 1978.

- [83] J. Jaeger. Numerical values for the temperature in radial heat flow. *J. Math. Phys.*, 34:316–321, 1956.
- [84] A. Janah. Pore volume variation of porous media with temperature and stress. Technical report, The University of California, Berkeley, 1980.
- [85] L. Jing, C.-F. Tsang, and O. Stephansson. Decovalex - an international cooperative research project on mathematical models of coupled thm process for safety analysis of radioactive waste repositories. *Int. J. Rock Mech. Min. Sci. & Geomech. Abstr.*, 32:5:389–398, 1995.
- [86] C. F. Knutson and B. F. Bohor. Reservoir rock behavior under moderate confining pressure. *Geophysics*, 18:298–309, 1953.
- [87] K. M. Kosar. *Geotechnical properties of oil sands and related strata*. Ph.D. dissertation, The University of Alberta, Edmonton, 1989.
- [88] M. Kurashige. A thermoelastic theory of fluid-filled porous materials. *Int. J. Solids Structures*, 25(9):1039–1052, 1989.
- [89] T. J. Lasseter, P. A. Witherspoon, and M. J. Lippmann. The numerical simulation of heat and mass transfer in multidimensional two-phased geothermal reservoirs. In *Proc. Second United Nation Symp. on the Devel. and Use of Geothermal Resource*, volume 3, pages 1715–1725, San Francisco, California, 1975.
- [90] R. W. Lewis. A coupled finite element model for the consolidation of non-isothermal elastoplastic porous media. *Transport in porous media*, Vol. 1:155–178, 1986.
- [91] R. W. Lewis, G. K. Roberts, and O. C. Zienkiewicz. A non linear flow and deformation analysis of consolidation problems. In *Proc. 2nd Int. Conf. Num. Meth. Geom.*, pages 1106–1118, Blacksburg, 1976.
- [92] R. W. Lewis and B. A. Schrefler. *The finite element method in the deformation and consolidation of porous media*. John Wiley & Sons Ltd, 1987.
- [93] X. Li and C. P. Tan. Fbore-3d: A program for borehole stability analysis with determination of horizontal stress bounds from wellbore data. Technical Report RMC-95-03, RMI, OU, Norman, OK, 1995.
- [94] X. Li, C. P. Tan, and J. C. Roegiers. Collaborative development of a wellbore stability analysis software with determination of horizontal stress bounds from wellbore data. In G. Barla, editor, *Prediction and performance in rock mechanics and rock engineering*, Torino, Italy, 1997.
- [95] J. K. Mackenzie. The elastic constants of a solid containing spherical holes. *Proc. Phys. Soc., Section B*, 63:2–11, 1950.

- [96] G. Maier and T. Hueckel. Nonassociated and coupled flow rules of elastoplasticity for rock-like materials. *Int. J. Rock. Mech. Min. Sci.*, 16:77-92, 1979.
- [97] A. Makurat. Decovalex test case 1 - distinct element simulation of coupled shear flow test. Technical Report Report 92106.2, Norwegian Geotechnical Institute, Norway, 1992.
- [98] V. Maury and Z. Christian. Wellbore instability due to shear displacements along preexisting fractures: are we overlooking a common cause of drilling problem ? *IADC/SPE 27492*, 1994.
- [99] V. Maury and J. L. Idelovici. Safe drilling of hp/ht wells, the role of the thermal regime in loss and gain phenomenon. *IADC/SPE Drilling Conference*. 1995.
- [100] W. D. McCain. *The properties of petroleum fluids*. PennWell Publishing Company, Tulsa, Oklahoma, 1990.
- [101] C. R. Mckee, A. C. Bumb, and R. A. Koeing. Stress-dependent permeability and porosity of coal. In *Proc. 1987 Coalbed Methane Symp.*, TUSCALOOSA, Alabama, 1987.
- [102] P. J. Mclellan and Y. Wang. Predicting the effects of pore pressure penetration on the extent of wellbore instability: application of a versatile poroelastoplastic model. In *Rock Mechanics in Petroleum Engineering, Proc. of Eurock'94*, Rotterdam, 1994. Balkema. Proc. of Eurock'94.
- [103] D. F. McTigue. Thermoelasticity response of fluid-saturated porous rock. *J. Geoph. Res.*, Vol. 91:9533-9542, 1986.
- [104] D. F. McTigue. Flow to a heated borehole in porous, thermoelastic rock: analysis. *Water Resources Research*, 26:8:1763-1774, 1990.
- [105] C. C. Mei and P. A. Tyvand. Thermal consolidation of a thick and soft soil layer. *ASCE Eng. Mech.*, 114, 1988.
- [106] J. W. Mercer and C. R. Faust. Simulation of water and vapor-dominated hydrothermal reservoirs. In *Paper SPE 5520*, 1975. Presented at the 50th Annu. Fall Meeting of SPE, AIME.
- [107] J. W. Mercer and C. R. Faust. A review of numerical simulation of hydrothermal systems. *Hydrological Sciences-Bulletin*, Vol. 24, No. 3, 1979.
- [108] J. L. Monte and R. J. Kritzen. One dimensional mathematical model for large-strain consolidation. *Geothchnique*, 26(3):495-510, 1976.

- [109] N. Morita, D. L. Whitfill, I. Massie, and T. W. Knudsen. Realistic sand production prediction: Numerical approach. In *SPE 16989*, 1987.
- [110] H. B. Muhlhaus. Stability of deep underground excavations in strongly cohesive rock. In *Proc. 6th ISRM congr.*, pages 1157–1161, Rotterdam, 1987. Balkema.
- [111] J. Noorishad and C.-F. Tsang. Coupled thermohydromechanical modelling. Technical Report DECOVALEX, phase I, Bench Mark Test 2 and Test Case 1, Earth Science Division, Lawrence Berkeley Laboratory, Berkeley, California, 1992.
- [112] J. Noorishad, C. F. Tsang, and P. A. Witherspoon. Coupled thermal-hydraulic-mechanical phenomena in saturated fractured porous rocks: numerical approach. *J. Geoph. Res.*, 89:10365–10373, 1984.
- [113] W. Nowacki. *Dynamic problems of thermoelasticity*. PWN-Polish Scientific Publishers, Warsaw, 1966.
- [114] W. Nowacki. *Thermoelasticity*. PWN-Polish Scientific Publishers, Warszawa, 1986.
- [115] J. L. Nowinski. *Theory of thermoelasticity with applications*. Sijthoff and Noordhoff international publishers, Alphen aan den Rijn, The Netherlands, 1978.
- [116] A. Nur and J. D. Byerlee. An exact effective stress law for elastic deformation of rock with fluids. *J. Geophys. Res.*, 76(26):6414–6419, 1971.
- [117] J. T. Oden. *Finite elements of non-linear continua*. McGraw-Hill, New York, 1972.
- [118] S. H. Ong. *Borehole Stability*. Ph.D. dissertation, The University of Oklahoma, 1994.
- [119] S. H. Ong and J.-C. Roegiers. Horizontal wellbore collapse in an anisotropic formation. *SPE 25504*, 1993.
- [120] S. H. Ong and J.-C. Roegiers. Influence of anisotropies in borehole stability. *Int. J. Rock. Mech. Min. Sci. & Geomech. Abstr.*, 30:7:1069–1075, 1993.
- [121] D. R. J. Owen and E. Hinton. *Finite elements in plasticity-theory and practice*. Pinerige Press Limited, Vienna, 1980.
- [122] H. Ozbek and S. Phillips. Thermal conductivity of aqueous nacl solution from 20°c to 330°c. Technical report, Lawrence Berk. Lab., 1979.

- [123] T. K. Perkins and J. A. Gonzalez. Changes in earth stresses around a wellbore caused by radially symmetrical pressure and temperature gradients. *Society of petroleum engineers journal*, pages 129–140, April 1984.
- [124] R. H. Perry, D. W. Green, and J. O. Maloney. *Perry's chemical engineer's handbook*. McGraw-Hill, Inc., New York, 1984.
- [125] S. Phillips, A. Igbene, J. Fair, H. Ozbek, and M. Tavana. A technical data book for geothermal energy utilization. Technical report, Lawrence Berk. Lab., 1981.
- [126] B. Plischke. Finite element analysis of compaction and subsidence - experiences gained from several chalk fields. Delft, 1994. Paper SPE 28129, SPE/ISRM Mechanics in Petroleum Engineering Conference.
- [127] C. G. Rawlings, N. R. Barton, S. C. Bandis, M. A. Addis, and M. S. Gutierrez. Laboratory and numerical discontinuum modeling of wellbore stability. *JPT*, 45:11:1086–1092, 1993.
- [128] G. Rehbinder. Analytical solutions of stationary coupled thermo-hydro-mechanical problems. *Int. J. Rock Mech. Min. Sci. & Geomech. Abstr.*, 32:5:453–463, 1995.
- [129] S. F. Reyes and D. U. Deere. Elastoplastic analysis of underground openings by the finite element method. In *Proc. 1st Congr. ISRM*, pages 477–483, Lisbon, 1966.
- [130] J. R. Rice and M. P. Cleary. Some basic stress-diffusion solutions for fluid-saturated elastic porous medium with compressible constituents. *Rev. Geophys. Space Phys.*, 14:227–241, 1976.
- [131] R. Risnes, R. K. Bratli, and P. Horsrud. Sand stresses around a wellbore. *SPE J.*, December:883–894, 1982.
- [132] D. P. Salisbury, G. G. Ramon, and B. S. Wilton. Wellbore instability of shales using a downhole simulation test cell. In R. (ed.), editor, *Rock Mechanics as a Multidisciplinary Science*, Rotterdam, 1991. Balkema.
- [133] A. E. Scheidegger. *Handbuch der Physik*, VIII/2. Springer-Verlag,, Berlin, 1963.
- [134] R. L. Schiffman. A thermoelastic theory of consolidation. *Environmental geophysics and heat transfer*, Vol. 4:78, 1971.
- [135] B. A. Schrefler. A partitioned solution procedure for geothermal reservoir analysis. *C. A. N. M.*, 1:53–56, 1985.

- [136] H. N. Seneviratne, J. P. Carter, D. W. Airey, and J. R. Booker. A review of models for predicting the thermomechanical behaviour of soft clays. *Int. J. Num. Anal. Meth. Geome.*, Vol. 17:715–733, 1993.
- [137] H. N. Seneviratne, J. P. Carter, and J. R. Booker. Analysis of fully coupled thermomechanical behavior around a rigid cylindrical heat source buried in clay. *Int. J. Num. Anal. Meth. Geome.*, Vol. 18:177–203, 1994.
- [138] J. F. Shao and J. P. Henry. Development of an elastoplastic model for porous rock. *Int. J. Plasticity*, 7:1–13, 1991.
- [139] A. W. Skempton. The pore pressure coefficients a and b. *Geotechnique*, Vol. 4:143–147, 1954.
- [140] D. W. Smith and J. R. Booker. Green's functions for a fully coupled thermo-poroelastic material. *Int. J. Num. Anal. Meth. Geome.*, 17:139–163, 1993.
- [141] W. H. Somerton. *Thermal properties and temperature-related behavior of rock/fluid system*. Elsevier Science Publishers, 1992.
- [142] M. L. Sorey. Numerical modelling of liquid geothermal systems. *Geol. Surv. Prof. Pap. U.S.*, 1044D, 1978.
- [143] H. Stehfest. Numerical inversion of laplace transforms. *Commun. Ass. Comput. Mach.*, 13:47–49, 624, 1970.
- [144] O. Stephansson. Introduction. *Int. J. Rock Mech. Min. Sci. & Geomech. Abstr.*, 32:5, 1995.
- [145] J. Sweet. Pressure effects on thermal conductivity and expansion of geologic materials. Technical Report DOE Report #SAN 78-1991, 1978.
- [146] K. Terzaghi. Die berechnung der durchlassigkeitsziffer des tones aus dem verlauf der hydrodynamischen spannungserscheinungen. *Sitzungsber. Akad. Wissen., Wien Math. Naturwiss. Kl., Abt., IIa* 132:105–124, 1923.
- [147] J. N. Thomas. An improved accelerated initial stress procedure for elastoplastic finite element analysis. *Int. J. Num. Anal. Meth. Geo.*, 8:359–379, 1984.
- [148] V. Tikhomirov. Conductivity of rocks and their relationship with density, saturation and temperature. *Neftianoe Khoziaistra*, 46(4:36), 1968.
- [149] J. R. Tillerson, J. A. Stricklin, and W. E. Haisler. Numerical methods for the solution of non-linear problems in structural analysis. In *Numerical solution of non-linear problems*, pages 67–101. ASME special publication, AMD-Vol 6., 1973.

- [150] H. H. Vaziri. Coupled fluid flow and stress analysis of oil sands subject to heating. *JCPT*, 27:5:84–91, 1988.
- [151] C. A. M. Veeken, J. V. Walters, C. J. Kenter, and D. R. Davis. Use of plasticity models for predicting borehole stability. In *Rock at great depth*, Rotterdam, 1989. Balkema.
- [152] W. Von Gonten and B. Choudhary. Effect of pressure and temperature on pore volume compressibility. *Soe. Pet. Engrs.*, reprint # 2526, 1969.
- [153] J. V. Walters and J. N. Thomas. Shear zone development in granular materials. In *Numerical Methods in Geomechanics*, pages 263–275, Rotterdam, 1982. Balkema.
- [154] Y. Wang and M. B. Dusseault. Borehole yield and hydraulic fracture initiation in poorly consolidated rock strata-part ii. permeable media. *Int. J. Rock. Mech. Min. Sci. and Geomech. Abs.*, 28:4:247–260, 1991.
- [155] Y. Wang and E. Papamichos. Conductive heat flow and thermally induced fluid flow around a well bore in a poroelastic medium. *Water Resources Research*, 30:12:3375–3384, 1994.
- [156] Y. Wang, E. Papamichos, and M. Dusseault. Thermal stresses and borehole stability. In *Rock Mechanics, tools and techniques, (vol 2)*, pages 1121–1127, Rotterdam, 1996. Balkema.
- [157] R. L. Whiting and H. J. J. Ramey. Application of material and energy balances to geothermal steam production. *JPT*, 21:7:893–900, 1969.
- [158] W. E. Wittke. *Proc. 3rd int. conf. numerical methods in geomechanics*. Balkema, Rotterdam, 1979.
- [159] T. Wong and W. Brace. Thermal expansion of rocks: some measurements at high pressure. *Tectonophics*, 57:95–117, 1979.
- [160] W. L. Wood and R. W. Lewis. A comparison of time marching schemes for the transient heat conduction equation. *Int. J. Num. Meth. Engr.*, 9:679–689, 1975.
- [161] W. Woodside and J. Messmer. Thermal conductivity of porous media. ii: Consolidated rocks. *J. Appl. Phys.*, 32:1699–1706, 1992.
- [162] O. C. Zienkiewicz. *The finite element method in engineering science (3rd edition)*. McGraw-hill, London, 1977.
- [163] O. C. Zienkiewicz. *The finite element method*. McGraw-hill, London, 1989.

- [164] O. C. Zienkiewicz and C. Humpheson. Viscoplasticity, a generalised model for description of soil behaviour. In C. S. Desai and J. T. Christian, editors, *Numerical Methods in Geotechnical Engineering*, pages 116–147, New York, 1977. McGraw-Hill.
- [165] O. C. Zienkiewicz and G. N. Pande. Some useful forms of isotropic yield surfaces for soil and rock mechanics. In G. Gudehus, editor, *Finite Element Methods in Geomechanics*, Chichester, 1972. Wiley.
- [166] R. W. Zimmerman. *Compressibility of sandstones*. Elsevier Science Publishers, 1991.
- [167] M. D. Zoback and J. D. Byerlee. Permeability and effective stress. *Am. Assoc. Pet. Geol. Bull.*, 59:1:154–158, 1975.

# Appendix A: Stress- and Temperature-dependent Formation Properties and Poroelastic Parameters

Isothermal effective stress-dependent porosity, permeability and poroelastic parameters are derived by Cui[42]. The work conducted here extended Cui's derivation by including temperature effects.

From the micromechanical model of linear poroelasticity[30], the volumetric response for the porous matrix and pore space can be expressed in terms of the volumetric deformation of the solid phase,  $dV_s/V_s$ , and the relative deformation of the pore space and porous solids,  $d\phi/(1 - \phi)$ :

$$\frac{dV}{V} = \frac{dV_s}{V_s} + \frac{d\phi}{1 - \phi} \quad (\text{A.1})$$

$$\frac{dV_p}{V_p} = \frac{dV_s}{V_s} + \frac{d\phi}{\phi(1 - \phi)} \quad (\text{A.2})$$

By including the temperature effects, the constitutive relations for the porous matrix and pore space can be expressed as:

$$\frac{dV}{V} = \frac{d\sigma'_m}{K} - \frac{dp}{K'_s} + \alpha_m^T dT \quad (\text{A.3})$$

$$\frac{dV_p}{V_p} = \frac{d\sigma'_m}{K_p} - \frac{dp}{K''_s} + \alpha_p^T dT \quad (\text{A.4})$$

Where  $K'_s$  and  $K''_s$  are two bulk moduli. Under the assumption of isotropy and homogeneity, both are equal to  $K_s$ [52].

Eliminating  $dV/V$  from (A.1) and (A.3), one obtains:

$$\frac{dV_s}{V_s} = \frac{d\sigma'_m}{K} - \frac{dp}{K'_s} + \alpha_m^T dT - \frac{d\phi}{1 - \phi} \quad (\text{A.5})$$

Eliminating  $dV_p/V_p$  from (A.2) and (A.4), one obtains:

$$\frac{dV_s}{V_s} = \frac{d\sigma'_m}{K_p} - \frac{dp}{K'_s} + \alpha_p^T dT - \frac{d\phi}{\phi(1-\phi)} \quad (\text{A.6})$$

Eliminating  $dV_s/V_s$  from (A.5) and (A.6) and solving for  $d\phi/\phi$ :

$$\frac{d\phi}{\phi} = d\sigma'_m \left( \frac{1}{K_p} - \frac{1}{K} \right) + \left( \frac{1}{K'_s} - \frac{1}{K''_s} \right) dp + (\alpha_p^T - \alpha_m^T) dT \quad (\text{A.7})$$

By invoking the Betti-Maxwell reciprocal theorem, it can be proven that[52]:

$$K_p = \frac{\phi}{\alpha} K \quad (\text{A.8})$$

By assuming spheric pores, Mackenzie[95] derived the following approximate relationship for the relationship between the drained bulk modulus of the bulk material, and the bulk modulus and the shear modulus of the solid phase, and porosity:

$$\frac{1}{K} = \frac{1}{1-\phi} \left( \frac{1}{K_s} + \frac{3\phi}{4G_s} \right) \quad (\text{A.9})$$

Solving  $\phi$  from (A.9):

$$\phi = \alpha \frac{4G_s}{4G_s + 3K} \quad (\text{A.10})$$

and substituting into (A.8), then into (A.7), one obtains:

$$\frac{d\phi}{\phi} = \frac{3}{4G_s} d\sigma'_m + (\alpha_p^T - \alpha_m^T) dT \quad (\text{A.11})$$

Integrating equation (A.11) yields the following expression for stress- and temperature-dependent porosity:

$$\phi = \phi_n \exp \left[ \frac{3}{4G_s} (\sigma'_m - \sigma'_{mn}) + (\alpha_p^T - \alpha_m^T) (T - T_n) \right] \quad (\text{A.12})$$

The stress- and temperature-dependent bulk modulus can be deduced by substituting (A.12) into (A.9):

$$\frac{1}{K} = \frac{1}{K_s} \frac{1}{1 - \phi_n \exp x} (1 + a\phi_n \exp x) \quad (\text{A.13})$$

where,

$$a = \frac{1 + \nu_s}{2(1 - 2\nu_s)} \quad (\text{A.14})$$

$$x = -\frac{3}{4G_s} (\sigma'_m - \sigma'_{mn}) + (\alpha_p^T - \alpha_m^T) (T - T_n) \quad (\text{A.15})$$

The relationship:

$$K_s = \frac{2G_s(1 + \nu_s)}{3(1 - 2\nu_s)} \quad (\text{A.16})$$

is applied in the above derivation.

Mackenzie[95] also derived a formula for the shear modulus of bulk material based on the shear modulus and bulk modulus of the solid phase, and porosity:

$$G = G_s \left[ 1 - \frac{5\phi(3K_s + 4G_s)}{9K_s + 8G_s} \right] \quad (\text{A.17})$$

Substituting (A.12) into (A.17), one obtains:

$$G = G_s \left[ 1 - \frac{15(1 - \nu_s)}{7 - 5\nu_s} \phi_n \exp x \right] \quad (\text{A.18})$$

For an isotropic material, the effective stress coefficient  $\alpha$  and Skempton's coefficient  $B$  can be expressed in terms of bulk moduli and porosity in the following form[52]:

$$\alpha = 1 - \frac{K}{K_s} \quad (\text{A.19})$$

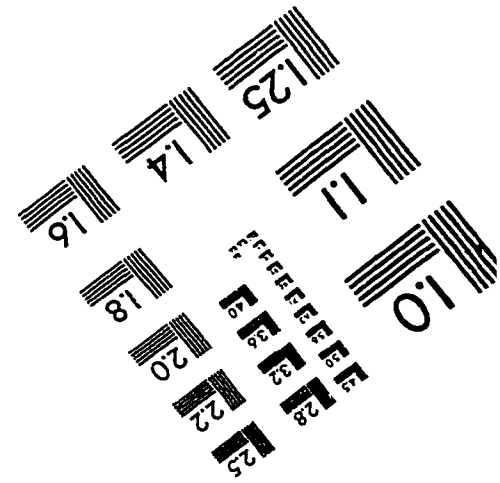
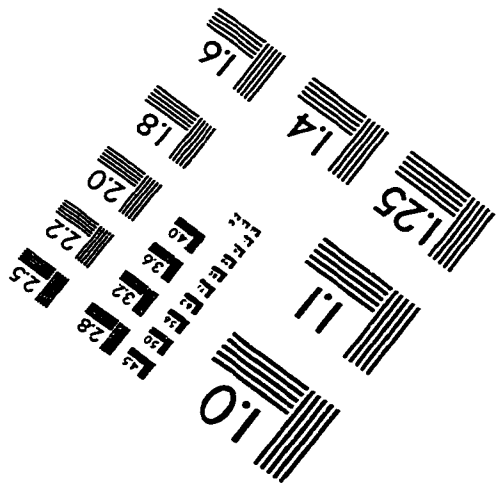
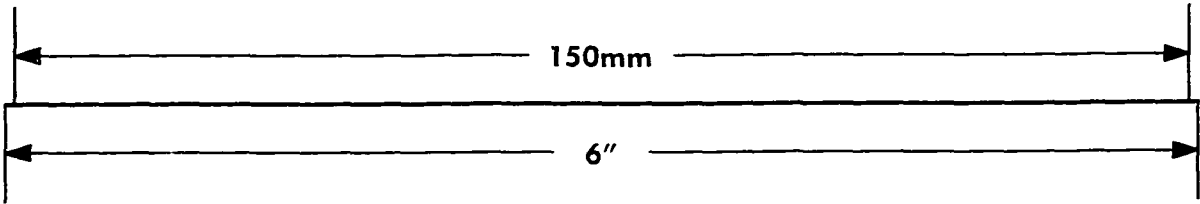
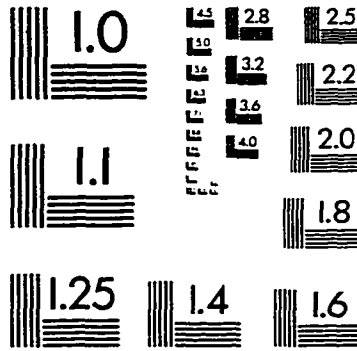
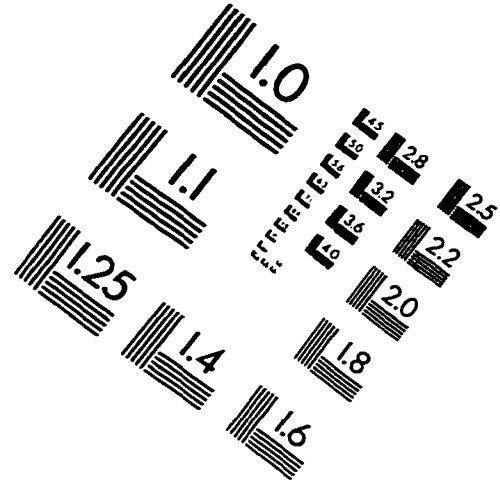
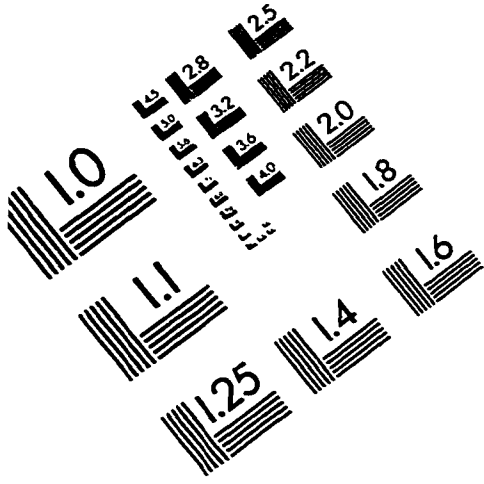
$$B = \frac{K_s/K - 1}{K_s/K + \phi K_s/K_f - (1 + \phi)} \quad (\text{A.20})$$

Substituting (A.12) into (A.19) and (A.20), the stress- and temperature-dependent effective stress and Skempton coefficients can be obtained:

$$\alpha = \frac{(1 + a) \phi_n \exp x}{1 + a \phi_n \exp x} \quad (\text{A.21})$$

$$B = \frac{1 + a}{a + (1 - \phi_n \exp x) K_s/K_f + \phi_n \exp x} \quad (\text{A.22})$$

# IMAGE EVALUATION TEST TARGET (QA-3)



APPLIED IMAGE, Inc  
1653 East Main Street  
Rochester, NY 14609 USA  
Phone: 716/482-0300  
Fax: 716/288-5989

© 1993, Applied Image, Inc., All Rights Reserved